The Vortex Dynamics of Laminar Separation Bubbles

by

John W. Kurelek

A thesis
presented to the University of Waterloo
in fulfillment of the
thesis requirement for the degree of
Doctor of Philosophy
in
Mechanical Engineering

Waterloo, Ontario, Canada, 2020

© John W. Kurelek 2020

Examining Committee Membership

The following served on the Examining Committee for this thesis. The decision of the Examining Committee is by majority vote.

External Examiner	Dr.-Ing. O. Marxen Lecturer Dept. of Mechanical Engineering Sciences University of Surrey, United Kingdom
Supervisors	Prof. dr. S. Yarusevych Professor Dept. of Mechanical and Mechatronics Engineering University of Waterloo
	Dr. M. Kotsonis Associate Professor Faculty of Aerospace Engineering Delft University of Technology, the Netherlands
Internal Member	Dr. S. Peterson Associate Professor Dept. of Mechanical and Mechatronics Engineering University of Waterloo
Internal-External Member	Prof. dr. K. Lamb Professor Dept. of Applied Mathematics University of Waterloo
TU Delft Member	Prof. dr. F. Scarano Professor and Chair of Aerodynamics Faculty of Aerospace Engineering Delft University of Technology, the Netherlands

Author's Declarations

I hereby declare that I am the sole author of this thesis. This is a true copy of the thesis, including any required final revisions, as accepted by my examiners.

I understand that this document may be made electronically available to the public.

Statements

The doctoral research has been carried out in the context of an agreement on joint doctoral supervision between Delft University of Technology, the Netherlands, and the University of Waterloo, Canada. Both institutions made important contributions to the work described in this thesis.

Funding was provided by the Natural Sciences and Engineering Research Council of Canada and the Ontario Graduate Scholarship Program.

Abstract

Laminar separation bubbles (LSBs) are common features in low Reynolds number flows, and can have considerable performance impacts in applications such as hydrofoils, small-to-medium scale wind turbines, micro and unmanned aerial vehicles, glider planes, and aircrafts operating at low speed or high altitude. In particular, the very presence of an LSB can cause loss in lift, increase in drag, and/or unwanted noise emissions, while also leaving the flow in an unstable configuration, as only slight changes in the environment or operating conditions can lead to further detrimental effects, such as the sudden onset of stall. All of these performance impacts are rooted in the laminar–turbulent transition process of an LSB, where disturbance growth in the unstable shear layer leads to its roll-up and the formation of coherent shear layer vortices that govern the reattachment process and are the source of unsteady loads and noise emissions. Therefore, a comprehensive understanding of LSB transition and vortex dynamics is a prerequisite to the development of effective control strategies. The work completed as part of this thesis is at the forefront of this effort, as flow development in laminar separation bubbles is studied and a new forcing technique is developed and tested. The supporting data is experimental and is collected primarily by means of particle image velocimetry (PIV).

First, flow development in a nominally two-dimensional LSB formed over an airfoil is studied. Forcing at the LSB fundamental frequency and the first subharmonic of this frequency are found to inhibit and promote the prevalence of vortex merging in the LSB, respectively. When left to develop naturally, the flow development is characterized by the periodic roll-up of the separated shear layer upstream of the mean maximum height location. The vortices are strongly two-dimensional at formation, but quickly develop spanwise deformations with downstream convection, leading to their breakdown to smaller scales near the mean reattachment point. The deformations take the form of spanwise undulations in the vortex filaments, which tend to develop at wavelengths ranging between one and seven times the streamwise wavelength of the structures. These undulations continually intensify, ultimately leading to the breakdown of the vortices, while re-orienting vorticity from the spanwise direction into the streamwise and wall-normal directions, creating hairpin-like structures.

An instability mechanism is hypothesized to be responsible for the development of these spanwise undulations, and a new forcing technique is developed to target it. The technique is capable of producing deterministic, three-dimensional disturbances modulated to a desired spanwise wavelength, while holding all other parameters (amplitude, frequency, and streamwise wavelength) constant. This is achieved using two alternating current, dielectric barrier discharge (AC-DBD) plasma actuators arranged in streamwise succession, which are operated simultaneously. The upstream actuator produces a spanwise uniform disturbance, which is then spanwise modulated by the output of the downstream actuator, with a relative phase delay introduced in order to spatially superimpose the two outputs. The technique is verified to produce the desired disturbance characteristics through a detailed experimental characterization that considers both quiescent and in-flow conditions.

The effects of this forcing technique and the subsequent growth in spanwise modes is studied in an LSB formed over a flat plate subject to an adverse pressure gradient. Disturbance growth is tracked throughout the LSB, identifying small amplitude disturbances of a frequency matching the

primary Kelvin-Helmholtz instability that undergo convective amplification downstream of the mean separation point. In comparing results from forcing the flow with two and three-dimensional disturbances, with the latter modulated to a spanwise-to-streamwise wavelength ratio of 2 : 1, disturbance amplitudes in this region are higher for the three-dimensional case, indicating a preferential amplification of spanwise modes in the upstream boundary layer. While this growth may result from the underlying stability of the upstream boundary layer, it could also stem from a low frequency modulation of the base flow, as significant spanwise non-uniformities of the same wavelength are found in the unforced natural flow. Nevertheless, stability predictions in the LSB find that, regardless of the forcing scenario, the normal (two-dimensional) modes are subject to the highest amplification rates throughout the length of the LSB, while disturbance modes of an oblique wave angle of less than 30° experience comparable, yet reduced, growth rates. Thus, disturbance growth in the LSB is confirmed to be spanwise wavelength dependent. The effectiveness of the spanwise modulated forcing, in terms of effecting change in disturbance and flow development, is justified, as its wavelength ratio (2 : 1) corresponds to a wave angle of 26.5°, while the other three-dimensional forcing configurations considered are less effective on account of their larger wave angles (33.7° and 45°).

The effect of unstable spanwise modal growth on the development of the LSB shear layer vortices and the ensuing vortex dynamics is assessed. The small amplitude perturbations tracked through the fore portion of the LSB manifest in the shear layer vortices, imparting a spanwise wavelength, if present, in the vortex filaments. Thus, in the case of two-dimensional forcing, the shear layer vortices remain largely two-dimensional until their breakdown, while for the three-dimensional forcing case, significant spanwise undulations develop at the 2 : 1 ratio prescribed by the forcing. The filaments surge forward in the streamwise direction downstream of the three-dimensional actuator's active regions, while lagging behind at spanwise locations downstream of the actuator gaps. A continual intensification of vortex stretching ensues, leading to rapid filament deformations. Through supporting observations from a simplified vortex filament model, the undulatory shape of the vortex filament is shown to self-induce a net rotational motion, causing the streamwise forward and rearward sections of the filament to tilt away and toward the wall, respectively. This, coupled with the wall-normal velocity gradient, causes the continual stretching of the filament. These vortex motions are observed consistently for all LSBs studied throughout this thesis, and apply more broadly to all LSBs, since regardless of how a spanwise undulations is initially produced, if present, a vortex filament will tend to develop in the way shown in any near-wall shear flow. Thus, these dynamics are found to be intrinsic to the breakup process of shear layer vortices in laminar separation bubbles.

Acknowledgements

I would like to thank my supervisors, Serhiy Yarsuveych and Marios Kotsonis, first, for providing the remarkable opportunity to engage in this dual PhD program. I am grateful to you both for the significant time and effort invested just to make this program possible. Second, thank you for the indispensable guidance and insight provided throughout this endeavour. Your teachings and infallible approach to research have taught me the skills and mindset needed for a successful career in academia.

Thank you to my examination committee members, Professors Olaf Marxen, Sean Peterson, Kevin Lamb, and Fulvio Scarano, for investing the time to read this document, the valuable questions posed, and the suggested improvements.

I would like to thank my graduate school colleagues, past and present, at the University of Waterloo: Supun Pieris, Jeff McClure, Yash Shah, Caddie Zhang, Nikhilesh Tumuluru Ramesh, Connor Toppings, Mark Istvan, Dallyn Wynnychuk, Erik Marble, Burak Tuna, Andrew Lambert, Ajith Airody, and Chris Morton. Thank you also to my colleagues at Delft University of Technology: Theo Michelis, Alberto Ruis Vidales, Jacopo Serpieri, Kaisheng Peng, Hongxin Zhang, and Rodrigo Castellanos. Thanks also to Anke van den Dries and Sven Westerbeek for the Dutch translations. To all of you, thank you for the helpful discussions, eagerness to lend a helping hand, and friendship. Special thanks are owed to Supun, for the many fruitful discussions always interlaced with banter, and Theo, who taught me the obsessive, and hence unhealthy, approach needed for quality PIV measurements.

I would like to thank my parents, Dianne and Andy, and siblings, Bill and Lynne, for their love and unwavering support in me and my decision to pursue higher education. Finally, to my wife, Nicole, you are at the core of everything I do, and your endless love and support have carried me to this finish line.

Contents

List of Abbreviations

AC	Alternating Current
AOA	Angle of Attack
DBD	Dielectric Barrier Discharge
DNS	Direct Numerical Simulation
HWA	Hot-Wire Anemometry
K-H	Kelvin-Helmholtz
LSB	Laminar Separation Bubble
LST	Linear Stability Theory
OSE	Orr-Sommerfeld Equation
PIV	Particle Image Velocimetry
POD	Proper Orthogonal Decomposition
PSD	Power Spectral Density
SPL	Sound Pressure Level
TS	Tollmien-Schlichting

List of Symbols

Accents and Subscripts

Example	Description
$\overline{a}$	time-averaged quantity
$\vec{a}$	vector quantity
$\langle a \rangle$	phase-averaged quantity
a'	fluctuating quantity
$\breve{a}$	unit vector
$\hat{a}$	perturbation mode
$\widetilde{a}$	quantity non-dimensionalized by $\delta_{1\mathrm{s}}$
a_∞	quantity evaluated in the free-stream
a_0	quantity pertaining to the LSB fundamental frequency
a_{cr}	quantity evaluated at location of incipient disturbance amplification
a_{h}	quantity evaluated at maximum bubble height point
a_i	imaginary component
a_{pp}	peak-to-peak quantity
a_r	real component
a_{r}	quantity evaluated at mean reattachment point
a_{rms}	root-mean-square quantity
a_{s}	quantity evaluated at mean separation point
a_{sw}	quantity pertaining to the test section standing wave
a_x	quantity evaluated in x-direction
a_y	quantity evaluated in y-direction
a_z	quantity evaluated in z-direction

Dimensionless Quantities

Symbol	Description	Definition
$C_{\overline{p}}$	mean pressure coefficient	$(\overline{p} - p_\infty) / \left(\frac{1}{2}\rho {u_\infty}^2\right)$
C_μ	momentum coefficient	$T_{\mathrm{tot}} / \left(\frac{1}{2}\rho {u_\infty}^2 l \delta_1\right)$
H	boundary layer shape factor	δ_1/δ_2
i	imaginary unit	$\sqrt{-1}$
N	disturbance amplification factor	$\int_{x_{\mathrm{cr}}}^{x} -\alpha_i \mathrm{d}x$
Re_a	Reynolds number; length scale a	$u_\infty a/\nu$
St_a	Strouhal number; length scale a	fa/u_∞
t_a^*	convective time scale; length scale a	tu_∞/a

Roman Symbols

Symbol	Description	Units
A	disturbance amplitude	$\mathrm{m^2\,s^{-1}}$
$b^{(m)}$	POD temporal coefficient; mode m	–
C	arbitrary closed curve; unit tangent vector $\breve{\ell}$	–
c	airfoil chord length	m
$e^{(m)}$	POD eigenvalue; mode m	–
E_{C}	POD cumulative modal energy	–
E_{R}	POD relative modal energy	–
f	frequency	Hz
f_{c}	carrier frequency	Hz
f_{m}	modulation frequency	Hz
h	LSB maximum height	m
k	wavenumber	$\mathrm{m^{-1}}$
l	plasma actuator length	m
L	LSB length; $x_{\mathrm{r}} - x_{\mathrm{s}}$	m
m	POD mode number	–
P_a	probability distribution of quantity a	–

p	pressure	Pa
Q	vortex identification criterion [84]	s^{-2}
q	dynamic pressure; $\frac{1}{2}\rho u^2$	Pa
$\vec{r}$	position vector; $x\breve{\imath} + y\breve{\jmath} + z\breve{k}$	m
R_{merg}	ratio of merged to primary structures	–
T	sectional thrust force	$\mathrm{N\,m}^{-1}$
T_{act}	sectional thrust force generated within actuator active region	$\mathrm{N\,m}^{-1}$
T_{tot}	total thrust force generated by actuator	$\mathrm{N\,m}^{-1}$
t	time	s
$\vec{u}$	velocity vector; $u\breve{\imath} + v\breve{\jmath} + w\breve{k}$	$\mathrm{m\,s}^{-1}$
u	wall-tangent/streamwise velocity	$\mathrm{m\,s}^{-1}$
u_{con}	convective wall-tangent/streamwise velocity	$\mathrm{m\,s}^{-1}$
u_{e}	LSB edge velocity	$\mathrm{m\,s}^{-1}$
U_a	uncertainty estimate in quantity a (95% confidence)	units of a
v	wall-normal velocity	$\mathrm{m\,s}^{-1}$
V	voltage	V
w	spanwise velocity	$\mathrm{m\,s}^{-1}$
x	wall-tangent/streamwise coordinate	m
y	wall-normal coordinate	m
z	spanwise coordinate	m

Greek Symbols

Symbol	Description	Units
α	streamwise complex wavenumber	m^{-1}
β	spanwise complex wavenumber	m^{-1}
$\gamma_a^{(m)}$	POD spatial mode/eigenfunction; a-component, mode m	–
Γ	circulation; $\oint_C \vec{u} \cdot \mathrm{d}\breve{\ell}$	$\mathrm{m}^2\,\mathrm{s}^{-1}$
δ	boundary layer thickness; $y\vert_{\overline{u}(y)=0.99u_{\mathrm{e}}}$	m
δ_1	displacement thickness; $\int_0^{\delta} \left[1 - \frac{\overline{u}(y)}{u_{\mathrm{e}}}\right] \mathrm{d}y$	m

δ_2	momentum thickness; $\int_0^\delta \frac{\overline{u}(y)}{u_e}\left[1-\frac{\overline{u}(y)}{u_e}\right]\mathrm{d}y$	m
θ	phase angle	rad / deg.
ϑ	oblique wave angle, $\tan^{-1}(\lambda_x/\lambda_z)$, $\tan^{-1}(\beta_r/\alpha_r)$	rad / deg.
λ	wavelength	m
λ_2	vortex identification criterion [88]	s^{-2}
μ	dynamic viscosity	$\mathrm{N\,s\,m}^{-2}$
ν	kinematic viscosity	$\mathrm{m\,s}^{-2}$
ρ	density	$\mathrm{kg\,m}^{-3}$
τ	equation parameter	–
τ_w	wall shear stress; $\mu\left.\frac{\partial u}{\partial y}\right\|_{y=0}$	Pa
ψ	wavelet coefficient	–
ϕ_{aa}	PSD of signal a	[units of a]^2
φ	disturbance eigenfunction	$\mathrm{m}^2\,\mathrm{s}^{-1}$
Ω	angular frequency	$\mathrm{rad\,s}^{-1}$
$\vec{\omega}$	vorticity; $\vec{\nabla}\times\vec{u}$	s^{-1}

Chapter 1

Introduction

The laminar separation bubble is introduced. Pressing questions in the research community are identified, which form the basis of this thesis and formulate its objectives.

Laminar separation bubbles (LSBs) are a common feature in low Reynolds number flows, typically characterized by a Reynolds number, based on the chord of an airfoil, of less than 5×10^5 [127]. Engineering applications that operate in this regime include hydrofoils, low-pressure turbomachinery [74], small-to-medium scale wind turbines [62], micro and unmanned aerial vehicles [166], glider planes, and aircrafts operating at low speed or high altitude [34, 127]. The main impediment to performance for these applications is boundary layer separation, which brings penalties so severe that its mitigation is typically one of, if not the, primary design consideration. At low Reynolds numbers the boundary layer on the suction side of an airfoil often remains laminar into the adverse pressure gradient region, and hence is likely to separate. In the event of separation, the formed separated shear layer is unstable and undergoes transition to turbulence, which enhances momentum exchange. The flow may remain separated or reattach to the surface in the mean sense, with the latter forming a closed region of recirculating fluid, *i.e.*, a laminar separation bubble. The very presence of an LSB can be detrimental to performance, causing loss of lift, increase in drag, and/or noise emissions [8, 34], while also leaving the flow in an unstable configuration, as only slight changes in the environment or operating conditions can lead to further unwanted effects, such as the sudden onset of stall [166].

In an effort to mitigate the undesirable effects associated with LSBs, recent research efforts have been focused on its laminar–turbulent transition process so that, ultimately, the underlying physics may be understood and effective control strategies developed. To this end, much progress has been made in the last several decades [19], finding that the primary mode for disturbance growth in LSBs is a Kelvin-Helmholtz type instability of the separated shear layer [47], leading to its roll-up and the formation of coherent shear layer vortices [243]. All performance impacts associated with LSB are rooted in the dynamics of these vortical structures, as they govern the reattachment process [134] and are the source of unsteady loads and noise emissions [29]. Thus, a comprehensive understanding of LSB stability and vortex dynamics is a prerequisite to the development of effective control strategies.

The most effective control strategies developed to-date target the LSB shear layer vortices and the associated Kelvin-Helmholtz instability [258]. Forcing at this 'fundamental' frequency has significant impact on the ensuing vortex dynamics [135, 260], as the vortex shedding process locks to the excitation frequency, vortex formation occurs farther upstream, and the spanwise coherence of the structures is increased; all resulting in a reduction in the size of the LSB and earlier mean reattachment. Lacking are studies examining the effects of forcing at subharmonics of the fundamental frequency. Such an investigation has merit since forcing of this type has been shown to have significant influence on the vortex dynamics of free shear layers [73], specifically through promoting vortex merging and thus increasing the rate of momentum transfer across the layer [72]. It remains to be determined if vortex merging plays a role of any significance with regard to LSBs, through the influence of the reattachment process or otherwise, and whether merging can be manipulated via forcing to the same effect seen in free shear layers.

Contributing to the difficulty in gaining a complete understanding of the structure and development of the shear layer vortices in LSBs is the confluence of factors that can affect flow development. In experiments, these include model imperfections [133], intrusive measurement techniques [24], and the disturbance environment [174]. With respect to the latter, the sensitivity of LSBs to the level of free-stream turbulence is well documented, with significant differences

noted in the topology and development of the shear layer vortices when levels increase from near zero to approximately 1% of the free-stream velocity [86, 125], while the underlying transition process is altered altogether at higher levels ($\gtrsim$ 2%) [77]. Furthermore, a number of secondary instabilities have been reported to be active in LSBs under certain conditions, including a Görter type [138], elliptical and hyperbolic instabilities [92, 137], and absolute and/or global instabilities [2, 201], all of which can interact with the primary Kelvin-Helmholtz instability. In studying LSB stability and transition, the introduction of controlled periodic disturbances is often used as a diagnostic tool, however, any study of this nature can be inherently problematic if the diagnostic means modifies the base flow, and hence the transition process under consideration [140]. This is particularly true of experimental investigations, with a significant portion of results collected for which the baseline LSB has been modified due to high amplitude forcing [135, 260], or by elevated turbulence intensity values [33, 69], all while being limited to two-dimensional assessments of a flow field that is inherently three-dimensional. Thus, a study that simultaneously limits the external factors known to influence LSBs while characterizing the three-dimensional development of the shear layer vortices is warranted.

While widely ranging descriptions of vortex development in LSBs can be found across the literature, a feature common to nearly all investigations is the development of spanwise deformations/undulations in the shear layer vortices [113, 137, 153, 170], which tend to develop over a relatively fixed range of spanwise wavelengths, found to range between one and seven times the streamwise wavelength of the structures. This raises the possibility of an underlying instability associated with vortex breakup in LSBs which, if present, could potentially be manipulated through targeted, three-dimensional forcing. Precedence for three-dimensional forcing techniques can be found in the literature, as key physical mechanisms have been elucidated in other canonical flows through the use of such techniques [15, 107, 209], most notably in the seminal works of Klebanoff *et al.* [107] on boundary layer transition. DNS studies have cross-examined two and three-dimensional disturbance development in LSBs [137, 198], finding that disturbances with a spanwise-to-streamwise wavelength ratio of approximately two can grow at comparable rates to the two-dimensional mode, leading to modifications of the mean flow field through a spanwise staggering of the vortex shedding process. Experimental studies of the same nature are scarce due to the difficulty in implementing a reliable three-dimensional forcing technique, which is then compounded by the need for three-dimensional flow field measurements.

1.1 Motivation and Objectives

The primary motivation of this work is the observation that spanwise undulations of a relatively fixed wavelength tend to develop in the shear layer vortices of laminar separation bubbles. These have been observed in a wide variety of LSBs [33, 92, 113, 137, 151, 153, 170], including those formed over airfoils (of different geometries) and flat plates, at different Reynolds numbers, and in cases of both natural and forced flow development. To the author, this raises the following research questions:

- Is the development of spanwise undulations fundamental to the development and breakdown of shear layer vortices in laminar separation bubbles?

- Is there an underlying instability associated with these undulations?
- Can the process be manipulated by targeted, three-dimensional forcing?

Ancillary to the primary motivation is the consideration of vortex merging in LSBs, specifically in terms of any influence the phenomenon may have in defining the mean flow topology, and whether or not the process can be manipulated via subharmonic forcing.

The answers to these research questions are pursued through experimental means of investigation, with particular attention paid toward limiting the number of external factors known to influence LSB flow development. In particular, this necessitates the use of carefully manufactured models, minimally invasive measurements techniques, and wind tunnel facilities with low levels of free-stream turbulence. Under these conditions, laminar separation bubble flow development is studied and the following objectives are pursued:

- Establish if vortex merging in LSBs can be influenced through subharmonic forcing. If so, assess the effects on the mean flow topology.
- Characterize the three-dimensional evolution of shear layer vortices in a laminar separation bubble. Elucidate the role, if any, played by the development of spanwise undulations.
- Develop a forcing technique capable of producing disturbances of a desired spanwise wavelength that holds all other parameters constant (amplitude, frequency, *etc.*).
- Establish if disturbance growth in an LSB is spanwise wavelength dependent. Evaluate the presence of any instability mechanism that may lead to preferential modal growth.
- Link spanwise disturbance growth to changes in the ensuing vortex dynamics, and hence changes in the mean flow topology.

1.2 Outline of the Thesis

This thesis is organized as follows. Chapter 2 presents a review of literature pertinent to laminar separation bubbles, while the methods of investigation, including those used for data acquisition and analysis, are discussed in Chapter 3. The core findings of this work are presented in Chapters 4 through 6. In Chapter 4, flow development in an LSB is examined, with a focus on the vortex merging process and the spanwise undulations that develop as part of the 'natural' vortex breakup process. Chapter 5 treats the characterization of the forcing technique developed as part of this thesis, in addition to results from a preliminary study of its effect on LSB flow development. An effective forcing configuration is identified from these results, which is then studied in detail through the follow-up investigation presented in Chapter 6. Finally, Chapter 7 presents the major conclusions drawn from this body of work, in addition to providing some suggestions for future research.

Chapter 2

Literature Review

A review of literature regarding laminar separation bubbles is given, from the seminal works of the nineteen-fifties and sixties to recent developments. Particular attention is paid to fundamental concepts of fluid mechanics that pertain to LSBs, the transition process of the separated shear layer, and the ensuing formation of coherent structures. Flow control strategies for performance improvement and diagnostics of LSB flows are also discussed.

2.1 Fundamental Principles of Fluid Mechanics

The fundamental concepts presented in this section, namely the governing equations of fluid mechanics, vortex dynamics, the boundary layer, flow separation, and laminar–turbulent transition, are essential aspects of nearly all fluid fluids; the laminar separation bubble in particular. As such, a brief review of each is provided.

2.1.1 The Governing Equations

Fluid flows, like all physical phenomena, are subject to the fundamental conservation of laws of nature. In particular, the motion of a fluid are governed by the conservations of mass, momentum and energy, which are mathematically formalized to give the governing equations for Newtonian fluids with constant physical properties:

$$\frac{\mathrm{D}\rho}{\mathrm{D}t} + \rho\left(\nabla \cdot \vec{u}\right) = 0, \tag{2.1}$$

$$\rho\frac{\mathrm{D}\vec{u}}{\mathrm{D}t} = -\nabla p + \mu\nabla^2\vec{u} + \rho\vec{F}, \tag{2.2}$$

$$\rho\frac{\mathrm{D}h}{\mathrm{D}t} = \frac{\mathrm{D}p}{\mathrm{D}t} + \nabla \cdot \left(k\nabla T\right) + \Phi. \tag{2.3}$$

Derivations of these equations may be found in Currie [42] and White [249]. $\mathrm{D}/\mathrm{D}t$ is the material derivative and encapsulates the change in a fluid property due to temporal and convective acceleration. Equation 2.3 represents the conservation of energy, and relates changes in the fluid enthalpy ($\mathrm{D}h/\mathrm{D}t$) due to pressure ($\mathrm{D}p/\mathrm{D}t$), thermal conduction [$\nabla \cdot (k\nabla T)$], and viscous dissipation (Φ). Refer to White [249] for the definition of Φ.

If thermal effects are insignificant, then only Eqns. 2.1 and 2.2 need to be considered in describing the fluid motion. These are the conservation equations of mass and linear momentum, respectively, or the continuity and Navier-Stokes equations as they are more commonly referred. The work in this thesis concerns flows that are incompressible, *i.e.*, $\mathrm{D}\rho/\mathrm{D}t = 0$, and therefore the continuity equation reduces to:

$$\nabla \cdot \vec{u} = 0, \tag{2.4}$$

indicating that the velocity field is divergence-free. Physical interpretation of the Navier-Stokes equations (Eqn. 2.2) reveals that acceleration in the fluid ($\mathrm{D}\vec{u}/\mathrm{D}t$) is dictated by the forces that act on it, namely, pressure ($-\nabla p$), viscous stresses ($\mu\nabla^2\vec{u}$), and body forces ($\rho\vec{F}$).

Typically, the fluid properties (fluid density ρ, and dynamic viscosity, μ) are known and the body forces are negligible, leaving the system posed by Eqns. 2.2 and 2.4 with four unknowns: the three components of velocity (u, v, and w in Cartesian coordinates), and pressure p. The convective terms in Eqn. 2.2 are non-linear and therefore pose significant mathematical challenges in determining a unique solution for a given set of initial and boundary conditions. As a result, only a limited number of analytical solutions are known, all which are for relatively simple flow configurations. As such, research efforts generally turn toward numerical and/or experimental evaluations of the governing equations when flows of any real complexity are considered.

In both numerical and experimental frameworks, it is convenient to decompose the unknown parameters into time-averaged (steady) and fluctuating (unsteady) quantities:

$$u = \overline{u} + u', \quad v = \overline{v} + v', \quad w = \overline{w} + w', \quad p = \overline{p} + p'.$$

The above constitutes the Reynolds decomposition and is a useful tool to both experimentalists and numericists, as it forces one to consider the range of time scales that must be resolved in order to produce accurate estimates of both the steady and unsteady terms. Therein lies one of the major challenges every investigator faces, as flows can exhibit a staggering range of time and length scales, and so trade-offs must be considered when selecting a method for investigation.

2.1.2 Vortex Dynamics

In fluid mechanics, the rotational motion of a fluid is quantified through vorticity, $\vec{\omega}$, and circulation, Γ. The former provides a measure of the magnitude and direction of the local rate of rotation in the fluid, while the latter gives a 'macroscopic' indication of rotation. When vorticity is everywhere zero, except at permitted singularities, the flow is said to be irrotational, which can be shown to be equivalent to invoking the inviscid assumption, as either lead to the reduction of the Navier-Stokes equations into Euler's equation.

The concept of a vortex is introduced through the consideration of vortex lines, which are defined as lines that are everywhere locally tangent to the vorticity field. An arbitrary surface can be chosen, through which all the vortex lines passing through its perimeter can be found. At some other location in the fluid, a second surface can always be found that reconnects all the vortex lines, thus forming a vortex tube. The process is analogous to the construction of a stream tube, within which the mass flow is constant on account of its being constructed of streamlines. By analogy, one might rightly conclude that circulation is then constant at all cross-sections of a vortex tube, which can be proven rigorously by integrating the divergence of the vorticity field over the volume of a vortex tube (*e.g.*, see Currie [42]). A vortex tube whose area is infinitesimally small is referred to as a vortex filament, and its vorticity is said to be concentrated at a point. In the strictest sense these vortex tube and filament definitions are precise, while the term 'vortex' is used more freely across the research community, usually in reference to an area of coherent rotational motional in a fluid, which almost always implies the presence of a vortex tube.

Constant circulation at all cross-sections of a vortex tube was first postulated by Helmholtz [70] as part of his four theorems on vortex motions, which he developed for an assumed inviscid, barotropic fluid subject to only conservative body forces. These assumptions are rather restrictive given, for example, inviscid flow is rarely encountered in practice, however the theorems allow for conclusions regarding vortex motions to be drawn when these conditions do and do not apply, both of which are equally impactful. Given the above restrictions, the vortex theorems of Helmholtz are:

1. The strength of a vortex is constant along its length.
2. A vortex tube cannot start or end within the fluid.
3. Vortex lines move with the fluid.
4. The strength of a vortex remains constant with time.

The first of Helmholtz's theorems was shown to be true through consideration of a vortex tube. The second must hold true, as a vortex that begins or ends within the fluid would imply the presence of a vorticity source or sink, respectively, which would violate Eqn. 2.4. While Helmholtz provided justification for theorems 3 and 4 in his paper [70], a more satisfactory proof was provided by Kelvin and his circulation theorem [103]. This theorem, developed under the same assumptions as Helmholtz, postulates that the circulation around a closed curve moving with the fluid remains constant with time [103]. Stated mathematically:

$$\frac{\mathrm{D}\Gamma}{\mathrm{D}t} = 0. \tag{2.5}$$

For proof of the theorem, the reader is referred to Kelvin's original paper [103], or alternatively Karamcheti [99]. Kelvin's theorem holds several important implications regarding vortex motions. First, it unequivocally proves Helmholtz's fourth theorem. Second, it verifies Helmholtz's third theorem, as one only need consider a closed contour on the side wall of a vortex tube. Since there is no component of vorticity normal to the side walls, the circulation of the contour is zero. Hence, under the conditions of Kelvin's theorem, the circulation of this contour must always be zero and therefore the contour must continue to lie on the vortex tube as the fluid moves. Third, the circulation of a vortex tube, and hence the vorticity contained within, can only be changed by the actions of viscosity, application of non-conservative body forces or density variations that are not only related to changes in pressure, since, in the absence of all of these effects, circulation remains constant (Eqn. 2.5). Fourth and finally, Kelvin's theorem provides further confirmation that an inviscid and incompressible flow remains everywhere irrotational if initially irrotational. For example, consider a flow over a body (*e.g.*, an airfoil). Far away from the body the vorticity is zero. As fluid elements move toward the body, some will flow adjacent to it, where they must remain irrotational by Kelvin's theorem. Thus, the no-slip condition is violated, implying the flow is inviscid. Therefore, Euler's equation may be bypassed, and the irrotational condition and continuity equation can be used to form a set of governing equations for inviscid flows, leading to the study of potential flow.

The Biot-Savart Law

The Biot-Savart law finds its origins in the field of electromagnetism, as it describes the magnetic field induced by a current flowing through a wire (*e.g.*, see Grant & Phillips [65]). An analogy to fluid mechanics can be drawn, allowing for prediction of the velocity induced at a point by a vortex filament, when, like the magnetic field, the velocity field can be represented by a potential function. Thus, the Biot Savart law applies when the velocity field is irrotational and divergence-free. For a derivation, the reader is referred to Karamcheti [99]. Here, the following expression is accepted:

$$\vec{u} = \frac{\Gamma}{4\pi} \int \frac{\mathrm{d}\breve{\ell} \times \vec{r}}{|\vec{r}|^3}, \tag{2.6}$$

which describes the velocity $\vec{u}$ induced at point $\vec{r}$, found by integrating over the length of a vortex filament of circulation Γ and arbitrary shape (defined by the differential length elements $\mathrm{d}\breve{l}$). Note

that the flow is assumed irrotational and therefore is inviscid, and thus Eqn. 2.6 does not apply to viscous flows. This is clear as the predicted velocity distribution can never exist in any real flow, as a singularity exists for $\vec{r} = 0$. Instead, in this region (*i.e.*, in the 'core' of the vortex), viscous forces will lead to solid body rotation.

Generation and Decay of Vorticity

In the analysis of vortex dominated flow, it is often useful to recast the Navier-Stokes equations (Eqn. 2.2) into a form in terms of vorticity, giving what is commonly referred to as the vorticity transport equation:

$$\frac{\mathrm{D}\vec{\omega}}{\mathrm{D}t} = (\vec{\omega} \cdot \nabla)\,\vec{u} + \nu\nabla^2\vec{\omega}, \tag{2.7}$$

the derivation of which is available in many textbooks, including those of Currie [42] and White [249]. The above expression applies to incompressible fluid flows of constant properties subject to conservative body forces, for which it governs the conservation of vorticity. Equation 2.7 indicates that rates of change in the vorticity field ($\mathrm{D}\vec{\omega}/\mathrm{D}t$) can result from only two mechanisms; the stretching and tilting of vortex filaments [$(\vec{\omega} \cdot \nabla)\vec{u}$], and viscous diffusion ($\nu\nabla^2\vec{\omega}$). The latter, through analogy to the viscous term in the Navier-Stokes equations, reveals that the role of viscosity is to spatially redistribute vorticity through a diffusive process, which has important implications for the previously discussed vortex motion theorems of Helmholtz and Kelvin. Specifically, viscous effects have no impact on the first three of Helmholtz's theorems, while they do invalidate the fourth, and therefore Kelvin's circulation theorem as well (Eqn. 2.5). In the derivation of the circulation theorem, it is necessary to assume that the velocity field is conservative, which does not hold true for a viscous flow, as the inclusion of viscous effects allows for vorticity generation.

Indeed, viscous effects are essential to the process of vorticity generation. The vorticity equation (Eqn. 2.7) does not contain any source or sink terms, and therefore vorticity can only be generated from the initial and/or boundary equations applied to Eqn. 2.7. As laid out by Morton [165], vorticity can only be generated at a fluid/solid interface, by the action of either tangential acceleration of the boundary or tangential pressure gradients acting along the boundary. The generation process occurs either instantly ('fast' vorticity generation, as in the Blasius boundary layer), or continually ('slow' vorticity generation, as in Poiseuille flow). In either case, once vorticity is generated, it is never lost by diffusion into or through another boundary. Rather, the only path by which vorticity may decay is by its viscous diffusion away from the boundary, where it will be cross-annihilated with vorticity of the opposing sense. Given enough time after a vorticity perturbation is introduced into the fluid domain, the fluid must decay to a zero vorticity state. Since the decay of vorticity can only occur by cross-annihilation, then any such perturbation must generate equal amounts of positive and negative circulation. The most famous example of this phenomenon is the 'starting vortex' that is shed from an airfoil as it begins to move, discovered by Prandtl & Tietjens [187].

2.1.3 The Boundary Layer and Flow Separation

As fluid flows next to a solid surface, frictional forces retard the fluid motion in a thin layer near the wall. In that layer the velocity of the fluid increases from zero at the wall (the no-slip condition) to its full value at some distance away, where the effect of friction is absent. This is the concept of a boundary layer, and was discovered by Prandtl [186]. As the flow develops along the surface, the height of the zone affected by friction, *i.e.*, the boundary layer thickness (δ), increases, with many factors influencing the rate at which this occurs [214]. One factor is the pressure gradient acting in the direction of motion (x, as defined in Fig. 2.1). Favourable ($\partial p/\partial x < 0$) and adverse ($\partial p/\partial x > 0$) pressure gradients decrease and increase the rate at which δ grows relative to a zero-pressure-gradient boundary layer ($\partial p/\partial x = 0$), respectively.

When left to develop in an adverse pressure gradient, the momentum of the fluid elements in the boundary layer will eventually be entirely consumed by the wall frictional forces and the pressure gradient. At some point (or line), the boundary layer will depart from the wall and the flow is said to separate, as depicted in Fig. 2.1. Prandtl [186], in the same paper in which he introduced the boundary layer concept, described these mechanics of separation, while also providing a precise criterion for its onset in a steady, two-dimensional boundary layer developing over a fixed wall. He noted that near-wall fluid particles, originally travelling with the bulk fluid motion, must be brought to rest at the separation point, while those downstream of separation move in a direction opposite to the external flow. Thus, the gradient of the streamwise velocity in the wall-normal direction evaluated at the wall ($\partial u/\partial y|_{y=0}$) is positive upstream of separation, negative downstream of separation, and exactly zero at the point of separation. Thus, separation can be located where the wall shear stress ($\tau_w = \mu \partial u/\partial y|_{y=0}$) is zero. Furthermore, at separation, the wall-normal velocity gradient is zero at both the wall and far away from it, while the velocities in these two regions are most certainly not equal, and therefore the velocity profile must contain an inflection point. This has important implications for the stability of the flow, as is discussed in Section 2.1.4. A region of re-circulating fluid is created when a flow separates, as the original boundary layer fluid passes over the reverse flow region. From the separation point, a dividing streamline, depicted in Fig. 2.1, can be identified that connects the points under which the streamwise mass flux is zero [58, 76].

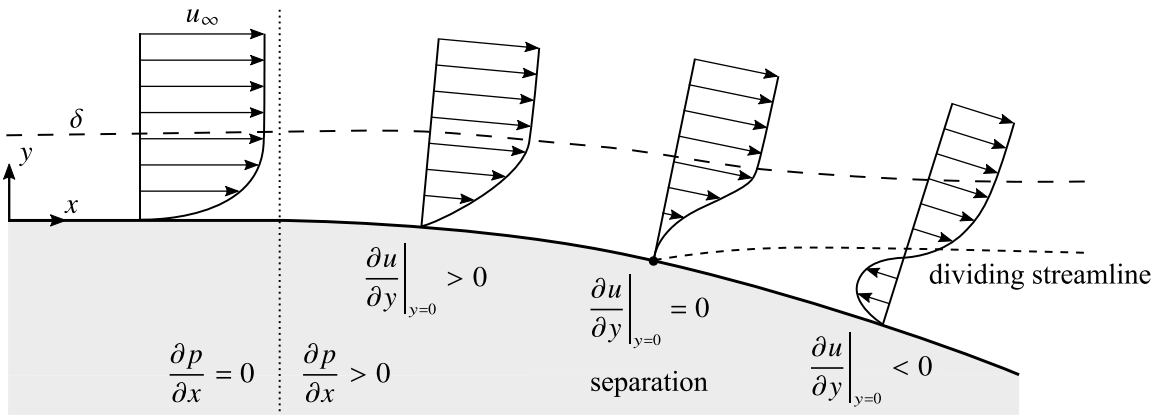

Figure 2.1: Schematic of boundary layer separation.

Flow separation is undesirable in a wide range of applications, bringing with it penalties so severe to performance that mitigating separation is typically one of, if not the, primary consideration driving the design of the device. For example, in flows over bluff bodies, delaying separation leads to a reduction in both the mean and unsteady loads [254], allowing for more efficient and/or safer designs for civil structures, and improved fuel efficiency for ground transportation vehicles. In aviation, separation on the aircraft body increases drag, while causing a large loss in lift and increase in drag if it occurs over the wings [34], *i.e.*, stall, which presents significant performance and safety concerns. Similarly, separation affects the performance and efficiency of turbo-machinery [74] and wind turbines [226]. It is for these reasons that flow separation is an important topic in fluid mechanics research, as many strategies aimed at mitigating its undesirable effects have been and continue to be developed, as discussed in Section 2.3.

2.1.4 Laminar–Turbulent Transition

Among the multitude of their defining characteristics, laminar and turbulent flows can be separated based on the behaviour of fluid motion in adjacent layers, with these layers following 'smooth' paths in laminar flow, while turbulent flows exhibit chaotic mixing across the layers. Then, transition is the process by which a laminar flow becomes turbulent, or, as the flow changes from an orderly state to one that is more chaotic. Much of the modern understanding of laminar–turbulent transition is built upon the study of boundary layers, and as such it is reviewed here in that context. The reader is referred to Schlichting & Gersten [214] for a full treatment on this topic.

A boundary layer's transition process may take one of many paths to turbulence [163], the full extent of which is discussed by Saric *et al.* [206]. The process begins with the laminar boundary layer's receptivity to free-stream disturbances [164], such as sound or vorticity, which establish the initial conditions of disturbance amplitude, phase and frequency for the breakdown process. Disturbances within the boundary layer undergo growth, governed by an instability whose nature is dependent on Reynolds number, wall curvature, surface roughness, and initial conditions, among others [206]. If the initial disturbance amplitude is sufficiently small, the process illustrated in Fig. 2.2 is followed, which involves the growth of unstable waves due to the flow's convective instability [59, 82], followed by three dimensional breakdown. However, it is worth noting that a vast number of flows do not follow this route to turbulence, as the slow convective growth of disturbances can be bypassed [164], leading to the flow quickly becoming turbulent. Such cases have been documented to occur in the presence of surface roughness or high free-stream turbulence [6, 193].

Figure 2.2 shows the idealized progression of boundary layer transition over a flat plate, which is described in Refs. [96, 208, 214, 249]. The unstable disturbances in the laminar boundary layer are of relatively small amplitude and undergo weak growth that occurs over a relatively long streamwise length scale, although the streamwise pressure gradient, among other factors, holds considerable influence over these growth rates. This initial stage can be successfully described by Linear Stability Theory (LST) (Section 3.3.1). As amplitudes grow, three-dimensional and non-linear interactions begin to occur. This leads to the formation of characteristic Λ-structures. Disturbance growth is very rapid in this stage, i.e. over a convective length scale, and the breakdown to turbulence begins to occur as the Λ-vortices decay and are replaced by turbulent spots. These

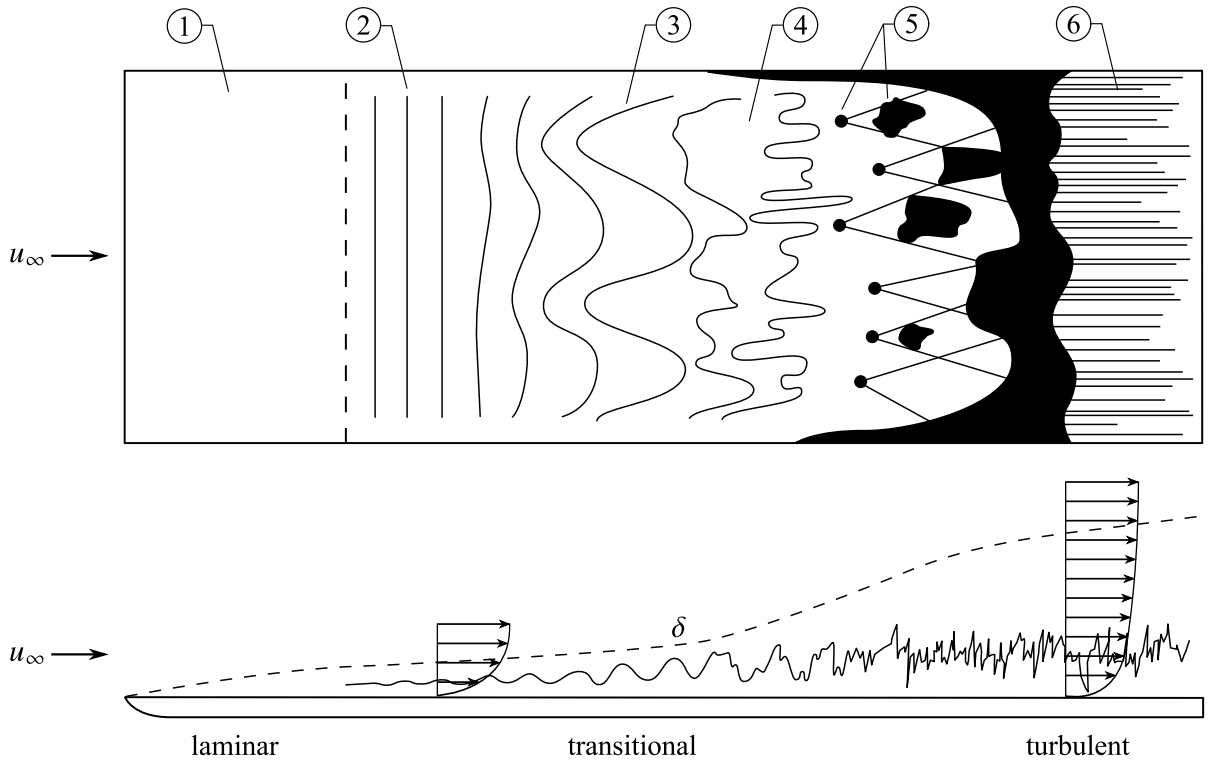

Figure 2.2: Idealized description of flat plate boundary layer transition, after White [249], Schlichting & Gersten [214], and Kachanov [96]. ① Stable laminar flow; ② unstable TS waves; ③ three-dimensional waves and vortex formation (Λ-structures); ④ vortex decay; ⑤ formation of turbulent spots; ⑥ fully turbulent flow.

turbulent spots increase in number, continue to spread, and lead to the completion of the transition process.

The methods developed by Orr [175] and Sommerfeld [225] serve as the foundation upon which the understanding of boundary layer transition is built. The flow is decomposed into a mean/base flow and unsteady fluctuations, with the amplitude of the latter assumed infinitesimal. Applying such assumptions to the governing equations (Eqns. 2.2 and 2.4) produces a set of linearized equations, which if accompanied by the parallel flow assumption, give the famous Orr-Sommerfeld equation (OSE) (Eqn. 3.6). Application of the OSE is commonly referred to as LST, which is treated in Section 3.3.1. Understanding the process by which a laminar flow begins to amplify unstable disturbances, as depicted in Fig. 2.2, began with the landmark work of Tollmien [236], who solved the OSE for flat plate boundary layer flow. Tollmien found boundary layer profiles with an inflection point to be inherently unstable and through this, computed the neutral stability curve, thus identifying the unstable wave frequencies and Reynolds numbers at which they are present. Schlichting [213] extended these results to include growth rates within the curve of neutral stability. The two-dimensional waves modelled in their analyses are now called Tollmien-Schlichting (TS) waves.

Experimental verification of TS waves was achieved by the investigation of Schubauer &

Skramstad [216]. In their investigation, the disturbances were made detectable by reducing the free-stream turbulence level and artificially disturbing the boundary layer by means of a thin vibrating ribbon. The presence of TS waves in natural transition has since been experimentally confirmed, *e.g.*, Arnal *et al.* [9]. The results of Schubauer & Skramstad [216], and others [204, 229], have reported good agreement with LST within the frequency range generally associated with the transition process, *i.e.*, low frequencies, however, disagreement emerges at higher frequencies where disturbance amplification is weak. The discrepancy has been attributed to the high sensitivity of such measurements to experimental conditions [17, 207] and the effect of disturbances produced by an oscillating band [10, 17].

Klebanoff *et al.* [107] were first to clearly show the deformation of amplified TS waves into three-dimensional structures, which when visualized form a streamwise aligned pattern of Λ-structures (*e.g.*, see Fig. 3 in Ref. [71]). Further experiments [97, 209] showed another type of three-dimensional deformation of TS waves, in which the Λ-structures align in a staggered pattern (*e.g.*, see Figs. 2 and 3 in Ref. [209]). Saric & Thomas [209] showed this modification of the transition process occurred by varying the amplitude and frequency of the initial TS wave. Theoretical explanation for the observed phenomena began with the works of Orszag *et al.* [176, 177], who unveiled the linear mechanism responsible for the growth of the three-dimensional mode. Herbert [71] used this observation as the basis to develop secondary instability analysis, where the solutions from LST are used as a new local base flow and three-dimensional perturbations are superimposed. The resulting analysis successfully reproduced the experimental results [97, 107, 209], showing that, for relatively large initial amplitudes of the primary TS wave, harmonic and subharmonic perturbations move in phase. The model of Craik [41], further developed by Zelman & Maslennikova [267], considered the interactions between these perturbations, showing that the harmonic mode forms a resonant triad with two of the subharmonic modes of equal but opposite angles, thus creating the streamwise peak-to-peak alignment of Λ-structures. The aligned and staggered Λ patterns are now referred to as K and H-type transition, after Klebanoff *et al.* [107] and Herbert [71], respectively.

The onset of secondary instabilities coincides with rapid disturbance growth and interaction, leading to significant non-linear effects, making the underlying assumptions of the OSE invalid. As such, the scientific community has shifted focus to numerical solutions of the Navier-Stokes equations to elucidate the 'later' stages of boundary layer transition. Early investigations [121, 228, 256] were successful in simulating incipient non-linear effects, showing that the onset of disturbance three-dimensionality and spikes in streamwise velocity fluctuations coincide with significant growth in local shearing, thus inducing the decay of the Λ-structures and the transition to turbulence. However, due to the computational capabilities of the time, these investigations were limited to a temporal formulation, where a spatially periodic domain travels with the disturbance and the temporal evolution is evaluated. These implementations lack physical integrity and so subsequent studies have focused on full spatial implementations [94, 192, 195]. In particular, Rist & Fasel [195] compared their DNS results of K-type transition to experiments [97, 107], finding good quantitative agreement up until the onset of non-linearities, and qualitative agreement on the dynamical behaviour of the Λ-structures. However, due to the slow spatial evolution of the primary TS wave, these DNS investigations employed large streamwise domains, and so suffered from either convergence issues [192] or truncated spanwise domains [94, 195]. These issues still

persist today and motivate the ongoing efforts of the research community [159].

2.2 Laminar Separation Bubble

For all fluid flows, the Reynolds number, Re, quantifies the relative importance of inertial and viscous effects. In aviation, when considering the aerodynamic properties of a wing, the employed length scale is the chord length of the wing cross-section (*i.e.*, airfoil), giving the chord-based Reynolds number, Re_c. The range of Re_c in applications is impressively large, spanning from 10^2 to 10^9. At the lower end of this spectrum, $Re_c < 10^4$, appreciable airfoil performance is difficult due to dominating viscous forces, while the well-established general aviation finds its home at $Re_c > 10^6$ [34, 127]. In between these two is the low Reynolds number range ($10^4 < Re_c < 5 \times 10^5$), where both viscous and inertial effects play important roles. Common engineering applications in this regime include hydrofoils, low-pressure turbomachinery [74], small-to-medium scale wind turbines [62], micro and unmanned aerial vehicles [166], glider planes, and aircraft operating at low speed or high altitude [34, 127].

The main impediment to aerodynamic performance in the low Reynolds number regime is separation (Section 2.1.3), since the boundary layer on an airfoil's suction surface often remains laminar into the adverse pressure gradient region, and hence is likely to separate. In the event of separation, the resulting detached shear layer is unstable and undergoes transition to turbulence, which enhances momentum exchange. Depending on flow conditions, the shear layer may remain separated or reattach to the airfoil surface in a mean sense, with the former leaving the airfoil in a stalled state and the latter forming a closed region of recirculating fluid, referred to as a laminar separation bubble (LSB) [58, 76, 232]. These two flow conditions are illustrated in Fig. 2.3. While aerodynamic performance decreases dramatically for the stalled case (Fig. 2.3a), reattachment (Fig. 2.3b) improves performance, but not to levels experienced in the absence of laminar separation [166]. Furthermore, the transition process associated with LSBs is highly susceptible to environmental disturbances, with only slight changes in the background disturbance environment or operating conditions leading to undesirable effects, such as stall, loss of lift, increase in drag, and/or noise emissions [8, 34]. As such, considerable research effort has been put toward the study of LSBs over the last half century, the breadth of which is discussed in the following sections. Although nearly all relevant applications relate to airfoil operation, LSBs

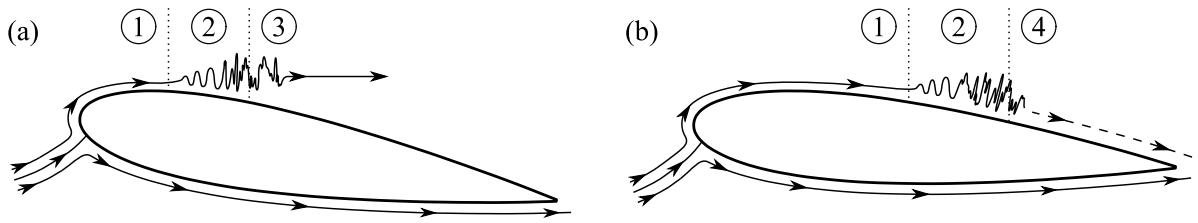

Figure 2.3: Low Reynolds number flow over an airfoil showing separation leading to (a) stall and (b) laminar separation bubble formation, after Yarusevych *et al.* [262]. ① Separation; ② transition; ③ separated turbulent flow; ④ turbulent reattachment.

formed over semi-infinite flat plates subject to an adverse pressure gradient exhibit the same fundamental aspects and have been used as a suitable platform for both experiments [58, 243] and simulations [2, 137].

2.2.1 Early Studies and Mean Characteristics

Early experimental characterization of LSBs focused on identifying the location and extent of the bubble on the airfoil surface. Owen & Klanfer [178] were first to classify bubbles as short or long, while Tani [232] extended this to distinguish short bubbles as those who have a minor effect on the static pressure distribution, while long bubbles have a greater effect by diminishing the suction peak. The now generally accepted time-averaged representation of the separation bubble was first proposed by Horton [76] and is shown in Fig. 2.4, which describes a region of recirculating fluid bounded by the airfoil surface and the dividing streamline. The latter is identified as the closed contour formed with the surface, within which the streamwise mass flux is zero [58, 76, 172]. The upstream and downstream extents of the dividing streamline are the mean separation and reattachment points, respectively. For convenience, a mean transition point is often identified, however it should be noted that transition occurs over a region rather than at a given location. It is important to note that these time-average characteristics of a separation bubble, while useful, do not provide a complete description as the separated shear layer is, by nature, unsteady. The unsteady features of a separation bubble are illustrated in Fig. 2.4 and are discussed from the context of the separated shear layer transition process in Section 2.2.2.

Mean surface pressure measurements have proven to be reliable in estimating the mean separation, transition, and reattachment points [34, 172, 232]. Tani [232] noted the presence of a mean pressure plateau between the separation and transition points, and as such the start and end of this region have been used to estimate these points [22, 172]. The pressure plateau is followed by a region of rapid pressure recovery, with the mean reattachment location estimated from where the rate of this pressure recovery decreases [172]. Velocity-based boundary layer parameters have also been used to characterize LSBs [20, 24, 172]. Boundary layer displacement thickness, δ_1, increases downstream of separation to a maximum approximately at the transition point and then decreases to a local minimum near the reattachment point [20, 24], while momentum thickness, δ_2, is relatively constant in the separated region, but then begins to increase near the transition

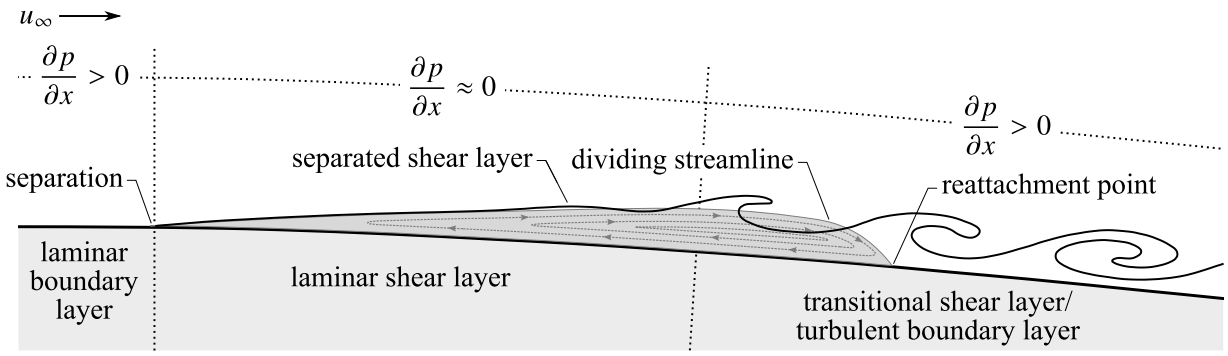

Figure 2.4: Schematic of a laminar separation bubble.

point [24, 172]. This has lead some investigators to use the displacement thickness or shape factor, H, to estimate the transition point [24, 143]. Other methods employed to estimate the transition location include turbulence intermittency parameters [26, 144], Reynolds shear stress parameters [32, 33, 69, 118, 173], and convective heat transfer rates [119, 156, 161, 257].

Given its importance related to airfoil performance and stall, much experimental effort has gone into detailing separation bubble characteristics on airfoils for a wide range of flow conditions and geometries [22, 34, 85, 114, 133, 183, 232], which have been successful in establishing general trends across Reynolds numbers and angles of attack [166]. At low angles of attack and sufficiently high Reynolds numbers, laminar separation is followed by reattachment, thus forming an LSB. With the Reynolds number held constant, increasing the angle of attack causes the bubble to move upstream and decrease in length, until some critical angle at which reattachment is not possible and the airfoil stalls. Changes to the Reynolds number at a fixed angle of attack has a less significant effect on the LSB location, however, decreasing the Reynolds number causes the bubble to increase in length until a critical value on the order of 50 000 is reached [34, 166], at which point the shear layer fails to reattach. At these conditions, and others, minor variations in flow parameters (*e.g.*, minor changes in Re_c or angle of attack), can cause a separation bubble to suddenly elongate, forming either a longer bubble or a detached shear layer. This phenomenon is called bursting and was first investigated in detail by Gaster [58]. Later studies would reveal the physical mechanism responsible for bursting, relating it to the underlying stability of the flow, which is discussed in Section 2.2.2.

In addition to the Reynolds number and angle of attack, low Reynolds flows over airfoils are extremely sensitive to factors that are difficult to control or vary systematically, making their study difficult. These factors include model imperfections [133, 168], free-stream turbulence [85, 86, 133, 167, 173, 174], acoustic disturbances [44, 93, 189], and intrusive experimental techniques [21, 24, 106]. Mueller *et al.* [167] found it difficult to relate the effect of free-stream turbulence intensity to airfoil performance, as they found the accurate measurement of relatively small aerodynamic forces to be further exacerbated by changes to the turbulence intensity. The examination of the effects of the experimental setup in separation bubble studies has shown that intrusive probes, *e.g.*, hot-wires, can alter the flow topology when placed near the separation point [24, 106]. Furthermore, Boutilier & Yarusevych [21] showed that end plates and corrections for blockage effects should be employed in two-dimensional airfoil studies in order to avoid errors in estimating separation bubble characteristics and lift forces, respectively. The extreme sensitivity of flows involving separation bubbles is exemplified by the investigation of Ol *et al.* [173], who, in compiling data from three different experimental facilities, found significant discrepancies in the measured location and mean topology of the LSB for nominally identical experiments. Similarly, Olson *et al.* [174] found it difficult to find agreement among experimental and computational results for, again, largely similar flow conditions. The challenges in conducting low Reynolds experiments therefore necessitates the careful documentation of free-stream conditions, as well as the use of carefully manufactured models and minimally-invasive measurement techniques.

2.2.2 Separated Shear Layer Transition

A schematic showing shear layer development in an LSB is presented in Fig. 2.4, which summarizes the essential features captured in a number of flow visualization experiments [106, 115, 118, 219]. The initial conditions for the transition process are set by the small amplitude disturbances present within the upstream boundary layer (Section 2.1.4). The disturbances convect into the fore portion of the bubble, where the initially laminar shear layer begins to exhibit unsteadiness on account of disturbance growth that occurs within a band of unstable frequencies [47, 197, 243]. This initial stage of transition in LSBs has been examined extensively, both experimentally [20, 46, 122, 132, 243] and through DNS [2, 92, 139, 141, 196], with investigators concluding that disturbance growth is primarily two-dimensional (*i.e.*, of the normal mode) and due to a Kelvin-Helmholtz type instability. This view of the initial stage in the transition process has become well accepted among the research community as a result of excellent agreement between experimental and numerical results with stability predictions [135, 136, 140, 261], with similarities to free shear layers noted [243].

The success of stability predictions in the fore portion of the bubble are attributed to low disturbance amplitudes, and the flow being two-dimensional and nearly wall parallel in this region, making the process amenable to LST analysis. Early studies applied LST to analytical profiles that resembled those measured in LSBs [45, 47, 66, 238], finding that the spectrum of growth rates is roughly bounded between those of the Blasius boundary layer and a free shear layer [19, 238]. With increasing shaper factor, the shear layer thickens and departs further from the wall, with the Rayleigh equation [215] providing accurate stability predictions in place of the OSE [20], indicating that the effects of viscosity on stability diminish as an LSB thickens.

LST based predictions of three-dimensional disturbance growth based on analytical LSB velocity profiles have shown that growth rates in the band of frequencies relevant to transition are always highest for the normal mode (*i.e.*, for a zero spanwise wavenumber, $\beta = 0$) [47]. These findings have been supported by both experimental [153, 198] and DNS [139, 141] studies, and are aligned with the Kelvin-Helmholtz instability's preferred amplification of two-dimensional modes in free shear layers [149]. As noted by Dovgal *et al.* [47], the growth of spanwise modes is less, yet comparable, to the normal modes in LSBs, while the amplification rates of three-dimensional modes in attached boundary layers can be up to ten times that of the two-dimensional TS wave, leading to the rapid three-dimensionalization noted in K and H-type transition (Section 2.1.4). Thus, when considering an LSB in isolation, as is the case when analytical approximations and simulations with prescribed in-flow conditions are utilized, three-dimensional disturbances appear to be of little significance [141]. However, when the continuous stability spectrum is considered, beginning from the upstream boundary layer and into LSB, the impact of three-dimensional disturbance development can be significant, as noted by Michelis *et al.* [153] and Rist & Augustin [198]. The specific effects, on both LSB topology and flow development are the subject of ongoing investigations, including the one presented in Chapter 6.

Other instability mechanisms have been found to be active in separation bubbles, including a Görtler type instability [138] associated with the formation of longitudinal vortices at the beginning of the adverse pressure gradient region due to streamline curvature created by separation. Additionally, Marxen *et al.* [137] suggests that two separate secondary instability may be present

in LSBs, taking effect in the aft portion where vortex shedding occurs. One is reported to be an elliptical instability [104], amplifying disturbances with spanwise wavelengths on the order of the diameter of the shed vortices, leading to spanwise distortions and waviness in the vortex filament. The second was found active in the braid region between consecutive vortices and occurred for much higher spanwise wavenumbers. Both instabilities were found to be in action simultaneously and of the fundamental and subharmonic frequency of the Kelvin-Helmholtz mode [92, 142], however, their presence has yet to be experimentally confirmed.

Jones *et al.* [92] and Spalart & Strelets [227] provided evidence that the LSB transition process can be self-sustaining. Modelled numerically, the transition process was found to continue even after the initializing disturbances present in the background were removed. This cannot be explained by convective instability mechanisms, which require constant disturbance input to sustain the transition process. Thus, this evidence points toward an absolute instability mechanism [82], where disturbances propagate in both the upstream and downstream direction, and are amplified in time. Several numerical and theoretical studies have examined absolute instabilities in LSBs [2, 52, 201], finding that the critical parameter for their onset is the strength of the reverse flow. Alam & Sandham [2] reported reverse flow magnitudes between between 15% and 20% of the local free-stream velocity are required, while a lower threshold of approximately 7% was identified by Rodríguez *et al.* [201] through global stability analysis [233]. This has been termed a centrifugal instability and was shown to incite spanwise waviness in the LSB through interaction with the primary K-H instability [200]. It must be noted that these absolute and global instability mechanisms stem from numerical investigations conducted in disturbance-free environments, and so their presence and/or relevance in practice remains to be determined.

Activities at frequencies typically an order of magnitude lower than that of the primary Kelvin-Helmholtz instability have been noted in flows involving LSBs. These included periodic switching between stalled and unstalled states on airfoils [264, 266], stall in localized 'cell' regions across the airfoil span [27], and significant oscillations in the overall length of the LSB [194, 205]. These have been associated with the phenomenon of bubble bursting proposed by Gaster [58], with several criteria for bursting conditions proposed [46, 58, 220]. Marxen & Rist [140] proposed the 'mean flow deformation' as the underlying casual mechanism for bubble bursting. They describe bursting as a dynamic process, in which incoming disturbances are amplified, leading to changes in the mean flow field (*i.e.*, the mean flow deformation). This in turn changes the stability characteristics of the flow, thus modifying the amplification of subsequent disturbances. This is supported by the findings of Michelis *et al.* [152], who in applying impulsive forcing to an LSB, caused an intense distortion of the mean flow field, leading to flow stabilization and bubble bursting. Thus, bubble bursting and low frequency modulations in LSBs can be viewed to occur over a spectrum that depends on incoming disturbance characteristics. If an intense change in disturbance amplitude occurs, there is an intense distortion of the mean flow and the LSB bursts. If the flow is forced in a periodic manner, then the stability characteristics become 'pegged' and no modulations are observed. Natural disturbances fall in between these two extremes, providing mild and intermittent changes in disturbances characteristics and so bursting events and/or other low frequency activities are sporadic.

2.2.3 Coherent Structures

A common feature of transitional shear flows, *e.g.*, boundary layers [71], separated shear layers formed on bluff bodies [254], and free shear layers [73], is the formation of coherent structures that precede the production of small-scale turbulence. The most prominent coherent structures formed during shear flow transition are elongated and two-dimensional spanwise-oriented vortices. Ho & Huerre [73] attribute the formation of such structures in free shear flows to the continued growth of the Kelvin-Helmholtz instability wave, leading to its saturation and the rise of harmonics and subharmonics. Consecutive and spanwise-uniform vortices connected by thin filaments form, with the process roughly completed at the location where growth in the main instability wave saturates.

A similar process has been observed in LSBs, regardless of whether the bubble is formed over a flat plate subject to an adverse pressure gradient or over an airfoil [33, 92, 137, 243, 262]. Continued disturbance growth in the LSB eventually leads to non-linear wave interactions, followed by shear layer roll-up and quasi-periodic vortex shedding in the aft portion (Fig. 2.4). These structures dominate the flow development [124, 125] and have been argued to be responsible for inducing mean reattachment [134, 260]. At formation, the vortices have been described as spanwise uniform [106, 113, 115, 170] or highly deformed and arranged in a staggered pattern [33, 69, 255]. Regardless of their characteristics at formation, the structures undergo further three-dimensional deformations, followed by the breakdown to turbulence.

Vortex merging is an intrinsic process to shear flows, where the pairing of consecutive, co-rotating vortices has been shown to play major roles in the decay of turbulence [38, 90, 145, 242] and in the growth of and momentum transfer across mixing layers [73, 83]. The fundamental aspects of vortex merging have been investigated by Cerretelli & Williamson [35] and Meunier *et al.* [148], with the initial stage of merging involving two vortices undergoing diffusive growth while orbiting one another. When the size of the vortex cores exceeds a critical proportion of the vortex spacing, the vortex centroids begin to approach each other. The cores eventually merge, forming a single merged vorticity structure that continues to expand through diffusion. In regard to free shear layers, the process of vortex merging has been captured in numerous investigations, summarized in the review of Ho & Huerre [73]. Through consecutive merging of vortex pairs, the vorticity contained within each structure is constantly redistributed into increasingly larger vortices, resulting in an approximate doubling of their wavelength and circulation after each merge, while their characteristic frequency is halved [105]. In contrast to free shear layers, while similar vortex merging has been observed in LSBs [106, 113, 115], the number of studies is limited and observations have been largely cursory and/or qualitative. A noted exception is the investigation of Lambert & Yarusevych [116], who studied the associated vortex dynamics through simultaneous time-resolved flow visualizations and surface pressure measurements. For an LSB formed over a NACA 0018 airfoil at $Re_c = 100\,000$ and angle of attack of 8°, they found up to 15% of vortices in the suction side LSB merge, with merging events occurring primarily upstream of the mean reattachment location and in an aperiodic fashion.

As previously mentioned, varied topologies of the shear layer vortices have been observed in LSBs at formation. In DNS studies, the prevailing observation is the formation of initially spanwise-uniform vortices, however, disparate vortex breakup mechanisms have been put forward. Brinkerhoff & Yaras [26] attributed the breakup of the spanwise rollers to an interaction with

streamwise oriented, smaller scale vortices that originate in the boundary layer upstream of separation, similar to the Görtler type instability observed by Marxen *et al.* [138]. This interaction lead to spanwise non-uniformity, followed by the three-dimensional breakdown and the emergence of hairpin-shaped structures in the reattached boundary layer. Balzer & Fasel [13] also noted streamwise structures in the upstream boundary layer, which they referred to as Klebanoff modes, finding that the transition process was governed by their interaction with the primary K-H instability. In other work, Jones *et al.* [92] and Marxen *et al.* [137] ascribe vortex breakup to the development of spanwise undulatory vortex filaments, followed by a rapid three-dimensionalization of the flow in the braid region, actions which were associated with the elliptical and hyperbolic instabilities, respectively, discussed in Section 2.2.2.

Much of the recent experimental progress in the study of separation bubbles is attributed to particle image velocimetry (PIV). Planar PIV has been used to study the streamwise flow development in the bubble, with the the quasi-periodic vortex shedding process identified through both phase-averaged [118, 124, 219], and time-resolved measurements [33, 69, 113, 125, 151, 170]. The majority of these investigations also employed techniques to elucidate the three-dimensional evolution of the structures, through either planar measurements in a second configuration [69, 113, 151], volumetric reconstructions [32, 33], or tomographic measurements [153, 170]. In agreement with DNS findings, a subset of the experimental work has observed spanwise-uniform vortices resulting from the two-dimensional roll-up of the separated shear layer, with the structures quickly developing spanwise deformations as they breakdown to turbulence [113, 151, 170]. In other studies, the observation of spanwise uniform structures in the formation region has been sporadic [33, 69] or all together absent [255, 268]. Instead, 'C-shaped' vortices localized to spanwise regions and arranged in staggered pattern have been observed [33]. No doubt, the confluence of factors that affect LSB flow development, including external factors present in experiments that cannot be controlled (Section 2.2.1), and the numerous instabilities that may be active (Section 2.2.2) have lead to these disparate descriptions.

One such factor that has received considerable attention in recent years is the influence of free-stream turbulence on LSB flow development and topology. For relatively low turbulence intensity values ($\lesssim 0.5\%$ of u_∞), vortex shedding has been observed to be largely two-dimensional and highly periodic, producing filaments with a high degree of spanwise coherence [123, 144, 170]. As the turbulence intensity is increased up to values of approximately 1.5%, the shedding process exhibits significant cycle-to-cycle variations and the vortices become increasing distorted across the span at formation [33, 144, 173]. At levels above 2%, experimental findings confirm that bypass transition can occur, characterized by the formation of streamwise streaks in the boundary layer upstream of separation [86, 123, 222], which have been noted in the previously discussed numerical studies [13, 26, 138]. Hosseinverdi & Fasel [77] summarize that these streamwise structures result from the free-stream turbulence, with the transition process driven by their interaction with the K-H mode. As the free-stream turbulence level is increased the process is increasingly dictated by the streamwise streaks, with an approximate threshold of 1% identified at which the spanwise coherence of the shear layer vortices is reduced to insignificant levels.

2.3 Active Control of LSB Flows

Section 2.2 outlines the significant influence of the disturbance environment on LSBs, thus making flow control an attractive and effective option for conditioning the LSB to some desirable state. Typical flow control goals for flows involving LSBs include separation control/mitigation, lift increase, drag reduction, and noise suppression. An introduction to the concepts of flow control are provided by Gad-el-Hak [57], with general classification based on whether or not the flow control device requires auxiliary power or not, referred to as active and passive methods, respectively. Active control methods are employed in this thesis and as such are the focus of this review. These methods primarily operate on the principle of introducing periodic disturbances that exploit an underlying instability within the LSB. This type of forcing has been employed in numerous experimental and numerical studies, with disturbances produced by various means, including acoustic excitation [67], synthetic jet actuators [64], mechanical oscillations [118] and surface-mounted plasma actuators [40].

Early studies established that improvements to airfoil performance could be realized through acoustic forcing, with the source located either in the external flow [39, 171, 265], or internal to the airfoil [36, 79, 80]. Regardless of the location of the acoustic source, at post stall angles of attack the large scale vortices shed in the airfoil wake are the dominant feature of the flow, and so forcing at a matching frequency can mitigate stall and recover lift [36, 79, 263]. At angles of attack below and close to stall, the optimal forcing frequencies, in terms of mitigating stall and moderate improvements to lift, were found to be an order of magnitude higher than those of the post stall case [79, 171, 265], with this frequency range later linked to the unstable disturbances present in LSBs [171, 258].

Synthetic jets effect flow changes by producing a train of vortices from alternating ejection and suction of fluid across an orifice, imparting momentum to the main flow while maintaining a net zero transfer of mass [64]. The emphasized control approach is the use of an actuation frequency high enough such that the forcing effects are decoupled from the time scales of the considered flow. Amitay *et al.* [5] describes this control approach as one that modifies the apparent aerodynamic shape of the flow surface, thereby changing the pressure gradient and suppressing flow separation. Amitay & Glezer [4] successfully applied this control approach to a low Reynolds number airfoil, showing that flow separation could be delayed to angles of attack greater than the stall angle of the baseline flow. However, although not expressly stated, the range of forcing frequencies considered overlapped with that of the separated shear layer instability, thus making it unclear when performance improvements were realized through targeting the unstable shear layer. Future investigations would clarify that optimal excitation frequencies correspond to the separated shear layer instability [16, 54, 63], finding that the threshold momentum required to reattach the flow is an order of magnitude smaller at these frequencies compared to high frequency excitation [54].

Regardless of the control method employed, there is consensus across the literature linking the optimal excitation frequency to that of the most amplified disturbances in the LSB [54, 171, 258, 265]. These investigations have shown that inducing flow reattachment on a stalled airfoil through the formation of an LSB or reducing the size of an existing LSB is most effective when the excitation frequency targets the natural K-H instability and the associated vortex shedding process. It has been demonstrated that forcing at this ‘fundamental’ frequency has significant impacts

on the ensuing vortex dynamics [112, 135, 260], as the shedding process locks the excitation frequency, vortex formation occurs further upstream, and the spanwise coherence of the structures is increased. This has been shown to have significant influence over the mean LSB topology [134, 260], with the upstream advancement of vortex formation being the most significant factor influencing the mean reattachment location [112].

While the topic of forcing an LSB at its fundamental frequency has been studied extensively, the effects of forcing at subharmonic frequencies on LSB flow development and vortex merging remain relatively unknown. In free shear flows, fundamental and subharmonic forcing has been shown to have significant influence over on vortex dynamics, specifically through manipulation of the vortex merging process. In particular, applying acoustic forcing at or near the fundamental frequency synchronizes the initial roll-up process, creating a well defined maximum in the fundamental perturbation mode at the streamwise roll-up location, at which point the subharmonic mode begins to grow, reaching a maximum at a pairing location further downstream [73]. However, forcing in the vicinity of the fundamental frequency inhibits merging with respect to the natural case [81]. Ho & Huang [72] showed that the process can be manipulated by altering the forcing frequency, as after disturbance growth at the fundamental frequency saturates, a subharmonic resonance mechanism gives rise to subharmonic disturbance growth [102, 160]. Thus, forcing applied at the subharmonic frequency accelerates the growth of the subharmonic mode, which was found to promote vortex merging and increase the rate of momentum transfer across the layer, relative to the unforced case [72]. Similar to the roll-up location coinciding with the peak in the fundamental mode, the pairing location occurs downstream where the subharmonic mode reaches a maximum. It remains to be determined if vortex merging in LSBs has a significant effect on the mean flow topology, through influence of the reattachment process or otherwise, and whether merging can be manipulated via forcing to the same effect as seen in free shear layers.

Mechanical oscillations [118, 139], such as those created by a vibrating ribbon, and the analogous numerical implementations [2, 141] have been primarily used a diagnostic tool to investigate the LSB transition process. One aspect that has received considerable attention is the relative influence of normal (two-dimensional) and oblique disturbances in LSB transition. Rist & Augustin [198], in a DNS study of an LSB formed over a flat plate, found that weakly oblique instability waves grew at lower but comparable rates to the normal mode, and when present lead to an earlier onset of turbulent breakdown. Furthermore, the introduction of these oblique waves caused a spanwise staggering of the LSB vortex shedding process, leading to a peak and valley distribution in the mean flow field. Similar observations have been made in other DNS studies, notably those of Marxen *et al.* [137] and Pauley [182]. Experimental studies of the same nature are relatively scarce due to the difficulty in implementing a reliable three-dimensional forcing technique, which is then compounded by the need for three-dimensional flow field measurements. One such study was that of Lang *et al.* [118], who reported insignificant differences between two and three-dimensional forcing, however the free-stream turbulence intensity of the employed water tunnel facility was approximately 1% [230], which may have had significant influence as discussed in Section 2.2.3.

Plasma actuators present a new avenue for LSB flow diagnostics, having only come into focus within the flow control research community within the last two decades [40]. Their control authority over LSBs has been demonstrated, with two-dimensional configurations employed in

which the wall-parallel jet produced by the actuator is pulsed at a frequency matching the shear layer instability [151, 199, 210, 260, 261]. The ensuing effects on the LSB are largely identical to those reported for other forcing techniques, namely the vortex shedding process locking to the forcing frequency, vortex formation at an earlier streamwise location and with a higher degree of spanwise coherence, and an overall reduction in LSB size. Furthermore, actuators can be rapidly prototyped due their mechanical simplicity and ease of manufacturing, allowing for a wide variety of forcing configurations to be considered. For example, novel plasma forcing configurations have been developed to investigate cross-flow instabilities on swept wings [221], drag reduction in turbulent boundary layers [234], and noise suppression of cylinders in cross-flow [235]. Thus, plasma actuators present themselves as an excellent diagnostic tool for examining the effects of controlled two and three-dimensional disturbances on transition and flow development in LSBs.

Chapter 3

Methodology

The methods of investigation are outlined, including the experimental facilities, models, and measurement techniques employed. Methods for data analysis are discussed, with the theoretical bases given for a select few, and the framework for uncertainty analysis is established.

3.1 Experimental Setup

The experiments conducted as part of this thesis were performed at the University of Waterloo and Delft University of Technology, in the Fluid Mechanics Research Laboratory and the Low Speed Laboratory, respectively. As such, a general overview of the relevant facilities and experimental models is provided here, with details specific to each campaign provided in Chapters 4–6.

3.1.1 UW Recirculating Wind Tunnel

At the University of Waterloo, experiments were conducted using a recirculating wind tunnel, shown in Fig. 3.1, located in the Fluid Mechanics Research Laboratory. The flow is circulated by a six blade, vane axial fan coupled to a variable frequency, alternating-current motor. The flow is conditioned in the settling chamber by an aluminum honeycomb grid and five wire mesh screens, upstream of a contraction with a 9 : 1 ratio. The test section is 0.61×0.61 m in cross-section, 2.44 m long, and is fabricated from clear polycarbonate. The facility was characterized by Kurelek [111]. At the investigated free-stream velocity ($u_\infty = 9.6\,\mathrm{m\,s^{-1}}$), the free-stream uniformity is within ±0.4%, while a minor favourable pressure gradient, equal to $\partial p/\partial x = 0.4\,\mathrm{Pa\,m^{-1}}$, is present over the length of the test section when empty. The free-stream turbulence intensity, as measured by hot-wire anemometry, is 0.1% with an integral length scale of 40 mm with signals low-pass filtered at 10 kHz. The free-stream has no significant spectral content within the frequency range $100 \leq f \leq 2000$ Hz, with the free-stream turbulence level reduced to 0.01% when bandpass filtered to within this range. These free-stream characteristics, in addition to its recirculating nature, make the facility well suited for investigations of laminar–turbulent transition by means of particle image velocimetry.

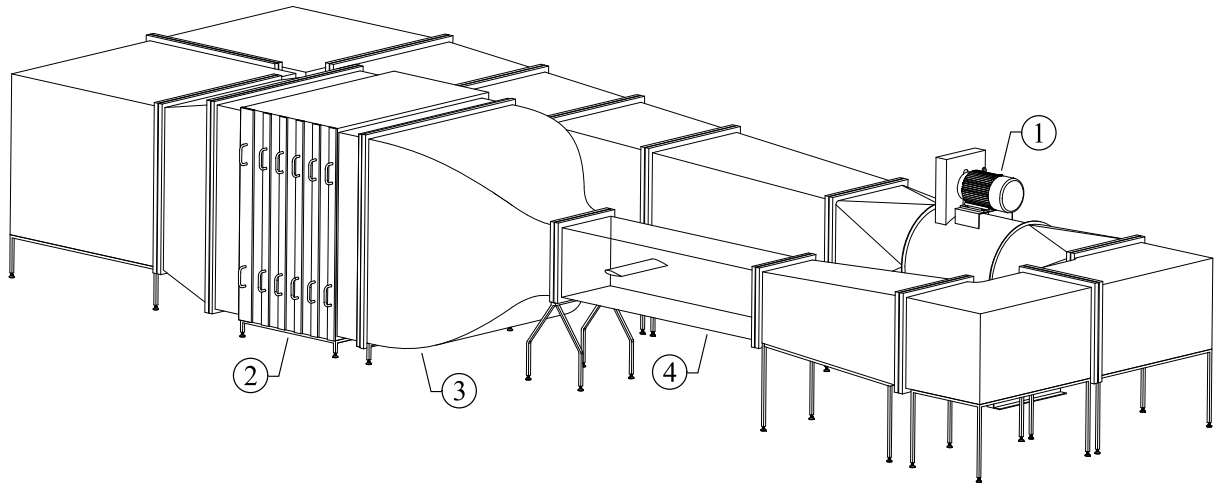

Figure 3.1: University of Waterloo recirculating wind tunnel. ① Motor and fan; ② settling chamber; ③ contraction; ④ test section.

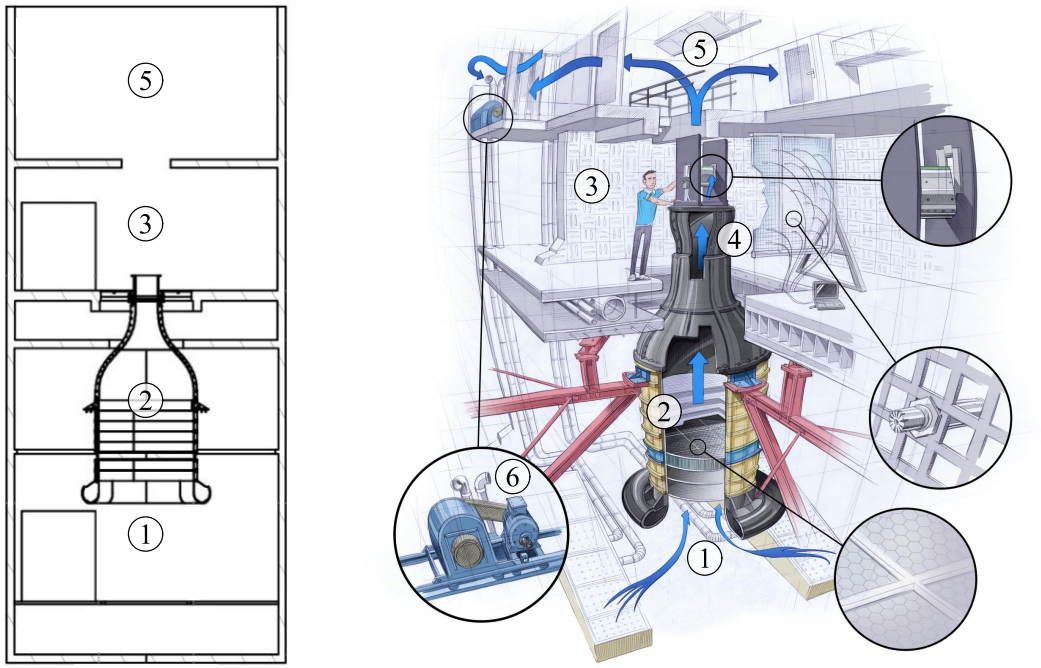

(a) (b)

Figure 3.2: (a) Side view cross-section and (b) artist's impression of the TU Delft A-Tunnel. ① Settling chamber; ② flow conditioning elements and contraction; ③ open jet test section/anechoic plenum; ④ interchangeable nozzle and model mount; ⑤ return chamber; ⑥ motor and fan. Reproduced with permission from Merino-Martínez *et al.* [147]. Illustration by Stephan Timmers.

3.1.2 TU Delft A-Tunnel

At Delft University of Technology, experiments were conducted in the Anechoic Vertical Low Turbulence Wind Tunnel (A-Tunnel), depicted in Fig. 3.2. The facility is an open-jet, closed-circuit, vertical wind tunnel that spans four stories at the Low Speed Laboratory. Spanning the first two stories are the settling chamber and contraction, with flow conditioning performed by a stainless steel honeycomb grid and four anti-turbulence wire mesh screens. Flow exits the contraction into an open-jet test section located within an anechoic plenum on the third story. Interchangeable nozzles are available for mounting flush to the contraction exit, with the particular nozzle employed throughout featuring a 0.5×0.5 m exit area, resulting in a total contraction ratio of $17:1$. Acrylic walls were mounted to the nozzle exit (not depicted in Fig. 3.2), forming a $0.5 \times 0.5 \times 1.1$ m test section that housed the flat plate test model (Section 3.1.4). The flow is circulated by two motor and centrifugal fan units, located on the fourth story in the return chamber.

A detailed characterization of the facility is presented in the work of Merino-Martínez *et al.* [147]. At the investigated free-stream velocity ($u_\infty = 5.75\,\mathrm{m\,s^{-1}}$), the free-stream uniformity is within ±1%, the turbulence intensity is 0.09%, and no significant spectral peaks are found in the free-stream velocity and pressure fluctuations within the frequency range $1 \leq f \leq 1000$ Hz. The facility is particularly well suited for aeroacoustic investigations and studies of laminar–turbulent transition, and can be equipped for a wide variety of measurement techniques, including hot-wire

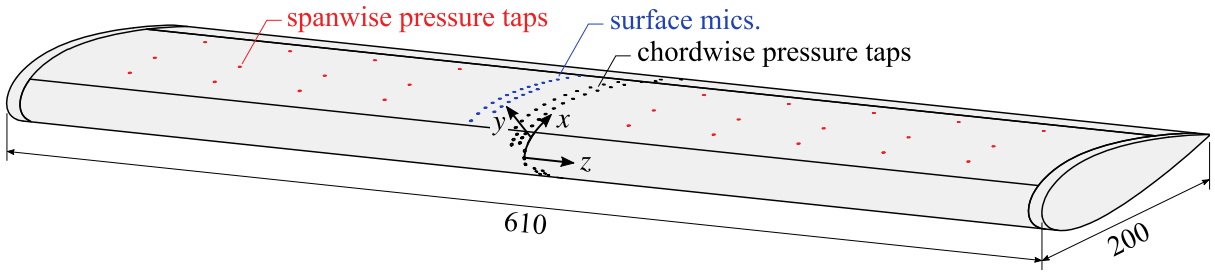

Figure 3.3: NACA 0018 airfoil model. All dimensions in millimetres.

anemometry and particle image velocimetry.

3.1.3 Airfoil Model

The employed airfoil model, Fig. 3.3, was designed and manufactured by Gerakopulos [61] and has been used extensively in studies of LSB transition (*e.g.*, Refs. [20, 86, 113, 115]), and hence its aerodynamic characteristics are well-established. The model has a NACA 0018 profile with a chord length, c, and span of 0.2 and 0.61 m, respectively, and thus spans the entire test section of the UW recirculating tunnel (Section 3.1.1). The model is equipped with 95 static pressure taps of 0.4 mm diameter, 65 of which are divided between chordwise staggered rows on the pressure and suction surfaces at the midspan plane ($z/c = 0$). The remaining pressure taps are divided into three spanwise rows on the suction surface at chordwise locations of $x/c = 0.15$, 0.30 and 0.60, and are spaced to allow for an assessment of flow uniformity over the central 84% of the airfoil span. The model is also equipped with 25 Panasonic WM-62C condenser microphones, embedded in the airfoil suction surface under 0.8 mm ports, 22 of which are arranged in a chordwise staggered row at $z/c = -0.2$.

3.1.4 Flat Plate Model

The employed flat plate model was developed by Michelis [150] and is manufactured from acrylic. It measures $1000 \times 500 \times 20$ mm (length $\times$ width $\times$ thickness), and has a modified super elliptical leading edge [126], ensuring seamless curvature change and the development of a laminar boundary layer on its top surface at appropriate Reynolds numbers. The trailing edge forms part of an adjustable flap, which can be deflected upwards to locate the leading edge stagnation point on the upper surface of the plate, thereby eliminating possible unsteady leading edge separation effects. Integrated into the model are 30 static pressure taps (0.4 mm diameter), 22 of which are arranged in a streamwise row at $z = 0$, with the remaining 8 arranged in two spanwise rows located at $x = 20$ and -160 mm that cover 40% of the plate's span. The model can also be equipped with up to 10 LinearX M53 condenser microphones to enable fluctuating surface pressure measurements. These are installed under 0.4 mm ports, 8 of which are arranged in a streamwise row at $z = 30$ mm. A rectangular trench, $55 \times 500 \times 1$ mm (length $\times$ width $\times$ depth), located 165 mm from the plate's leading edge allows for the installation of flush mounted plasma actuators, while a blank can be inserted into the trench when no actuator is installed.

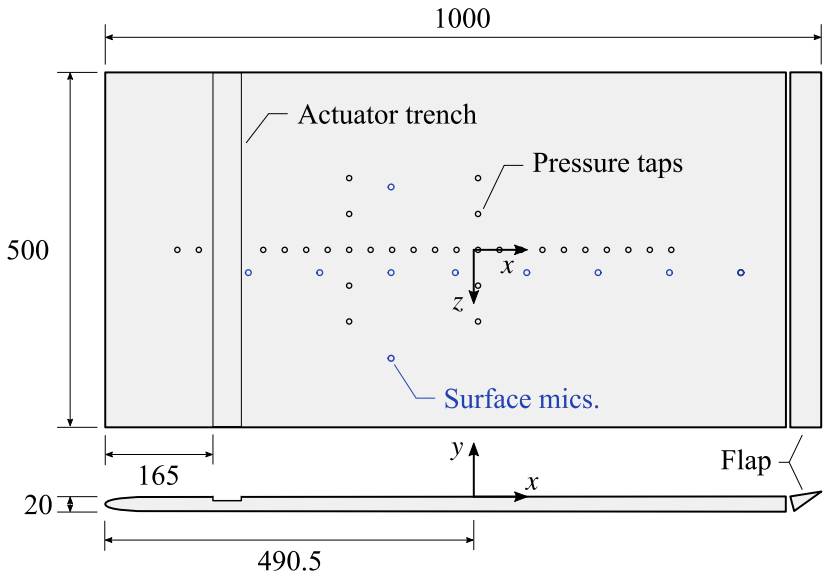

Figure 3.4: Flat plate model. All dimensions in millimetres.

3.2 Experimental Techniques

While a number of experimental techniques are employed throughout, the main forcing technique under consideration utilizes dielectric barrier discharge plasma actuators, while the vast majority of results are derived from particle image velocimetry measurements. As such, brief introductions to these techniques are provided, alongside some basic considerations when implementing them in practice. Specifics on the other techniques employed are found in the relevant chapters.

3.2.1 Particle Image Velocimetry

Particle image velocimetry (PIV) was selected as the primary means of investigation throughout this work since it provides velocity field measurements through optical means, and therefore is minimally invasive. Overviews of the technique are available in the books of Adrian & Westerweel [1] and Raffel *et al.* [191]. In essence, the technique involves the imaging of illuminated tracer particles present in the flow, with the displacement, and hence velocity, of the particles estimated through a statistical image matching process.

The three most common PIV configurations are planar, stereoscopic and tomographic, with the first two providing two and three-component velocity measurements in a plane, respectively, while tomographic provides three component velocity measurements in a volume. A simplified schematic showing a planar PIV setup is provided in Fig. 3.5a. PIV measurements rely on seeding the flow with tracer particles, which, ideally, would be free of inertia and therefore follow the flow 'faithfully'. For this reason, and to ensure the presence of the particles does not alter the natural flow development, the seeding particle diameter should be minimized, however, this is in direct opposition with their requirement to maximize light scattering. For low speed flows in air, fog particles with a diameter on the order of 1 µm produced by vapourizing a mixture of

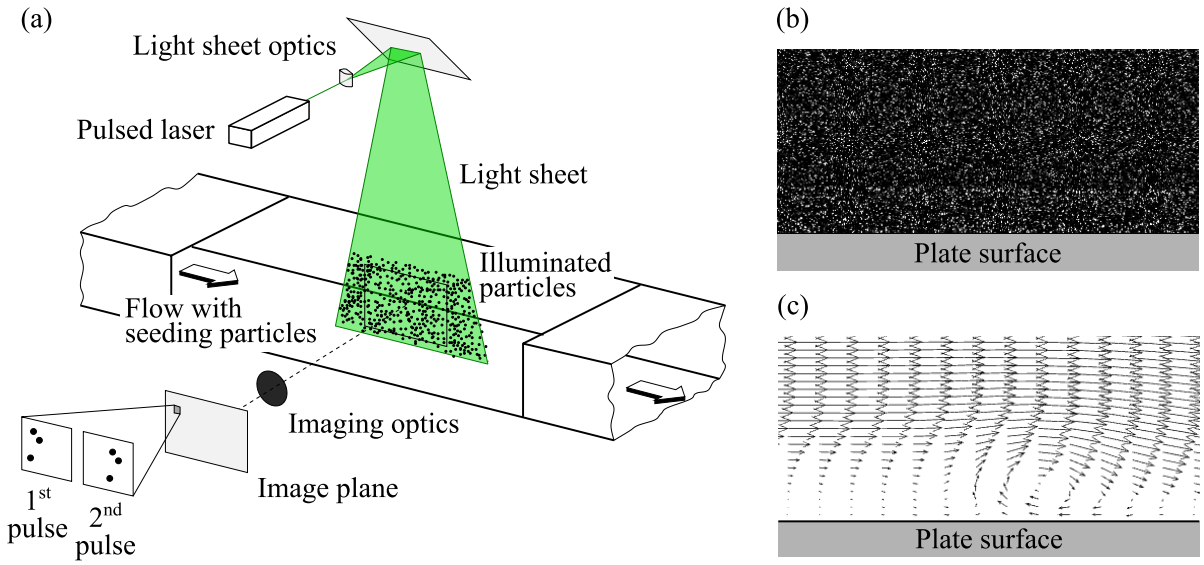

Figure 3.5: (a) Schematic of a typical planar PIV setup, after Raffel *et al.* [191]. (b) Sample particle image from flow over a flat plate with laminar separation and (c) resulting vector field.

water and glycol offer a good compromise. Particles with increasing oil content offer improved scattering properties at similar particles sizes, however, they present maintenance and health concerns, particularly when used in facilities with open test sections, *e.g.*, the TU Delft A-Tunnel (Fig. 3.2). Solid seeding particles, usually in the form a metal oxide powder, must be used for measurements in compressible or reactive flows.

Particle illumination is achieved by a pulsed laser, typically an Nd:YAG or Nd:YLF type, with the scattered light captured by one or more digital cameras. A similar spectacle can be observed regularly on the island of Ibiza. The laser pulse duration is on the order of a few nanoseconds, during which the particles are essentially motionless. An exemplary particle image is provided in Fig. 3.5b, where light scattered by the particles is recorded as a distribution in pixel intensities (*i.e.*, a digital image). Image acquisition is performed with the laser and camera(s) synchronized, with the repetition rate of the system dictating the acquisition frequency. Systems are generally classified as either low or high speed based on their repetition rate. Low speed acquisition rates are generally on order of 10 Hz, while current laser and camera technologies allow for high speed acquisition rates of up to 20 kHz. While low speed PIV is usually insufficient in resolving relevant time scales, in general, more powerful lasers and higher resolution cameras can be employed in comparison to high speed PIV. Consequently, the investigated area and/or spatial resolution of the measurement can be increased.

In planar PIV (Fig. 3.5a), the laser output is transformed by a set of optics, typically consisting of spherical and cylindrical lenses, to form a sheet that is typically 1 to 2 mm thick. The camera is oriented normal to and focused on the illumination plane. The relationship between the position of the particles in the image and physical space is determined through a calibration process, in which a target bearing marks at known locations in placed in the illumination plane and imaged. Images are acquired at two successive time instances, separated by the laser pulse separation,

Δt. In single frame operation, the acquisition frequency is equal to the inverse of the laser pulse separation, $f_a = 1/\Delta t$, and a series of images is acquired. In double frame operation, the acquisition frequency and laser pulse separation are independent parameters, and a series of images pairs separated by Δt are acquired at f_a. Regardless of single or double frame operation, Δt should be significantly smaller than the time scales of the fluid motion, such that the motion of particles between successive images, *i.e.*, the particle displacements, is approximately linear.

Estimation of the particle displacements is a statistical process that begins with dividing two successive images into interrogation windows. From the images, two corresponding windows are cross-correlated for variable overlap values. In the case of planar PIV, a two-dimensional correlation map is produced containing a peak, whose location signifies the linear shift that maximizes the cross-correlation between the windows, and hence gives a statistical estimate of the average linear motion of the contained particles. Thus, a two-dimensional velocity vector local to the windows can be estimated since Δt is known. This process is repeated for all interrogation windows and then all time realizations, thus giving a time series of velocity fields. An exemplary velocity field is shown in Fig. 3.5c.

Based on these operating principles, several important practical guidelines can be formulated for PIV. First, the imaged particles should be distinct (non-overlapping), with the number in a given interrogation window maximized in order to maximize the statistical certainty of the cross-correlation. Thus, smaller imaged particles are desired as this allows for smaller window sizes, and hence improved spatial resolution. However, imaged particles should be larger than a single pixel, otherwise 'peak-locking' will result and sub-pixel displacements will not be resolvable [252]. This sets the practical limit for the minimum window size, with most investigators opting for windows that are 16 to 32 pixels squared, containing, on average, 10 to 15 imaged particles that are 2 to 3 pixels in diameter. Additionally, a laser pulse separation should be selected to keep particles displacements less than the size of window, otherwise no peak will be found in the correlation map and an erroneous estimate will result. In practice this is quite restrictive as particle displacements must be kept relatively small, resulting in a limited dynamic range. This is alleviated through an iterative vector calculation procedure [212], beginning with a relative coarse window size that is successively reduced to the minimum size. Through this larger particle displacements are possible, leading to an improved dynamic range of the measurement.

Tomographic PIV, developed by Elsinga *et al.* [51], is the extension of the planar approach to volumetric measurements, providing estimates for all three components of velocity. The first requirement is, therefore, that illumination is volumetric, achieved by the expanding the light sheet about its thickness. The flow is again seeded with particles, which are imaged simultaneously by a minimum of three, but typically four or more cameras. The cameras are arranged at different viewing angles and are equipped with Scheimpflug adapters so that uniform focus may be achieved within the volume. A calibration relationship to the physical space is determined by imaging a target with marks at known locations across the three-dimensional space, which can then be refined using the volume self-calibration technique [250]. A volume is reconstructed from the camera images using this calibration relationship, locating the particles in space by constructing a three-dimensional representation of the scattered light intensity. Different methods for volume reconstruction are available, with the Simultaneous Implementation of Multiplicative Algebraic Reconstruction Technique (SMART) [12] used throughout this work. The method for vector

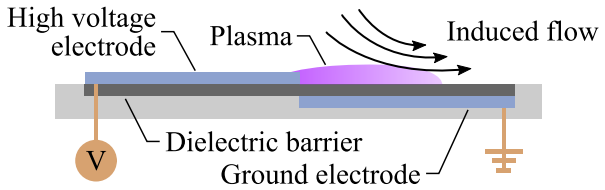

Figure 3.6: Cross-section of a typical asymmetric AC-DBD plasma actuator.

estimation is essentially preserved from planar PIV, with two successive volumes divided into three-dimensional interrogation windows, which are then cross-correlated in three-dimensions to give a local estimate of velocity.

3.2.2 Dielectric Barrier Discharge Plasma Actuators

Plasma is one of the four fundamental states of matter and is a gas of free floating ions that is electrically conductive and greatly responsive to electromagnetic fields. Creating and maintaining plasma requires input energy such that ionization overcomes recombination in the plasma medium. Controlled generation is most commonly achieved by applying an electric field across a gas volume by means of opposing electrodes driven by either DC or AC voltage. For a given gas and electrode separation, a breakdown voltage exists that depends on factors such as temperature and pressure, which if exceeded will lead to electrical breakdown of the gas, and thus the formation of plasma arcs and the flow of current between the electrodes. For air at standard temperature and pressure this voltage is on the order of several kV, with the formed plasma characterized by incomplete ionization and a lack of thermal equilibrium, with most of the energy contained in free electrons. Thus, its overall temperature is relatively low and the plasma is referred to as non-thermal, *i.e.*, cold plasma. A full treatment of plasma physics is available in the works of Fridman [56].

If the two electrodes are separated by an insulating layer, then a dielectric barrier discharge (DBD) is formed. During such a discharge, ions accumulate on the barrier, leading to a reduction in the local electrical field and the discharge is quenched. This self-limiting nature of DBD is a main feature and necessitates the use of AC voltage in order to sustain the plasma. Thus, the configuration is referred to as an AC-DBD plasma actuator. In the context of flow control for aerodynamic applications, a typical configuration featuring asymmetrically positioned electrodes is shown in Fig. 3.6. During operation, heavy oxygen and nitrogen ions in the plasma are driven back and forth between the high voltage and ground electrodes due to the alternating current. Momentum is exchanged with the surrounding air through ion-neutral collisions, with the asymmetrical positioning of the electrodes and the presence of the dielectric barrier leading to unequal amounts transfered during the two AC half-cycles. Thus, a net body force directed from the high voltage to the ground electrode is generated, giving rise to a relatively weak and nearly wall parallel jet. The velocity of the jet depends on many factors, such as the AC peak-to-peak voltage and frequency, electrode and dielectric materials and thickness, and actuator geometry, among others, with maximum achievable velocities of approximately $10\,\mathrm{m\,s^{-1}}$ reported [162].

AC-DBD plasma actuators are electrical devices and therefore offer several advantages over other flow control methods (*e.g.*, synthetic jets, acoustics, mechanical oscillations) [40]. These

include mechanical simplicity (no moving parts), relative ease of manufacturing, and fast response times. What's more, they offer a relatively wide range of operating frequencies free of resonance restrictions, as the AC frequency (*i.e.*, the carrier frequency, f_c) can be modulated to produce time-periodic forcing, with the duty cycle of this modulation providing control over the momentum output per forcing cycle. In addition, based on the manufacturing method and electrode and dielectric materials, total thicknesses of less than 1 mm, and even on the order of 10 µm, can be achieved. Thus, a device can usually be integrated into a test model with relative ease and minimal impact on skin friction and pressure drag. It is for these reasons that AC-DBD plasma actuators are selected as the flow control method for flow diagnostics in Chapters 5 and 6.

The momentum imparted to the fluid by a plasma actuator is commonly expressed as a momentum coefficient, as proposed by Amitay *et al.* [5]:

$$C_\mu = \frac{T}{\frac{1}{2}\rho {u_\infty}^2 a},$$

where T is the generated sectional body/thrust force, ρ and u_∞ are the free-stream density and velocity, respectively, and a is an appropriate length scale. Determination of T through experimental means generally takes one of two approaches [109]: (i) direct force measurements or (ii) control volume analysis of the generated velocity field (indirect). The second approach is selected for this work, as characterization of both the imparted momentum and spatial topology of velocity output are required given the novel configuration employed (Chapter 5). For this indirect method, velocity field measurements in the cross-sectional plane of the actuator and near the discharge area are required, for which planar PIV measurements are particular well suited. Then, T can be calculated using a control volume based momentum balance, as described by Kotsonis *et al.* [109]. The specifics of applying this method in the current work are discussed in Section 5.3. Most notably, actuator output depends on the external flow [184], with most investigators relying on characterization in quiescent conditions. Such an approach is insufficient for the current work, and therefore a characterization approach that considers both quiescent and in-flow conditions is taken (Sections 5.3 and 5.4, respectively).

3.3 Analysis Methods

While a number of analysis methods are employed throughout, linear stability theory, proper orthogonal decomposition, and wavelet analysis are the three more specialized techniques employed, and as such, a brief overview of each is provided.

3.3.1 Linear Stability Theory

The origins of Linear stability theory (LST) lie in the works of Orr [175] and Sommerfeld [225]. Here the fundamentals of LST are reviewed, while full treatments of the topic are provided by Mack [131] and Schlichting & Gersten [214].

LST concerns itself with the theoretical investigation of a laminar base flow acted upon by small, wave-like perturbations. The aim is to determine if the amplitude of the perturbations diminish or grow, corresponding to stable and unstable states of the flow, respectively. Here, the framework for LST is formalized for an isothermal and incompressible flow absent of any body forces, for which the governing equations (Eqns. 2.1 and 2.2) simplify to:

$$\begin{aligned} \nabla \cdot \vec{u} &= 0, \\ \frac{\partial \vec{u}}{\partial t} + (\vec{u} \cdot \nabla)\, \vec{u} &= -\frac{1}{\rho} \nabla p + \nu \nabla^2 \vec{u}. \end{aligned} \tag{3.1}$$

The flow is decomposed into a base flow (denoted by over-line quantities), whose stability is studied, and superimposed perturbations (denoted by hat quantities). In order to ensure the mathematics remain tractable, several assumptions must be invoked on the base flow, namely, that it has no dependence on time, and is fully developed in and parallel to the streamwise direction, x. Such assumptions are entirely valid in channel and pipe flows, and have been applied to boundary layer flows with great success [18]. Thus, the velocity and pressure are:

$$\begin{gathered} u = \overline{u}(y) + \hat{u}(x, y, z, t), \quad v = \hat{v}(x, y, z, t), \quad w = \overline{w}(y) + \hat{w}(x, y, z, t), \\ p = \overline{p}(x, y, z) + \hat{p}(x, y, z, t), \end{gathered} \tag{3.2}$$

which must satisfy the governing equations. To once again maintain tractability, the amplitude of the perturbations is assumed infinitesimally small so that any non-linear perturbation terms that arise from substitution into the governing equations may be ignored, effectively neglecting disturbance interaction effects. Performing the substitution and making all the simplifications afforded by the assumptions yields:

$$\begin{aligned} \frac{\partial \hat{u}}{\partial x} + \frac{\partial \hat{v}}{\partial y} + \frac{\partial \hat{w}}{\partial z} &= 0, \\ \frac{\partial \hat{u}}{\partial t} + \overline{u}\frac{\partial \hat{u}}{\partial x} + \overline{w}\frac{\partial \hat{u}}{\partial z} + \hat{v}\frac{\mathrm{d}\overline{u}}{\mathrm{d}y} &= -\frac{1}{\rho}\frac{\partial \hat{p}}{\partial x} + \nu \nabla^2 \hat{u}, \\ \frac{\partial \hat{v}}{\partial t} + \overline{u}\frac{\partial \hat{v}}{\partial x} + \overline{w}\frac{\partial \hat{v}}{\partial z} &= -\frac{1}{\rho}\frac{\partial \hat{p}}{\partial y} + \nu \nabla^2 \hat{v}, \\ \frac{\partial \hat{w}}{\partial t} + \overline{u}\frac{\partial \hat{w}}{\partial x} + \overline{w}\frac{\partial \hat{w}}{\partial z} + \hat{v}\frac{\mathrm{d}\overline{w}}{\mathrm{d}y} &= -\frac{1}{\rho}\frac{\partial \hat{p}}{\partial y} + \nu \nabla^2 \hat{w}. \end{aligned} \tag{3.3}$$

In order to solve the system of equations above, a trial solution for the perturbations is employed:

$$\begin{aligned} \hat{u} &= \varphi_u(y) \exp\left[i\left(\alpha x + \beta z - \Omega t\right)\right], \quad \hat{v} = \varphi_v(y) \exp\left[i\left(\alpha x + \beta z - \Omega t\right)\right], \\ \hat{w} &= \varphi_w(y) \exp\left[i\left(\alpha x + \beta z - \Omega t\right)\right], \quad \hat{p} = \varphi_p(y) \exp\left[i\left(\alpha x + \beta z - \Omega t\right)\right]. \end{aligned} \tag{3.4}$$

which assumes each perturbation to be sinusoidal and composed of a single frequency, streamwise wavenumber, and spanwise wavenumber, *i.e.*, a mode. Here, φ is the disturbance eigenfunction, Ω is the angular frequency, and α and β are the streamwise and spanwise wavenumbers, respectively.

If α and β are assumed real, then Ω is complex and so the temporal formulation of the problem is employed, where disturbances grow or decay in time. Conversely, if the perturbation frequency is assumed real, then α and β are complex ($\alpha = \alpha_r + i\alpha_i$, $\beta = \beta_r + i\beta_i$) and the real and imaginary components correspond to the wavenumbers and spatial growth rates of the mode, respectively. In turn, the wave angle is defined as the angle between the streamwise and spanwise wavenumbers, $\vartheta = \tan^{-1}(\beta_r/\alpha_r)$. The sign of the growth rate indicates whether the perturbation grows ($\alpha_i, \beta_i < 0$), decays ($\alpha_i, \beta_i > 0$), or remains invariant ($\alpha_i, \beta_i = 0$). This spatial formulation is well suited for the study of convectively amplified disturbances, such as those in separation bubbles, and so is employed here.

Substitution of Eqn. 3.4 into Eqn. 3.3 yields a sixth-order set of ordinary differential equations for the perturbation eigenfunctions, which can be reduced and combined to give a single fourth-order equation in terms of φ_v. The exact steps are outlined by Mack [131]. The final expression is:

$$\left[\frac{\mathrm{d}^2}{\mathrm{d}y^2} - \left(\alpha^2+\beta^2\right)\right]^2 \varphi_v = iRe_{\delta_1}\left\{(\alpha\overline{u} + \beta\overline{w} - \Omega)\left[\frac{\mathrm{d}^2}{\mathrm{d}y^2} - \left(\alpha^2+\beta^2\right)\right] - \left(\alpha\frac{\mathrm{d}^2\overline{u}}{\mathrm{d}y^2} + \beta\frac{\mathrm{d}^2\overline{w}}{\mathrm{d}y^2}\right)\right\}\varphi_v, \tag{3.5}$$

where the equation has been non-dimensionalized by the local edge velocity, u_e, and the displacement thickness, δ_1, leading to the emergence of the Reynolds number based on these two quantities, Re_{δ_1}. Equation 3.5 is the stability equation for a three-dimensional wall-bounded flow subject to the boundary conditions that disturbances vanish at and far away from the wall, *i.e.*,

$$\varphi_v = 0, \text{ and } \frac{\mathrm{d}\varphi_v}{\mathrm{d}y} = 0, \quad \text{for} \quad y = 0, \text{ and } y \to \infty.$$

If the flow and disturbances are assumed two-dimensional, then $\overline{w} = 0$ and $\beta = 0$, respectively, and Eqn. 3.5 reduces to:

$$\left(\frac{\mathrm{d}^2}{\mathrm{d}y^2} - \alpha^2\right)^2 \varphi_v = iRe_{\delta_1}\left[(\alpha\overline{u} - \Omega)\left(\frac{\mathrm{d}^2}{\mathrm{d}y^2} - \alpha^2\right) - \alpha\frac{\mathrm{d}^2\overline{u}}{\mathrm{d}y^2}\right]\varphi_v, \tag{3.6}$$

which is the classic Orr-Sommerfeld equation for a two-dimensional boundary layer. Equations 3.5 and 3.6 are those employed for all stability calculations in this work. In solving either, Ω is specified (and β in the case of Eqn. 3.5) and the equation is solved numerically using Chebyshev polynomial base functions, with the companion matrix technique used to treat eigenvalue non-linearity [25]. Details on the solution methodology can be found in van Ingen & Kotsonis [240].

As outlined by van Ingen [239], it is often convenient to quantify the ratio of amplitudes for a two-dimensional disturbance ($\beta = 0$) at two arbitrary streamwise locations, x and $x + \mathrm{d}x$, which may be expressed through Eqn. 3.4 as:

$$\frac{A + \mathrm{d}A}{A} = \frac{e^{-\alpha_i(x+\mathrm{d}x)}}{e^{-\alpha_i x}} = e^{-\alpha_i \mathrm{d}x},$$

which may be further manipulated:

$$\ln(A + \mathrm{d}A) - \ln(A) = -\alpha_i \mathrm{d}x$$
$$\mathrm{d}\ln(A) = -\alpha_i \mathrm{d}x,$$

and then integrated definitely to give:

$$N = \ln\left(\frac{A}{A_{\mathrm{cr}}}\right) = \int_{x_{\mathrm{cr}}}^{x} -\alpha_i \mathrm{d}x, \tag{3.7}$$

where x_{cr} is the location at which a perturbation of frequency Ω and amplitude A_{cr} first becomes unstable. N is referred to as the amplification factor, and the Orr-Sommerfeld equation may be solved for a range of disturbance frequencies producing an envelope of N-curves that indicates the disturbances which are most destabilizing to the flow.

3.3.2 Proper Orthogonal Decomposition

Proper orthogonal decomposition (POD) is a statistical method that utilizes the orthogonal transformation in order to identify components of large variance in a system. Through this, a low order approximation of the system can be constructed through identification of the most significant modes. POD finds applications in many disciplines, such as random variables, image processing, signal analysis, data compression, and oceanography, where it is more commonly referred to as principal component analysis. In the context of fluid mechanics, it was first applied by Lumley [128] in the study of turbulence, and has been used extensively since, primarily for identification of coherent structures in a wide variety of flows [14]. POD can be formulated as the classical direct method [14] or the snapshot method [223].

The snapshot method is employed throughout this work. It begins with constructing a snapshot matrix, S, containing all realizations of a known/measured quantity. Commonly, the velocity fluctuations are taken, $\vec{u}'$, which are arranged along the rows and columns of S according to space ($\vec{r}$) and time (t), respectively:

$$S = \begin{bmatrix} \vec{u}'(\vec{r}_1, t_1) & \vec{u}'(\vec{r}_1, t_2) & \dots & \vec{u}'(\vec{r}_1, t_M) \\ \vec{u}'(\vec{r}_2, t_1) & \vec{u}'(\vec{r}_2, t_2) & \dots & \vec{u}'(\vec{r}_2, t_M) \\ \vdots & \vdots & \ddots & \vdots \\ \vec{u}'(\vec{r}_N, t_1) & \vec{u}'(\vec{r}_N, t_2) & \dots & \vec{u}'(\vec{r}_N, t_M) \end{bmatrix}, \tag{3.8}$$

where N and M are the number of spatial locations and time snapshots, respectively. Then, an eigenvalue problem may be formulated based on the autocovariance matrix of S, $R = S^{\mathrm{T}}S$. This is expressed as:

$$Rb = eb,$$

where e and b are the eigenvalues and temporal coefficients, respectively, and are of the form:

$$e = \begin{bmatrix} e^{(1)} & 0 & \dots & 0 \\ 0 & e^{(2)} & \dots & 0 \\ \vdots & \vdots & \ddots & \vdots \\ 0 & 0 & \dots & e^{(M)} \end{bmatrix}, \quad b = \begin{bmatrix} b^{(1)}(t_1) & b^{(2)}(t_1) & \dots & b^{(M)}(t_1) \\ b^{(1)}(t_2) & b^{(2)}(t_2) & \dots & b^{(M)}(t_2) \\ \vdots & \vdots & \ddots & \vdots \\ b^{(1)}(t_M) & b^{(2)}(t_M) & \dots & b^{(M)}(t_M) \end{bmatrix},$$

where the superscript denotes the mode number. For an individual mode, m, the spatial eigenfunction, *i.e.*, a POD spatial mode, $\gamma^{(m)}$, can therefore be found by considering the contributions of the snapshots based on the associated temporal coefficients:

$$\gamma^{(m)}(\vec{r}) = \sum_{i=1}^{M} b^{(m)}(t_i)\vec{u}'(\vec{r}, t_i),$$

with the set of eigenfunctions being spatially orthogonal. The eigenvalues indicate the energy content of the modes, and therefore the energy of a particular mode relative to the total energy of the fluctuating flow field, $E_{\mathrm{R}}^{(m)}$, can be quantified:

$$E_{\mathrm{R}}^{(m)} = \frac{e^{(m)}}{\sum_{i=1}^{M} e^{(i)}}.$$

Therefore, sorting the POD modes in order of decreasing eigenvalue reveals the most dominant (*i.e.*, energy containing) modes. Through this, POD analysis can identify dominant spatially coherent patterns in a flow field, and an efficient reduced order model can be constructed if a small number of modes contain a significant portion of the total fluctuating energy. This is often the case for flows dominated by large-scale convective structures, such as LSBs, where the most energetic POD modes are found to occur in pairs that represent the vortex shedding process [124, 130, 241].

3.3.3 Wavelet Analysis

Wavelets are useful in the analysis of non-stationary processes, as they can be used to estimate the power of a given signal as a function of both frequency and position in time. An in-depth overview of wavelet analysis is provided by Daubechies [43]. Analysis of a temporal signal of interest, $u(t)$, begins with the selection of a baseline wavelet function, $\Psi(t)$, which must have a zero mean value and be localized in time. Throughout this work, the Morlet/Gabor wavelet is used:

$$\Psi(t) = \exp\left[(-t/a)^2\right] \exp\left(i2\pi f_a t\right),$$

which is plotted in Fig. 3.7 using arbitrary units. In order to satisfy the admissibility condition [53], the wavelet central frequency, f_a, and damping parameter, a, are selected to be $5/2\pi$ rad s^{-1} and 2 s, respectively. The convolution of $u(t)$ with the complex conjugate of the baseline wavelet,

denoted by Ψ^*, gives the wavelet coefficient function:

$$\psi(\tau, s) = \frac{s^{-1/2}}{\sqrt{2\pi f}} \int_{-\infty}^{\infty} \Psi^* \left(\frac{t-\tau}{s} \right) u(t) \mathrm{d}t$$

where τ and s are the baseline wavelet translation and dilatation scales, respectively. Unit power per scale is achieved by scaling the wavelet coefficients by $\sqrt{2\pi f}$, where f is the sampling frequency of $u(t)$. Thus, the wavelet coefficient function gives a measure of the power contained in $u(t)$ as a function of the baseline wavelet's dilatation and translation scales, which are directly related to frequency and position in the time domain, respectively. Furthermore, the analysis is not limited to the time domain, as spatial signals can be analyzed to infer power as a function of wavelength and spatial position.

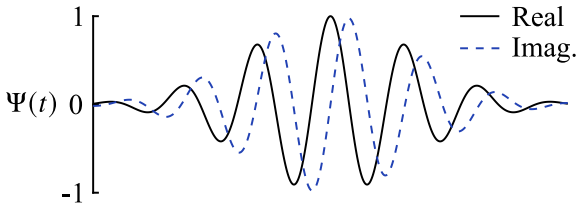

Figure 3.7: Form of the Morlet/Gabor wavelet.

3.4 Uncertainty Estimation

All uncertainties presented as part of this work are determined using the n^{th} order uncertainty methodology of Moffat [157], where the uncertainty in a particular quantity a is the result of the n sources of error in the measurement, with the total uncertainty, U_a, estimated as the root-sum-square of all the error estimates:

$$U_a = \left(\sum_{i=1}^{n} {U_i}^2 \right)^{1/2}. \tag{3.9}$$

Inevitably, all n sources of error cannot be accounted for, in which case the contributions are evaluated in order of most to least significant, with a sufficient level of confidence achieved in the uncertainty estimate once unambiguous observations and conclusions can be drawn from the results.

Two approaches are taken with regards to the propagation of uncertainty. First, in the case where the relationship between the desired quantity, a, and the measured quantities, b_i, is known,

i.e., $a = f(b_1, b_2, \ldots b_n)$, then the uncertainty in a is determined as follows:

$$U_a = \left[\left(\frac{\partial f}{\partial b_1} U_{b_1} \right)^2 + \left(\frac{\partial f}{\partial b_2} U_{b_2} \right)^2 \cdots + \left(\frac{\partial f}{\partial b_n} U_{b_n} \right)^2 \right]^{1/2}. \tag{3.10}$$

This approach is employed when the function f is known and evaluation of its partial derivatives is straightforward. When this is not possible, *e.g.*, in the application of advanced analysis techniques, then the uncertainty in the final result is estimated by propagating the uncertainty in the input quantities through the analysis. This is handled on a case-by-case basis based on the particulars of the analysis method, with details provided in Appendix B.

Throughout this thesis, quantitative results are presented with uncertainty estimates produced using this framework. Briefs descriptions of how the estimates are obtained are provided where appropriate, while the reader is referred to Appendix B for more detailed information.

Chapter 4

Laminar Separation Bubble Flow Development

The vortex dynamics of an LSB formed over an airfoil at a low Reynolds number and in a low free-stream turbulence environment are studied. Weak acoustic excitation that does not modify the mean LSB topology is applied, allowing for conditional volumetric reconstructions of the flow field. Forcing at the LSB fundamental frequency and the first subharmonic of this frequency are found to inhibit and promote the prevalence of vortex merging in the LSB. When left to develop naturally, vortex formation is found to be nominally two-dimensional, with spanwise undulations developing as part of the vortex breakup process.

Parts of this chapter have been adapted from the following publications:

Kurelek, J. W., Yarusevych, S., & Kotsonis, M. 2019 Vortex merging in a laminar separation bubble under natural and forced conditions. *Phys. Rev. Fluids*, **4** (6), 063903. DOI.

Kurelek, J. W., Tuna, B. A., Yarusevych, S., & Kotsonis, M. 2020 Three-Dimensional Development of Coherent Structures in a Two-Dimensional Laminar Separation Bubble. *AIAA J.* Article in Advance. DOI.

4.1 Introduction

The discussion presented in Section 2.2 established that the shear layer vortices formed in LSBs are critical to the flow development and impact performance in a wide variety of engineering applications operating at low Reynolds numbers [62, 75, 166]. In particular, these structures have been argued to be responsible for inducing mean reattachment [134, 260] and can lead to the production of sharp acoustic tones when LSBs form near the trailing edge of an airfoil [7, 44, 190]. Thus, in order to develop effective control strategies, a more comprehensive understanding of LSB dynamics is needed, since the most effective strategies to-date have target the shear layer vortices and the associated Kelvin-Helmholtz instability.

The prevailing control techniques found throughout the literature involve the introduction of controlled periodic disturbances at the 'fundamental' frequency of the Kelvin-Helmholtz instability. An in-depth discussion of this type of forcing and the effects on LSBs is provided in Section 2.3. What lacks in the literature are studies examining the effect of forcing at subharmonic frequencies on LSB flow development. Such an investigation has merit since, in the case of free shear layers, subharmonic forcing has been shown to have significant influence over the vortex dynamics, specifically through manipulation of the vortex merging process. In particular, applying forcing at or near the fundamental frequency synchronizes the initial vortex roll-up, while also inhibiting vortex merging in comparison to the natural case [81]. When forcing is applied at the first subharmonic of the fundamental frequency, vortex merging is promoted and the rate of momentum transfer across the shear layer increases [72]. Despite the major role played by vortex merging in the development of free shear layers, there is a lack of insight in this area with respect to laminar separation bubbles. It remains to be determined if vortex merging has a significant effect on LSB mean topology, through the influence of the reattachment process or otherwise, and whether merging can be manipulated via forcing to the same effect as seen in free shear layers.

Adding to the difficulty in gaining a complete understanding of the structure and development of the shear layer vortices in LSBs are the confluence of factors that can affect flow development. These are discussed in Section 2.2, and include the external disturbance environment, with moderate to high levels of free-stream turbulence intensity causing the vortex shedding process to exhibit significant cycle-to-cycle variations, with the vortices becoming increasingly distorted across the span. Furthermore, a number of potentially active instabilities have been reported, including Görtler type [138], elliptical and hyperbolic secondary instabilities [92, 137, 142], absolute instability [2], and a global centrifugal instability [200, 201], all of which can interact with the primary Kelvin-Helmholtz instability. The majority of studies to-date examining transition and flow development in LSBs often 'probe' the flow using controlled periodic disturbances (Section 2.3). However, any study of this nature can be inherently problematic if the introduction of the disturbances modifies the base flow, since the stability and hence the transition process of the flow being considered is modified. This is particularly true of experimental investigations, with a significant portion of results collected for LSBs for which the base flow has been modified due to high amplitude forcing [112, 260, 261], or by elevated turbulence intensity levels ($> 1\%$) [31, 33, 69, 255], all while being limited to two-dimensional assessments [69, 113, 124, 260] of a flow field that is inherently three-dimensional. Thus, a study that simultaneously limits the external factors known to influence LSBs while characterizing the three-dimensional development

of the dominant coherent structures is needed.

In this chapter experimental results examining an LSB formed over a NACA 0018 at a low Reynolds number are presented. The LSB is studied in a low free-stream turbulence facility ($< 0.1\%$) and is subject only to the primary convective Kelvin-Helmholtz instability. In addition to leaving the flow to develop naturally, controlled disturbances are introduced through weak acoustic excitation that do not significantly modify the mean topology of the flow. Two excitation cases are considered: (i) tonal acoustic excitation at the frequency of the most amplified disturbances in the natural flow, *i.e.*, the fundamental frequency, and (ii) at the first subharmonic of the fundamental frequency. These two cases, along side the natural flow, allow for the study of the vortex dynamics in the LSB, with a focus on the three-dimensionality of the structures and the vortex merging process.

4.2 Description of Experiments

Experiments were conducted in the University of Waterloo's recirculating wind tunnel, described in Section 3.1.1. The free-stream velocity was set based on the static pressure drop through the wind tunnel contraction calibrated against dynamic pressure in the empty test section measured via a Pitot-static tube, with uniformity verified to be within $\pm 0.5\%$ over 95% of the test section span. As outlined in Section 2.2, LSBs are highly sensitive to free-stream disturbances. As such, careful attention was paid to the frequency content of free-stream perturbations (Fig. 4.1), which was measured in the empty test section with a hot-wire. Figure 4.1 compares velocity spectra in the free-stream and LSB shear layer, each obtained at the conditions investigated throughout this chapter via hot-wire and PIV measurements, respectively. It is apparent that the free-stream velocity fluctuations are at least two orders of magnitude less than those present in the LSB, and in particular no significant spectral peaks are present in the free-stream with the frequency range of dominant fluctuations within the LSB, $2 \leq St_c \leq 42$ ($100 \leq f \leq 2000\,\text{Hz}$), where St_c is the Strouhal number based on the free-stream velocity and chord length. The resulting free-stream turbulence intensity and integral length scale values are 0.07% and $0.2c$, respectively, with signals low-pass filtered at 5 kHz.

The experiments were performed with using the NACA 0018 airfoil model described in Section 3.1.3. An aerodynamic angle of attack of $4° \pm 0.1$ was investigated at a free-steam velocity of $u_\infty = 9.6\,\text{m}\,\text{s}^{-1} \pm 0.2$, corresponding to a chord-based Reynolds number of $Re_c \approx 125\,000$. The solid blockage ratio at the investigated angle of attack is 6.1%. For the given flow conditions, separation bubbles form on both the suction and pressure surfaces of the airfoil, with the latter forming close to the trailing edge. To avoid tonal noise emissions due to the pressure side LSB [190], the pressure side boundary layer was tripped at $x/c = 0.4$ by a 10 mm wide strip of randomly distributed roughness elements with an average height of approximately 0.2 mm. For surface pressure measurements, the model's static pressure taps were connected to a Scanivalve mechanical multiplexer and pressure were measured using Setra Model 239 pressure transducers with a full range of ± 250 Pa. The uncertainty in all measured mean static pressures is estimated to be $\pm 0.8\%$ of q_∞ (Section B.4). Fluctuating surface pressures were measured using the model's surface embedded microphone array. The microphones were calibrated *in situ* using a reference

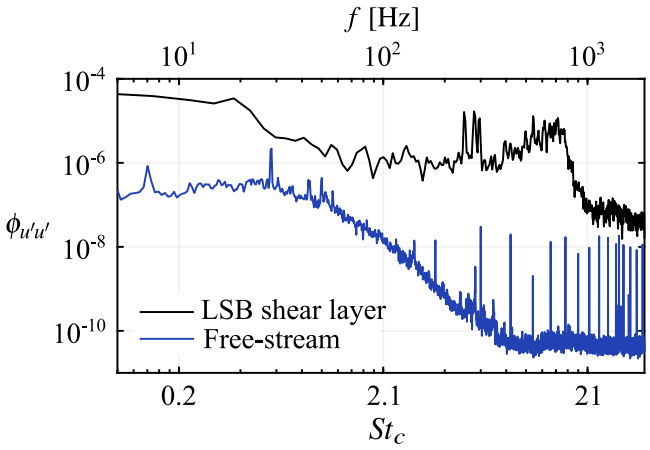

Figure 4.1: Spectra of streamwise velocity fluctuations.

Brüel and Kjær 4189 microphone, finding that the response of each microphone is flat within ±1 dB for the range of hydrodynamically relevant frequencies, $2 \leq St_c \leq 42$. All microphones were sampled simultaneously at 25.6 kHz using two 16-bit National Instruments 9220 modules in a CompactDAQ chassis. The estimated uncertainty in the measured pressure fluctuations ranges between ±1% and ±3% of q_∞ (Section B.4).

The flow was forced by means of acoustic excitation, with a sub-woofer placed in the wind tunnel test section six chord lengths downstream of the airfoil trailing edge. The presence of the sub-woofer was verified to have no measurable impact on the mean flow characteristics through surface pressure measurements. A 4189 Brüel and Kjær condenser microphone was used to characterize the acoustic environment, consisting of background noise and excitation at the airfoil surface. In addition to the unperturbed case, where the flow was left to develop naturally, two excitation cases were considered: (i) tonal excitation at the frequency of the most amplified disturbances in the unperturbed flow (St_{0_c}), and (ii) tonal excitation at the subharmonic of the fundamental frequency ($\frac{1}{2}St_{0_c}$). In order to ensure proper comparison between cases, care was taken to ensure equivalent acoustic input levels within $2 \leq St_c \leq 42$. To this end, the sound press level (SPL) within this frequency range was kept at 89.5 dB for both the fundamental and subharmonic tone cases. In comparison, the SPL for the natural case was 87.1 dB. The spanwise uniformity of the excitation was verified through microphone measurements at the airfoil surface, with SPLs verified to be uniform within the uncertainty limits of the microphones (less than ±0.1 dB) across the centre 20% of the investigated span.

Excitation levels at the airfoil surface were also characterized using the airfoil's embedded microphone array (Section 3.1.3). Spectra of the fluctuating pressure measured near the natural separation point are presented in Fig. 4.2. Figure 4.2a presents spectra corresponding to the two types of excitation compared to the spectrum of background pressure fluctuations in quiescent conditions. It can be seen that each excitation primarily produces elevated spectral content at the intended frequency and does not incite any resonant modes in the test facility. For the subharmonic case, peaks at higher harmonics are detectable, however, their amplitude are four orders of magnitude less than that at the targeted frequency. Spectra corresponding to the same location at $Re_c = 125\,000$ are presented in Fig. 4.2b. In comparison to quiescent conditions, all

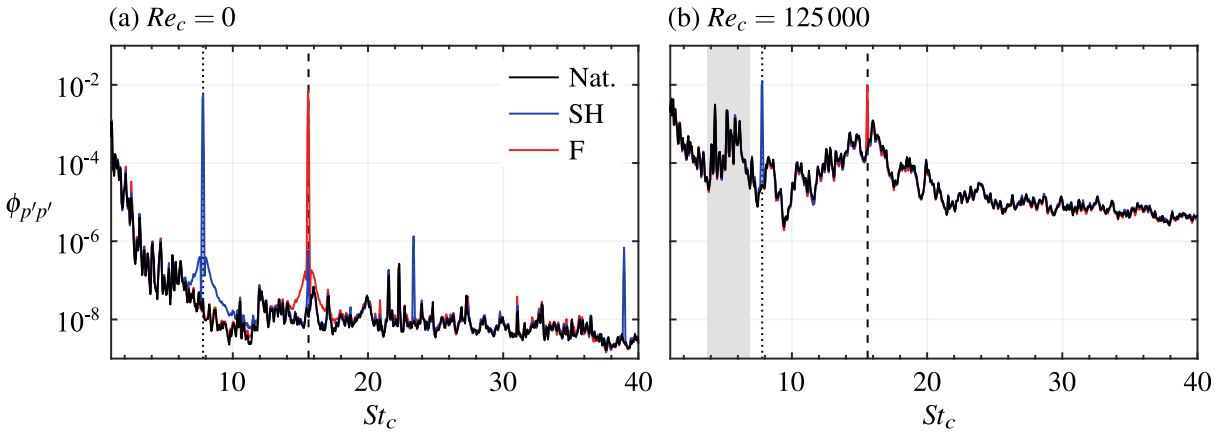

Figure 4.2: Spectra of fluctuating pressure near the natural separation point for the natural (Nat.), fundamental (F) and subharmonic (SH) cases in (a) quiescent and (b) the investigated flow conditions. Dashed and dotted lines denote St_{0_c} and $\frac{1}{2}St_{0_c}$, respectively. Gray shaded region indicates frequencies associated with the test section standing wave.

spectra here show elevated energy content over a broad range of frequencies centred at St_{0_c}, which is attributed to transition occurring in the LSB. Furthermore, the spectra are devoid of significant spectral peaks at extraneous frequencies, therefore ensuring no unexpected narrow-band acoustic sources are influencing the transition process. However, relatively broadband acoustic activity is present around $St_c \approx 6$ (grey shaded region in Fig. 4.2b), which is due to acoustic standing waves that establish in all hard walled test sections [169, 179, 180]. The frequencies associated with this standing wave are denoted by $St_{\mathrm{sw}c}$, and their effect on flow development and transition is assessed in Section 4.3.2.

Two-component, planar PIV measurements were performed in the configurations shown in Fig. 4.3. For both configurations, measurements were performed using a high-speed PIV system for time-resolved measurements at a single plane, in addition to scanning measurements at multiple planes using a low-speed system. Table 4.1 provides an overview of the salient measurement parameters. For all measurements, the flow was seeded using a glycol-water based fog with a mean particle diameter on the order of 1 µm, whose characteristic response frequency [146, 191] is above the Nyquist limit of the time-resolved PIV sampling frequencies. The laser beam was introduced through the side wall of the test section and conditioned into a sheet approximately 1 mm thick. Further conditioning oriented the sheet into x-y and x-z planes for the side and top view configurations, respectively (Fig. 4.3). Synchronization between cameras and the laser was handled by a timing unit controlled through LaVision's DaVis 8 software, which was also used for image acquisition.

For the time-resolved measurements, a Photonics Nd:YLF laser was used alongside two Photron SA4 cameras. For the side view configuration (Fig. 4.3a), the cameras were fitted with Nikon 200 mm focal length macro lenses set to an aperture number ($f_\#$) of 4. The cameras' sensors were cropped to 1024×512 px and the fields of view were selected to maximize the spatial resolution in the aft portion of the LSB, while maintaining equal magnification factors of 0.67. The fields of view were overlapped by 10%, covering a total area of 54×12.5 mm, and

(a) Side view
TR: 1 plane at mid-span
Scan: 29 planes on 5 mm spacing

(b) Top view
TR: 1 plane 1.8 mm from surface
Scan: 11 planes on 0.5 mm spacing

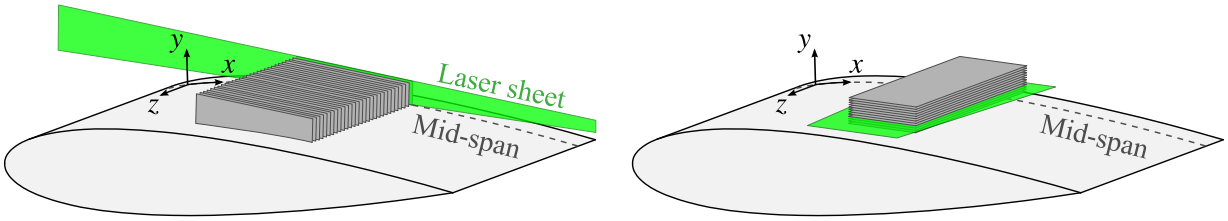

Figure 4.3: (a) Side and (b) top view configurations for time-resolved (TR) and scanning planar PIV measurements. Coordinate system origin is located at the airfoil leading edge and midspan point. Full spanwise extent not depicted.

Table 4.1: Parameters for PIV experiments.

Parameter	Time-Resolved		Scanning		Unit
	Side	Top	Side	Top	
Laser	Photonics 20 mJ/pulse Nd:YLF		EverGreen 70 mJ/pulse Nd:YAG		–
Cameras	Photron SA4		LaVision Imager Pro-X 2M		–
Lens focal length	200	105	200	200	mm
Lens $f_\#$	4	2.5	4	4	–
Mag. factor	0.67	0.33	0.62	0.37	–
Sensor resolution	1024×512	1024×1024	1600×860	1600×1200	px
Planes	1		29	11	–
FOVs per plane	2		3	6	
Area/volume	54×12.5	54×102	$52 \times 10 \times 140$	$30 \times 5 \times 134$	mm
PIV mode	Double-frame		Double-frame		–
Acquisition mode	Indep. sampling		Indep. sampling & phase-locked		–
Sampling rate	3800	1950	15 (indep.), 14.4 (phase-locked)		Hz
Laser pulse sep.	40	60	19	17–26	µs
Max. particle disp.	17	9	20	11	px
No. of samples	5000	2728	1000 (indep.), 250 (per phase)		–
Final window size	16×16 (75% overlap)		24×24 (75% overlap)		px
Vector pitch	0.12×0.12	0.24×0.24	$0.07 \times 0.07 \times 5$	$0.12 \times 0.5 \times 0.12$	mm
Avg. uncertainty	6	6.5	5	12	% of u_∞

double-frame images were acquired at 3.8 kHz. For the time-resolved, top view PIV measurements (Fig. 4.3b), the cameras were fitted with Nikon 105 mm focal length macro lenses set to $f_\# = 2.8$. The streamwise extent of the FOV was set to match that of the combined side view FOV, with the second camera employed to extent the FOV in the spanwise direction, while maintaining a 10% overlap. The full sensor resolution of 1024×1024 px and equal magnification factors of 0.33 were used for both cameras. The combined top view FOV for the time-resolved measurements is 54×102 mm, with double-frame images acquired at a rate of 1.95 kHz.

For the scanning PIV measurements, the measurement system equipment consisted of an

EverGreen Nd:YAG laser, one LaVision Imager Pro-X 2M camera fitted with a Nikon 200 mm macro lens set to $f_\# = 4$, and a timing unit; all controlled through LaVision's DaVis 8 software. For the side view configuration (Fig. 4.3a), the camera's sensor was cropped to 1600×860 px and the imaged field of view was set to 19×10 mm, resulting in a magnification factor of 0.62. For the top view (Fig. 4.3b), the camera's full sensor resolution of 1600×1200 px was used, and the FOV was 30×24 mm, resulting in a magnification factor of 0.37. To achieve the desired spatial resolution in the data, three and seven fields of view per plane were captured in the top and side view configurations, respectively, with 10% overlap employed between adjacent views.

The flow field was volumetrically reconstructed using the scanning PIV measurements. For the side view configuration (Fig. 4.3a), a total of 29 streamwise planes were measured, each spaced by 5 mm in the z-direction, resulting in a total measurement volume of $52 \times 10 \times 140$ mm. For the top view (Fig. 4.3b), 11 planes were measured each spaced by 0.5 mm in the y-direction, resulting a measurement volume of $30 \times 5 \times 155$ mm. The camera and laser were moved synchronously using an automated traversing system, with calibration images taken at multiple planes. Vortex shedding in a separation bubble is naturally quasi-periodic [20, 33, 113, 243] and therefore does not lend well to phase-averaging. However, when excited using an acoustic tone, the shedding process can lock to the excitation frequency, thus greatly reducing temporal variability [112]. This technique was employed to enable phase-locked PIV measurements for the fundamental excitation case. The excitation signal served as the phase-locking reference and therefore was split prior to amplification and sent to the PIV timing unit. Independently sampled (non-phase-locked) scanning PIV measurements were taken for the natural and fundamental cases. No scanning measurements were performed for the subharmonic case.

All image processing and vector calculations were performed in LaVision's DaVis 8 software. All imaged particles were approximately 2 to 3 px in diameter. Iterative, multi-grid cross correlation schemes with window deformation [212] were used to compute velocity fields. Final interrogation windows sizes of 16×16 px and 24×24 px, both with 75% overlap, were used for the time-resolved and scanning measurements, respectively. The resulting data vector pitches are reported in Table 4.1. The results were post-processed using the universal outlier detection algorithm [247]. Individual velocity fields were then interpolated onto the common surface attached coordinate system, with cosine weighted blending functions employed in the overlap regions. The random errors in the PIV measurements were evaluated using the correlation statistics method [251], with the average uncertainties associated with each configuration and measurement type reported in Table 4.1, while higher uncertainties (approximately 10% of u_∞) are present near the airfoil surface. A full treatment of the uncertainty estimates related to the PIV measurements and quantities that are subsequently derived from the PIV results is given in Section B.2.

4.3 Results

The results presented pertain to an LSB formed on the suction side of a NACA 0018 airfoil at an angle of attack of 4° and chord-based Reynolds number of 125 000. In addition to leaving the flow to develop naturally, tonal acoustic excitation is applied at the frequency of the most amplified disturbances in the natural flow, *i.e.*, the fundamental frequency, $St_{0_c} = 15.6$ ($f_0 = 750$ Hz), and

at the first subharmonic of St_{0_c}, $\frac{1}{2}St_{0_c} = 7.8$ ($\frac{1}{2}f_0 = 375\,\text{Hz}$), which were determined *a priori* via fluctuating surface pressure measurements (Fig. 4.2). The excitation amplitude for both the fundamental and subharmonic cases is characterized by an increase in the SPL measured at the airfoil surface of 0.6 dB over the natural case. This low excitation level was selected to avoid any substantial mean flow modifications, while enabling assessment of the effects of forcing on the ensuing vortex dynamics. In the discussion that follows, the flow development of the LSB is first established, followed by an in-depth examination of the vortex merging phenomenon and the three-dimensional development of the dominant coherent structures. Throughout the presentation of results, the natural, fundamental, and subharmonic forcing cases are denoted by the shorthands Nat., F, and SH, respectively.

4.3.1 General Flow Development

A two-dimensional view of flow development in the LSB is assessed from results of the time-resolved PIV measurements, performed at the midspan plane for all cases. Time-averaged velocity field statistics are plotted in Fig. 4.4 and are analyzed to identify the presence and extent of the separation bubble. A region of reverse flow is identifiable in the mean streamwise velocity, $\overline{u}$, contours of the natural flow, indicating the presence of flow separation and subsequent reattachment (in a time-averaged sense), and thus the formation of an LSB. The maximum reverse flow velocity is approximately 4% of u_∞, thus indicating the flow is convectively unstable and is not subject to a local absolute instability [2] or global instability [200, 201], which have minimum reverse flow velocity thresholds of 15% and 7%, respectively. The mean outline of the bubble is identified using the dividing streamline, which forms a closed contour with the surface within which the streamwise mass flux is zero [58, 76, 172]. The intersection points of the dividing streamline with the surface are the mean separation and reattachment points, $\overline{x_\text{s}}$ and $\overline{x_\text{r}}$, respectively, with the estimates of the former lying upstream of the measurement domain for all cases. The maximum bubble height, yh and its streamwise position, $\overline{x_\text{h}}$, are also indicated and are found where the maximum wall-normal distance between the surface and dividing streamline occurs. The uncertainties in determining $\overline{x_\text{s}}$, $\overline{x_\text{h}}$, and $\overline{x_\text{r}}$ are indicated by the dotted lines in Fig. 4.4, whose determination is outlined in Section B.2.

From Fig. 4.4, on accord of the relatively weak levels of forcing employed, neither type of excitation results in significant changes in the mean topology of the bubble, with all changes in mean separation, maximum bubble height, and reattachment falling within the experimental uncertainty. Accordingly, the root-mean-square contours of streamwise and wall-normal velocity fluctuations, u'_rms and v'_rms, respectively, are not appreciably altered by the excitation. Overall, all rms contours closely match previous reports for naturally developing separation bubbles [113, 260]. The rising rms levels along the trajectory of the displacement thickness indicate that the well-established process of streamwise disturbance amplification in the separated shear layer leading to roll up and the formation of shear layer vortices [20, 243] occurs in a similar manner for the cases presented in Fig. 4.4. However, subtle differences are detected in the rms contours, in particular in the near wall region of the u'_rms contours for the subharmonic case, and in the v'_rms at $x/c = 0.46$ for both the fundamental and subharmonic cases, which indicates that flow development may be affected by the excitation.

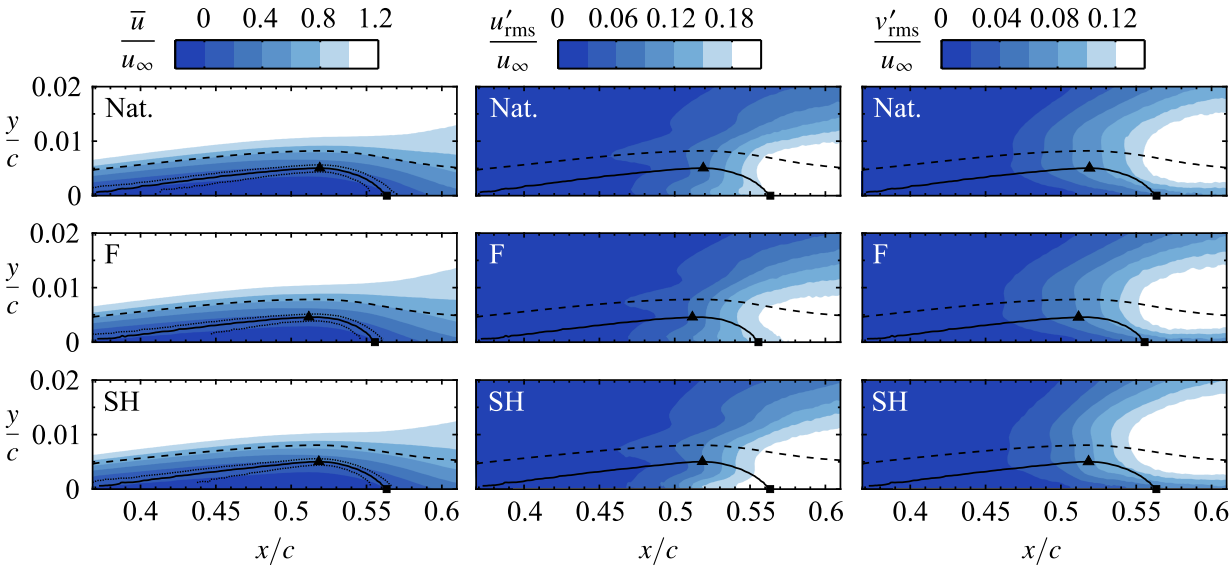

Figure 4.4: Mean streamwise velocity ($\overline{u}$), and rms of fluctuating streamwise (u'_{rms}) and wall-normal (v'_{rms}) velocity. Solid lines mark the dividing streamlines, whose uncertainty bounds are indicated by the dotted lines. Triangle and square markers denote estimated mean maximum bubble height and reattachment points, respectively. Dashed lines indicate displacement thickness.

Flow development in the LSB is assessed via the sequences of spanwise vorticity, ω_z, contours presented in Fig. 4.5. Contours of the λ_2-criterion [88] are added to aid in identifying coherent structures. The natural flow development (Fig. 4.5a) is characterized by periodic roll-up of the separated shear layer into vortices upstream of the maximum height location, $\overline{x_{\mathrm{h}}}/c = 0.52$. These structures interact and deform within $0.52 < x/c < 0.56$, followed by the onset of breakdown to smaller scales beyond mean reattachment, $\overline{x_{\mathrm{r}}}/c = 0.56$. Dashed lines are used to track structures frame-to-frame, with the slope and streamwise spacing of the lines representing convective velocity and streamwise wavelength, respectively. The majority of structures in the naturally transitioning flow are characterized by similar convective velocities and wavelengths; however, sporadic merging between subsequent vortices can occur. This is capture for vortices A and B in Fig. 4.5a, where the convective velocity of the downstream structure in the merging pair (B) decreases, while that of the upstream vortex (A) remains constant. Consequently, the distance between the vortex cores decreases and they merge, forming A+B, which is separated from the nearest downstream vortex by approximately twice the average streamwise wavelength. The observed process is in general agreement with the stages of vortex merging described by Cerretelli & Williamson [35] and Meunier *et al.* [148].

Figures 4.5b and 4.5c show flow development in the LSB for the fundamental and subharmonic excited cases, respectively, where similar to the natural case (Fig. 4.5a), the separated shear layer rolls up to form periodic vortices upstream of the maximum bubble height location. The shed structures then convect downstream, deform, and eventually begin to break down to smaller scales. However, for the subharmonic case, vortex merging is observed regularly through the entire recorded sequence. This is exemplified by the results in Fig. 4.5c, as all vortices initially identified in the roll-up region ($x/c < 0.53$) undergo merging. In stark contrast, Fig. 4.5b shows that forcing

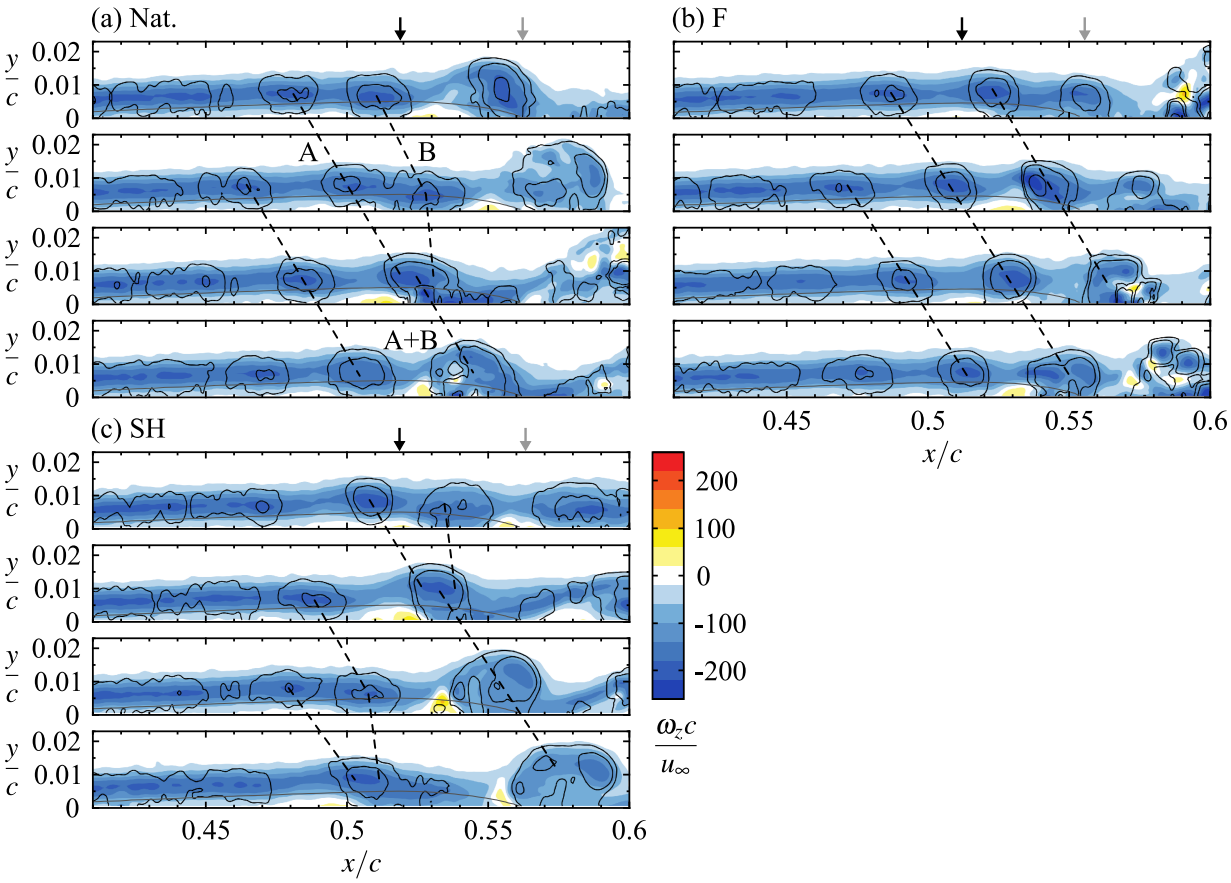

Figure 4.5: Sequences of instantaneous spanwise vorticity contours. Consecutive frames separated by $t_c^* = 3.8 \times 10^{-2}$. Solid black lines indicated λ_2 contours [88]. Solid grey lines mark the dividing streamlines. Dashed lines trace the same vortices. Black and grey arrows mark $\overline{x_h}/c$ and $\overline{x_r}/c$, respectively.

the flow at the fundamental frequency locks vortex shedding to the excitation frequency; evident from the significantly reduced variability in the convective velocity and streamwise wavelength of the shed structures. As such, vortex merging is difficult to identify through visual inspection and thus is speculated to be inhibited by the forcing applied at the fundamental frequency.

To quantify and compare the frequency content and streamwise growth of flow disturbances across the studied cases, spectra of wall-normal velocity fluctuations, $\phi_{v'v'}$, in the separated shear layer (along $y = \delta_1$) are computed. The results are presented in Figs. 4.6a–c, which are computed using Welch's method [245] by dividing signals into 7 windows containing 2^{11} points with 75% overlap, resulting in a non-dimensional frequency resolution of 0.04. Plotted alongside are spectra of surface pressure fluctuations, $\phi_{p'p'}$, (Figs. 4.6d–f), computed from signals divided into 255 windows each containing 2^{15} points (50% overlap), resulting in a resolution of $\Delta St_c = 0.03$. Surface pressure fluctuations have the demonstrated capability of capturing the development of hydrodynamic disturbances present within the flow [60], given disturbances reach sufficient amplitudes to produce measurable surface pressure fluctuations. Such is the case presented in Fig. 4.6, as the velocity and pressure spectra for any particular case provide

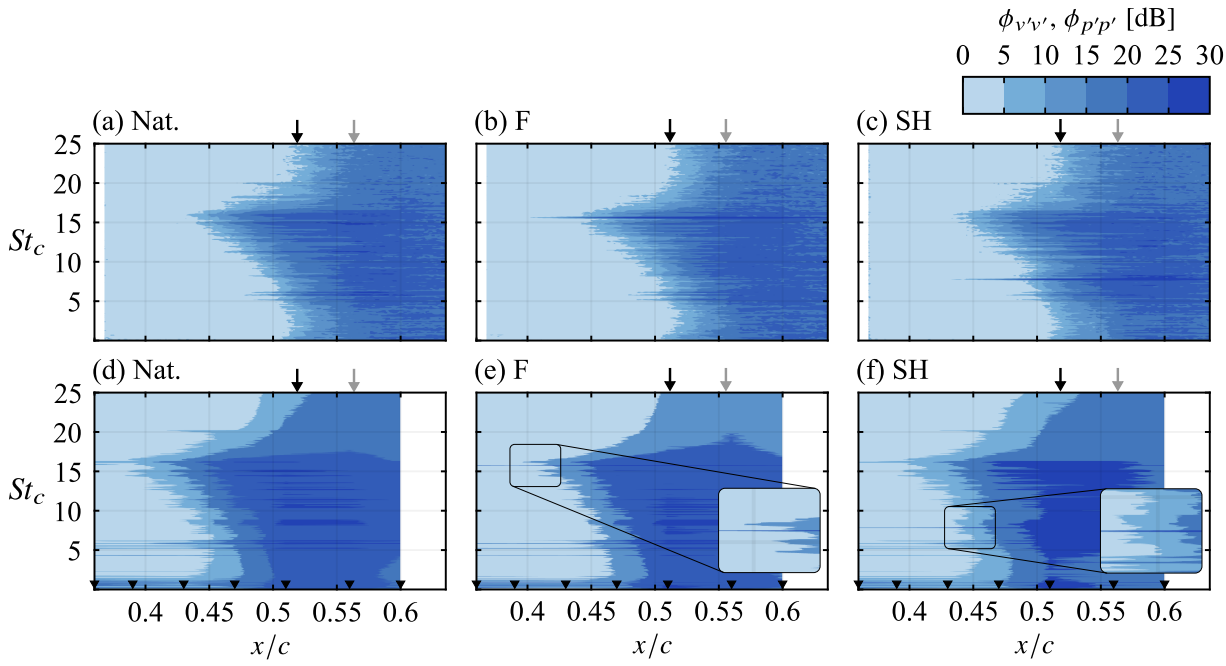

Figure 4.6: Frequency spectra of wall-normal velocity (a–c) and surface pressure (d–f) fluctuations. Velocity fluctuations measured within the separated shear layer ($y = \delta_1$). Pressure measurement points (microphone locations) indicated by arrow heads. Black and grey arrows mark $\overline{x_h}/c$ and $\overline{x_r}/c$, respectively.

largely similar descriptions of the streamwise disturbance development. Specifically, measurable streamwise amplification of disturbances begins downstream of separation primarily in a band centred on $St_{0_c} = 15.6$, followed by the redistribution of energy to a wide frequency range as a result of transition to turbulence. Notable differences between the velocity and pressure spectra include the earlier detection of disturbances in the pressure signals, which is a result of PIV's relatively high noise floor (Section B.2), and better resolved low frequency activity in the pressure measurements, which is a result of significantly longer sampling. The activity at $St < 2.5$ is due to low frequency environmental noise (fan blade passage, *etc.*) and is largely irrelevant to the investigated hydrodynamics. However, the activity associated with the test section standing wave, $St_{sw_c} \approx 6$, is significant, as it is detectable in both the pressure and velocity spectra for all cases. Therefore, this purely acoustic phenomenon results in the manifestation of velocity disturbances at the same frequency (Figs. 4.6a–c) and therefore serves to influence the flow development in some capacity. The extent of this effect and the relation to vortex merging is examined in Section 4.3.2.

The spectral results of the natural case (Figs. 4.6a and 4.6d) show that disturbances within a band of frequencies centred on St_{0_c} are amplified and undergo convective growth within $0.4 \lesssim x/c \lesssim 0.5$, *i.e.*, upstream of the mean maximum height location. At $\overline{x_h}/c$, the energy within the unstable frequency band has begun redistribution to a wider range of frequencies, consistent with the breakup of the rollers in the final stage of transition to turbulence observed in Fig. 4.5a. The spectra for the fundamental and subharmonic cases (Figs. 4.6b and 4.6e, and Figs. 4.6c and 4.6f) show no appreciable alterations to the natural band of amplified disturbances; while

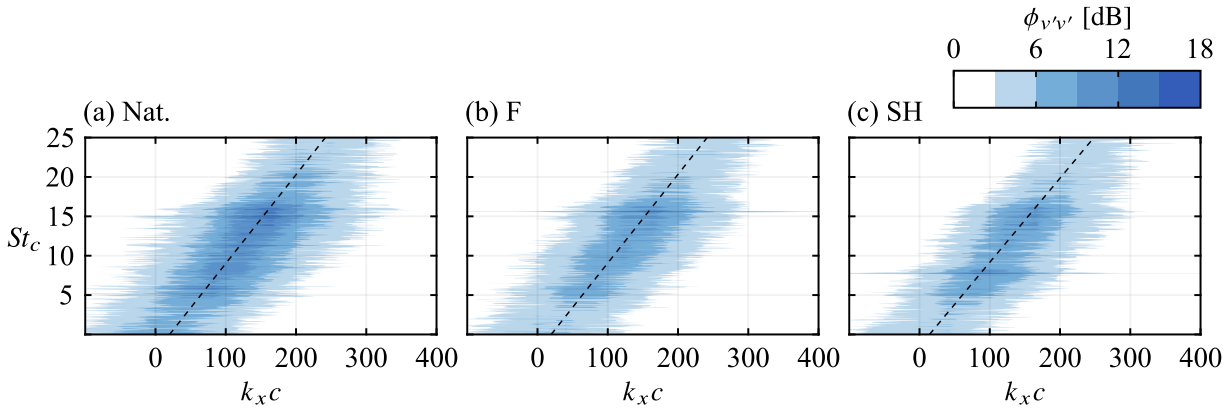

Figure 4.7: Wavenumber-frequency spectra of wall-normal velocity fluctuations. Velocity fluctuations measured within the separated shear layer ($y = \delta_1$). Dashed line is a linear fit estimate the convective ridge.

significant velocity fluctuations are detected at the respective forcing frequencies (*i.e.*, St_0 for the fundamental case, and $\frac{1}{2}St_{0_c}$ for the subharmonic case; see zoomed in region in Figs. 4.6e and 4.6f). Thus, each forcing technique is successful in promoting the growth of velocity disturbances at the frequency of the applied acoustics; indicating that there are sustained effects on the periodicity of the vortex shedding phenomena seen in Fig. 4.5.

Wavenumber-frequency spectra (Fig. 4.7) allow for the determination of the predominant disturbance wavenumber and convective velocity. For all cases, spectral energy is primarily concentrated along a line of constant slope, which is commonly referred to as the convective ridge [78]. Along this ridge, the disturbance wavenumber and frequency are related by their convective velocity, $u_{\text{con}} = 2\pi f/k_x$. For the natural case (Fig. 4.7a), the wavenumber and convective velocity corresponding to St_{0_c} are $k_x c = 158$ and $u_{\text{con}}/u_{\text{e}} = 0.52$, where the edge velocity is taken outside of the separated bubble ($u_e = 1.2u_\infty$ from Fig. 4.4). The obtained estimate for u_{con} agrees well with the range $0.3 \lesssim u_{\text{con}}/u_{\text{e}} \lesssim 0.6$ observed in previous investigations [20, 33, 190]. Figures 4.7b and 4.7c show that excitation at either the fundamental or subharmonic frequency concentrates spectral energy at the forcing frequency, while not appreciably altering the convective ridge. Estimating the convective velocities for these two cases yields $u_{\text{con}}/u_e = 0.52$ and 0.51, respectively, which closely matches the natural case. Therefore, consistent with the ascertainable convective velocities from the vortex traces in Fig. 4.5, neither forcing case affects the convective velocity of the periodic disturbances.

The PIV measurements from the top view configuration (Fig. 4.3b) allow for analysis of both streamwise and spanwise aspects of the flow development. For these measurements, the laser sheet was positioned such that it passed through the top halves of the shear layer vortices, thus allowing for their identification as periodic spanwise bands of high streamwise velocity in the planar images, which are visible throughout Fig. 4.8. For all cases, coherent and spanwise uniform structures are first identified at $x/c \approx 0.5$, which is consistent with where roll-up is observed in Fig. 4.5. At and beyond formation, significant spanwise undulations develop in the vortex filaments, which intensify as the structures convect downstream. This leads to the onset of the breakup to smaller scales seen for $x/c > 0.6$. The formation of spanwise uniform shear layer vortices is consistent

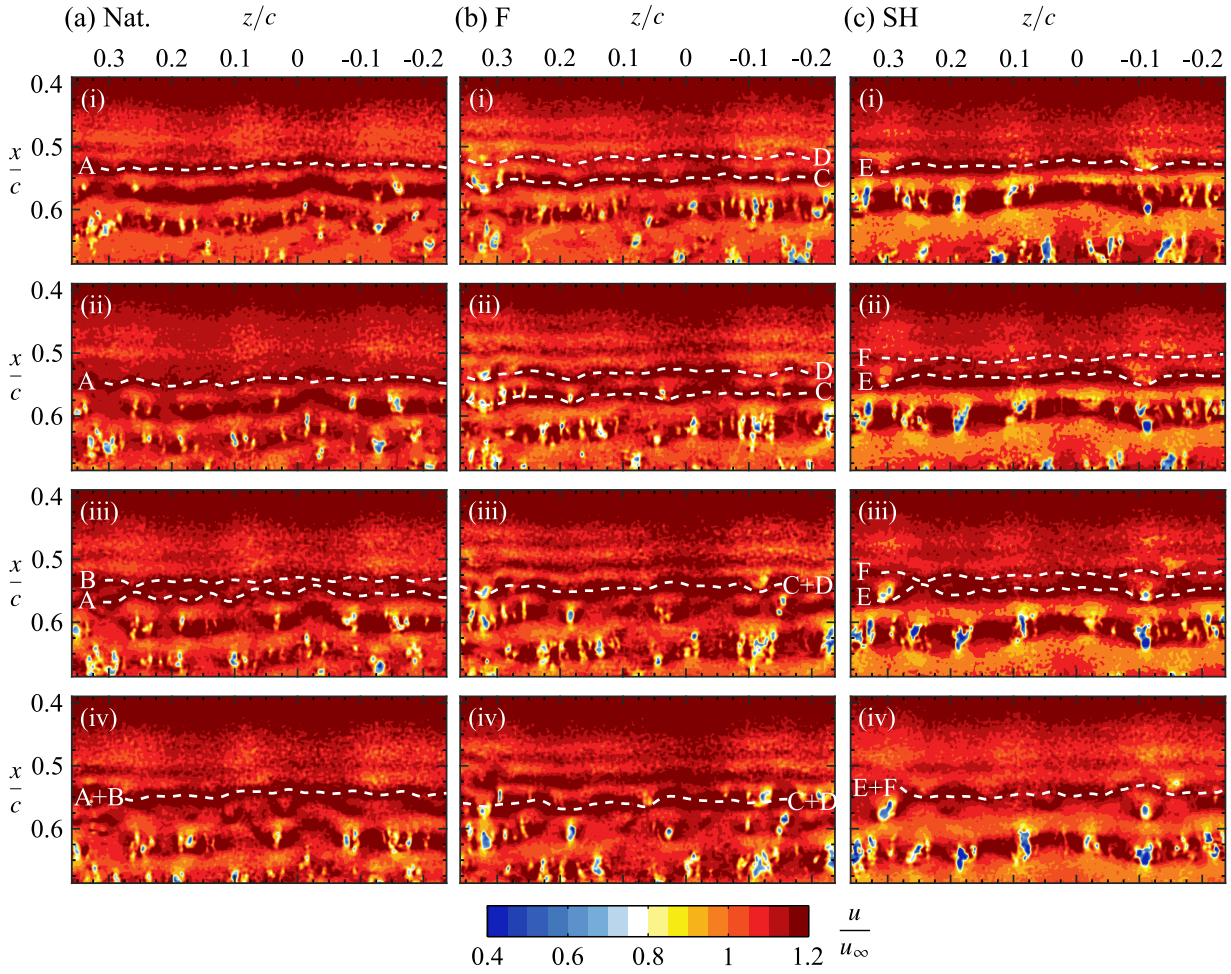

Figure 4.8: Sequences of instantaneous streamwise velocity contours. Flow is from top-to-bottom. Consecutive frames separated by $t_c^* = 2.5 \times 10^{-2}$. Dashed lines indicate smoothed spline fits to the centre of selected structures (labelled A–F).

with the observations of other similar investigations [92, 137, 170], which according to Michelis *et al.* [153] is an indication of the relative dominance of normal over oblique disturbance modes. Furthermore, the development of spanwise deformations leading to localized regions of vortex breakup is consistent with the vortex breakup mechanism for an LSB proposed by Kurelek *et al.* [113].

For each of the studied cases, exemplary merging events are depicted in the sequences presented in Figs. 4.8a–c. For example, Fig. 4.8c shows merging between two shear layer vortices, labelled as E and F, for the subharmonic excited flow. In Figs. 4.8c-i and 4.8c-ii, vortex E convects downstream while developing spanwise undulations, which are most notable at $z/c = -0.1$ and 0.3, as the vortex filament bulges forward in the streamwise direction. Concurrently, vortex F is formed and also develops spanwise undulations in Figs. 4.8c-ii and 4.8c-iii. The merging process between E and F begins to take place in Fig. 4.8c-iii, as the vortex filaments intertwine, while the structures do not merge at the locations where the streamwise forward bulges developed in E. The merged

structure, labelled E+F in Fig. 4.8c-iv, then continues to convect downstream while retaining two separate vortex filaments over some spanwise segments, *e.g.*, at $z/c \approx -0.1$ and 0.3. Overall, similar progressions are seen for the merging of structures A and B in the natural flow (Fig. 4.8a), and C and D in the flow excited at the fundamental frequency (Fig. 4.8b). In particular, the depicted merging events occur in a non-uniform spanwise manner, resulting in structures that are merged within some spanwise segments, *e.g.*, within $0.15 < z/c < 0.25$ and $0.05 < z/c < 0.15$ in Figs. 4.8a-iv and 4.8b-iv, respectively, while distinct segments of unmerged filaments persist at other locations, *e.g.*, at $z/c = 0.025$ and $z/c > 0.25$ in the same two figures. The three instances of vortex merging depicted here are representative of most merging events observed across the studied cases, and so the results demonstrate that vortex merging in a separation bubble occurs non-uniformly across the span, with the spanwise undulations that develop in the vortex filaments playing an intrinsic role in the process.

It should be noted that the spanwise wavelengths, λ_z, that develop in the vortex filaments exhibit significant cycle-to-cycle variations for all three cases. There variations are characterized in a statistical sense using a wavelet based analysis (Section 3.3.3), which is preferred over Fourier analysis due to the limited spanwise extent of the PIV field of view. From the top view PIV measurements, streamwise velocity fluctuating velocity signals are extracted at $x/c = 0.55$, smoothed using a spatial kernal of width $0.02c$, and wavelet coefficients are calculated using the Morlet wavelet [43]. For a given time instant, the predominant spanwise wavelength is estimated from the maximum wavelet coefficient, with the process repeated for all time realizations and statistical samples obtained as a result. The data are presented using histograms in Fig. 4.9, which show similar distributions of λ_z, each with a mean value of approximately $\overline{\lambda_z}/c = 0.15$ and predominant wavelengths concentrated within $0.04 \lesssim \lambda_z/c \lesssim 0.28$, which is in good agreement with the visualized structures in Fig. 4.8. Comparing these results with the predominant streamwise wavelength of the primary structures ($k_x c \approx 158 \Rightarrow \lambda_x/c \approx 0.04$, from Fig. 4.7), gives a ratio of wavelengths that ranges between $1 \lesssim \lambda_z/\lambda_x \lesssim 7$, which is consistent with the results of previous investigations [113, 137, 153]. While the undulations that develop in the vortex filaments play an intrinsic role in the merging process (Fig. 4.8), the lack of appreciable differences in the histograms across the three studied cases (Fig. 4.9) indicates that any effect the forcing may have on the vortex merging process does not manifest through modification of the spanwise wavelengths.

4.3.2 Vortex Merging

Section 4.3.1 provided anecdotal evidence of the fundamental and subharmonic forcing affecting the vortex merging process in the LSB. To substantiate these findings, wavelet analysis (Section 3.3.3) is employed to quantify vortex merging in the flow and the subsequent effect of forcing. This tool is preferred over traditional Fourier analysis since the merging phenomenon is localized in both time and space, while not necessarily being periodic in time. For each case examined, fluctuating wall-normal velocity signals are extracted at $y = \delta_1$ and the midpoint between the mean maximum height location and reattachment points ($x/c \approx 0.54$ for all cases), where most vortex merging events occur (Fig. 4.5). Wavelet coefficients, ψ, are then calculated using the Morlet wavelet [43] for all time instants and across the relevant spectrum of frequencies, with the results presented in Fig. 4.10. For the natural and fundamental cases, examination of Figs. 4.10a and 4.10b shows

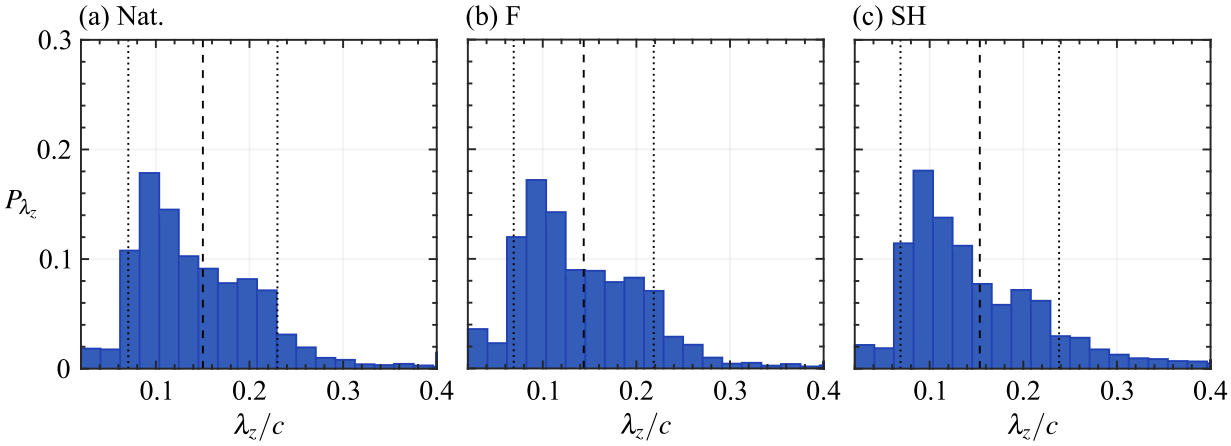

Figure 4.9: Spanwise wavelength probability distributions at $x/c = 0.55$. Dotted lines indicate standard deviation from the mean (dashed line).

that velocity fluctuations are predominantly concentrated within a band of frequencies centred at $St_{0_c} = 15.6$ over the entire recorded sequence. Instants at which significant wavelet coefficients exist ta $\frac{1}{2}St_{0_c} = 7.8$ do occur for these cases, however they are relatively infrequent compared to the subharmonic case (Fig. 4.10c), where activity at $\frac{1}{2}St_{0_c}$ is widespread over the entire measurement.

To link vortex merging with the trends observed in the wavelet coefficients, short segments that encompass the time periods corresponding to the vorticity sequences presented in Fig. 4.5 are shown in Figs. 4.10d–f. For the natural and subharmonic cases, when vortex merging is visually identified in Figs. 4.5a and 4.5c, the corresponding maximum wavelet coefficients (within the dotted intervals in Figs. 4.10a and 4.10c) are concentrated at $\frac{1}{2}St_{0_c}$. In contrast, the wavelet coefficients for the fundamental case (Fig. 4.10e) are confined to a relatively narrow band centred at St_{0_c}, which is consistent with the highly organized and periodic nature of the structures observed in Fig. 4.5b. Thus, the identification of local maxima in the wavelet coefficients at frequencies of interest can serve to identify instances at which vortex merging occurs, allowing for a quantitative comparison of the prevalence of the phenomenon between the three studied cases. It must be noted that, in particular for the natural case (Fig. 4.10d), significant low-frequency activity is detected at $St_{\mathrm{sw}_c} = 6$ in addition to $\frac{1}{2}St_{0_c}$. This activity is a result of the standing wave present in the test section (Fig. 4.2b), whose frequency is close to the subharmonic frequency. Therefore, it is possible that the standing wave serves to influence the flow, leading to merged structures with this characteristics frequency. For this reason, quantitative analysis of the results is performed for both $\frac{1}{2}St_{0_c}$ and St_{sw_c}, and the possible relation of the standing wave frequency to vortex merging is considered in detail later in this section.

The proposed method for vortex merging quantification involves identifying all local maxima in the wavelet coefficients at the frequencies of interest, namely, $\frac{1}{2}St_{0_c}$ and St_{sw_c}, within a non-dimensional frequency band of ± 0.1. Conditional filtering is applied, with a maximum only being retained if its magnitude exceed a signal-to-noise ratio of five and is greater than other maxima detected at $St_{0_c} \pm 0.1$ within a temporal window of width equal to twice the fundamental shedding period. The resulting detected maxima are indicated by the black markers in Figs. 4.10d–f. Estimates for the percentage of merged structures detected in the flow, R_{merg}, are made by taking

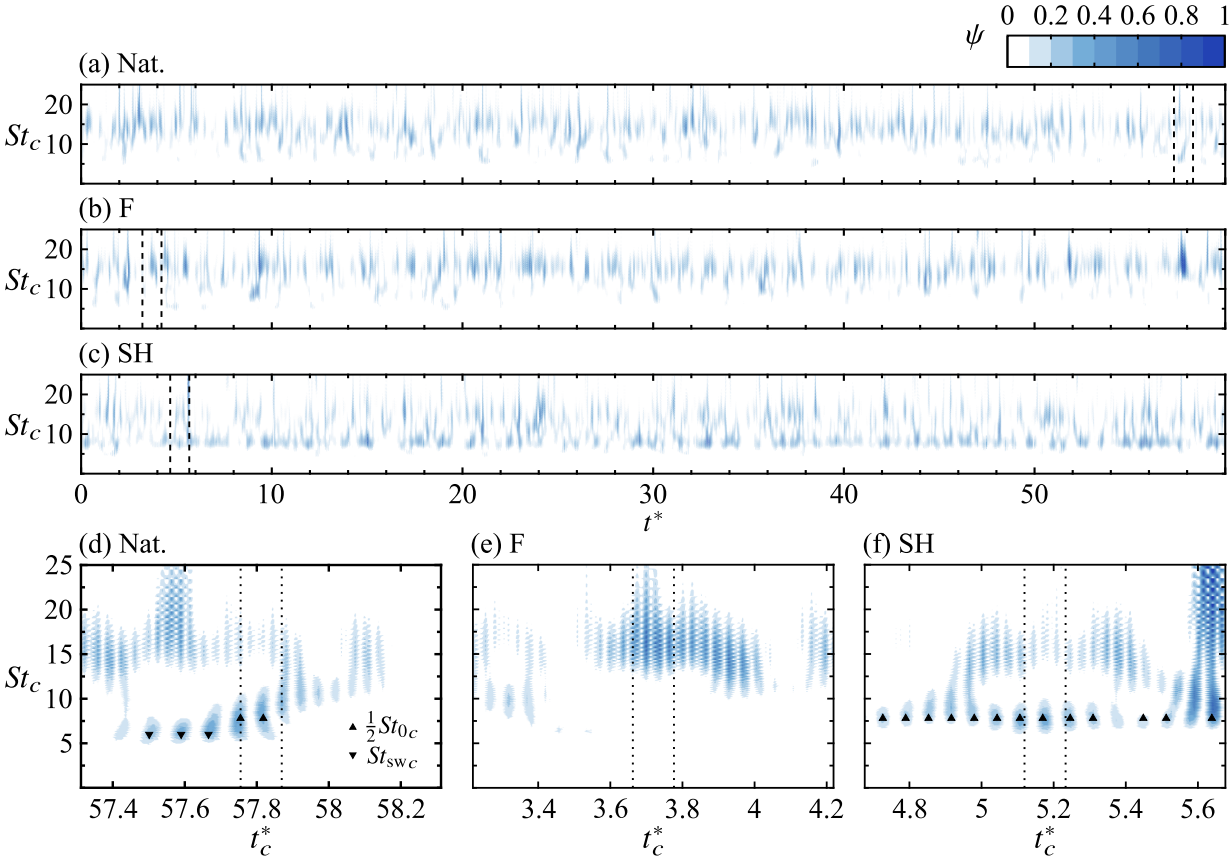

Figure 4.10: Wavelet coefficient contours computed from wall-normal velocity fluctuations sampled at $y = \delta_1$ and at the midpoint between $\overline{x_\mathrm{h}}$ and $\overline{x_\mathrm{r}}$. Dashed regions in (a)–(c) replotted in (d)–(f). Dotted regions in (d)–(f) correspond to intervals shown in Fig. 4.5. Markers denote local maxima identified at frequencies of interest.

the ratio of combined number of maxima detected at $\frac{1}{2}St_{0c}$ and $St_{\mathrm{sw}c}$ to an estimated number of primary structures shed during the measurement sample (1.32 s) at the fundamental shedding frequency, $St_{0c} = 15.6$ ($f_0 = 750$ Hz). Prior to evaluating all data sets, the proposed methodology was applied to a test signal (0.35 s long) extracted at $y = \delta_1$ and the midpoint between $\overline{x_\mathrm{h}}$ and $\overline{x_\mathrm{r}}$ for the subharmonic data set. Through a detailed manual inspection of the vorticity contours, it was determined that this test segment contained approximately 80 merging events, which the method was able to estimate within 4%. The method was then applied to the full data sets and at all streamwise positions, yielding the results shown in Fig. 4.11. The results are smoothed using a sliding spatial window ($0.01c$ width) and the indicated uncertainty bounds are determined based on the variability of the estimates within the smoothing window. Note that results are plotted up until the mean reattachment locations, where the uncertainty was found to sharply increase from approximately ±3% to over ±10% due to the onset of vortex breakdown (Fig. 4.5).

Figure 4.11 provides several key insights regarding the vortex merging process and the effects of forcing. Namely, for all cases, no merged structures are detected in the fore portion of the bubble ($x/c < 0.48$), indicating that all vortices are formed and shed at the fundamental frequency.

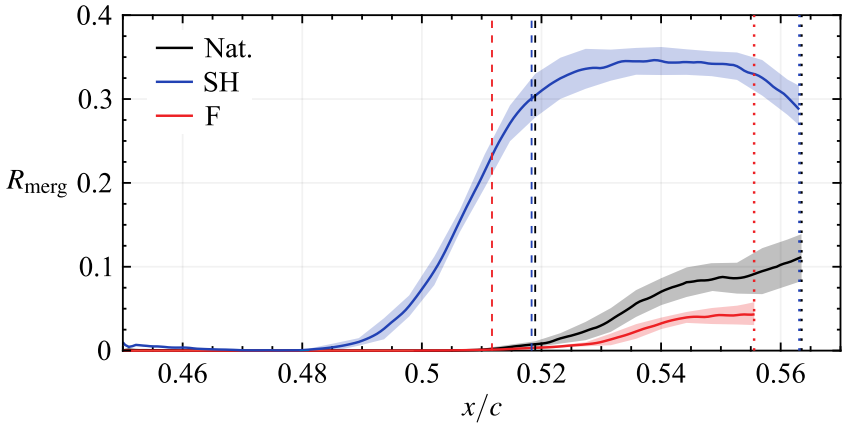

Figure 4.11: Ratio of detected merged structures to total number of shed primary structures determined using wavelet methodology (Fig. 4.10). Dashed and dotted lines (coloured according to legend) mark $\overline{x_{\text{h}}}/c$ and $\overline{x_{\text{r}}}/c$, respectively. Shaded regions (coloured according to legend) indicate uncertainty bounds.

Further downstream, all cases shown an eventual rise in the number of detected merged structures indicating the onset of merging, with the start of the region where R_{merg} plateaus indicating the location at which most merging events are completed. For the natural flow, the first merging events are detected at $x/c \approx 0.51$, followed gradual increases until R_{merg} plateaus to a value of 9% ± 3 at $x/c = 0.55$. Further downstream, R_{merg} begins to rise again, however, the changes are within the uncertainty of the estimates and may be a result of turbulent breakdown. The fundamental case shows a similar trend to the natural flow, with R_{merg} also peaking at approximately $x/c = 0.55$, but the maximum value is reduced to 4% ± 1. For the subharmonic forcing, the onset of vortex merging is seen at a much earlier streamwise position compared to the natural flow, followed by a sharper rise in the ratio of merged structures that begins to plateau at $x/c = 0.53$, attaining a value of 34% ± 2. Thus, supporting the analysis of the time-resolved flow development and spectra of flow disturbances (Figs. 4.5 and 4.6, respectively), these results conclusively show vortex merging occurs naturally in the studied LSB, while forcing at the subharmonic and fundamental frequencies promotes and inhibits merging, respectively. Such observations are in agreement with those made for free shear layers [72, 81]. The results of this investigation clearly indicate that forcing specifically affects the streamwise position at which merging events take place and the total percentage of vortices that undergo merging.

From the peak ratio of detected merged structures determined from Fig. 4.11, it is possible to estimate the ratio of primary structures that are involved in vortex merging for a given case. For example, when the flow is forced subharmonically, at $x/c = 0.54$ the merged vortices account for 34% of the total number of shed primary vortices. Since merged structures are formed by two primary vortices, this implies that 68% of all primary vortices undergo merging. Similarly, the percentage of primary structures engaged in merging is 18% and 8% for the natural and fundamental cases, respectively. In the investigation of Lambert & Yarusevych [115], they found that up to 15% of the total number of shed vortices merge in an unforced LSB formed over the same NACA 0018 profile at a comparable Reynolds number and angle of attack, which agrees

well with the 18% reported here.

It is now possible to clarify the relationship between vortex merging and separation bubble topology given that the effects of forcing on vortex merging have been established. In free shear layers, it is well documented that the promotion of vortex merging through subharmonic forcing lends to an increase of momentum transfer across the layer [72]. For separation bubbles, it is generally accepted that mean reattachment is induced by the exchange of momentum from the outer flow to the wall by the shear layer vortices [134, 260]. Therefore, one might expect a promotion of vortex merging in an LSB to lead to earlier mean reattachment. However, the findings of this investigation clear show that this is not the case, as the percentage of primary structures that merge in the aft portion of the bubble increases significantly from 18% in the natural flow to 68% when forced subharmonically, yet the mean reattachment location does change within the uncertainty of the PIV measurements (Fig. 4.4). This indicates that the enhancement of momentum exchange due to the increase in merged vortex circulation [35, 148] is balanced by the reduced frequency of the structures, producing a comparable mean flux of momentum to that produced by unmerged primary structures. Consequently, the mean bubble position, length, and maximum height remain largely unchanged (Fig. 4.4).

The present results have established that, similar to free shear layers, targeted forcing applied at the subharmonic and fundamental frequencies promotes and inhibits vortex merging in an LSB, respectively. Further parallels can be drawn with free shear layers, as Ho & Huang [72] demonstrated that periodic vortex merging coincides with the growth of perturbation energy at the subharmonic frequency for acoustically forced free shear layers. A similar analysis is performed here, where modal amplitudes for wall-normal velocity perturbations of a given frequency, $\hat{v}'$, are determined by integrating the frequency spectra within an St_c band of width 1. The streamwise evolution of the modes in the separated shear layer ($y = \delta_1$) is shown in Fig. 4.12, where St_{0c}, $\frac{1}{2}St_{0c}$, and $St_{\mathrm{sw}c}$ are the frequencies of interest. When left to develop naturally (Fig. 4.12a), exponential growth is detected in the St_{0c} mode within $0.42 < x/c < 0.48$, followed by a reducing growth rate and eventual saturation by $x/c \approx 0.5$, which lies upstream of the mean maximum height location and coincides with the roll-up region, *i.e.*, where coherent vortices are first formed. At the streamwise location where the fundamental mode begins to deviate from an exponential growth rate ($x/c \approx 0.48$), growth is detected in the subharmonic and standing wave modes, which precedes the detection of vortex merging onset seen in Fig. 4.11. A similar progression is seen for the fundamental case (Fig. 4.12b), namely exponential growth in the fundamental mode followed by growth in other modes at a streamwise position slightly upstream of where vortex merging is first detected; however, here earlier detectable growth in St_{0c} is observed as a result of forcing the fundamental mode.

In contrast to the natural and fundamental cases, when the flow is forced at the subharmonic frequency (Fig. 4.12c), both the St_{0c} and $\frac{1}{2}St_{0c}$ modes undergo similar initial amplification. The fundamental mode then saturates at approximately the same streamwise location as that of the natural case, while the subharmonic mode continues to grow, reaching its peak at approximately $x/c = 0.55$. The streamwise location where this maximum is reached approximately coincides with where vortex merging is observed in Fig. 4.5c and where R_{merg} plateaus (Fig. 4.11), thus supporting the assertion of Ho & Huang [72]. In fact, the trends reported in Fig. 4.12c agree well with those reported by Ho & Huang (*cf.* their Figs. 15 and 16). However, one distinction

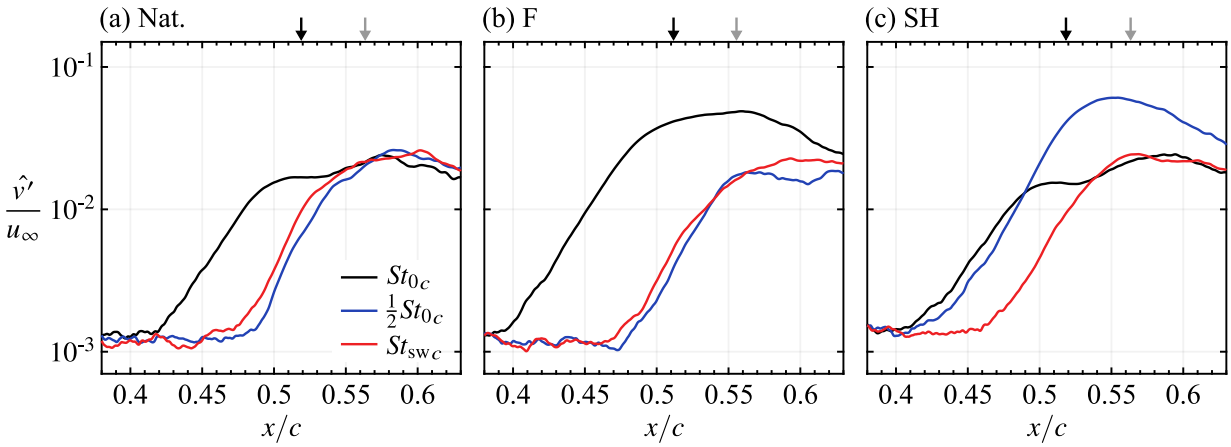

Figure 4.12: Streamwise growth of wall-normal velocity perturbation modes within the separated shear layer ($y = \delta_1$). Black and grey arrows mark $\overline{x_\mathrm{h}}/c$ and $\overline{x_\mathrm{r}}/c$, respectively.

must be highlighted here, as a secondary resonance mechanism has been proposed for free shear layers [102, 160]. This mechanism dictates that the growth in the subharmonic mode follows the saturation of the fundamental mode, with subharmonic growth occurring as a result of energy cascading from the fundamental mode, even when forced at the subharmonic frequency. This appears not the case for the studied LSB, as here the subharmonic forcing is capable of affecting the intended mode directly without a secondary transfer mechanism.

Analysis of the LSB coherent structures and their merging characteristics is furthered through proper orthogonal decomposition analysis (Section 3.3.2), which is performed using the snapshot method of Sirovich [223]. Figure 4.13 presents the relative, E_R, and cumulative, E_C, energy distributions across the first 20 modes, with m indicating mode number. As is typically seen for flows involving large-scale, propagating coherent structures [124, 241, 244, 260], a significant portion of the total turbulent kinetic energy is captured within a small number of modes (approximately 71–78% in the first 20 modes, as seen in Fig. 4.13b), and the most energetic modes are grouped into pairs of similar energy levels (*i.e.*, modes 1 and 2, and modes 3 and 4 in Fig. 4.13a). The paired nature of the modes is confirmed through visual inspection of their spatial distribution, which show a distinct phase offset of $\pi/2$ between pairs. Therefore, every other mode is plotted in terms of its wall-normal component, $\gamma_v^{(m)}$, in Fig. 4.14. For all cases, the most energetic mode pair features a distinct periodic spatial structure that is characterized by a streamwise wavelength of approximately double the primary wavelength of the shear layer vortices in the natural flow ($k_x c = 158 \Rightarrow \lambda_x/c = 0.04$, from Fig. 4.7a). This, in addition to these structures being found in the aft portion of the bubble, indicates that these modes are associated with the merged shear layer vortices. The unmerged, primary structures are captured by the higher mode pairs (modes 3 and 4 for the natural and fundamental cases, and modes 5 and 6 for all cases), as these structures have wavelength of approximately $0.04c$ and form further upstream. Based on these results, a few key observations can be made. First, consistent with the effect of these two types of forcing on vortex merging, forcing at the subharmonic frequency increases the relative energy content of the modes associated with the merged structures, while the opposite effect is produced by forcing at the fundamental frequency. It must be noted that a commensurate increase in the energy levels of

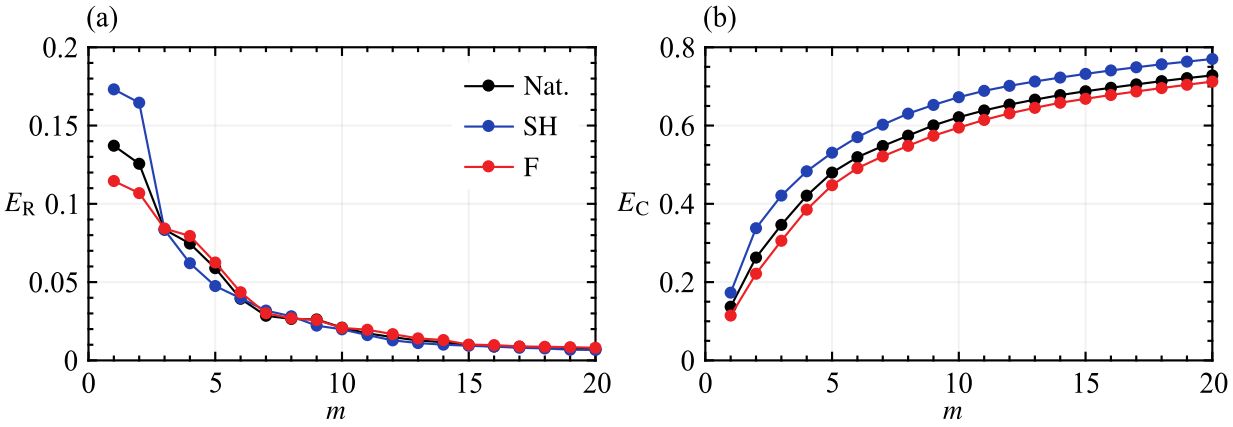

Figure 4.13: POD (a) relative and (b) cumulative modal energy distributions.

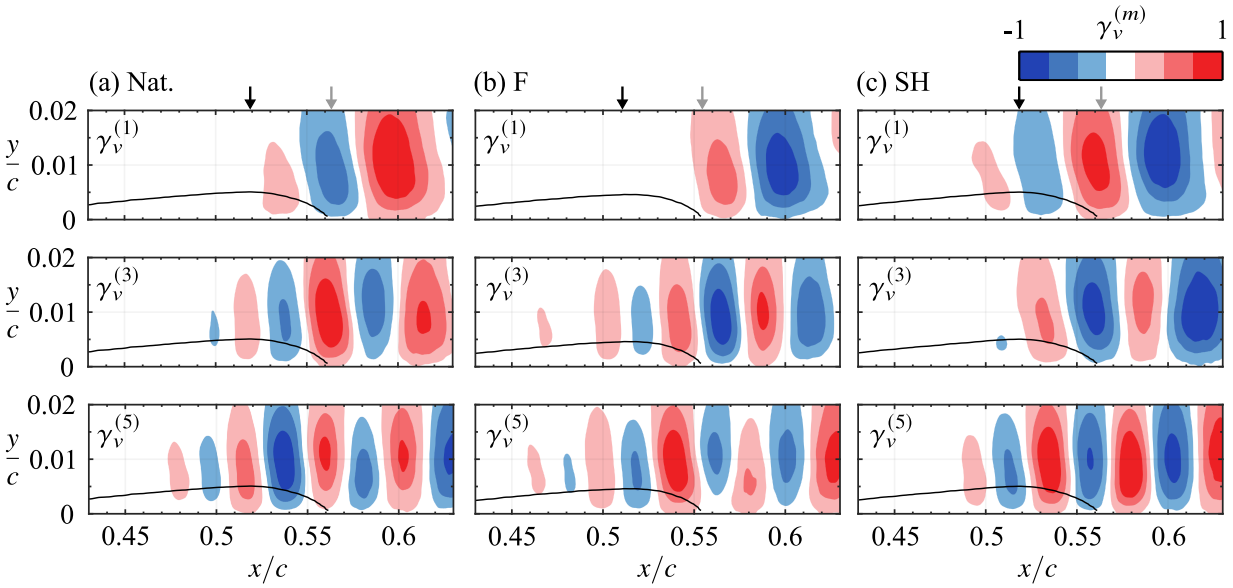

Figure 4.14: Wall-normal component of normalized POD spatial modes. Solid lines mark the dividing streamlines. Black and grey arrows mark $\overline{x_h}/c$ and $\overline{x_r}/c$, respectively.

modes 3–6 is not seen when forced at the fundamental frequency (Fig. 4.13a), which has been previously reported [260]. This is likely the consequence of employing a spatial decomposition technique, resulting in modes with the same frequency content being split across several modes. Thus, when the flow is forced small increases in the energy levels of many modes are observed, rather than a large increase for a single mode pair.

Further insight into the vortex merging process is gained through examination of the spectra of the POD temporal coefficients, $b^{(m)}$, presented in Fig. 4.15. Beginning with the subharmonic case (Fig. 4.15c), the results reveal that the most significant frequency content of the modes associated with the merged structures (*e.g.*, $b^{(1)}$ and $b^{(3)}$) is found at $\frac{1}{2}St_{0_c}$, while the temporal coefficients for mode 5 show periodicity over a relatively broad range of frequencies centred at St_{0_c}. Thus, the

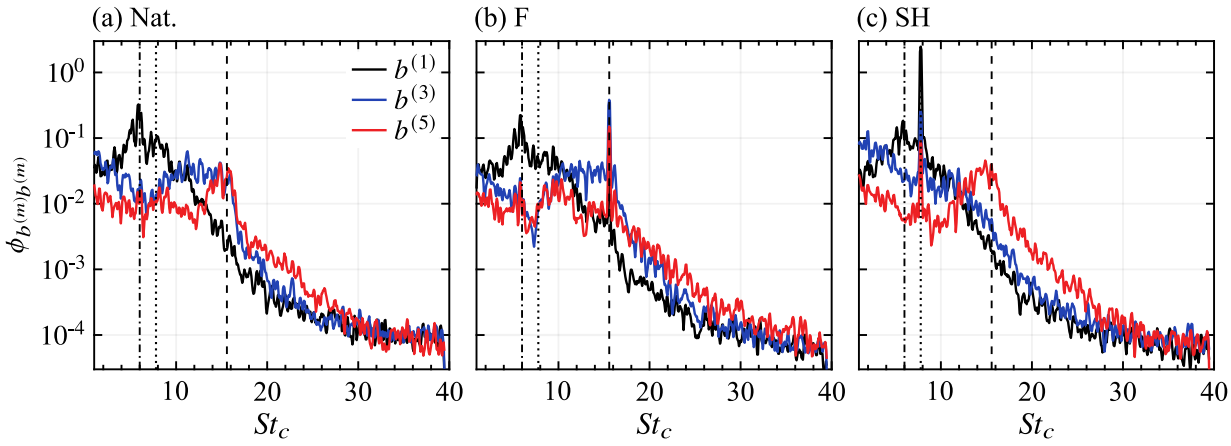

Figure 4.15: Frequency spectra of POD temporal coefficients. Dashed, dotted, and dash-dotted lines mark St_{0_c}, $\frac{1}{2}St_{0_c}$, and $St_{\mathrm{sw}c}$, respectively.

previous analysis is confirmed, associating these modes with the merged and unmerged structures, respectively. For the natural and fundamental cases, (Figs. 4.15a and 4.15b), as expected, activity at St_{0_c} is found for modes 3 and 5, while for mode 1 elevated energy levels are found at both $\frac{1}{2}St_{0_c}$ and $St_{\mathrm{sw}c}$. Therefore, these results support the earlier conjecture that the standing wave serve to influence the flow in a subharmonic fashion, leading to the formation of merged structures with this characteristic frequency. That being said, an important distinction must be highlighted. Namely vortex merging does not solely result due to the presence of the standing wave, but rather the merging process is influenced by the presence of the standing wave, resulting in merged structures with characteristic frequencies that match either the subharmonic or standing wave frequencies, as revealed by both the wavelet (Fig. 4.10) and POD analysis (Fig. 4.15).

A statistical characterization of vortex merging was carried out using the side view PIV measurements taken at $z/c = 0$, while results from the top view PIV measurements indicate that process occurs in a spanwise non-uniform manner (Fig. 4.8). Therefore, it is necessary to statistically characterize the spanwise behaviour of vortex merging to evaluate if the results at $z/c = 0$ are representative of those over the full spanwise domain. This is carried out through an assessment of the spanwise variation in the ratio of detected merged structures over a range of streamwise location using the previously applied wavelet methodology (Fig. 4.10). The approach is unchanged from that previously described, save for the analysis is now applied to u' signals from the top view measurements. The signals are extracted across the span and at streamwise locations within $0.545 \leq x/c \leq 0.555$ for all cases. The results at each spanwise position are then averaged to give a single curve that is representative of the region where R_{merg} plateaus in Fig. 4.11. The results are presented in Fig. 4.16, which are smoothed using a sliding spatial window ($0.03c$ in width) and the indicated uncertainty bounds are determined based on the variability within the smoothing window. Evaluating R_{merg} at $z/c = 0$ for the natural, fundamental, and subharmonic cases gives 7.5% ± 2, 3.5% ± 4, and 30% ± 4, respectively, all of which are in good agreement with the values determined from the side view analysis (9%, 4%, and 34%).

It should be noted that in applying the wavelet detection method to the top view data, no attempt is made to correlate merging at a given spanwise location with other events occurring

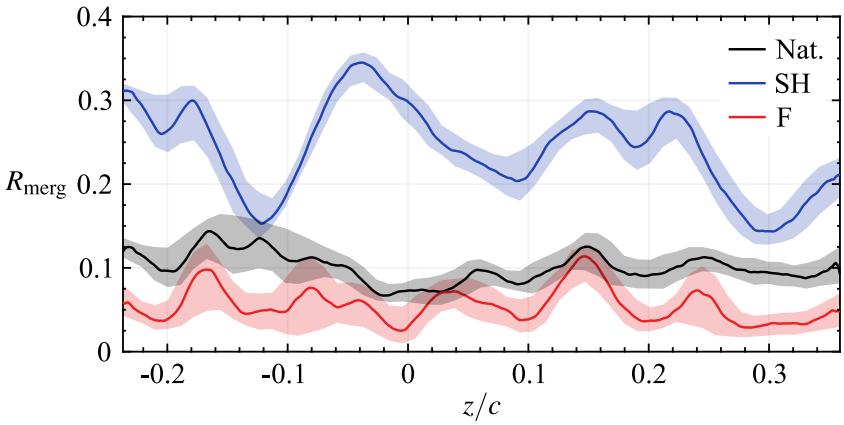

Figure 4.16: Spanwise variation in ratio of detected merged structures to total number of shed primary structures using wavelet methodology (Fig. 4.10). Method is evaluated at streamwise locations within $0.545 \leq x/c \leq 0.555$, with results averaged to produce a single curve representative of the region where R_{merg} plateaus in Fig. 4.10. Shaded regions (coloured according to legend) indicate uncertainty bounds.

at the same instant in time. Thus, the results in Fig. 4.16 do not give an indication toward the spanwise uniformity of any given merging event, but rather give a measure of the overall variability in the prevalence of merging over the entire span, while also revealing statistical tendencies for merging events toward particular spanwise locations. Beginning with the natural case, the ratio of detected merged structures varies within $6.5\% \leq R_{\text{merg}} \leq 14.5\%$ over the spanwise extent of the measurement domain. Discernible peaks in R_{merg} can be identified, *e.g.*, at $z/c = -0.16$, 0.15, and 0.25; however, the peak values fall well within the uncertainty bounds. The prevalence of merging events toward particular spanwise locations becomes clearer for the two forcing cases, where peaks in R_{merg} are found, with some at the same spanwise locations (*e.g.*, $z/c = -0.16$, 0.15, and 0.25). The most pronounced variability is observed for the subharmonic case, where the locations of the most prominent valleys in Fig. 4.16 (*e.g.*, $z/c = -0.12$ and 0.3) correspond to locations in Fig. 4.8c where merging between vortices E and F is delayed. This indicates that local vortex merging tends to occur more often in certain flow regions, where in other regions merging is more likely to be delayed and may not complete before the onset of turbulent breakdown. In the experiment, careful attention was paid to the model and facility to prevent any spanwise modulation of the flow, and the fact that the number and location of the peaks and valleys in Fig. 4.16 differ across the cases suggests that the observed spanwise non-uniformity in the merging process is likely linked to LSB dynamics. Nevertheless, across the studied cases, it is apparent that there is significant variability in the prevalence of vortex merging across the span, with the ratio of detected merged structures varying by as much as 50% of the midspan value.

4.3.3 Three-Dimensional Features

In this chapter, the results presented thus far have been restricted to planar, two-dimensional evaluations of a flow in which significant three-dimensional features develop, with the most

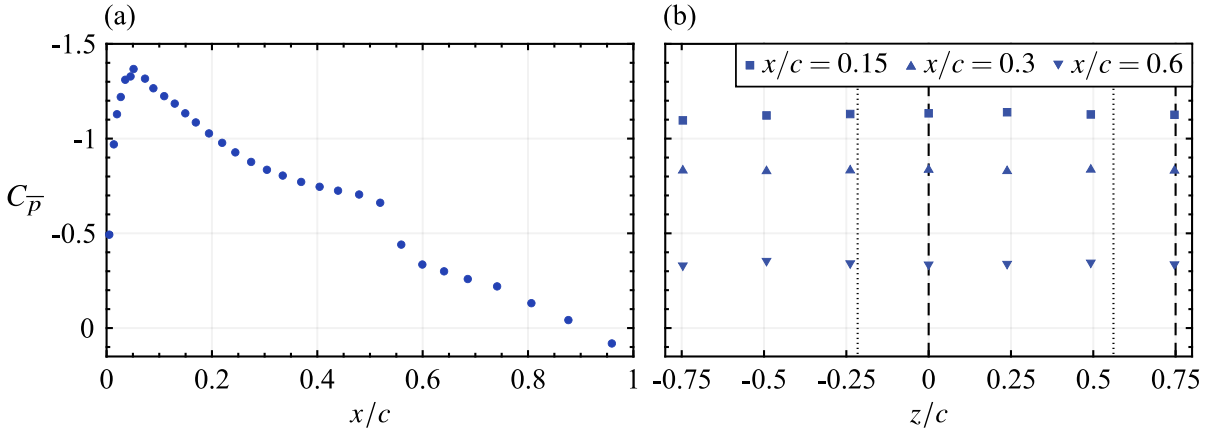

Figure 4.17: Mean static pressure on the suction surface for the natural case at (a) the midspan plane and (b) across the span at three streamwise position. Measurement uncertainty is given by the marker size. Dashed and dotted lines indicate spanwise extents of the scanning PIV measurement volume for the side and top view configurations, respectively.

notable features relating to the primary shear layer vortices (*e.g.*, Fig. 4.8). Therefore, the analysis now shifts to the examination of the three-dimensional flow development in an LSB, made possible through volumetric reconstructions of the flow field through scanning, phase-locked PIV measurements. The natural and fundamental forcing cases are focused on, with the relatively low forcing amplitude of the latter case leaving the base flow largely unmodified (Fig. 4.4), while also enabling three-dimensional reconstructions of the vortex dynamics through phase-locking.

Mean static pressure distributions, $C_{\overline{p}}$, on the airfoil suction side are plotted in Fig. 4.17 for the natural case. The streamwise distribution at the midspan plane (Fig. 4.17a) agree well with the time-resolved PIV measurements (Fig. 4.4), as the pressure measurements show the presence of the LSB within the region $0.3 \lesssim x/c \lesssim 0.6$, as marked by a pressure plateau resulting from flow separation, followed by a region of rapid pressure recovery due to the flow reattachment in the mean sense [172, 232]. Spanwise pressure distributions are also plotted (Fig. 4.17b), with data available at streamwise locations well upstream of the bubble ($x/c = 0.15$), and near the mean separation and reattachment locations ($x/c = 0.3$ and 0.6, respectively). Across all streamwise locations, the spanwise pressure data show good uniformity over the entire domain (±4%), and in particular within the region of the scanning PIV measurements (±1.5%). Thus, the LSB mean topology is expected to be relatively two-dimensional.

Contours of mean streamwise velocity from the scanning PIV measurements in x-y planes (Fig. 4.3a) are plotted in Fig. 4.18 at multiple spanwise locations. As was performed for the time-resolved measurements (Fig. 4.4), the dividing streamlines are identified, along with the mean separation, maximum bubble height, and reattachment locations. Comparisons between the LSB characteristics from the time-resolved and scanning PIV measurements are favourable for both cases, with the values summarized in Table 4.2. For the natural case, at the midspan ($z/c = 0$) the mean separation and reattachment points are estimated as $\overline{x_s}/c = 0.38 \pm 0.03$ and $\overline{x_r}/c = 0.58 \pm 0.01$, respectively, while the maximum height is found to be $\overline{y_h}/c = 6 \times 10^{-3} \pm 9 \times 10^{-4}$ at $\overline{x_h}/c = 0.52 \pm 0.01$. Thus, the length-to-height ratio of the LSB at the midspan is $\overline{L}/\overline{y_h} = 37 \pm 5$.

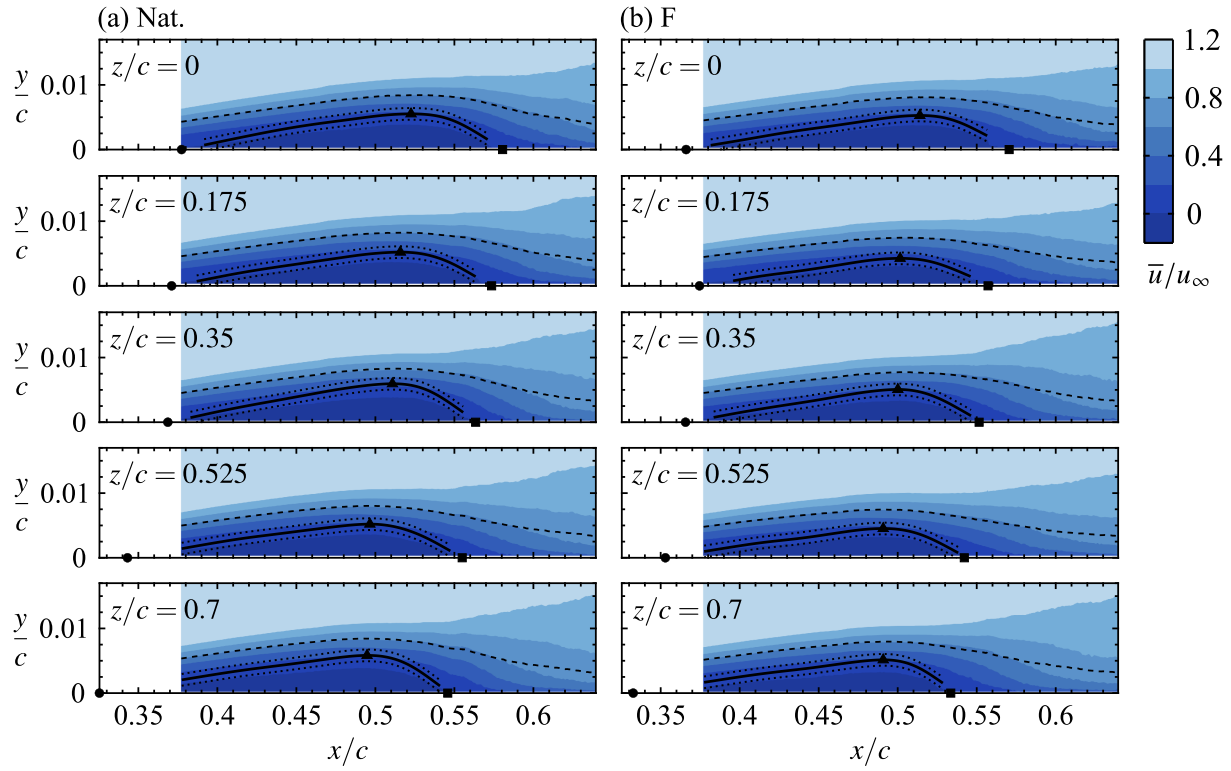

Figure 4.18: Contours of mean streamwise velocity at selected spanwise locations. Solid lines mark the dividing streamlines, whose uncertainty bounds are indicated by the dotted lines. Circle, triangle, and square markers denoted estimated mean separation, maximum height, and reattachment points, respectively. Dashed lines mark displacement thickness.

The results in Fig. 4.18a, in addition to those in Fig. 4.19, where $\overline{x_s}$, $\overline{x_h}$, and $\overline{x_r}$ are plotted over the entire investigated span, indicate that the mean topology of the LSB is relatively two-dimensional. In particular, the length-to-height ratio of the natural LSB over the span falls within the relatively narrow range $\overline{L}/\overline{y_h} = 38 \pm 5$, with the variance primarily driven by the relatively high uncertainty associated with the separation point (Fig. 4.19a), which arises as a consequence of extrapolating outside of the measurement domain (Fig. 4.18a).

For the fundamental case, the results in Figs. 4.18b and 4.19b reveal that the excitation causes minor changes in the LSB topology, as was seen previously (Fig. 4.4). Specifically, the changes in separation consistently fall within the uncertainty bounds across the span, while minor upstream shifts in the maximum bubble height and reattachment locations are apparent. Upstream shifts in these locations when subjected to periodic forcing are expected based on previous findings [151, 260], however, it is reinforced that these shifts are relatively minor, with $\overline{x_h}$ and $\overline{x_r}$ shifting upstream by on average 4% and 6% of the length of the natural LSB, respectively. Furthermore, the spanwise-averaged length-to-height ratio of the excited LSB is found to be 41 ± 4.7, thus closely matching the natural case (38 ± 5). It is of particular significance that the excitation does not alter the mean two-dimensionality and provides an LSB that is topologically similar to the natural case, while also providing the means for phase-averaging.

Table 4.2: Comparison of LSB characteristics from time-resolved and scanning PIV measurements at the midspan plane.

Case	Parameter	Time-Resolved PIV	Scanning PIV
Nat.	$\overline{x_s}/c$	0.35 ± 0.05	0.38 ± 0.03
	$\overline{x_h}/c$	0.52 ± 0.01	0.52 ± 0.01
	$\overline{x_r}/c$	0.56 ± 0.01	0.58 ± 0.01
F	$\overline{x_s}/c$	0.36 ± 0.05	0.36 ± 0.03
	$\overline{x_h}/c$	0.51 ± 0.01	0.51 ± 0.01
	$\overline{x_r}/c$	0.56 ± 0.01	0.57 ± 0.01

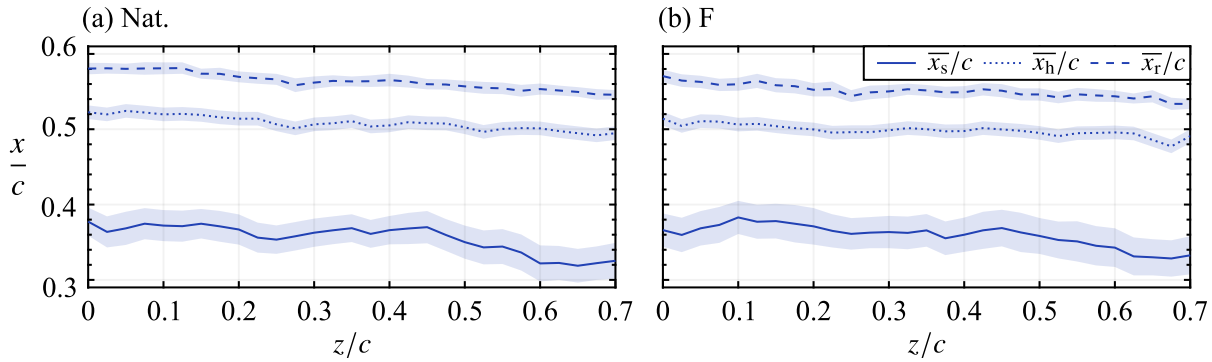

Figure 4.19: Spanwise topology of mean separation bubble characteristics. Shaded regions indicate uncertainty bounds.

While the topology of the LSB is relatively two-dimensional, it is apparent from Figs. 4.18 and 4.19 that there is an upstream shift in the bubble position with increasing z for both cases. When expressed as the average of the linear trends over z in $\overline{x_s}$, $\overline{x_h}$, and $\overline{x_r}$, the upstream shift in bubble position over the spanwise distance of $0.7c$ is $0.038c$ and $0.030c$ (5.5% and 4.2% of $0.7c$) for the natural and fundamental cases, respectively. These values are relatively minor and are attributed to inevitable minor imperfections in the experiment (*e.g.*, incoming free-stream non-uniformity and/or airfoil misalignment), which fall within the uncertainty of the spanwise pressure measurements (±1% of the free-stream dynamic pressure, q_∞, see Fig. 4.17b).

From Fig. 4.18, the maximum reported reverse flow within the LSB is 7.5% and 6.0% (with respect to the local edge velocity) for the natural and fundamental cases, respectively. While these values are lower than the threshold for the possible onset of absolute disturbance growth (15 to 20% of u_e) reported by Alam & Sandham [2], the natural case exceeds the minimum threshold of 7% for the onset of global instability reported by Rodríguez & Gennaro [200] and Rodríguez *et al.* [201]. This instability is characterized by spanwise variations in the mean topology of the LSB, leading to spanwise varied disturbances with peaks and valleys that align with spanwise locations of higher and lesser reverse flow, respectively (see Fig. 5 in Ref. [200]). Here, no significant spanwise variability in the reverse flow is observed (Fig. 4.18), suggesting that the investigated LSB is not subject to the global instability discussed in Refs. [200, 201]. What's more, analysis of

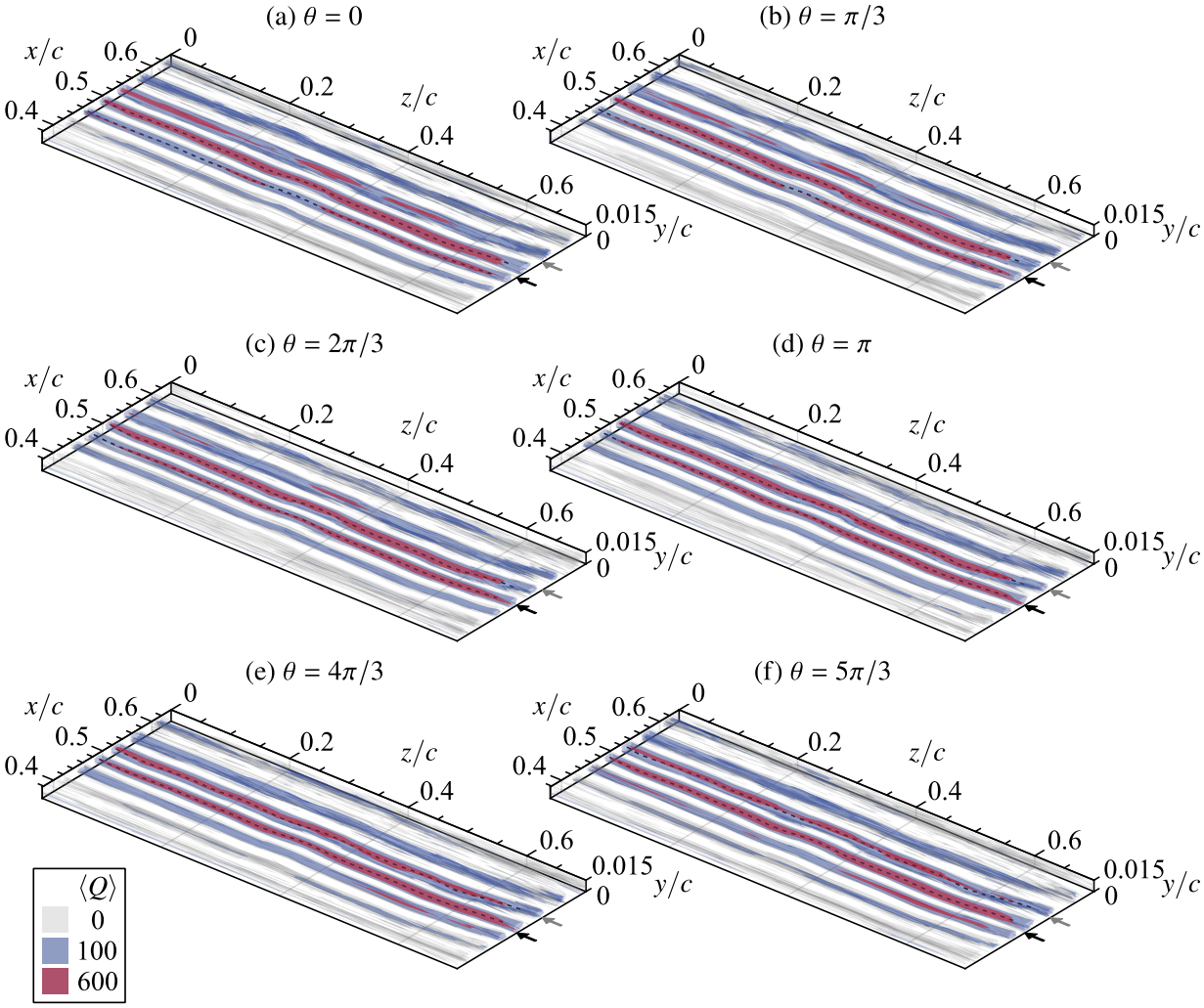

Figure 4.20: Sequence of phase-averaged Q-criterion [84] for the fundamental case. Dashed lines indicate smoothed spline fits to the core of selected structures. Black and grey arrows mark spanwise-averaged $\overline{x_h}/c$ and $\overline{x_r}/c$, respectively.

the disturbance development for these two cases in Section 4.3.1 (Figs. 4.6 and 4.7) established that disturbance growth is entirely convective, which points toward a Kelvin-Helmholtz type instability of the shear layer [20, 135, 243]. Thus, no effect on the three-dimensionality of the LSB and its coherent structures are expected on account of a local absolute instability or a global instability.

The three-dimensional development of coherent structures is examined in Fig. 4.20, where phase-averaged results measured using the side view PIV configuration (Fig. 4.3a) are shown for several phases in the fundamental forcing cycle. Iso-surfaces of the Q-criterion [84] are used to identify the spanwise vortices formed as a result of the shear layer roll-up in the LSB (Fig. 4.5b). Throughout Fig. 4.20, cores of selected structures are identified in the aft portion of the bubble (from just upstream of $\overline{x_h}/c$ to $\overline{x_r}/c$) via smoothing spline fits to detect local maxima in $\langle Q \rangle$. For convenience, these are plotted in Fig. 4.21, which includes phases not depicted in Fig. 4.20.

The results in Fig. 4.20 show strongly two-dimensional, spanwise-oriented vortices that form

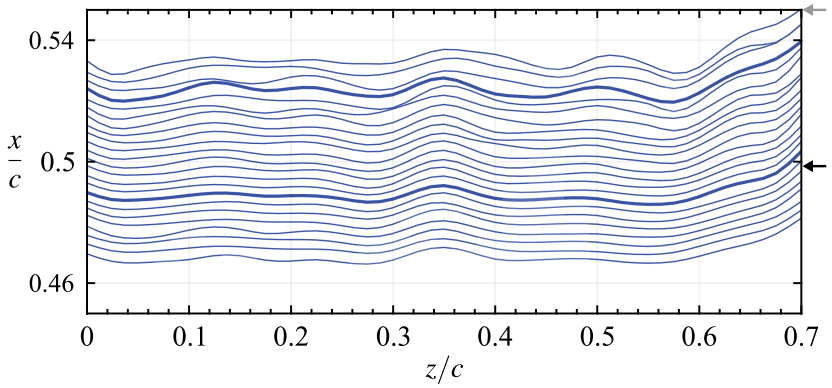

Figure 4.21: Identified vortex cores (Fig. 4.20) for all recorded phases. Thick lines indicate cores identified for $\theta = 4\pi/3$. Black and grey arrows mark spanwise-averaged $\overline{x_\mathrm{h}}/c$ and $\overline{x_\mathrm{r}}/c$, respectively.

upstream of the mean maximum bubble height location. These structures maintain a strong spanwise coherence up until the mean reattachment location, beyond which coherence begins to degrade on account of the breakdown to turbulence and the associated redistribution of energy to all other frequencies (Fig. 4.6b). The characteristics of the shear layer vortices captured here are consistent with those reported for convectively unstable LSBs in low free-stream turbulence environments [123, 144, 170]. Here, the roll-up and initial shedding of the vortices arising from the convective amplification of perturbations in the shear layer is spanwise uniform, with the onset to three-dimensionality following past the location of maximum bubble height. The necessary conditions for this to take place is the absence of both local absolute and global instabilities (verified through levels of reverse flow [2, 201] and/or spanwise modulation of the mean flow [200]), and sufficiently low free-stream turbulence levels.

In Fig. 4.20, the vortex filaments develop spanwise undulations as the structures convect downstream. This is particularly evident in Fig. 4.21, where filaments are relatively straight upstream of $\overline{x_\mathrm{h}}/c$, with notable spanwise deformations at a wavelength of $\langle\lambda_z\rangle/c \approx 0.13$ developing as mean reattachment is approached. Based on the spanwise-averaged streamwise wavelength of the structures, $\langle\lambda_x\rangle/c = 0.035$, the ratio of spanwise to streamwise wavelengths is $\langle\lambda_z/\lambda_z\rangle \approx 3.7$. These values compare favourably with the analysis of the time-resolved PIV measurements (Section 4.3.1), which found predominant spanwise and streamwise wavelengths of $\overline{\lambda_z}/c = 0.15$ and $\overline{\lambda_x}/c = 0.04$, and wavelength ratios that range between $1 \lesssim \lambda_z/\lambda_x \lesssim 7$ (Fig. 4.9b). It must be noted that the presence of spanwise undulations in the phase-averaged data indicates that they occur at consistent spanwise locations, which was also reported by Michelis *et al.* [153] (see their Fig. 4b), who studied an LSB formed over a flat plate. The nature of such spanwise deformations is considered further.

The proposed development of a vortex filament in the LSB is as follows. The filament is essentially two-dimensional at formation, however small variations in wall-normal distance across the span of the filament are inevitable, leading to sections of the filament experiencing varied convective velocity as a result of the strong wall-normal velocity gradient (Fig. 4.18). Thus, segments further from the wall progress downstream at a greater rate than those closer to the

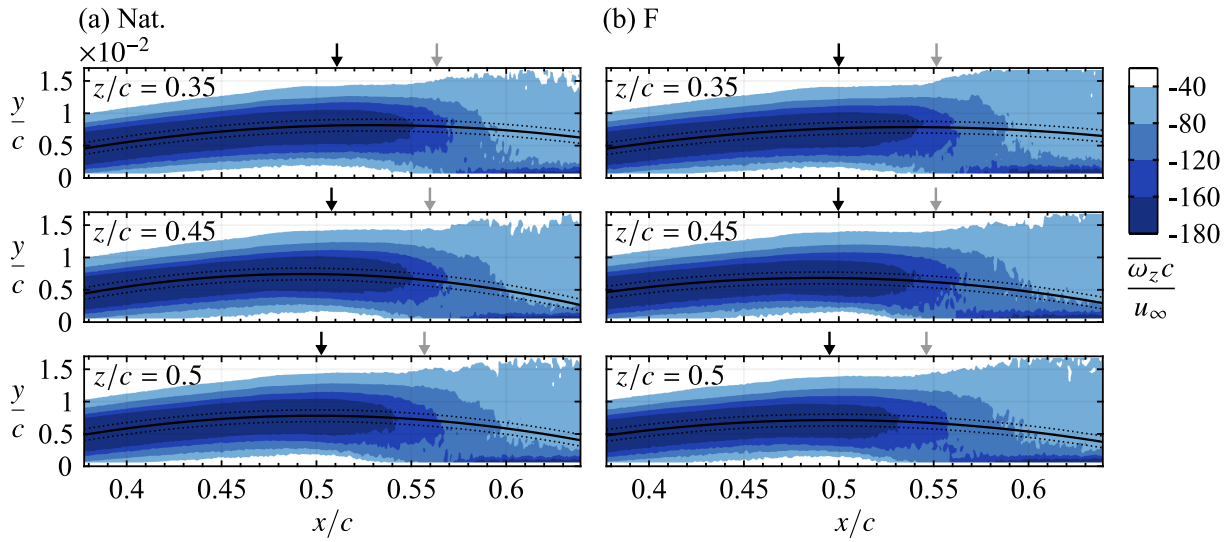

Figure 4.22: Contours of time-averaged spanwise vorticity at exemplary locations where peaks ($z/c = 0.35$ and 0.5) and valleys ($z/c = 0.45$) form in the vortex filaments (Fig. 4.21). Solid lines mark 2nd order polynomial fits to vorticity minima upstream of $x/c = 0.55$, the uncertainty bounds of which are indicated by the dotted lines. Black and grey arrows mark $\overline{x_h}/c$ and $\overline{x_r}/c$, respectively.

Table 4.3: Wall-normal distance of time-averaged shear layer trajectory from surface at $x/c = 0.6$ (Fig. 4.22).

z/c plane	Nat.	F
0.35	$(7.0 \pm 0.9) \times 10^{-3}$	$(7.1 \pm 1.0) \times 10^{-3}$
0.45	$(4.9 \pm 0.9) \times 10^{-3}$	$(4.7 \pm 1.0) \times 10^{-3}$
0.5	$(5.9 \pm 1.0) \times 10^{-3}$	$(5.7 \pm 0.9) \times 10^{-3}$

wall, leading to the continual intensification of the spanwise undulation in the filament, as seen in Fig. 4.21. If the vortex develops as proposed, then the streamwise forward and rearward sections of the filaments (peaks and valleys, respectively) should depart from and approach the surface, respectively, due to mutual induction. This is verified through an examination of the streamwise development of time-averaged vorticity (Fig. 4.22), at spanwise locations where peaks ($z/c = 0.35$ and 0.5 from Fig. 4.21) and valleys ($z/c = 0.45$, also Fig. 4.21) are found in the vortex filaments. Time-averaged trajectories of the shear layer are shown as solid lines in Fig. 4.22, which are determined through 2nd order polynomial fits to vorticity minima upstream of $x/c = 0.55$. For both the natural and fundamental cases, the results in Fig. 4.22 confirm that time-average trajectories at $z/c = 0.35$ and 0.5 are farther from the wall than those at $z/c = 0.45$, particularly in the aft portion of the LSB ($x/c \gtrsim 0.55$), with heights of the shear layer trajectories at $x/c = 0.6$ reported in Table 4.3. These results imply there is a consistent variation in the distance to the wall along the span of the filament in both the natural and excited flow, supporting the proposed development of the spanwise undulations in the vortex filaments.

Further insight into the development of the shear layer vortices is gained from the top

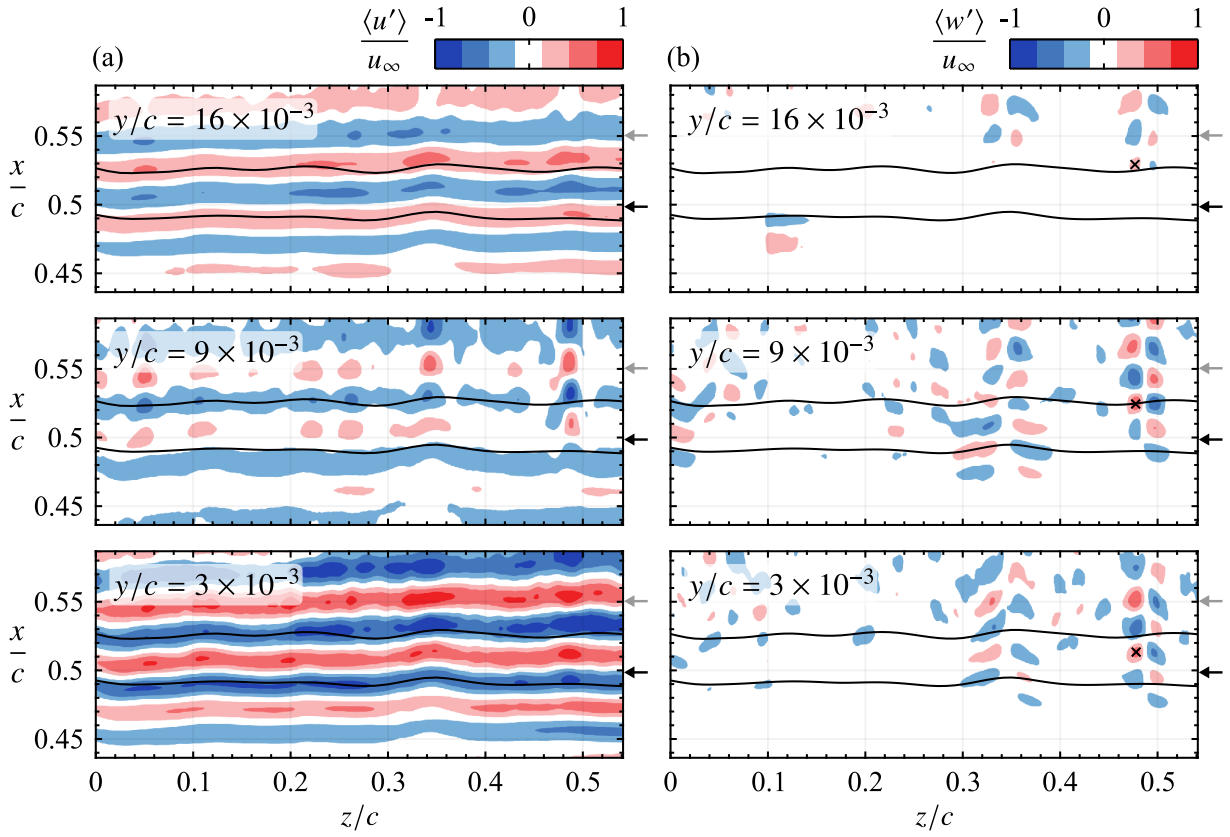

Figure 4.23: Phase-averaged (a) streamwise and (b) spanwise velocity fluctuations for phase $\theta = 4\pi/3$ of the fundamental case. Black lines indicate vortex cores identified from side view PIV measurements (Fig. 4.21). $\times$ marks the same structure across the planes. Black and grey arrows mark spanwise-averaged $\overline{x_h}/c$ and $\overline{x_r}/c$, respectively.

view, scanning PIV measurements (Fig. 4.3b). Figure 4.23 presents contours of phase-averaged streamwise and spanwise velocity fluctuations in x-z planes at wall-normal heights of $y/c = 3 \times 10^{-3}$, 9×10^{-3}, and 16×10^{-3}, approximately corresponding to planes that intersect through the top, middle, and bottom portions of the shear layer vortices. As such, the structures are identified at $y/c = 3 \times 10^{-3}$ and 16×10^{-3} in Fig. 4.23a as spanwise bands of negative and positive fluctuating streamwise velocity, respectively, with the bands of opposite sign corresponding to the induced flow between structures. For the same phase in the excitation cycle, the vortex cores identified from the side view PIV measurements (Fig. 4.21) are superimposed and confirm the identification of the structures in the results of the top view PIV configuration. Overall, good agreement is found between the results of the two configurations in terms of the streamwise position of the structures and the spanwise locations at which peaks and valleys form in the vortex filaments, with some minor discrepancies likely stemming from the higher measurement uncertainty associated with the top view configuration (Table 4.1). This general agreement was verified for all other phases in the excitation cycle (not shown for brevity).

The contours of phase-averaged spanwise velocity fluctuations in Fig. 4.23b show organized patterns of strong positive and negative fluctuations centred at spanwise locations where streamwise

forward undulations develop in the vortex filaments, *i.e.*, at $z/c \approx 0.1$, 0.36, and 0.5. Furthermore, these regions of strong spanwise fluctuations are tilted forward in the streamwise direction. For example, tracing the structure marked by the $\times$ symbol up from $y/c = 3 \times 10^{-3}$ to 16×10^{-3} reveals that it and its adjacent pair shift downstream with increasing wall-normal height. Thus, these patterns in the spanwise velocity fluctuations confirm that the spanwise undulations in the vortex filaments are associated with wall-normal deformations, with the filaments tilting away from the wall at locations where they surge forward in the streamwise direction. Such a deformation re-distributes the filament's spanwise vorticity into both the streamwise and wall-normal directions, thus creating spanwise and wall-normal velocity fluctuations, with the former captured in Fig. 4.23b.

The results in Fig. 4.22 suggest that the spanwise deformations of the vortex filaments seen for the fundamental case develop in a similar manner in the natural flow. Further evidence of this is provided through POD analysis (Section 3.3.2), which is performed on measurements from a single field of view from the top view PIV measurements using the snapshot method of Sirovich [223]. A set of 1000 independent snapshots is used, with modes computed at $y/c = 3 \times 10^{-3}$ and within $0.44 \lesssim z/c \lesssim 0.54$, where notable signatures of vortex deformations are observed in Fig. 4.23. The relative and cumulative energy distributions of the computed modes are shown in Fig. 4.24, with the latter showing that approximately 52% and 45% of the total energy contained in the velocity fluctuations is recovered within the first 30 modes for the natural and fundamental cases, respectively. The three most energetic modes have been verified to capture velocity fluctuations attributed to the primary shear layer vortices. This is depicted by the spatial topology of the first POD mode plotted in Fig. 4.25. For both cases, the plotted streamwise component is topologically similar to that seen in Fig. 4.23a, featuring strong spanwise uniformity and a similar streamwise wavelength. It should be noted that an increase in the energy levels of the first mode pair is expected when the flow is forced, however, this is not seen in Fig. 4.24. Since the employed weak forcing produces minor effect on flow characteristics, the associated changes in the modal energy content fall within the uncertainty associated with the near-wall x-z measurement plane. The expected increase in energy levels when excitation is applied is seen at x-z planes farther from the wall, which is examined in detail in Appendix C.1.1.

The spanwise deformations seen in the vortex filaments through the phase-averaged results (*e.g.*, Figs. 4.21 and 4.23) are also captured in the POD results. In Fig. 4.25b, a forward bulge (peak) in the spatial mode is apparent at $z/c = 0.49$, which matches closely with the location where peaks in the vortex filaments are consistently observed in Figs. 4.21 and 4.23. As was seen with Fig. 4.23b, the deformation of the shear layer vortices is accompanied by the generation of strong spanwise velocity fluctuations, with the same distinct pattern captured in the spanwise component plotted in Fig. 4.25b. For the natural case (Fig. 4.25a), a similar characteristic signature is seen in the spanwise component of the first mode at $z/c = 0.49$, and a streamwise forward peak is also identifiable in the streamwise component of the mode at this location. Thus, the POD results confirm that the identified vortex deformations also occur in the natural flow. However, the signature of these events in the most energetic POD modes is significantly decreased in terms of spatial coherence, suggesting that the associated vortex deformations either occur less frequently and/or are less pronounced compared to the fundamental case.

With observed development of the shear layer vortices involving streamwise forward sections

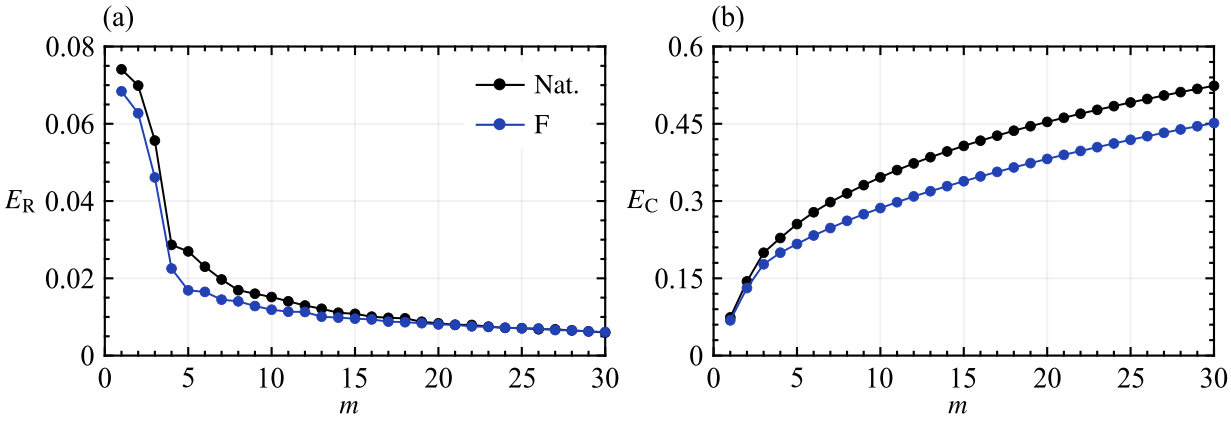

Figure 4.24: POD (a) relative and (b) cumulative modal energy distributions for (u,w) modes computed at $y/c = 3 \times 10^{-3}$ from a single view of the top view PIV configuration.

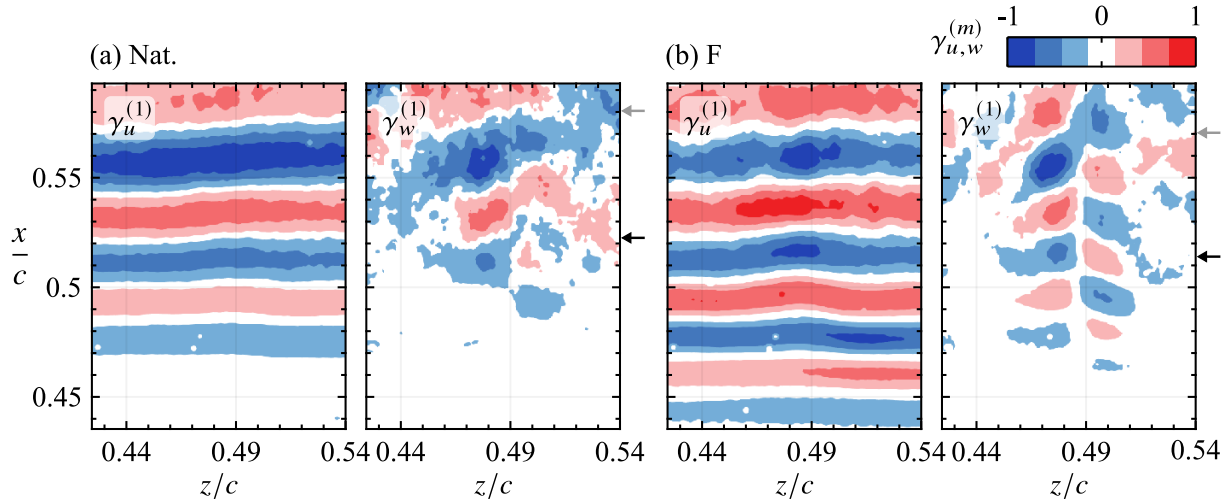

Figure 4.25: Normalized POD spatial modes computed at $y/c = 3 \times 10^{-3}$ from a single view of the top view PIV configuration. Black and grey arrows mark spanwise-averaged $\overline{x_h}/c$ and $\overline{x_r}/c$, respectively.

lifting away from the surface (Fig. 4.22), a re-orientation of vorticity into the wall-normal direction is also expected. An exemplary case is examined in Fig. 4.26, where a sequence of phase-averaged wall-normal vorticity iso-surfaces is plotted in a region zoomed-in centred on $z/c = 0.5$. Contours of phase-averaged spanwise vorticity at $z/c = 0.5$ (shifted to $z/c = 0.45$ for clarity) and contours of phase-averaged negative streamwise velocity fluctuations at $y/c = 3 \times 10^{-3}$ are also plotted to help identify the primary structures. In Fig. 4.26a, the primary roller I shows relatively strong spanwise coherence, however, a local deformation has initiated, as the filament begins to bulge forward at $z/c \approx 0.5$. This is marked by a concentration of streamwise velocity fluctuations that intensifies as the structure convects downstream, along with the emergence of a distinct pair of positive and negative wall-normal vorticity, labelled i in Fig. 4.26b–d. The effect becomes more pronounced with downstream development, as seen with primary vortex II and the associated wall-normal

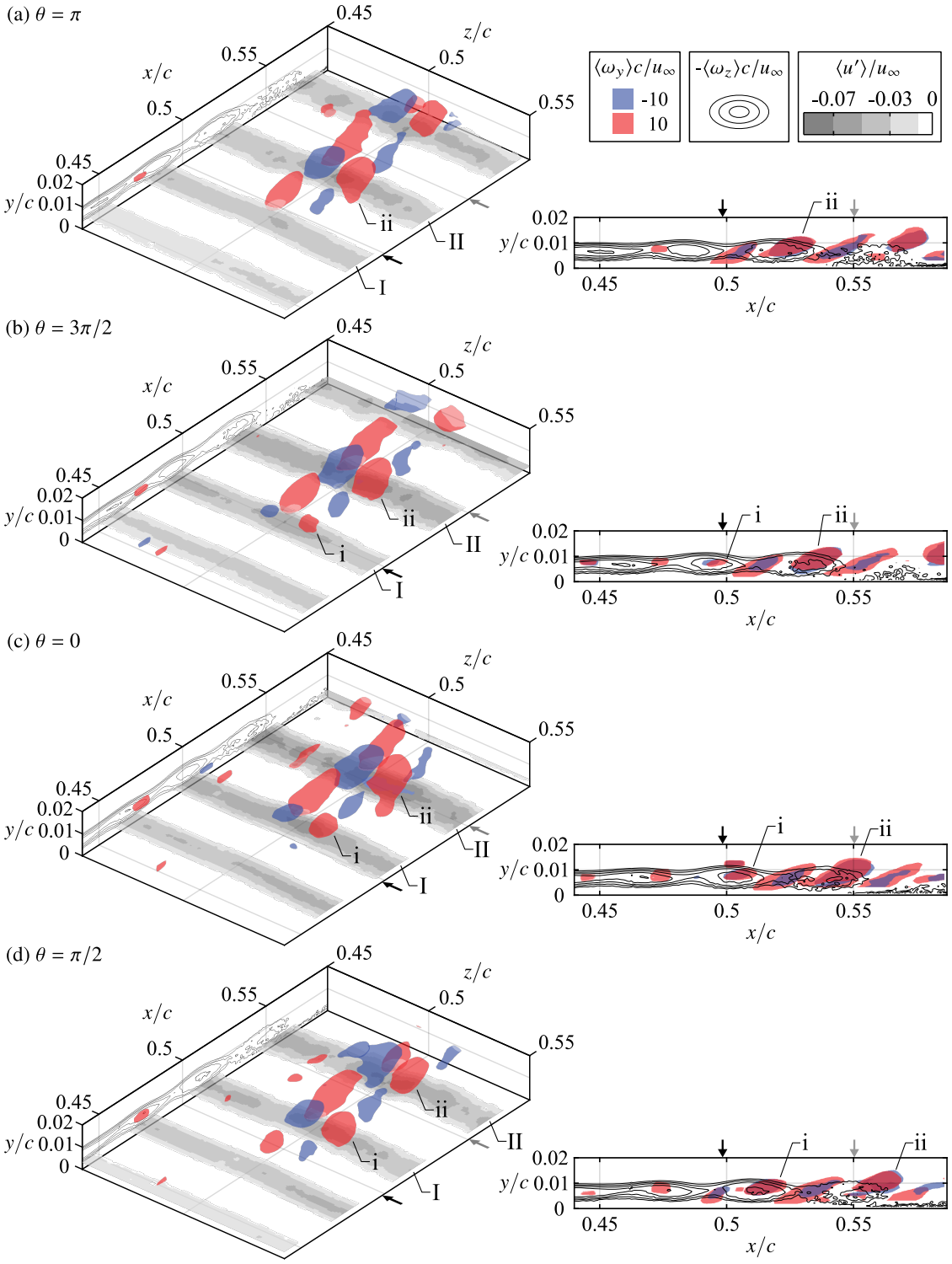

Figure 4.26: Sequence of phase-averaged wall-normal vorticity iso-surfaces, negative spanwise vorticity contours at $z/c = 0.5$ (shifted to $z/c = 0.45$ for clarity), and contours of negative streamwise velocity fluctuations at $y/c = 3 \times 10^{-3}$ for the fundamental case. Black and grey arrows mark spanwise-averaged $\overline{x_\mathrm{h}}/c$ and $\overline{x_\mathrm{r}}/c$, respectively.

vorticity pair ii. Given that the vorticity pairs i and ii are tilted forward in the streamwise direction, seen in the x-y projections in Fig. 4.26, and form where the primary spanwise vortices bulge forward, the formation of these structures is consistent with the negative spanwise vorticity of the main shear layer vortices re-orienting through lift-up of the main filament and subsequent stretching in the streamwise direction. Thus, positive and negative wall-normal vorticity results, forming the legs of a hairpin like structure. Note that the streamwise wavelength of the wall-normal vorticity pairs is half that of the primary structures, with vorticity pairs of opposite sign present in the region between consecutive rollers (*i.e.*, between structures i and ii) that may be created via induction from the neighbouring wall-normal structures. Similar secondary structures in both the vortex core region and in the gap region between consecutive rollers have been reported in DNS studies of LSBS [92, 137], which have drawn comparisons to the 'rib' vortices reported in free shear layers [15] and bluff body wakes [253]. Whether or not the secondary structure reported here are of the same nature is unclear given the limitations of the measurement techniques employed, which merits future investigation.

The proposed description of the vortex dynamics within the LSB is summarized as follows. The shear layer rolls up to form spanwise oriented vortices with strong spanwise coherence. However, inevitable minor variances in wall-normal height, in conjunction with strong mean wall-normal shear, lead to the development of spanwise undulations. These undulations intensify as the structures convect downstream, while the forward sections of the filament lift away from the surface, which re-orients the filament's spanwise vorticity into both the streamwise and wall-normal directions. Thus, hairpin like structures form (structures i and ii in Fig. 4.26), which are tilted forward and extend above the vortex core region, and are marked by the localized production of streamwise and spanwise velocity fluctuations (Figs. 4.23 and 4.25).

4.4 Concluding Remarks

In this chaptern the general flow development and vortex dynamics in a laminar separation bubble were examined, with emphasis placed on the vortex merging phenomenon and the three-dimensional development of the primary shear layer vortices. This was accomplished through an experimental examination of an LSB formed over a NACA 0018 airfoil at a chord Reynolds number of 125 000, an angle of attack of 4°, and a free-stream turbulence level of 0.07%. Much of the experimental findings came from PIV results collected in a variety of configurations, allowing for two-dimensional, time-resolved evaluations of the flow, in addition to conditional volumetric reconstructions of the flow field using phase-locked, scanning PIV measurements. In addition to leaving the flow to develop naturally, acoustic forcing was applied at the LSB's fundamental and subharmonic frequencies, with a relatively low excitation amplitude selected to avoid any substantial mean flow modifications.

The flow development in the LSB is characterized by the periodic roll-up of the separated shear layer into vortices upstream of the LSB maximum height location, where flow disturbances are amplified within a band centred on the fundamental frequency. The shear layer vortices interact and deform as they convect downstream, followed by the breakdown to smaller scales downstream of the mean reattachment point. This is marked by the redistribution of spectral energy to a wider

range of frequencies as the flow transitions to turbulence.

With respect to vortex merging, the results show that this phenomenon occurs naturally in the LSB, while forcing at the subharmonic and fundamental frequencies promotes and inhibits merging, respectively, as is the case for free shear layers [72]. A vortex merging detecting scheme was developed using wavelet analysis, which showed that, at the midspan plane, 18% of the primary structures formed in the naturally developing LSB merge. This value increased to 64% when forced at the subharmonic frequency and decreased to 8% when forced at the fundamental frequency. For all cases, the majority of merging events occurred in the aft portion of the bubble, while subharmonic forcing lead to a significant number of merging events shifting upstream. Despite subharmonic forcing having a significant effect on the prevalence of vortex merging, the mean topology of the bubble remained relatively unchanged from the natural flow. Since it is generally accepted that reattachment is facilitated by the shear layer vortices [134, 260], these results imply that the increase in strength of individual structures as a result of merging is balanced by the reduction in their frequency, resulting in a largely unchanged mean LSB topology. Furthermore, the vortex merging process is found to occur in a spanwise non-uniform manner, with localized merging events occurring away from where forward and rearward streamwise bugles develop in the vortex filaments. Thus, the spanwise undulations that develop in the vortex filaments are shown to be intrinsic to the LSB vortex merging process.

In examining the three-dimensional development of the shear layer vortices, the fundamental forcing case is first established as a suitable analog in studying the natural flow since the low level of forcing does not substantially alter the mean flow or the disturbance development, while also enabling volumetric reconstruction of the flow field through phase-averaging. Time-averaged reconstructions revealed a strongly two-dimensional LSB topology for both the natural and forced cases, while analysis of the flow development demonstrated that in both flows the shear layer vortices that form in the separation bubble are spanwise-oriented and strongly two-dimensional. The previously seen spanwise undulations in the vortex filaments are captured and are shown to continually intensify with downstream convection as a result of the streamwise forward sections lifting away from the surface. This motion re-orients the shear layer vortices' spanwise vorticity into the streamwise and wall-normal directions, forming hairpin-like structures that are tilted forward and extend above the vortex core region.

These results have made it clear that flow development in a separation bubble, particularly in the aft portion, is inherently three-dimensional. In particular, spanwise undulations develop in the filaments of the shear layer vortices over a fixed range of values, $1.5 \lesssim \lambda_z/\lambda_x \lesssim 7$, and are critical to the merging and breakdown processes of the vortices. In the following chapters, a three-dimensional forcing technique is developed to target the LSB at these spanwise wavelengths (Chapter 5), and the effect of these deterministic disturbances on three-dimensional flow development in an LSB is assessed (Chapter 6).

Chapter 5

Characterization of Three-Dimensional Input Disturbances

A three-dimensional forcing technique capable of producing disturbances modulated to a desired spanwise wavelength is developed and characterized. The technique utilizes surface-mounted, AC-DBD plasma actuators arranged in streamwise succession, the outputs of which are superimposed to produce the desired disturbance topology while keeping total imparted momentum constant. Assessment of the forcing on flow development in an LSB reveals that disturbance growth is spanwise wavelength dependent, with significant amplification observed for disturbances with a spanwise to streamwise wavelength ratio of 2 : 1. For this case, significant undulations develop in the initially spanwise uniform shear layer vortices at the forcing wavelength, which impact the ensuing vortex dynamics.

Parts of this chapter have been adapted from the following publications:

Kurelek, J. W., Yarusevych, S., & Kotsonis, M. 2018 An Assessment of Flow Development in a Separation Bubble Subjected to Spanwise Modulated Disturbances using Particle Image Velocimetry. In *48th AIAA Fluid Dyn. Conf.*, Atlanta GA, June 25–29. DOI.

Kurelek, J. W., Yarusevych, S., & Kotsonis, M. 2019 The effect of three-dimensional forcing on flow development with a laminar separation bubble. In *11th Int. Symp. Turbul. Shear Flow Phenom.*, Southampton UK, July 30–Aug 2. URL.

5.1 Introduction

The discussions in Section 2.3 and the results of Chapter 4 highlight that the introduction of periodic flow disturbances aimed at control of separation bubble dynamics have a significant effect on the ensuing three-dimensional flow development. The majority of studies to-date have examined the problem in two dimensions, employing techniques that introduce periodic and spanwise uniform disturbances through wall oscillations [2, 118, 140], external acoustics [91, 112], or surface-mounted plasma actuators [151, 260, 261]. Several investigators have linked the optimal excitation frequency to the frequency of the most amplified disturbances in the natural flow [134, 258, 260], showing that inducing mean flow reattachment on stalled airfoil (and thus forming an LSB) or reducing the size of an existing LSB is most effective when the excitation targets this frequency. When forcing at this fundamental frequency, the vortex shedding process locks to the excitation frequency and the spanwise coherence of the structures is increased, which is related to a higher entrainment of momentum from the surrounding flow to the surface, thus resulting in an upstream shift in the LSB mean reattachment location.

Complementing this work, a number of studies [33, 69, 92, 113, 137, 151, 153, 170], including those presented in Chapter 4 and Appendix A, have gone on to characterize the development of LSB shear layer vortices through the later stages of transition, where significant three-dimensionality is observed. While these studies have put forward widely ranging descriptions of the vortex development, the results of Chapter 4 clarify that for LSBs in a low turbulence intensity environments, the shear layer vortices show strong spanwise coherence at formation, but then quickly undergo significant spanwise deformations prior to the breakdown to turbulence. Surveying the literature for LSBs investigated under similar conditions [113, 137, 153, 170] reveals that the spanwise deformations are a common feature, which tend to develop over a relatively fixed range of wavelengths, $1 \lesssim \lambda_z/\lambda_x \lesssim 7$, where λ_z and λ_x are the spanwise and streamwise wavelengths of the deformations and shear layer vortices, respectively. This raises the possibility of an underlying instability associated with vortex breakup in LSBs which, if present, could potentially be manipulated through targeted, three-dimensional forcing.

Precedence for three-dimensional forcing techniques can be found in the literature, as key physical mechanisms have been elucidated in boundary layers [97, 107, 209] and free shear layers [15, 89, 203] through the use of such techniques. Most notably, Klebanoff *et al.* [107] introduced three-dimensional disturbances into a laminar boundary layer by modulating the output of a thin vibrating ribbon, showing the spanwise deformation of the TS instability waves into three-dimensional structures, which has been established as a critical step in the transition process of boundary layers [214]. A limited number of investigations have pursued three-dimensional forcing of LSBs due to the difficulty in implementing the forcing technique in a reliable manner, which is then compounded by the need for three-dimensional flow field measurements. A limited number of investigations have been pursued [118, 139, 141], with the prevailing conclusion being that the introduction of three-dimensional disturbance has little effect on the LSB transition process. This is in contrast to the effects noted in boundary layers [107, 209] and free shear layers [89, 203], in addition to other reports that note a dependence of LSB flow development on three-dimensional disturbance characteristics [153, 182, 198].

In this chapter, a new forcing technique capable of producing deterministic two and three-

dimensional disturbances is developed using surface-mounted, dielectric barrier discharge plasma actuators (Section 3.2.2), with three-dimensional forcing at a prescribed spanwise wavelength achieved through the superposition of disturbances created by actuators arranged in streamwise succession. As both the imparted momentum and spatial topology of the forcing are critical, a characterization approach that considers both quiescent and in-flow conditions is taken, since it is well documented that plasma actuator output depends on the external flow conditions [184]. Following this, a preliminarily investigation of the effects of the forcing on flow development in a laminar separation bubble formed over a flat plat is conducted.

5.2 Description of Experiments

5.2.1 Quiescent Characterization

The alternating current, dielectric barrier discharge (AC-DBD) plasma actuators used in this investigation are shown in Fig. 5.1. Each actuator consisted of two pairs of high voltage and ground electrodes, with each pair arranged in an asymmetric configuration on opposites sides of a dielectric barrier (*e.g.*, see Fig. 3.6). As will be demonstrated, a weak wall-parallel jet near the surface is produced during operation in the region where a high voltage and ground electrode overlap. A 400 µm thick polyethylene terephthalate (PET) strip served as the dielectric layer, onto which the electrodes were painted using conductive silver paint. Each painted electrode was approximately 5 µm thick, making the total thickness of the actuator 410 µm, with groves of equal depth machined into the test model to allow for flush mounting. The high voltage and ground electrodes extended 10 and 6 mm in the streamwise direction, respectively, and were overlapped by 1 mm to create the discharge area. Three-dimensional disturbances were produced by arranging the electrode pairs in streamwise succession, with the upstream set used to produce a two-dimensional disturbance, while the downstream set forced in a spanwise modulated fashion as a result of gaps in the ground electrode. Three actuator configurations were fabricated, with spanwise wavelengths of 25, 37.5, and 50 mm, which correspond to $\widetilde{\lambda}_z = 12.5$, 18.75, and 25 when non-dimensionalized by the displacement thickness at separation when the flow is not forced ($\delta_{1s} = 2$ mm). Characterization was performed for four forcing configurations, the first consisting of purely two-dimensional forcing achieved through operation of only the upstream set of electrodes. The other three cases are three-dimensional forcing at spanwise wavelengths of $\widetilde{\lambda}_z = 12.5$, 18.75, and 25, with each achieved by operating both sets of electrodes on a given actuator with a relative phase delay used to superimpose the two disturbances introduced into the flow.

The experimental setup is shown in Fig. 5.2. Each set of electrodes was characterized individually, with flow visualization and planar PIV measurements conducted in the region of the electrode overlap, where ionization occurs and the wall jet is produced. The measurements were carried out in quiescent conditions created within a contained volume with dimensions $610 \times 610 \times 2400$ mm, with the actuator mounted flush to the surface of a $250 \times 510 \times 6$ mm ABS plate. The volume was seeded by atomizing olive oil into particles with a mean diameter of 1 µm using a Laskin nozzle style atomizer based on the designs of Kähler *et al.* [98]. These seeding

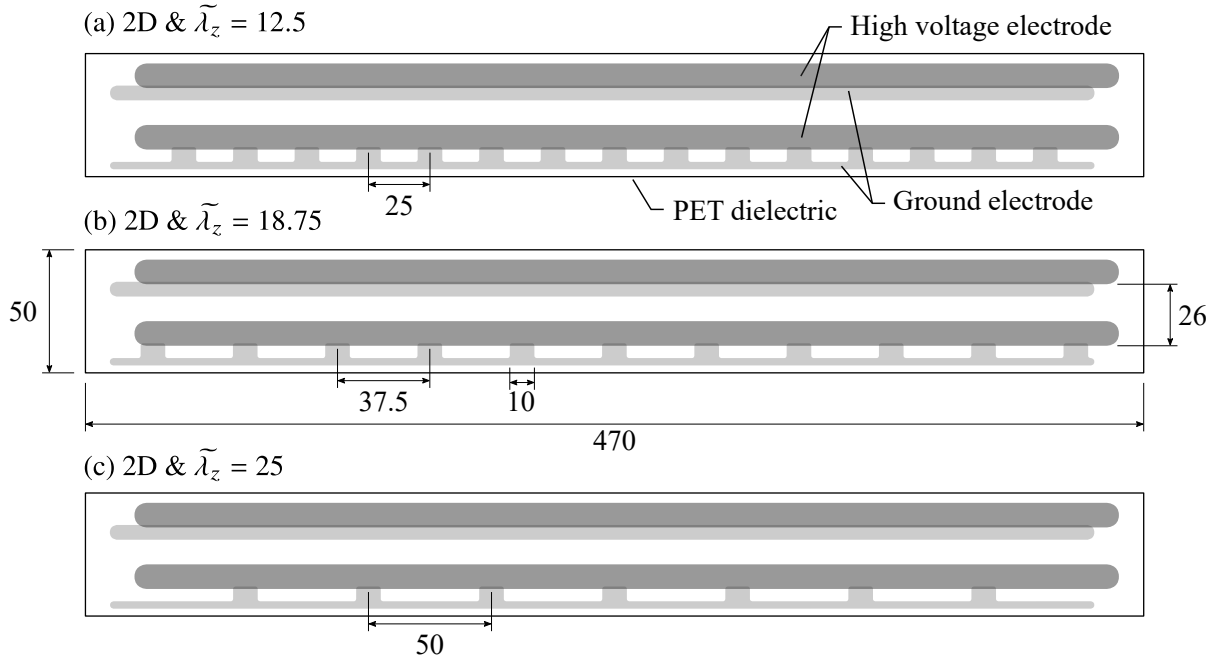

Figure 5.1: Plasma actuator configurations. All dimensions in millimetres.

particles had to be used in place of the water-based particles due to the significant electrodynamic effects that prevent substances with strongly polar molecules from entering the ionization region [49, 110].

Particle image acquisition for both the PIV measurements and flow visualizations was carried out using an EverGreen 70 mJ/pulse Nd:YAG laser, a LaVision Imager Pro-X 2M camera, a timing unit, and LaVision's DaVis 8 software. The flow visualizations (Fig. 5.2b) were completed in a top view configuration, with the laser beam conditioned into a 2 mm thick sheet that was positioned into an x-z plane, whose centre was 3 mm from the surface. The camera was fitted with a 60 mm focal length Nikon macro lens set to $f_\# = 5.6$, its sensor cropped to 1600×711 px from its full resolution of 1600×1200 px, and an imaged area of 127×57 mm was set, resulting in a magnification factor of 0.09. The PIV measurements (Fig. 5.2a) were completed in a side view configuration, with measurements completed at multiple x-y planes. The camera and laser were moved in tandem using an automated traversing system, with calibration images taken at multiple planes to ensure fidelity of the movements. The laser sheet thickness and camera resolution were maintained from the flow visualizations, while the camera was fitted with a 200 mm focal length Nikon macro lens set to $f_\# = 8$, and the field of view was set to 21.5×8.5 mm, resulting in a magnification factor of 0.55. 2000 double-frame images were acquired per measurement plane at 14.67 Hz with a frame separation time of 800 µs, which kept particle displacements under 15 px. Velocity fields were computed using an iterative, multi-grid cross-correlation scheme with window deformation [212], and a final window size of 24×24 px with 75% overlap. As a result, the vector pitch in the PIV data is 0.08 mm. The results were post-processed using the universal outlier detection algorithm [247].

Maintaining tractability between a characterization conducted in quiescent conditions and test

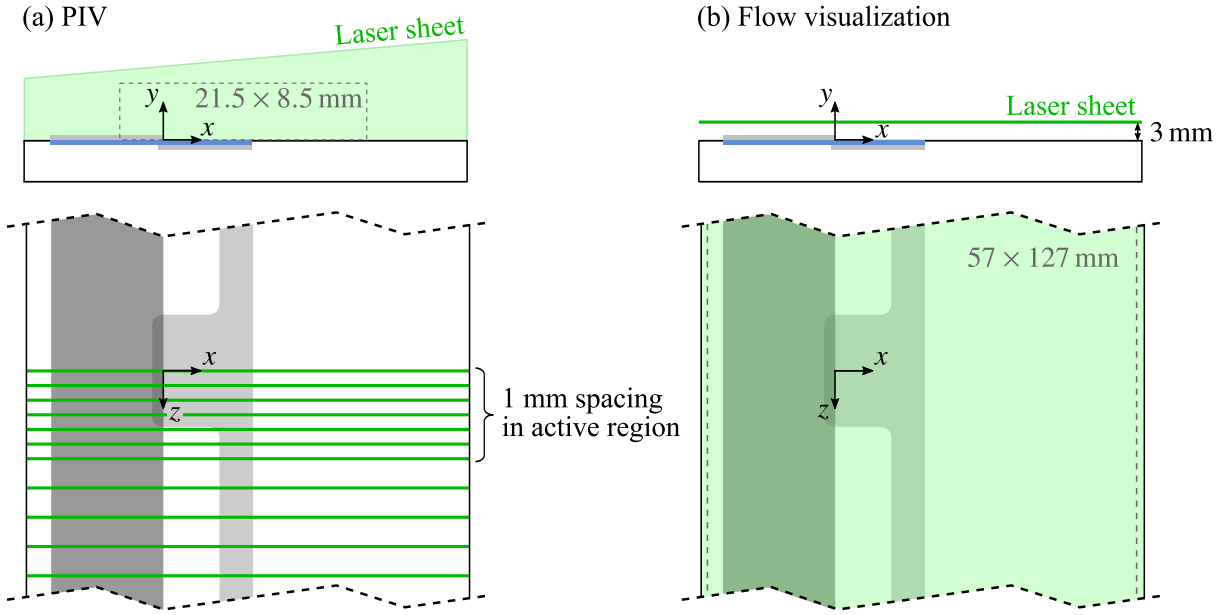

Figure 5.2: Experimental setup for actuator characterization in quiescent conditions. (a) PIV measurements and (b) flow visualizations.

conditions with an external flow presents a challenge since the external flow is expected to alter the produced disturbances. The investigation of Pereira *et al.* [184] established the effects of external flow on the momentum transfer from an AC-DBD, noting that quiescent characterization tends to only slightly under-predict the generated thrust force, which has allowed several investigations to rely on quiescent characterization [153, 260, 261]. Furthermore, while the external flow can alter the streamwise characteristics of the disturbances, it is theorized that the general spanwise periodicity will not be significantly affected owing to the spanwise uniformity of the external flow to be investigated (Section 5.2.2). As such, the quiescent characterization is aimed at determining spanwise topology and thrust generation only, both of which are assumed to be relatively invariant to external flow conditions. The streamwise characteristics of the produced disturbances will be established through the in-flow characterization (Section 5.2.2).

The actuators were driven by a TREK 20/20C high voltage amplifier, with signals generated using National Instrument's LabVIEW software and a PCIe-6321 DAQ. The forcing signals consisted of a $f_c = 5\,\text{kHz}$ carrier sine wave amplified to a peak-to-peak voltage of $V_{pp} = 6\,\text{kV}$ and modulated by a $f_m = 133\,\text{Hz}$ square wave, with the modulation frequency selected based on preliminary flow measurements and targeted the primary convective instability in the LSB (Appendix C.2.2). The effects of viscosity is expected to be significant for these forcing conditions given the relatively low wall jet velocities generated in quiescent conditions (on the order of $1\,\text{m}\,\text{s}^{-1}$). This results in low levels of turbulent mixing and an uneven distribution of seeding particles, with very low particle density found in the ionization region (*i.e.*, the region of interest). This is especially true for low duty cycle actuation, and as a result it is necessary to operate the actuator at higher duty cycles to enable sufficient mixing of seeding particles, and then scale the net momentum injection accordingly. Such an approach is feasible due to the large separation of characteristic time scales between the fluid and plasma dynamics, effectively decoupling the

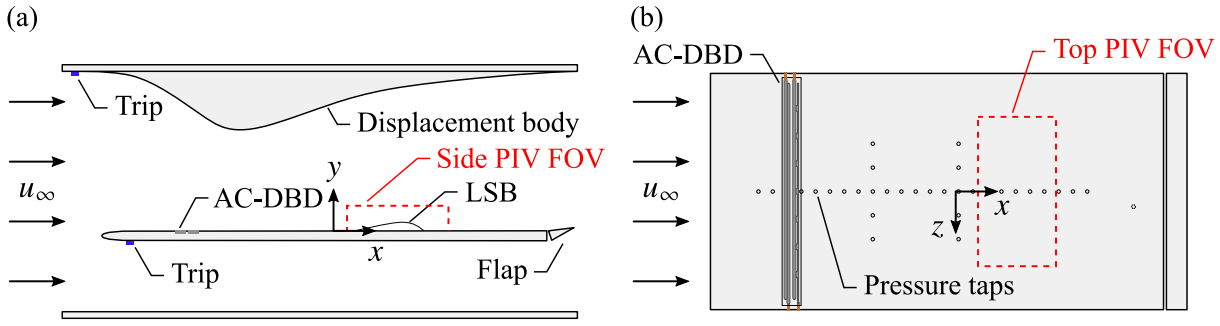

Figure 5.3: (a) Side and (b) top view of experimental setup.

phenomena [87]. Therefore, the modulating duty cycle of the forcing was varied between 18% and 100%, thus covering the range of duty cycles employed for the in-flow measurements (21% to 25%), while allowing for more reliable results collected at higher duty cycle to be included in the interpolation.

5.2.2 In-Flow Characterization

In-flow characterization was performed in the TU Delft A-Tunnel (Section 3.1.2), where an LSB was formed over a flat plate through application of an adverse pressure gradient. A schematic of the experimental setup is provided in Fig. 5.3. The acrylic flat plate described in Section 3.1.4 was installed in the test section 150 mm from the floor, with the trailing edge flap rotated upwards to mitigate unsteady separation effects. The pressure gradient on the plate's top surface was conditioned using an adjustable displacement body on the top wall of the test section. The boundary layer developing on the displacement body was tripped to turbulence by a zip-zag turbulator in order to avoid flow separation in the adverse pressure gradient region, the effectiveness of which was verified through tuft flow visualization. The same tripping technique was employed on the bottom surface of the flat plate to suppress possible vortex shedding at the plate trailing edge. A Cartesian coordinate system is used throughout this chapter (Fig. 5.3), with the origin selected such that $x = 0$ corresponds to the location of mean flow separation with no forcing (490.5 mm from the plate leading edge), while $y = 0$ and $z = 0$ are located at the top surface and midspan of the plate, respectively. The free-stream velocity was set to $u_\infty = 5.75\,\mathrm{m\,s^{-1}}$, measured by a Pitot-static tube located upstream of the flat plate leading edge. A detailed characterization the facility was conducted by Merino-Martínez *et al.* [147], showing that at the investigated free-stream velocity the streamwise turbulence intensity is 0.09% and no significant spectral peaks are found in the free-stream velocity and pressure fluctuations within the frequency range of interest to this investigation, $1 \leq f \leq 1000\,\mathrm{Hz}$. Based on the displacement thickness at separation when the flow is not forced, the Reynolds number for the experiments is $Re_{\delta_{1_s}} \approx 750$.

The imposed pressure distribution on the flat plate was measured via static pressure taps (Section 3.1.4 and Fig. 5.3). All taps were measured simultaneously at 100 Hz for 20 s using a set of Honeywell HSC series differential pressure transducers with a full range of ±160 Pa. The resulting pressure distributions are shown in Fig. 5.4, where the estimated uncertainty for all measurement is ±4.6% of q_∞ (Appendix B). As indicated by the pressure plateau region in the

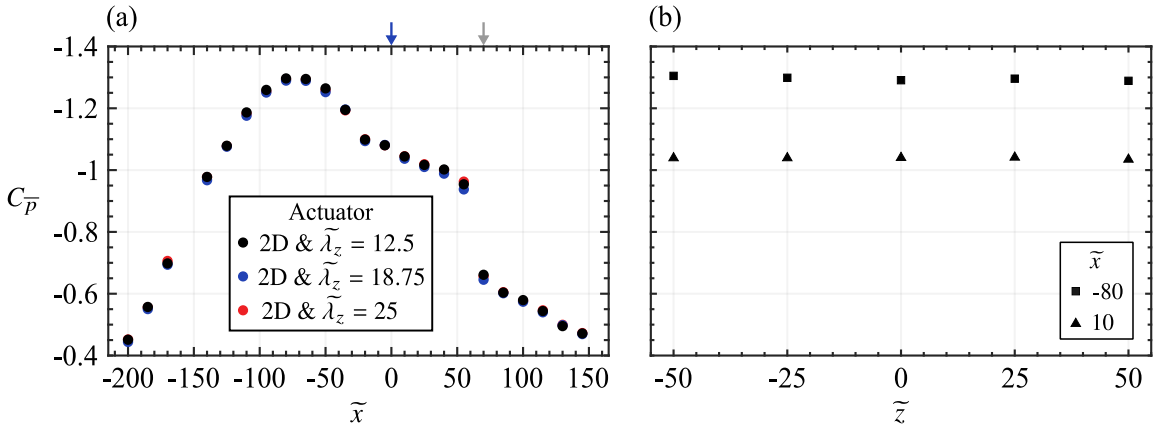

Figure 5.4: Mean surface (a) streamwise and (b) spanwise static pressure distributions with actuator installed but not active. Measurement uncertainty is given by the marker size. Blue and grey arrows mark of $\overline{\widetilde{x}_s}$ and $\overline{\widetilde{x}_r}$, respectively.

streamwise $C_{\overline{p}}$ distribution (black markers in Fig. 5.4a), a separation bubble is present with mean separation and reattachment locations of approximately $\overline{\widetilde{x}_s} = 0$ and $\overline{\widetilde{x}_r} = 70$, respectively. The spanwise pressure distributions (Fig. 5.4b) indicate that the flow is essentially two-dimensional, with the uniformity falling within ±0.8%.

The AC-DBD actuators described in Section 5.2.1 (Fig. 5.1) were used, with a total of five cases investigated: (i) no forcing (actuator installed but not active), (ii) two-dimensional forcing, and three-dimensional forcing with spanwise wavelengths ($\widetilde{\lambda}_z$) of (iii) 12.5, (iv) 18.75, and (v) 25. Figure 5.4a confirms that there is no change in the mean LSB topology, within the experimental uncertainty, as a result of changing the actuator. All actuators were recessed into the plate so as not to perturb the flow and were placed to locate the two-dimensional discharge area at $\widetilde{x} = -310$. Positioning the actuator within the favourable pressure gradient region allowed for sufficient control authority, while allowing for the disturbances to develop through the boundary layer upstream of the mean separation point. The actuators were driven by the same equipment used for the quiescent characterization experiments (Section 5.2.1), and the generated forcing signals were also kept the same. Only the modulating duty cycle was varied, with values between 21% and 25% employed on a per forcing case, with values chosen to achieve equal total momentum input across all the forcing cases considered.

Streamwise and spanwise aspects of the flow development within the LSB were assessed using planar, time-resolved PIV in two separate configurations, referred to as the side and top view configurations. The approximate fields of view for these configurations are depicted in Fig. 5.3 and an overview of the PIV parameters are provided in Table 5.1. The flow was seeded using a water-glycol based fog with a mean particle diameter of 1 µm produced by a SAFEX generator. Illumination was provided by a Continuum 532-120M Nd:YAG high-speed laser, with the beam conditioned into a sheet approximately 2 mm thick. Images were captured by a PCO Dimax HS4 camera fitted with a Nikon 105 mm macro lens set to $f_\# = 5.6$ and 2.8 for the side and top views, respectively. The cameras were synchronized with the laser via a LaVision timing unit and image acquisition was done using LaVision's DaVis 8 software.

Table 5.1: Parameters for PIV experiments.

Parameter	Side view	Top view	Unit
Laser	Continuum 523-120M Nd:YAG		–
Camera	PCO Dimax HS4		–
Lens focal length	105		mm
Lens $f_\#$	5.6	2.8	–
Magnification factor	0.28	0.14	–
Sensor resolution	2016×432	1680×848	px
Total field of view	79×16	135×63	mm
PIV mode	Double-frame		–
Sampling rate	2	1.75	kHz
Laser pulse sep.	80	140	µs
Max. particle disp.	15	12	px
No. of samples	7238	4480	–
Final window size	24×24 (75% overlap)		px
Vector pitch	0.24	0.48	mm
Avg. uncertainty	3.5	5.2	% of u_∞

For the side view configuration, measurements were taken at multiple x-y planes so that the flow field could be volumetrically reconstructed using phase-averaging. This was achieved by translating the actuator in the z-direction, thus shifting the origin of the measurement domain relative to the measurement system, rather than vice versa which requires re-calibration. This multi-plane measurement approach is possible due to the fact that the flow is essentially two-dimensional when left to develop naturally (Fig. 5.4b). Therefore, the camera's field of view was set to a fixed x-y plane (relative to the plate and test section), and the full resolution of 2016×2016 px was cropped to 2016×432 px to cover an area of 79×16 mm, resulting in a magnification factor of 0.28. For the top view configuration, measurements were performed in a single x-z plane located 7 mm from the top surface of the plate. In order to achieve the desired sampling rate, the camera's sensor was cropped to 1680×848 px, covering a field of view of 135×63 mm at a magnification factor of 0.14. Sampling was performed at 2 and 1.75 kHz for a total of 7328 and 4480 samples for the side and top view configurations, respectively. Prior to amplification, the plasma forcing signal was split and sent to the PIV timing unit, thus allowing for the phase information between the forcing and the PIV acquisitions to be determined.

For both PIV configurations, the focus was adjusted to produce imaged particles approximately 3 to 4 px in diameter. An iterative multi-grid cross-correlation scheme with window deformation [212] was used to compute velocity fields. A final interrogation window size of 24×24 px with 75% overlap was used, with windows of this size containing, on average, 12 particles. As a result, the vector pitches in the data are 0.24 and 0.48 mm for the side and top view configurations, respectively. The results were post-processed using the universal outlier detection method [247]. The random errors in the PIV measurements were evaluated using the correlation statistics method [251]. The average uncertainties within the region of the separated shear layer are estimated to be

less than 3.5% and 5.2% of u_∞ for the side and top view configurations, respectively, while higher uncertainties are present near the wall for the side view configuration. A full treatment of the uncertainty estimates related to the PIV measurements and quantities derived from the PIV results is given in Appendix B.

5.3 Quiescent Characterization

The results presented in this section establish the characteristics of the employed plasma actuators (Fig. 5.1) in terms of the spanwise topology and net momentum injection of the forcing. These characteristics are assumed invariant to the external flow conditions and so PIV measurements and flow visualizations are conducted in quiescent conditions. Four forcing configurations are characterized, covering (i) two-dimensional forcing, and spanwise wavelengths ($\widetilde{\lambda}_z$) of (ii) 12.5, (iii) 18.75, and (iv) 25.

Figure 5.5 shows visualizations of the flow induced by the plasma actuation for the two-dimensional and $\widetilde{\lambda}_z = 25$ actuators. The electrode overlap is located at $\widetilde{x} = 0$ with the high voltage and ground electrodes above and below, respectively. The induced jets are visible in the images due to the non-uniform dispersion of seeding particles in regions of high shear, which reveals that the jets are aligned in the streamwise direction and appear to originate at approximately $\widetilde{x} = 5$. As will be shown later, the jets originate closer to $\widetilde{x} = 0$, which could not be captured in the flow visualizations due to significant surface reflections that resulted when locating the laser closer to the surface. Nevertheless, the results demonstrate that the output of the two-dimensional actuator (Fig. 5.5a) is spanwise uniform after the start-up phase, while the $\widetilde{\lambda}_z = 25$ actuator (Fig. 5.5b) only induces flow within the regions of electrode overlap, *i.e.*, the active regions, with the flow remaining essentially stagnant in between. Similar flow visualizations results are reported for other actuators in Appendix C.2.1. Thus, the flow visualizations confirm that the spanwise modulated actuators are successful in creating spatially modulated flow disturbances at the desired spanwise wavelengths.

The side PIV measurements are used to quantify the momentum imparted to the fluid. Figure 5.6 presents contours of mean streamwise velocity across the span of the four investigated actuators. As is typically seen for surface mounted AC-DBD plasma actuators [108], at active locations away from the edges of actuator overlap, all actuators produce a wall jet predominantly in the streamwise direction with a minor inclination angle relative to the surface that originates just downstream of the electrode overlap ($\widetilde{x} = 0$). For the two-dimensional actuator (Fig. 5.6a), consistent with the flow visualizations (Fig. 5.5a), good spanwise uniformity is seen across the four measurement planes, with the variability quantified in the control volume analysis that follows. For the spanwise modulated actuators (Fig. 5.6b–d), the jet exhibits strong spanwise uniformity near the centre of the active region ($0 \leq \widetilde{z} \leq 1$), while the jet's streamwise velocity magnitude decreases as the edge is approach ($1.5 \leq \widetilde{z} \leq 2$), reaching zero at the edge of the actuator overlap ($\widetilde{z} = 2.5$) and in the gap region ($\widetilde{z} > 2.5$) where no positive streamwise velocity is observed. These observations are consistent with the flow visualizations, showing that the produced jets are more narrow than their active regions and are separated by stagnant fluid. Upon close inspection of the $\widetilde{z} = 2$ plane in Figs. 5.6b–d there is clear decrease in jet streamwise velocity with increasing wavelength, which

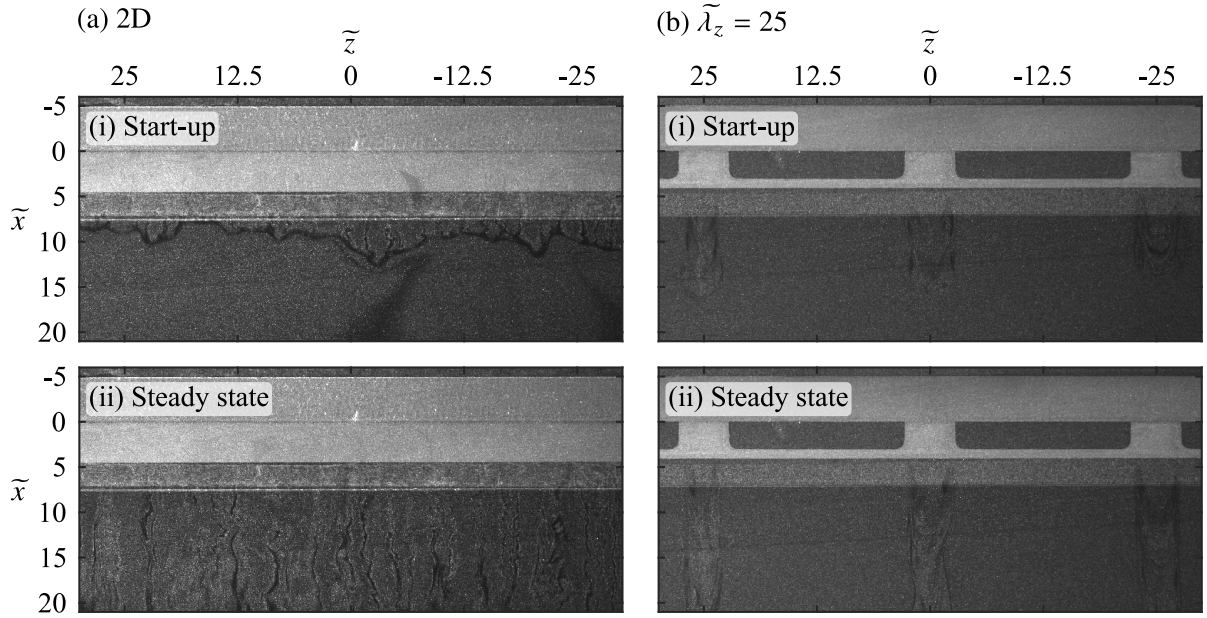

Figure 5.5: Visualization of flow induced due to plasma actuation during the (i) start-up and (ii) steady state phases ($V_{pp} = 6\,\text{kV}$, $f_c = 5\,\text{kHz}$, 100% duty cycle). Flow is from top-to-bottom.

may be the result of a weak interaction effect between adjacent jets of a given actuator. Overall the effect is weak, but it will result in a small difference in total momentum input per active region between the three spanwise modulated actuators.

A control volume analysis is employed to quantify the momentum imparted to the fluid. The selected control volume is shown in Fig. 5.7, which is employed for all actuators. It is noted that the use of planar PIV measurements in this configuration does not provide a measure of the spanwise transport of momentum, however, the flow visualizations (Fig. 5.5) provide qualitative evidence that this component is not significant, even for the spanwise modulated actuators. The control volume boundaries are selected to be sufficiently removed from the strong pressure gradients near the electrode overlap [109] since an estimate of pressure is not available. Performing a momentum balance in the x-direction gives:

$$T_x = \rho \left[\int_{ab} \overline{u}^2 \mathrm{d}y + \int_{bc} \overline{u}\,\overline{v} \mathrm{d}x - \int_{cd} \overline{u}^2 \mathrm{d}y \right], \tag{5.1}$$

where T_x captures the streamwise body/thrust force applied to the fluid and the generated wall shear stress. Separation of these two forces is not possible given the experimental limitations, however this is not critical given that the objective is quantification of differences in generated forces between the different configurations. Therefore, T_x is assumed to be a good representation of the total thrust forced applied to the fluid.

The results of the momentum calculations are presented in Fig. 5.8, which show that, thrust values ranging between $0.14 \leq T_x \leq 0.25\,\text{mN m}^{-1}$ are produced by the two-dimensional actuator (Fig. 5.8a) and the spanwise modulated actuators within the $0 \leq \widetilde{z} \leq 1$ section of the active region (Fig. 5.8b). These values are expected to be more or less equivalent given that thrust generation is

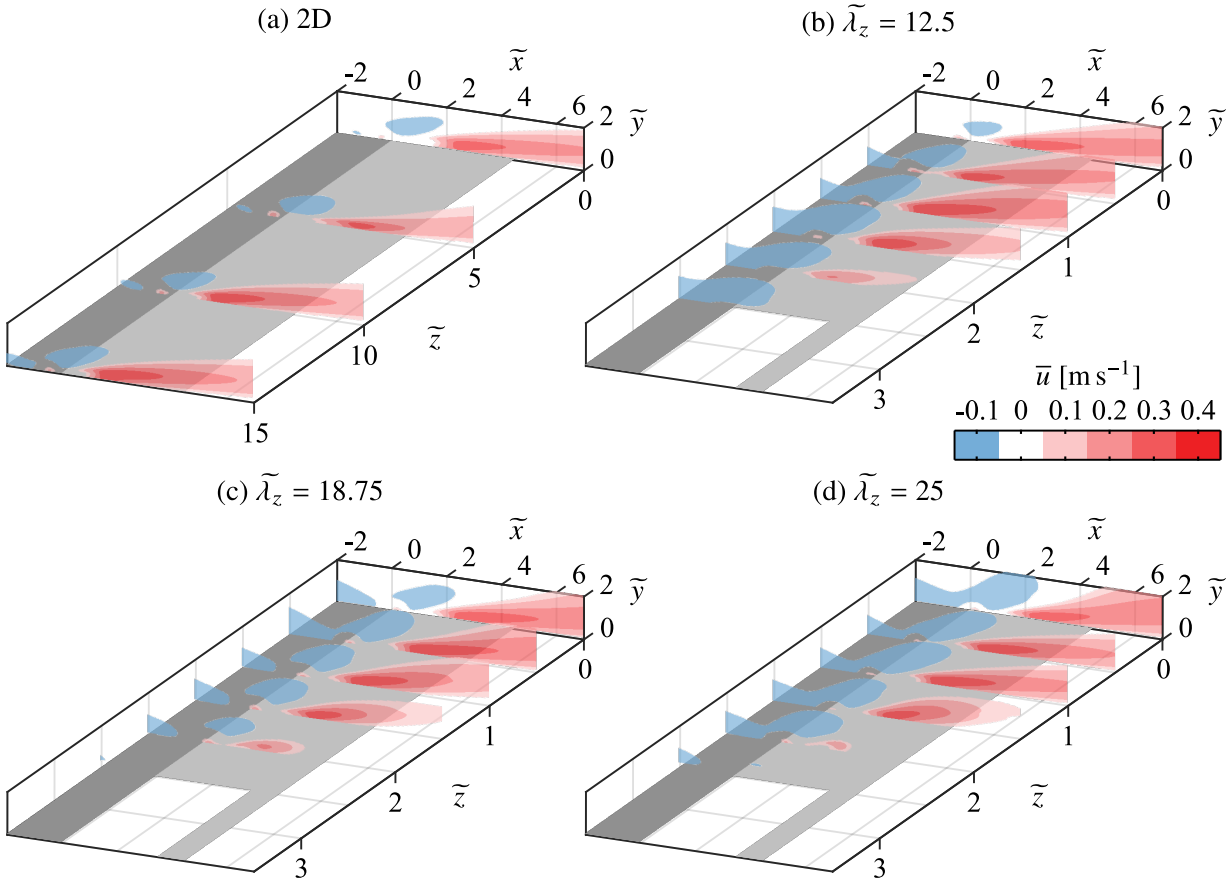

Figure 5.6: Contours of mean streamwise velocity across actuator spans (V_{pp} = 6 kV, f_c = 5 kHz, 100% duty cycle). Note different aspect ratios ($\widetilde{z}$-direction) between (a) and (b)–(d).

expected to be spanwise uniform in these areas, yet the values vary by as much as 33% from their mean. This variability in 'spanwise uniform' thrust generation is noted and is the likely result of imperfections in the manufacturing process (defects/contamination during paint application or drying) since the variability extends beyond the limits of the measurement uncertainty. On that note, the measurement uncertainty is relatively high given a number of challenges in the PIV experiments, the most significant of which is the low particle density levels in the region surrounding the electrode overlap, leading to a propensity for erroneous vectors in this region. A full discussion of the uncertainty related to these measurements is provided in Appendix B. Nevertheless, the measurements are still capable in resolving the decrease in thrust generated as the edge of the active region is approached and passed for the spanwise modulated actuators. Averaging T_x within the active regions (all measured values for the two-dimensional actuator, and within $0 \leq \widetilde{z} \leq 2.5$ for the spanwise modulated actuators) gives the average thrusts generated in the active regions, T_{act}, which are plotted in Fig. 5.8 as dashed lines. As expected, T_{act} is highest for the two-dimensional actuator, which is not subject to any end effects, while T_{act} is equal, within the experimental uncertainty, for the three spanwise modulated actuators. More sensitive experimental measurements are required to determine if the minimal decreases in T_{act} seen with increasing spanwise wavelength are due to weakening jet interaction effects.

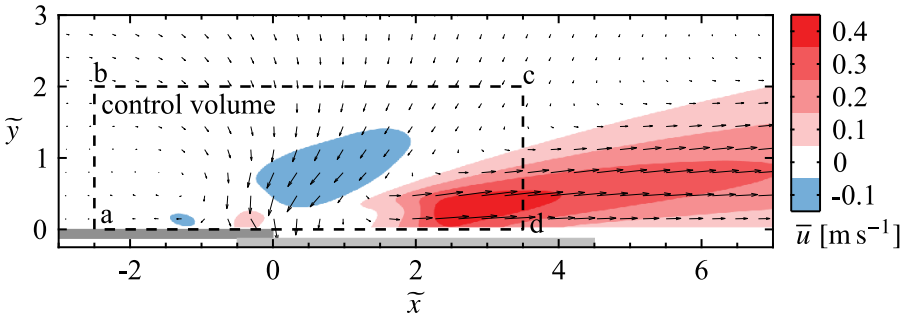

Figure 5.7: Contours of mean streamwise velocity at $\widetilde{z} = 0$ for the 2D actuator ($V_{pp} = 6\,\text{kV}$, $f_c = 5\,\text{kHz}$, 100% duty cycle). Dashed outline (corners abcd) indicates control volume for momentum analysis.

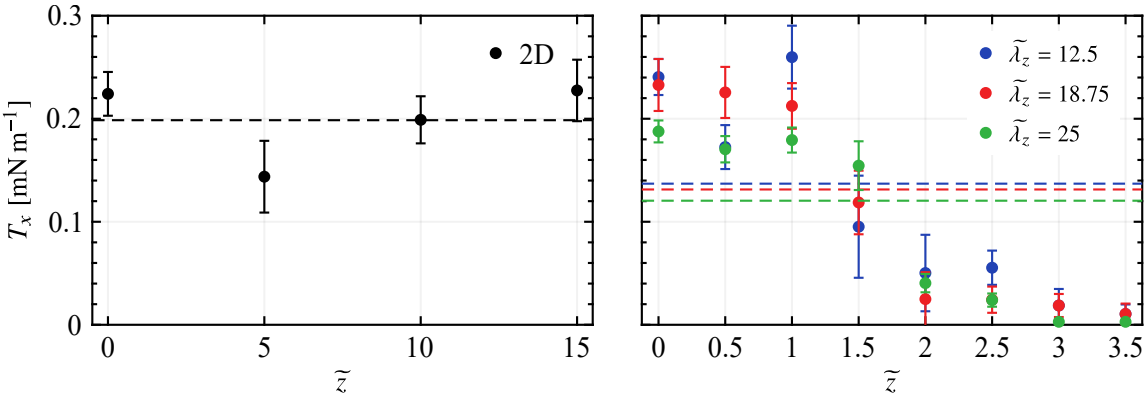

Figure 5.8: Sectional thrust generated across actuator spans ($V_{pp} = 6\,\text{kV}$, $f_c = 5\,\text{kHz}$, 100% duty cycle). Dashed lines (coloured according to legend) indicate average within the actuator active region (T_{act}).

The results presented thus far have been at a duty cycle of 100%, while in the experiments that follow (Section 5.5) it is the intention to operate the actuator outputs at lower duty cycles in order to produce disturbances that target the main instability within the LSB. As previously discussed (Section 5.2.1), this was necessary to provide sufficient mixing of seeding particles, which even still yielded relatively high uncertainty levels (Fig. 5.8). The approach is then to collect results over a range of duty cycles so that the higher uncertainties associated with lower duty cycle operation can be somewhat mitigated through consideration of the entire dataset and the use of linear interpolation. The effect of duty cycle on thrust generated at a single plane ($\widetilde{z} = 0$) for the two-dimensional actuator is plotted in Fig. 5.9. The uncertainty intervals remain relatively constant with duty cycle, confirming that results at lower duty cycles are subject to much higher relative uncertainties. Within the experimental uncertainty, the trend in T_x with duty cycle is approximately linear, and thus the thrust generated by the actuators at other duty cycles is estimated through linear interpolation of the current results.

Since negligible thrust is produced in areas where the electrodes do not overlap (Figs. 5.5 and 5.6), estimates of the total thrust produced by an actuator can be made from the average

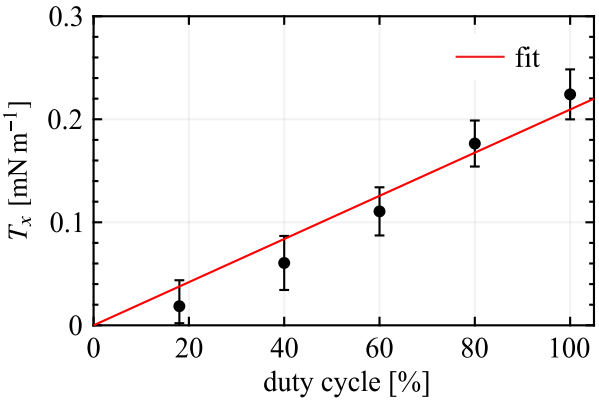

Figure 5.9: Effect of duty cycle on sectional thrust generated at $\widetilde{z} = 0$ for the 2D actuator ($V_{pp} = 6\,\text{kV}$, $f_c = 5\,\text{kHz}$, $f_m = 133\,\text{Hz}$).

sectional thrust generated in the active regions (T_{act}, Fig. 5.8) and the actuator's total active length, which are 385, 150, 110 and 70 mm for the $\widetilde{\lambda}_z = 0$, 12.5, 18.75, and 25 actuators, respectively. These results are presented in Table 5.2, which shows that for a given duty cycle, as expected, the total thrust produced decreases with increasing spanwise wavelength. Also, the results highlight that achieving equal momentum output across all the four actuators through varying the duty cycle is not practically possible since, for example, the $\widetilde{\lambda}_z = 25$ actuator at 100% duty cycle produces less than half the momentum of the two-dimensional actuator at 25% duty cycle. One approach to producing spanwise modulated disturbances of different wavelengths while holding the output momentum constant is to superimpose the output of the two-dimensional actuator with that of a spanwise modulated actuator by arranging them in streamwise succession (Fig. 5.1), with the key assumption being that the momentum outputs of each actuator will linearly superimpose in this arrangement. To this end, a streamwise separation of 26 mm ($\widetilde{x} = 13$) is used between actuators (Fig. 5.1) which, based on the results seen in Fig. 5.6, should ensure the momentum outputs of the two actuators remain independent. Therefore, the superposition of momentum output is assumed valid and duty cycles for various actuator combinations are found that give equal amounts of total momentum output. These values are reported in Table 5.2 as superposition momentum coefficients, showing that the outputs of the $\widetilde{\lambda}_z = 12.5$, 18.75, and 25 actuators superimposed with that of the two-dimensional actuator at duty cycles of 21%, 22%, and 23%, respectively, give total C_μ values that match the output of just the two-dimensional actuator at a duty cycle of 25%. Thus, operating conditions for the two-dimensional actuator and three cases of superposition with the spanwise modulated actuators have been identified. These conditions produce equivalent total output momentum across all four cases and will be used in the experiments that follow (Section 5.5).

5.4 In-Flow Characterization

The characterization efforts now shift to determining the phase delay needed to superimpose the actuator outputs and the resulting streamwise topology of the disturbances. This requires the

Table 5.2: Thrust and momentum coefficient estimates ($V_{pp} = 6\,\text{kV}$, $f_c = 5\,\text{kHz}$, $f_m = 133\,\text{Hz}$).

Actuator ($\widetilde{\lambda_z}$)	Duty cycle [%]	T_{tot} [μN]	C_μ [$\times 10^{-4}$]	Superposition C_μ [$\times 10^{-4}$]
2D	100	71.4 ± 6.8	46.8 ± 4.5	–
12.5	100	19.2 ± 1.8	12.6 ± 1.2	–
18.75	100	13.5 ± 1.2	8.8 ± 0.8	–
25	100	7.9 ± 0.9	5.2 ± 0.6	–
2D	25	18.6 ± 3.8	12.2 ± 2.4	12.2 ± 2.4
2D	21	15.0 ± 3.4	9.8 ± 2.2	12.4 ± 2.3
12.5	21	4.0 ± 0.8	2.6 ± 0.6	
2D	22	15.7 ± 3.4	10.3 ± 2.2	12.2 ± 2.3
18.75	22	3.0 ± 0.6	1.9 ± 0.4	
2D	23	16.4 ± 3.6	10.8 ± 2.4	12.0 ± 2.4
25	23	1.8 ± 0.4	1.2 ± 0.2	

correct external flow conditions, and so the experimental setup described in Section 5.2.2 is used. Thus, a laminar separation bubble is formed over a flat plate at a nominal Reynolds number of $Re_{\delta_{1_s}} = 750$ and the flow is forced by the surface-mounted, AC-DBD plasma actuators (Fig. 5.1), characterized in Section 5.3. Five cases are considered: (i) the natural/unforced flow (shorthand Nat.), (ii) two-dimensional forcing (shorthand 2D), and three-dimensional forcing with spanwise wavelengths ($\widetilde{\lambda_z}$) of (iii) 12.5, (iv) 18.75, and (v) 25. Two-dimensional forcing is achieved through operation of a single spanwise uniform actuator, while for the three-dimensional forcing cases two actuators are arranged in streamwise succession and operated simultaneously. The total momentum imparted to the fluid is kept constant across all forcing cases by using duty cycles of 25%, 21%, 22%, and 23% for the 2D, and $\widetilde{\lambda_z} = 12.5$, 18.75, and 25 cases (Table 5.2), respectively, while keeping all other forcing parameters constant ($V_{pp} = 6\,\text{kV}$, $f_c = 5\,\text{kHz}$, $f_m = 133\,\text{Hz}$).

A phase delay between the two-dimensional and a given three-dimensional actuator must be determined in order to spatially superimpose the produced disturbances. The phase delay is expected to depend on the spatial separation of the actuators, the forcing parameters, and the external flow. To this end, PIV measurements synchronized to the forcing cycle were acquired in the top view configuration (Fig. 5.3b) with each actuator operating in isolation (no superposition), with the results presented in Fig. 5.10 showing phase-averaged streamwise velocity. The measurements were performed in the aft portion of the LSB ($\overline{\widetilde{x_s}} = 0$ for the unforced case) so that the disturbances reached measurable amplitudes, with the laser sheet positioned such that is passed through the top halves of formed shear layer vortices in this region, thus resulting in the capture of the disturbances as bands of relatively high streamwise velocity.

From Fig. 5.10, the disturbances produced from the three-dimensional actuators (Fig. 5.10c–e) are at approximately equivalent spatial locations for the same phase angles of their forcing cycles, indicating that upstream of the measurement domain the disturbances travel at roughly equivalent convective velocities. For the same phase angle in the two-dimensional actuator's forcing cycle

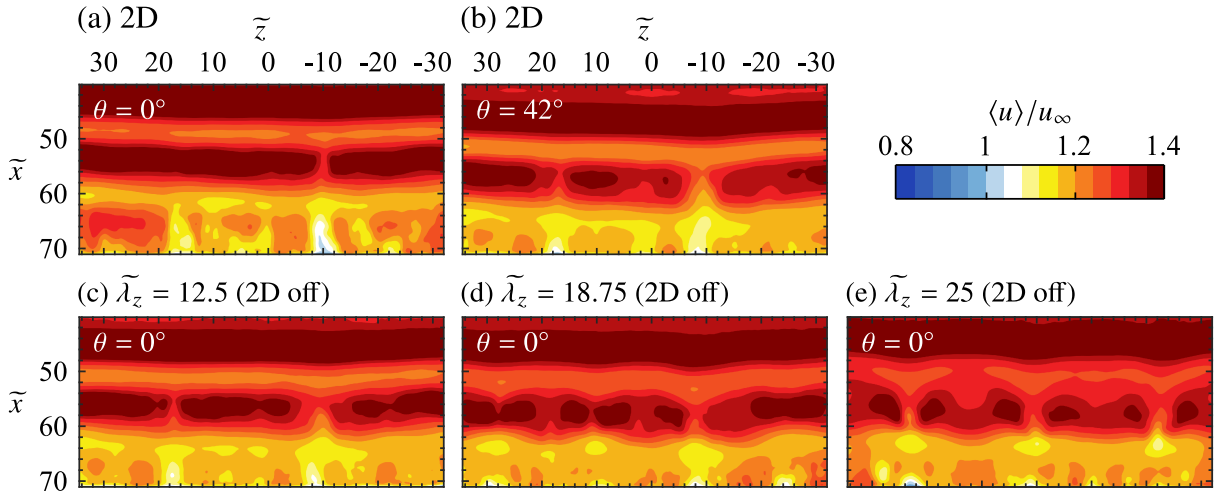

Figure 5.10: Phase-averaged streamwise velocity contours. Flow is from top-to-bottom. Note that the 2D actuator is off for (c)–(e).

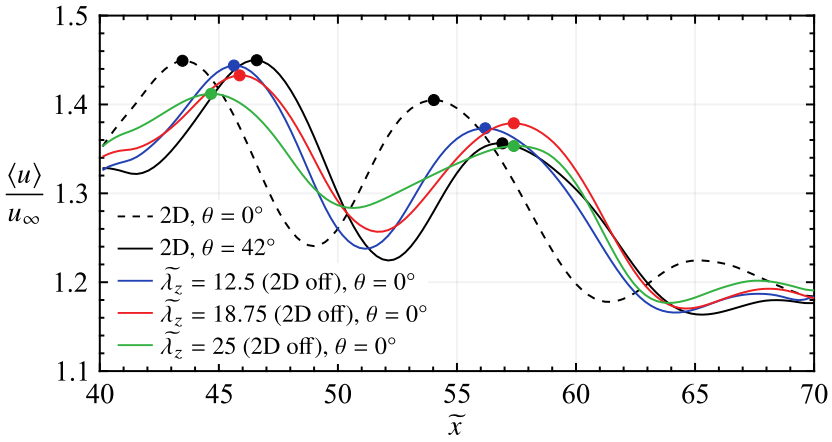

Figure 5.11: Phase and spanwise-averaged streamwise velocity for the same cases presented in Fig. 5.10. Markers (coloured according to legend) indicate selected local maxima.

(θ = 0° in Fig. 5.10a), disturbances are further upstream compared to Fig. 5.10c–e, which is attributed to the upstream positioning the two-dimensional actuator (Fig. 5.1). Advancing 42° in the 2D forcing cycle (Fig. 5.10b) positions the disturbances at similar streamwise locations to three spanwise modulated cases, which is verified in Fig. 5.11, where the velocity fields in Fig. 5.10 are spanwise-averaged and plotted. Selected local maxima in the spanwise-averaged velocity (markers in Fig. 5.11) estimate the position of the disturbances and are used to determine the optimal phase shift in order to spatially superimpose the two-dimensional disturbances with all three outputs of the spanwise modulated actuators. This phase shift is determined to be 42°, meaning when two actuators are operated simultaneously, the two-dimensional forcing cycle must lead that of the three-dimensional forcing by 42°.

The result of operating the $\widetilde{\lambda}_z$ = 12.5, 18.75, and 25 forcing configurations for disturbance superposition using the determined phase delay is presented in Fig. 5.12, where all three cases

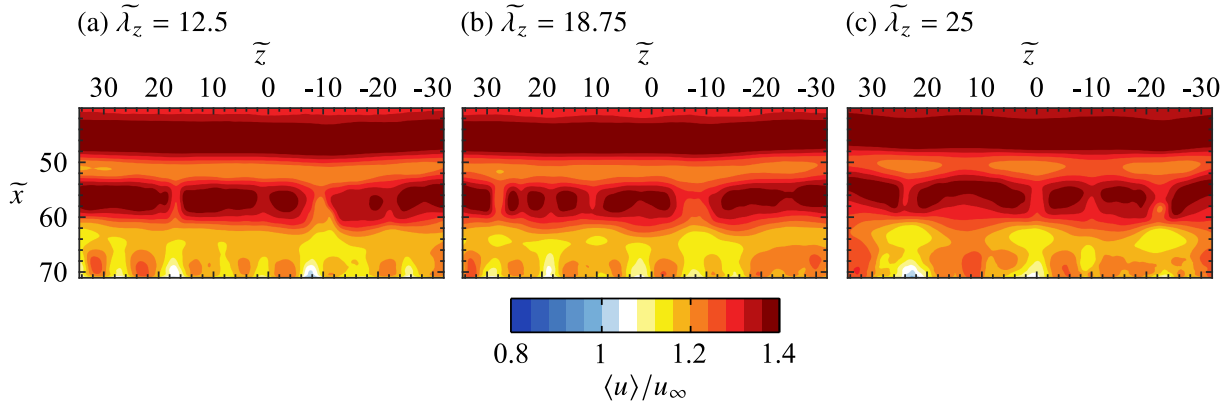

Figure 5.12: Phase-averaged streamwise velocity contours for phase $\theta = 0$ showing disturbance superposition. Flow is from top-to-bottom.

show the same streamwise disturbance wavelength ($\widetilde{\lambda}_x \approx 12.5$) as the two-dimensional forcing case (*cf.* Figs. 5.10a and 5.10b). Thus, across all the forcing configurations considered, the produced disturbances are of the same frequency and streamwise wavelength. The former is by virtue of operating all actuators at the same modulation frequency ($f_m = 133$ Hz), while the latter is achieved by successful superposition of disturbances for the three-dimensional forcing cases (Fig. 5.12). Additionally, the results of the quiescent characterization confirm that the total momentum imparted to the fluid is equal across all these case (Table 5.2).

5.5 Effect on LSB Flow Development: Preliminary Study

With the forcing technique fully characterized, three-dimensional forcing with superposition may be applied to the flow, and flow development in the LSB may be contrasted with that of the natural and two-dimensional forcing cases. Figure 5.13 presents these results with sequences of instantaneous streamwise velocity measured via the top view PIV configuration. For the natural case (Fig. 5.13a), strongly coherent spanwise vortices with significant spanwise undulations are apparent in the upstream portion of the field of view ($\widetilde{x} < 50$). Further downstream, structures of a similar spanwise wavelength are identifiable, however their spanwise coherence is decreased. For the particular instant depicted in Fig. 5.13a, the predominant spanwise wavelength in the vortex filaments is approximately $\widetilde{\lambda}_z = 30$. A rigorous statistical characterization of the spanwise wavelengths that develop in the vortex filaments follows later in this section. With respect to the streamwise wavelength of the structures, across all of Fig. 5.13, the predominant streamwise wavelength of the structures is $\widetilde{\lambda}_x = 12.5$. This is confirmed via POD analysis (see Appendix C.2.2) to be the mean streamwise wavelength of the LSB shear layer vortices for all cases, which is a direct result of the forcing targeting the frequency of the most amplified disturbances in the natural flow. Thus, representing the spanwise forcing wavelengths with respect the predominant streamwise wavelength gives $\widetilde{\lambda}_z = \widetilde{\lambda}_x$, $1.5\widetilde{\lambda}_x$, and $2\widetilde{\lambda}_x$ for the $\widetilde{\lambda}_z = 12.5$, 18.75, and 25 cases, respectively. These cases cover the lower portion of the range $1 \lesssim \lambda_z/\lambda_x \lesssim 7$ reported in Chapter 4 (Section 4.3.1) and other previous investigations [113, 137, 153].

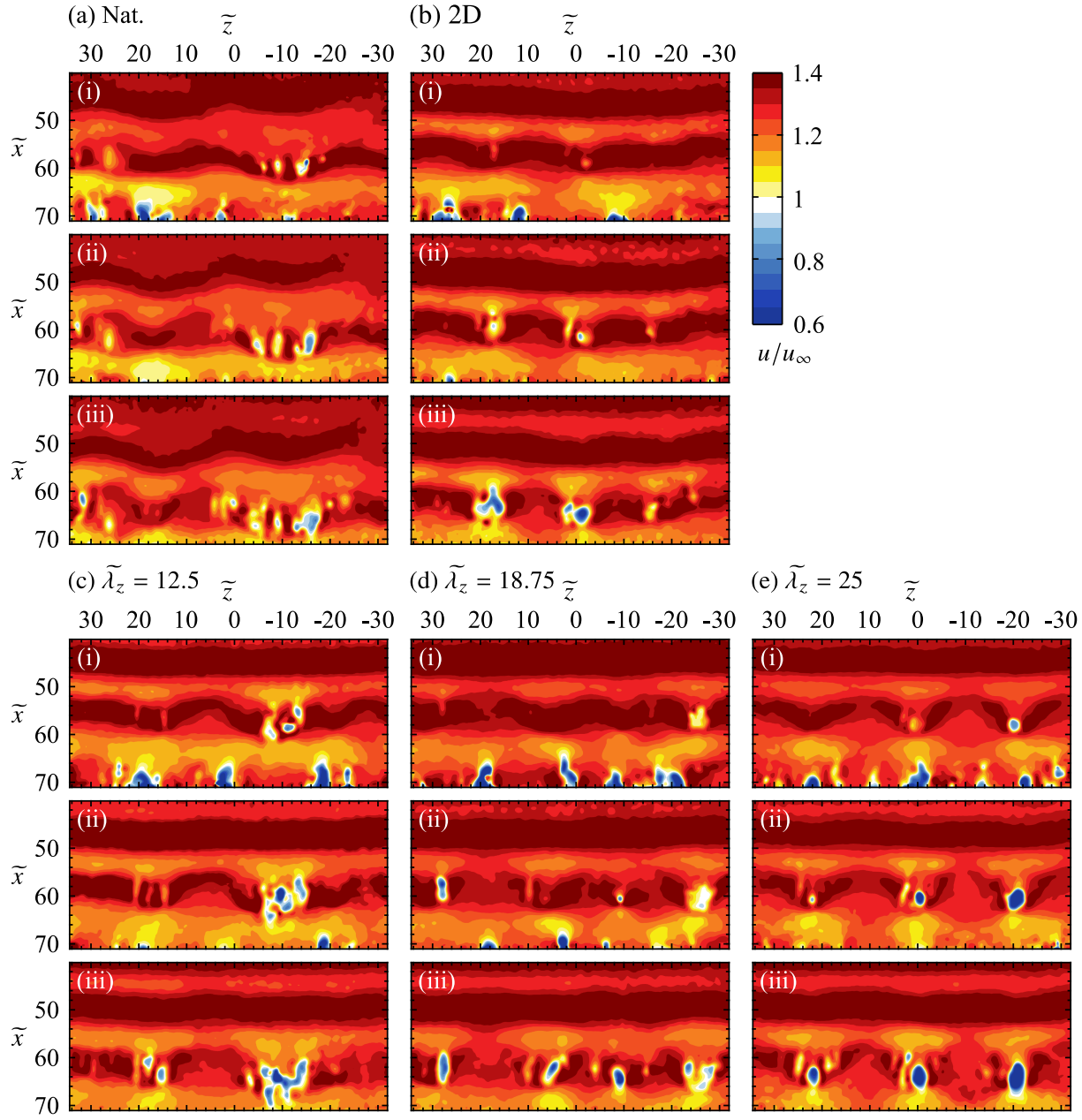

Figure 5.13: Sequences of instantaneous streamwise velocity contours. Flow is from top-to-bottom. Consecutive frames separated by $t^*_{\delta_{1s}} = 4.6$.

From Fig. 5.13, significant changes in the flow development are observed when the flow is forced. Specifically, for the two-dimensional forcing case, the most upstream vortex in Fig. 5.13a-i is uniform across the span and remains largely two-dimensional as it convects downstream, while developing relatively minor spanwise undulations. These undulations are more apparent in the downstream structure, located at $\widetilde{x} \approx 56$ in Fig. 5.13a-i. As this structure convects downstream, localized breakup regions develop at the locations where the filament bulges forward in the streamwise direction as was noted in Fig. 4.8. That being said, comparing the downstream structure in Fig. 5.13b-ii to the structures at the same streamwise locations in the natural flow (*e.g.*, at $\widetilde{x} \approx 62$ in Fig. 5.13a–ii) reveals that the two-dimensional forcing leads to an increase in spanwise coherence in the formed shear layer vortices, which persists as the vortices develop downstream. In a similar manner, results for the three-dimensional forcing cases (Fig. 5.13c–e) show highly spanwise uniform vortex filaments upstream of $\widetilde{x} = 50$. This reflects the fact that the disturbances introduced into the flow for the spanwise modulated forcing cases are primarily two-dimensional, with only a weak three-dimensional component. This is to be expected given that the two-dimensional actuator provides 80 to 90% of the total momentum for the three-dimensional forcing cases. However, despite the relative weakness of the three-dimensional forcing components, spanwise wavelengths that match the forcing wavelength are evident for the $\widetilde{\lambda}_z = 25$ forcing, particularly in the structure at $\widetilde{x} = 54$ in Fig. 5.13e-i. Note that regions where the downstream vortex in Fig. 5.13e bulge forward are downstream of where the spanwise modulated actuator is active ($\widetilde{z} = -25$, 0, and 25, see Fig. 5.1), while the filament lags behind at spanwise locations downstream of the actuator gaps.

The flow development depicted in Fig. 5.13e confirms a crucial aspect of this investigation, as the $\widetilde{\lambda}_z = 25$ forcing does not result in a simple spanwise modulation of the base flow. Rather, the results point to the presence of an instability mechanism within the LSB that amplifies the spanwise component of the input disturbances, causing the initially two-dimensional vortex filament to develop significant spanwise undulations at the prescribed wavelength. Furthermore, there is an apparent spanwise wavelength dependence, as spanwise undulations in the vortex filaments matching the input of the $\widetilde{\lambda}_z = 12.5$ and 18.75 forcing are not readily identified in the flow (Figs. 5.13c and 5.13d, respectively). Therefore, these cases may serve to force the flow in a manner more akin to the two-dimensional forcing, however, statistical evidence is needed to support this claim.

A statistical characterization of the spanwise wavelengths that develop in the LSB shear layer vortices is carried out using wavelet analysis (Section 3.3.3), which is preferred over spatial Fourier analysis due to the limited spanwise extent of the PIV field of view. From the top view PIV measurements (*e.g.*, Fig. 5.13), fluctuating streamwise velocity signals are extracted at $\widetilde{x} = 45$, 55, and 65, smoothed using a spatial kernel of width $\widetilde{x} = 1.5$, and wavelet coefficients are calculated using the Morlet wavelet [43]. An exemplary signal and its corresponding wavelet coefficients are presented in Fig. 5.14. For a given time instant, the predominant spanwise wavelength is estimated from the maximum wavelet coefficient, with the process repeated for all time realizations, resulting in 4480 statistical samples obtained per streamwise location. The resulting histograms are presented in Fig. 5.15. For the natural case (Fig. 5.15a), the distribution at $\widetilde{x} = 45$ is evenly spread across a wide range of wavelengths, $12 \lesssim \widetilde{\lambda}_z \lesssim 60$, with a minor peak at $\widetilde{\lambda}_z = 29$, which roughly matches what is seen in Fig. 5.13 at this location. The wide dispersion of values indicates

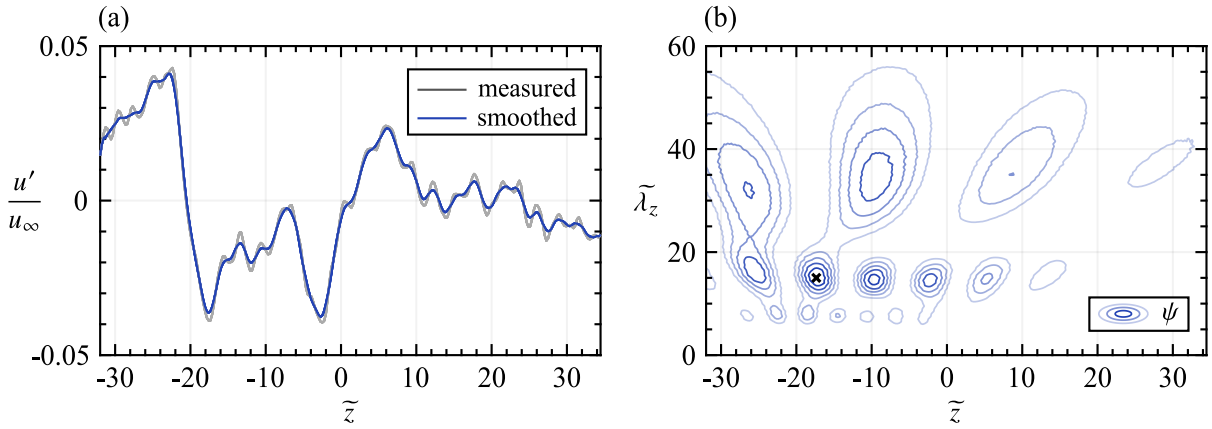

Figure 5.14: (a) Exemplary fluctuating streamwise velocity sampled across the span at $\widetilde{x} = 45$ in the natural flow and (b) corresponding wavelet coefficient contours. Maximum wavelet coefficient indicated by × marker.

that there is significant variability in the initial undulations of the naturally developing shear layer vortices, with a minor preference toward spanwise wavelengths of $\widetilde{\lambda}_z \approx 30$. When compared to the predominant streamwise wavelength of the structures, $\widetilde{\lambda}_x = 12.5$, the general range of wavelengths observed at $\widetilde{x} = 45$ in Fig. 5.15a is $1 \lesssim \lambda_z/\lambda_x \lesssim 5$, which is in agreement with previous LSB investigations [113, 137, 153].

From Fig. 5.15a, the wavelength distributions shift to lower values as the vortices convect downstream to $\widetilde{x} = 55$ and 65, with a significant peak centred at $\widetilde{\lambda}_z = 5$ seen in the distribution of the most downstream station. This shift is associated with the turbulent breakup of the shear layer vortices, seen in Fig. 5.13, as the prominent fluctuations that are localized to the breakup regions in the vortex filaments are characterized by these short wavelengths. In fact, all cases presented in Fig. 5.15 show this shift to shorter wavelengths as the flow develops downstream, confirming that this trend is indicative of turbulent breakdown. When the flow is subjected to the two-dimensional forcing, the shear layer vortices are initially spanwise uniform (Fig. 5.13b), while the results at $\widetilde{x} = 45$ in Fig. 5.15b show a distribution that spans the entire detectable range of wavelengths, which is indicative of the structures being spanwise uniform, with the analysis method detecting small amplitude undulations present in the velocity signals, with wavelengths concentrated at three minor peaks, two of which roughly match the natural case at the same streamwise location ($\widetilde{\lambda}_z \approx 28$ and 50). The peak at the lowest wavelength value, $\widetilde{\lambda}_z = 5$, may indicate an intermittent onset of turbulent breakdown, but could also result from noise in the PIV measurement that is not completely removed by the smoothing process.

It is instructive to begin the examination of the spanwise modulated forcing results with the $\widetilde{\lambda}_z = 25$ case (Fig. 5.15e), where spanwise undulations at and near the forcing wavelength are detected in the flow at $\widetilde{x} = 45$. The peak in the histogram is found at $\widetilde{\lambda}_z = 22$, which indicates that there is a tendency for the input wavelength of the disturbance to be modified slightly as the disturbances grows through the upstream boundary layer and into the LSB. It must be noted that the wavelet analysis only quantifies the probability distribution of spanwise wavelengths present in the velocity signals, and does not provide a measure of the magnitude of any particular

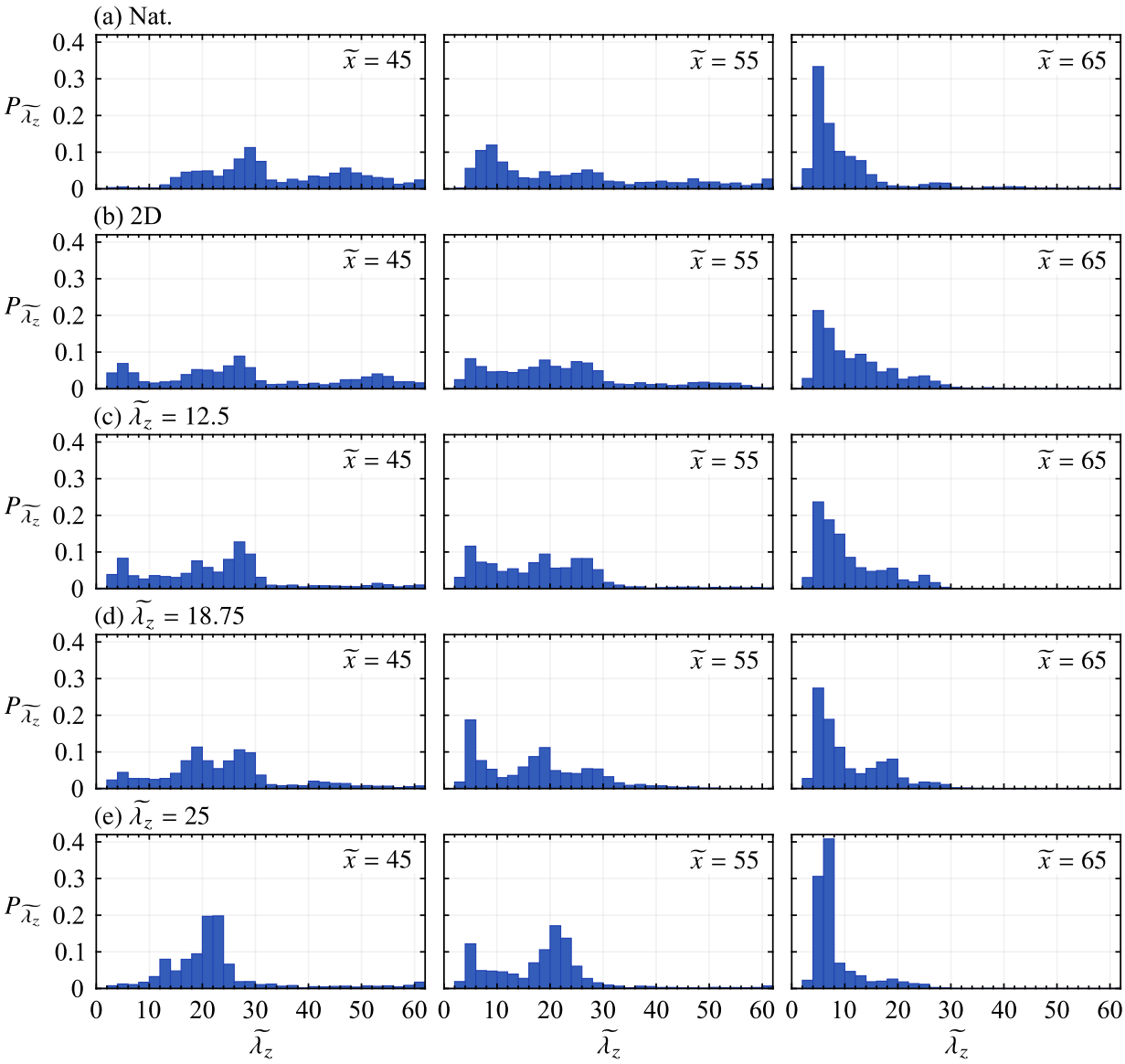

Figure 5.15: Spanwise wavelength probability distributions determined from spatial wavelet analysis (Fig. 5.14). Dotted lines indicate standard deviation from the mean (dashed line).

spanwise deformation present in the flow. Therefore, the $\widetilde{\lambda}_z \approx 25$ peak in the histogram at $\widetilde{x} = 45$ is reflective of a tendency for undulations at this wavelength, with evaluation of the flow development (Fig. 5.13e) affirming that these undulations are of a relatively minor amplitude at this streamwise location. As the structures develop downstream to $\widetilde{x} = 55$ and 65, the distributions shift toward lower wavelengths as a result of turbulent breakdown. A similar trend can be seen for the $\widetilde{\lambda}_z = 18.75$ case (Fig. 5.15d), as a minor peak centred at the input wavelength is found in the distribution at $\widetilde{x} = 45$, albeit the effect is not as apparent as seen for the $\widetilde{\lambda}_z = 25$ forcing, which indicates that indeed three-dimensional disturbance growth is wavelength dependent, with growth at $\widetilde{\lambda}_z \approx 25$ being preferred over $\widetilde{\lambda}_z = 18.75$ and 12.5. In fact, in examining the results

of the $\widetilde{\lambda}_z = 12.5$ forcing case (Fig. 5.15c), none of the distributions show peaks at the forcing wavelength. Instead the distributions resemble that of the two-dimensional forcing case, indicating that spanwise component introduced by the forcing has been damped out and the flow is primarily forced in a two-dimensional manner.

Given the perceived increased receptivity of the flow to spanwise disturbances with wavelength $\widetilde{\lambda}_z = 25$, the focus now shifts to contrasting the results of that case in particular with those of the natural flow and the two-dimensional forcing case. Contours of phase-averaged spanwise vorticity, measured using the side view PIV configuration (Fig. 5.3a), are presented in Fig. 5.16. Results for only the two-dimensional and $\widetilde{\lambda}_z = 25$ cases are presented since phase-averaging is not possible for the natural case. To aid in visualizing the development of the shear layer vortices throughout the forcing cycle, the cores of vorticity for a selected vortex are identified using the λ_2-criterion [88], and are connected using a smoothing spline fit. The results in Fig. 5.16 affirm the observations made from the top view PIV measurements (Fig. 5.13), as vortex filaments are initially two-dimensional under both types of forcing. As the vortices develop downstream, a clear spanwise undulations matching the forcing wavelength develop for the $\widetilde{\lambda}_z = 25$ case (Fig. 5.16b-iii) that is absent in the presence of purely two-dimensional forcing (Fig. 5.16a-iii). Figure 5.16b provides further insight into the effects of the spanwise modulated forcing, as it shows the core of the shear layer vortex is closer to the surface in the region $\widetilde{z} \geq 7.5$, which is where the filaments lags behind the streamwise forward section that develops within $\widetilde{z} \leq 5$. This type of motion could be the result of the spanwise undulation in the filament, since a filament of such topology would self-induce a net rotational motion, causing lift-up and push-down on the regions where the filament bulges forward and lags behind, respectively. This, coupled with the strong wall-normal velocity gradient, would lead to a continual intensification of the vortex stretching, until localized breakup takes place, as seen in Fig. 5.13e-ii at $\widetilde{x} \approx 60$. These dynamics are examined in detail through the development of vortex filament in Section 5.5.1.

Previous investigators [134, 260] and the findings presented in Appendix A demonstrate that the reattachment process in LSBs is almost entirely governed by the dynamics of the shear layer vortices, and so significant changes in the mean flow topology are expected as a result of the investigated forcing techniques. This is first examined through contours of mean streamwise velocity from the side view PIV measurements, presented in Fig. 5.17. As in Chapter 4, the topology of the separation bubble is characterized using the dividing streamline, which forms a closed contour with surface within which the streamwise mass flux is zero [58, 76, 172]. The intersection points of the dividing streamline with the surface give the mean separation and reattachment points, with the former not being estimated as a result of lying well upstream of the measurement domain for all cases. The maximum bubble height and its streamwise location are also estimated, and are found where the maximum wall-normal distance between the surface and dividing streamline occurs.

The results plotted in Fig. 5.17a show the natural separation bubble reaches a maximum height of $\widetilde{h} = 0.8 \pm 0.12$ at $\widetilde{x}_\mathrm{h} = 44.6 \pm 0.10$ and reattaches to the surface, in the mean sense, at $\widetilde{x}_\mathrm{r} = 57.0 \pm 0.55$. Examining the same spanwise plane, $\widetilde{z} = 0$, when the flow is forced reveals small changes in the mean characteristics of the LSB for both the two-dimensional and $\widetilde{\lambda}_z = 25$ cases, which is to be expected given the relatively small forcing amplitudes employed (Table 5.2). That being said, both types of forcing do lead to slight upstream shifts in the maximum bubble height

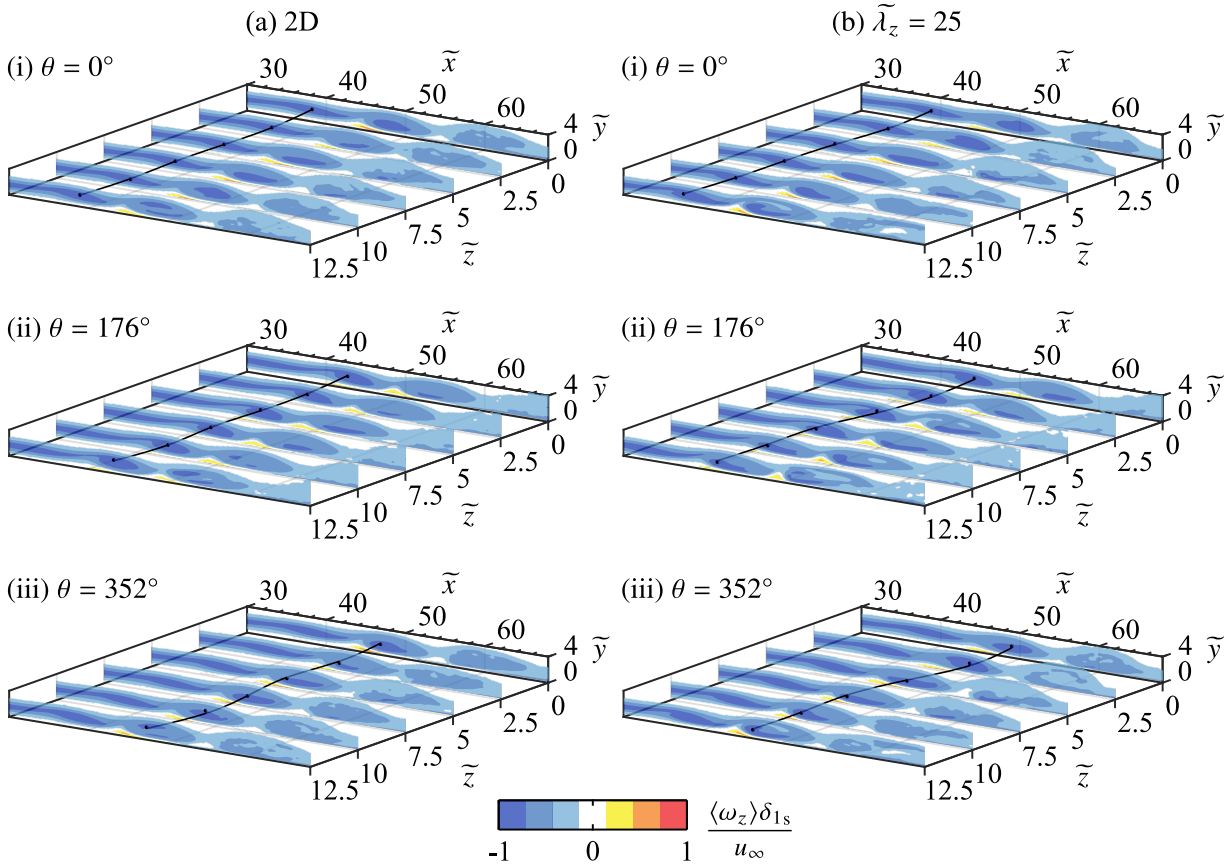

Figure 5.16: Sequence of phase-averaged spanwise vorticity contours. Circle markers indicate vorticity cores for a given structure, identified via the λ_2-criterion [88], and are connected using smoothing spline fits.

and reattachment locations, which is consistent with the findings in Appendix A (Fig. A.3) and other previous reports on the effects of periodic forcing on separation bubble mean topology [151, 260]. However, in all other investigations, forcing also leads to a reduction in the maximum bubble height, while the opposite is found here as the maximum bubble height increases to approximately $\widetilde{h} = 1.1 \pm 0.12$ for both the 2D and $\widetilde{\lambda}_z = 25$ cases. A detailed comparison between these two cases and the natural flow is presented in Chapter 6, which clarifies that this results from low frequency activity in the natural LSB.

With regards to spanwise topology of the bubble, as outlined in Section 5.2.2, data at spanwise planes other than $\widetilde{z} = 0$ are only available for the forcing cases. Therefore, an examination of the spanwise topology of the natural LSB is reserved for Chapter 6, while here the spanwise topology between the two forcing cases can be compared. Fig. 5.17b reveals negligible difference between the $\widetilde{z} = 0$ and 12.5 planes for the two-dimensional forcing case, with the small differences between the maximum bubble height and reattachment locations lying within the experimental uncertainty. Given this and the inevitable minor imperfections present in experiments, the mean bubble topology for this case can be considered essentially two-dimensional, which is to be expected given the type of forcing. In contrast, significant differences are observed between the

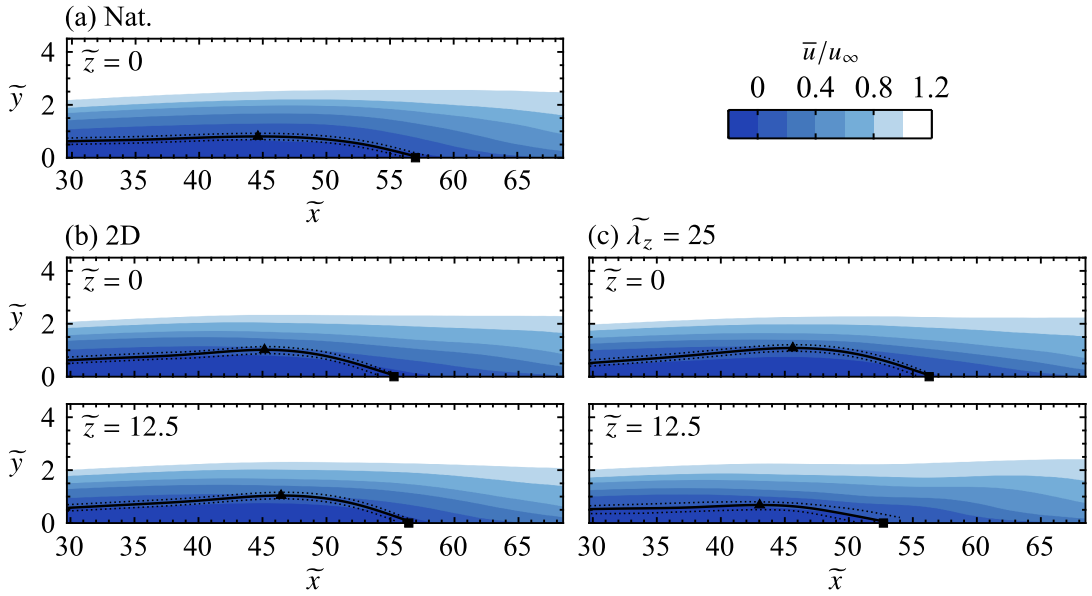

Figure 5.17: Contours of mean streamwise velocity at selected spanwise locations. Solid lines mark the dividing streamlines, whose uncertainty bounds are indicated by the dotted lines. Triangle and square markers denote estimated mean maximum bubble height and reattachment points, respectively.

$\widetilde{z} = 0$ and 12.5 planes for the $\widetilde{\lambda}_z = 25$ forcing case. The mean topology at $\widetilde{z} = 0$ largely resembles that at the same plane for the two-dimensional forcing case, while significant upstream shifts in $\widetilde{x}_h$ and $\widetilde{x}_r$ and a reduction in $\widetilde{h}$ is found at the $\widetilde{z} = 12.5$ plane for the $\widetilde{\lambda}_z = 25$ case. These results indicate that the effects of the spanwise modulated forcing on the mean flow topology are most pronounced in regions of the streamwise rearward 'valleys' of the input disturbance (*e.g.*, $\widetilde{z} = 12.5$, from Fig. 5.16b), while in the regions of the disturbance's streamwise forward 'crests' ($\widetilde{z} = 0$), the forcing acts in a similar manner to equivalent (in terms of momentum input), yet purely two-dimensional forcing. Relating the changes observed in the mean topology of the LSB at $\widetilde{z} = 12.5$ to the vortex dynamics, Fig. 5.16b revealed that the shear layer vortices are closer to the surface in this region, which is consistent with the upstream advancement in reattachment and reduction in bubble height seen in Fig. 5.17c.

Further insight into the disturbance development within the LSB is gained through an examination of root-mean-square contours of the wall-normal velocity fluctuations, which are plotted in Fig. 5.18. Overall, the contours for the natural case (Fig. 5.18a) match previous results for naturally developing separation bubbles (Figs. 4.4 and A.3, and in Refs. [113, 125, 260]), with the streamwise amplification of disturbances first detected just upstream of the maximum bubble height location. This is followed by strong growth in disturbance amplitudes in the aft portion of the bubble due to the shedding of the shear layer vortices. A similar trend is seen for the two-dimensional forcing case (Fig. 5.18b), albeit amplification is detected at earlier streamwise locations as a result of the forcing targeting the primary instability with the LSB. Moreover, Fig. 5.18b provides further evidence that the two-dimensional forcing is indeed two-dimensional, as the rms contours for the $\widetilde{z} = 0$ and 12.5 planes only show minor differences.

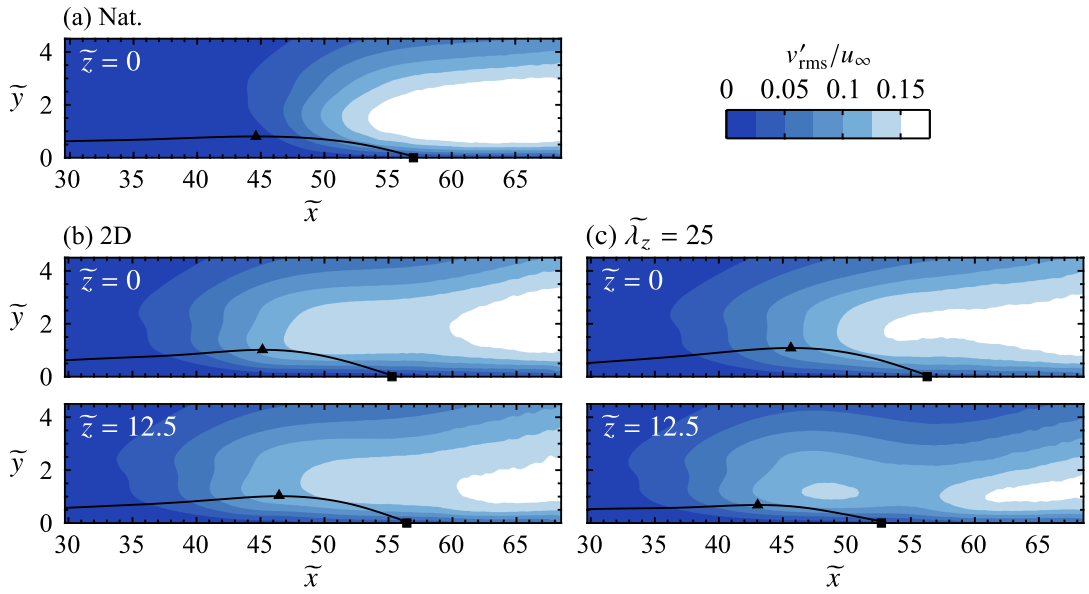

Figure 5.18: Rms of fluctuating wall-normal velocity contours at same spanwise locations as Fig. 5.17. Solid lines mark the dividing streamlines. Triangle and square markers denote estimated mean maximum bubble height and reattachment points, respectively.

Examining the v'_{rms} contours for the $\widetilde{\lambda}_z = 25$ case (Fig. 5.18c) reveals similar disturbance amplification for the $\widetilde{z} = 0$ plane to that of the two-dimensional forcing case, although higher amplitude disturbances are found for the $\widetilde{\lambda}_z = 25$ case in the aft portion of the bubble, which may be related to an earlier onset of turbulent breakdown as a result of the vortex stretching (Fig. 5.16b) and localized breakup (Fig. 5.13e) that occurs in this region. However, this does not impact the mean topology of the LSB, which is consistent with the arguments put forward in Section A.3.3, where it is contended that the location at which vortex formation occurs is the most significant factor affecting separation bubble topology. The strong effect of vortex formation and the associated dynamics on the rms contours is further reinforced at the $\widetilde{z} = 12.5$ plane for the $\widetilde{\lambda}_z = 25$ case. Here, as a result of the vortex being stretched and pushed toward the surface, a localized region of high velocity fluctuations is found relatively close to the surface at $\widetilde{x} \approx 49$. Moving downstream, the rms levels do not rise continuously as the reattachment point is approached, indicating that the fluctuating energy has been redistributed into another velocity component. No discontinuity is seen in the u'_{rms} contours (Fig. C.7c), indicating that the velocity fluctuations have been redistributed into either the streamwise, spanwise, or both direction. Since the spanwise component is not captured in the current experiments, measurements capturing all three components of velocity for this LSB and the forcing configurations are required in order to be able to accurately describe the observed the disturbance development.

5.5.1 Vortex Filament Model

An assertion was made that self-induced motion affects the development of the observed spanwise modulated vortex filaments, leading to sections of the filament being lifted away and pushed toward

the surface (Fig. 5.16c), which then has significant impact on the mean topology of the flow field (Figs. 5.17c and 5.18c). This assertion is examined through the development of an analytical model that considers a sinusoidal vortex filament in the vicinity of a wall subject to a mean shear flow and Biot-Savart induction. Specifically, velocity fields are computed through the superposition of mean flow profile typical of a separated shear layer and the time-dependent induced flow resulting from a real and mirror vortex filament pair, with the latter governed by Eqn. 2.6. Such a model is expected to capture the self-induced motions of an undulatory-shaped vortex filament, which can then be studied in the presence of wall effect and a wall-normal velocity gradient. It is noted that the model will be subject to significant limitations, since only a single vortex is modelled in isolation and the model does not enforce the conservation laws, and theferefore the effects of inertia, pressure, and viscosity are not fully accounted for in the modelled flow. That being said, through the inclusion of the aforementioned phenomena and subsequent study of their interaction, the model may prove useful in elucidating certain mechanisms present in the investigated flow.

The modelled filament is initialized from the following set of parametric equations:

$$\widetilde{x} = b \sin\left(\frac{2\pi}{\widetilde{\lambda}_z}\tau\right), \quad \widetilde{y} = 2, \quad \widetilde{z} = \tau, \quad 0 \leq \tau \leq n\pi, \tag{5.2}$$

where n is the number of spanwise wavelengths in the filament within the span of the modelled domain. The spanwise wavelength is set to $\widetilde{\lambda}_z = 25$, and the amplitude of the sinusoid, $b = 1.25$, is estimated from the PIV measurements (Fig. 5.16b-iii). The motion of the filament is modelled through the consideration of three phenomena, which are visualized in Fig. 5.19. The first is convection by the mean flow (Fig. 5.19a). An estimate of this is provided by the time-averaged PIV measurements, with the profile at $\widetilde{z} = 0$ and $\widetilde{x} = 45$ from the $\widetilde{\lambda}_z = 25$ case used (Fig. 5.17c). As the model requires an analytical expression for the mean velocity profile, the following fit is used:

$$\frac{\overline{u}}{u_e} = \frac{1 - a_1}{2} + \frac{1 + a_1}{2} \tanh\left[\frac{a_2\,(\widetilde{y} - a_3)}{a_4}\right], \tag{5.3}$$

which is a modified form of that proposed by Dini *et al.* [45] that allows for reverse flow and has been shown to suitably model separated boundary layer profiles in a number of analytical applications [20, 23]. The profile edge velocity, u_e, is again estimated from the PIV measurements, while the coefficients a_n are estimated through a least-squares curve fitting operation to the measured data.

The second aspect to be modelled is the filament's self-induced velocity; governed by the Biot-Savart law (Eqn. 2.6). The circulation of the filament is estimated as $\Gamma/u_\infty\delta_{1s} = -19.5$, found from phase-averaged PIV measurements (Fig. 5.16b), where spanwise vorticity within a contour on the $\widetilde{z} = 0$ plane that encompasses a single shear layer vortex is integrated. To evaluate the filament's self-induced velocity, Eqn. 2.6 is evaluated at the points lying along the filament. A singularity results when the velocity a point induces on itself is evaluated (*i.e.*, $\vec{r} = 0$ in Eqn. 2.6), which is remedied by defining a 'solid core' radius of the filament, within which Biot-Savart induction does not apply. The self-induced velocity distribution for the initial filament position is depicted in Fig. 5.19b.

The final aspect to be modelled is the wall effect. This is modelled by a mirror image of the

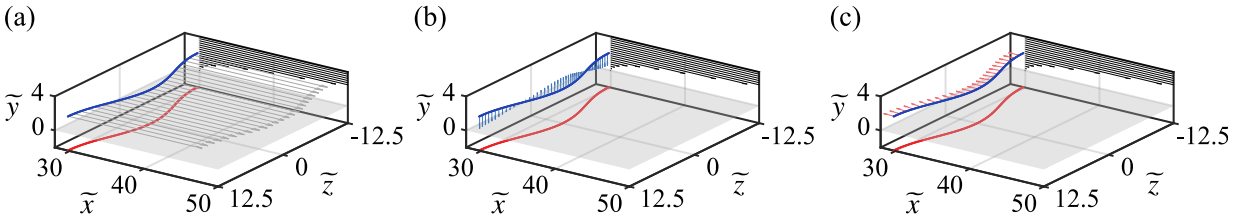

Figure 5.19: Segment of modelled vortex filament (blue) subject to (a) mean shear flow, (b) Biot-Savart self-induction, and (c) Biot-Savart induction from the filament mirrored about the wall plane (red).

vortex filament about the wall plane ($\widetilde{y} = 0$) with an equal but opposite circulation. The induced velocity on the 'real' filament is then evaluated using Eqn. 2.6, with the result for the initial filament position shown in Fig. 5.19c.

The motion of the filament is simulated through numerical evaluation of the model, with the implementation written in MATLAB, the source code of which is available in Appendix D.1. The filament is discretized in space and the velocity at each of its points is evaluated as previously described. Each point is then advanced in space according to its total estimated velocity and a prescribed time step, with the process repeated for a set number of time steps. Through an iterative process, the model was found to be stable and give converged results for a solid core radius size of $\pi/18$, a spatial discretization size of $\tau = \pi/36$, and a time step of $\mathrm{d}t^*_{\delta_{1s}} = 0.1$. As prescribed by the vortex theorems of Helmholtz [70], a vortex filament may not start or end in the fluid, however this is unavoidable in the current model. In order to minimize the 'unnatural' end effects present, a total filament length covering 32 spanwise wavelengths is modelled, with the end effects assumed negligible in the region covering the centre-most two wavelengths.

The results of the simulation are shown in Fig. 5.20. At initialization (Fig. 5.20a), the filament is confined to the $\widetilde{y} = 2$ plane, while the mean flow serves to convect the filament purely in the $\widetilde{x}$-direction (Fig. 5.19a), which is slightly opposed by the wall effect (Fig. 5.19c). Due to the spanwise undulatory shape of the filament, a rotational motion about the filament's $\widetilde{z}$-axis is imparted as a result of Biot-Savart self-induction (Fig. 5.19b). Thus, as the filament convects downstream in Figs. 5.19b–d, this rotational motion causes the streamwise forward and rearward sections of the filament to tilt away and toward from the surface, respectively, visualized in Fig. 5.20 by colouring the filament according to its wall-normal height. As a result of the self-induced tilting motion, the filament is stretched in the $\widetilde{x}$-direction, both by the wall-normal shear and wall effect. The result is an approximate 50% increase in the spanwise amplitude of the filament's undulations between $\widetilde{x} = 40$ and 50, which is most clearly seen in the x-z views of Figs. 5.20b and 5.20c.

The model and experimental results are compared in Fig. 5.21 in terms of the stretching observed in the vortex filaments. This is quantified by the peak-to-peak distance in the filament in a given coordinate direction, *i.e.*, $\widetilde{x}_{\mathrm{pp}}$ and $\widetilde{y}_{\mathrm{pp}}$ for the streamwise and wall-normal directions, respectively. The experimental data are taken from the phase-averaged side view PIV measurements for the $\widetilde{\lambda}_z = 25$ case, in which the vortex cores were identified using the λ_2-criterion (Fig. 5.16b). Both the model and experimental results presented in Fig. 5.21 are normalized by the results at $\widetilde{x} = 40$ since this gives a measure of the relative stretching with downstream development, in

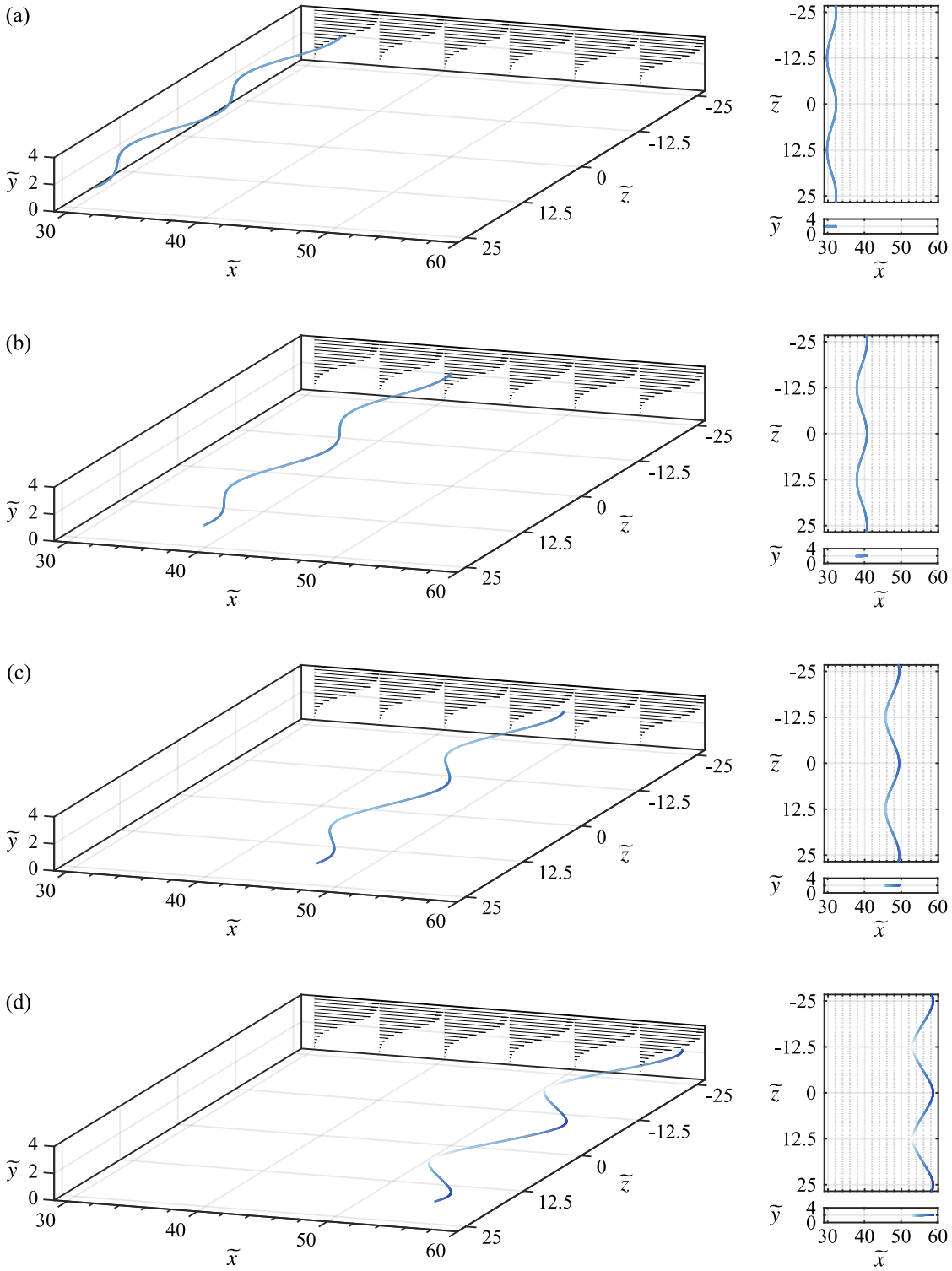

Figure 5.20: Development of modelled vortex filament subject to mean shear and Biot-Savart induction (Fig. 5.19). Filament coloured according to its wall-normal height. Consecutive frames separated by $t^*_{\delta_{1s}} = 15.9$.

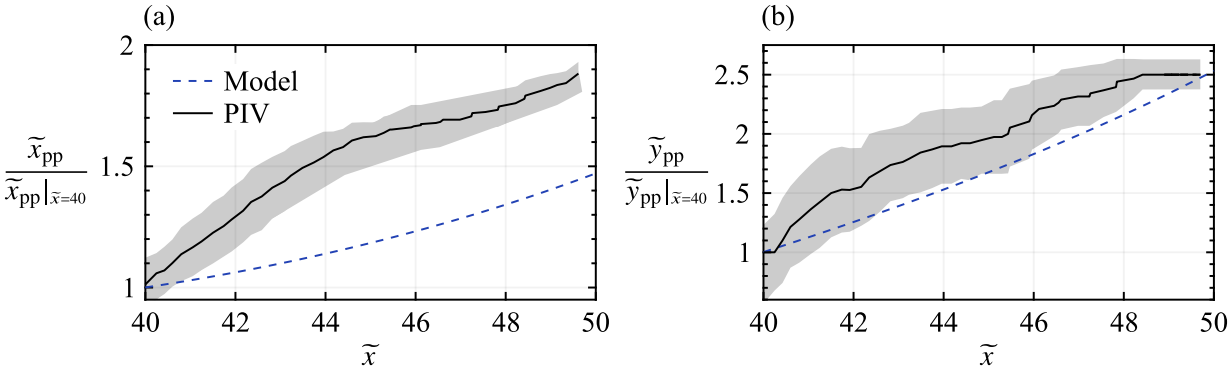

Figure 5.21: Vortex filament stretching in the (a) streamwise and (b) wall-normal directions. PIV data is taken from the vortex cores determined in Fig. 5.16b and is smoothed using a sliding kernel of width $\Delta\widetilde{x} = 2.6$. The uncertainty bounds (grey shaded regions) are based on the variability within the smoothing kernel.

addition to the model and experimental values being matched at this location through selection of the model's initial spanwise amplitude in the $\widetilde{x}$-direction (b in Eqn. 5.2). From Fig. 5.21, it is apparent that the experimental measurements show more significant vortex stretching in both the streamwise and wall-normal directions than the model predicts. Fair agreement is seen on the magnitude of stretching in the $\widetilde{y}$-direction (Fig. 5.21b), while in the $\widetilde{x}$-direction (Fig. 5.21a), both the magnitude and rate at which the stretching occurs is higher in the experiments. This indicates that factors not captured in the model must also contribute significantly, such as the model not accounting for changes in the mean velocity profile with x, viscous effects, and other vorticity sources present in the real flow. That being said, the vortex strecthing predicted by the model is similar in trend and of the same order of magnitude as seen in the experiments, which indicates that the mechanisms present in the model contribute significantly to the vortex stretching, in addition to other unaccounted effects.

From the perspective of the dynamics considered in the vortex filament model, the spanwise modulated shape of the vortex filament observed in the experiments (Fig. 5.16b-iii) will self-induce a rotational motion which, alongside the wall-normal shear and wall effect, will cause a continual intensification of the vortex stretching. Not only is this motion seen in Fig. 5.16b, but it is also reported in Chapter 4, where even in the absence of intentional spanwise modulated forcing, spanwise undulations develop in the LSB shear layer vortices, leading to the streamwise forward sections of the filament lifting away from the surface and tilting forward in the streamwise direction (Fig. 4.26). Thus, for the investigated LSBs, one formed over an airfoil and the other over a flat plate with an applied adverse pressure gradient, a fundamental aspect of the shear layer vortex development appears to be the development of spanwise undulations which, due to the self-induced motions they incur, are intrinsic to the breakup of the vortex and therefore to the overall transitional process to turbulence. These observations can be applied more broadly to all LSBs, since regardless of how the spanwise undulations are initially produced, if present, they will tend to develop in the way shown in any near-wall shear flow.

5.6 Concluding Remarks

In this chapter a three-dimensional forcing technique capable of producing deterministic disturbances modulated to a desired spanwise wavelength was developed and characterized, with a preliminary look taken at the effects of this forcing on flow development in an LSB. The separation bubble was formed over a flat plate with an imposed adverse pressure gradient at a nominal Reynolds number of $Re_{\delta_{1_s}} = 750$. Forcing was provided by surface-mounted, AC-DBD plasma actuators installed well upstream of the natural LSB separation point, thus leaving the disturbances to develop as they convect through the upstream boundary layer and into the LSB. Five cases were investigated: (i) the natural/unforced flow, (ii) two-dimensional forcing, and three-dimensional forcing with spanwise wavelengths ($\widetilde{\lambda_z}$) of (iii) 12.5, (iv) 18.75, and (v) 25. These spanwise forcing wavelengths were chosen since, when considered with respect to the predominant streamwise wavelength of disturbances in the LSB ($\widetilde{\lambda_x} = 12.5$), they correspond to $\widetilde{\lambda_z} = \widetilde{\lambda_x}$, $1.5\widetilde{\lambda_x}$, and $2\widetilde{\lambda_x}$, respectively, thus covering the lower portion of the range $1 \lesssim \lambda_z/\lambda_x \lesssim 7$ reported in Chapter 4 and other previous investigations [113, 137, 153]. Two-dimensional forcing was achieved through operation of a single spanwise uniform actuator, while for the three-dimensional forcing cases, two actuators were arranged in streamwise succession and operated simultaneously. The upstream actuator produced a spanwise uniform disturbance, which was then spanwise modulated by the output of the downstream actuator, with a relative phase delay used to superimpose the two outputs.

Prior to studying the effects of the forcing on LSB flow development, a detailed characterization of the plasma actuators was carried out in both quiescent and in-flow conditions to determine the spanwise and streamwise disturbance topology, net momentum injection, and phase delayed needed for disturbance superposition. The quiescent characterization involved flow visualizations and planar PIV measurements, showing that all actuators provide a spanwise uniform injection of streamwise momentum through the production of relatively weak, wall-parallel streamwise jets in regions where the actuator's high voltage and ground electrodes overlap. Thus, two-dimensional output is achieved from an actuator with electrode overlap that is spanwise continuous, while three-dimensional disturbances at a desired spanwise wavelength are achieved through introducing gaps in the electrode overlap, as no streamwise velocity is generated in the gap regions.

From the planar PIV measurements, the generated thrust and associated momentum coefficients were estimated for all actuators using a control volume analysis. The results highlight higher sectional thrust generated by the two-dimensional actuator due to end effects that decrease momentum output at the edges of the overlap regions. This, coupled with different total active region (thrust producing) lengths, results in varied total thrust production for all actuators considered. The assumed superposition of momentum output for actuators arranged in streamwise succession was shown to be reasonably valid, which coupled with the established linear trend between thrust output and forcing duty cycle, allowed for the identification of forcing parameters for the desired actuator combinations that gave equal amounts of total momentum output. In particular, duty cycles of 25%, 21%, 22% and 23% were found to give equal total momentum across the two-dimensional, $\widetilde{\lambda_z} = 12.5$, $\widetilde{\lambda_z} = 18.75$, and $\widetilde{\lambda_z} = 25$ cases, respectively, while all other forcing parameters were kept constant. The phase delay required to superimpose the disturbance outputs of the actuators was invariant to spanwise wavelength, with a value of 42° leading to successful disturbance superposition within the LSB.

Significant changes in the development of the LSB shear layer vortices were observed as a result of the forcing. When left to develop naturally, the vortices formed with significant spanwise undulations, the wavelengths of which exhibited a high degree of variability over a relatively wide range of values, $1 \lesssim \lambda_z/\lambda_x \lesssim 5$. When the flow was forced in a two-dimensional manner, vortex formation was essentially two-dimensional, with the vortex being uniform across the entire investigated span. This two-dimensionality was maintained as the vortex developed downstream, with only minor undulations developing prior to localized breakdown to turbulence. In a similar manner, the vortex filaments were predominantly spanwise uniform at formation for all the spanwise modulated forcing cases. Differences were observed based on the spanwise wavelength of the forcing as the vortex developed downstream, as substantial spanwise undulations that essentially matched that of the forcing resulted only for the $\widetilde{\lambda_z} = 25$ case, while the effect was much less pronounced for the $\widetilde{\lambda_z} = 18.75$ and 12.5 cases. In fact, the results of the $\widetilde{\lambda_z} = 12.5$ case were largely similar to those of the two-dimensional forcing case, indicating that the spanwise component introduced by forcing at that particular wavelength was damped out. Thus, evidence of three-dimensional disturbance growth that is spanwise wavelength dependent was established. In the case of forcing at a spanwise wavelength of $\widetilde{\lambda_z} = 25$, this led to the relatively weak three-dimensional component of the introduced disturbances to be significantly amplified in the aft portion of the bubble, causing the initially two-dimensional vortex to develop significant spanwise undulations at a prescribed wavelength.

Further analysis of the vortex dynamics revealed that, in the case of the $\widetilde{\lambda_z} = 25$ forcing, the vortex filaments surged forward in the streamwise direction in the region downstream of where the three-dimensional actuator was active, while the filament lagged behind at spanwise locations downstream of the actuator gaps. These filament motions, coupled with the strong mean shear, were speculated to lead to a continual intensification of vortex stretching, leading to rapid filament deformation. The validity of this assertion was established through the development of simplified model that considered the development of a vortex filament subject to Biot-Savart induction and mean flow convection. The results of the model confirmed that, as a result of the filament's spanwise undulatory shape, a net rotational motion is imparted on the filament through Biot-Savart self-induction, causing the crests and valleys of the filament to tilt away and toward the surface, respectively. This, coupled with the mean shear flow, caused the filament to stretch in the streamwise direction.

The discussed vortex dynamics were linked to the mean topological features, as the two-dimensional forcing was shown to shift the mean maximum bubble height and reattachment locations upstream, while also causing the mean bubble height to increase. Similar results were found for the $\widetilde{\lambda_z} = 25$ case where the vortex filaments surged forward, indicating that the effect of the forcing at these locations was similar to that of the two-dimensional forcing. That being said, the most significant effects on the mean characteristics of the flow were seen in regions where the vortex filaments were pushed toward the surface, which in turn caused significant upstream shifts in reattachment and reductions in the maximum bubble height. This lead to disturbance growth in the aft portion of the bubble occurring in a region much closer to the surface, where the streamwise and wall-normal components of the fluctuating energy were redistributed into the spanwise direction prior to the breakdown to turbulence.

These results have shown that significant changes to LSB flow development can be made

through spanwise modulated forcing, with the outcome dependent on the input wavelength. For the particular LSB investigated, the effect was most significant for a spanwise wavelength that was approximately double the streamwise wavelength of the LSB shear layer vortices. To further elucidate the effects of this type of forcing, more comprehensive measurements that capture all three components of velocity are required, so that the ensuing vortex dynamics can be fully observed and connections can be drawn to the three-dimensional time-averaged flow topology. Furthermore, the observed vortex dynamics should be linked to flow stability, with focus placed on whether two or three-dimensional disturbances are most destabilizing to the flow. These are the objectives laid out for Chapter 6.

Chapter 6

Growth of Spanwise Modes in a Laminar Separation Bubble

A follow-up campaign to that of Chapter 5 is conducted, where the growth of spanwise disturbances in the LSB is considered in detail. Measurements near the mean separation point reveal a preferential amplification of spanwise modes in the upstream boundary layer. In the LSB, both measurements and LST predictions show two-dimensional modes are the most amplified, while spanwise modes grow at reduced, yet comparable rates. The end result, in the case of three-dimensional forcing, is the manifestation of the unstable spanwise modes in the shear layer vortices as spanwise undulations, which lead to a continual intensification of vortex stretching that is intrinsic to the vortex breakup process.

6.1 Introduction

The results of Chapter 5 made it clear that significant changes to the flow development in a laminar separation bubble can be made through the introduction of controlled disturbances of varied spanwise wavelengths. Of the three spanwise wavelengths considered, the most significant changes resulted from spanwise forcing at a wavelength that corresponded to two times the streamwise wavelength of the fundamental disturbances in the LSB. Precedence for unstable disturbance growth of similar spanwise modes can be found in the study of laminar boundary layers. In the work of Mack [131], in which linear stability analysis was applied to a Blasius boundary layer, albeit at much higher Reynolds numbers, spanwise modes were found to be more unstable than the normal Tollmien-Schlichting waves for certain frequencies and oblique wave angles. Furthermore, the interaction between normal and oblique modes is responsible for the onset of three-dimensionality in K-type [107] and H-type [71] transition. A model of such interactions was developed by Craik [41] and Zelman & Maslennikova [267], and considers the formation of a resonant triad of a two-dimensional TS wave and two oblique waves of equal but opposite angles. Most notably, the frequency of the oblique wave pair is half of the normal TS mode and so the interaction is referred as subharmonic. Thus, there is evidence linking the most amplified normal and oblique modes in certain cases of laminar boundary layer transition to the forcing technique found to be most effective in Chapter 5, as both report a spanwise to streamwise wavelength ratio of $2:1$. This supports the notion that the upstream boundary layer sets the initial conditions for the transition process within the LSB, as it conditions the incoming disturbances (*e.g.*, Ref. [46]).

Previous studies have examined the effect of oblique disturbances on LSB transition and flow development. Rist & Augustin [198], in a direct numerical simulation of an LSB formed on a flat plate, found that weakly oblique instability waves grew at comparable rates to the two-dimensional normal mode and lead to an earlier onset of turbulent breakdown, as long as oblique wave angles were below 30°. Note that a wave angle of 30° corresponds to a spanwise to streamwise wavelength ratio of 1.73, again closely matching the most effective forcing wavelength from Chapter 5. Furthermore, the introduction of these oblique waves caused a spanwise staggering of the LSB vortex shedding process, leading to a peak and valley distribution in mean flow field quantities. Similar observations have been made in other DNS studies, notably those of Marxen *et al.* [137] and Pauley [182]. Experimental studies of the same nature are relatively scarce due to the difficulty in implementing a reliable spanwise modulated forcing technique, which is then compounded by the need for three-dimensional flow field measurements. Notable exceptions are Michelis *et al.* [151, 153], who noted spanwise deformations in naturally developing LSBs. In Ref. [153] the spanwise to streamwise wavelength ratio of the deoformattions was found to be 1.94, while applying two-dimensional forcing almost entirely eliminated the spanwise modulations. As a result, a model based on the amplitude ratio between normal and oblique disturbance modes was proposed for vortex deformations in LSBs.

From surveying the literature, it is clear that the development of disturbances upstream of the LSB must be considered. In doing so, a more comprehensive understanding of the effects imparted by spanwise modulated forcing on LSB flow development can be gained. In particular, special consideration can be given to the stability characteristics of the flow that dictate the growth of the modes introduced by the forcing, which can then be linked to the development of the LSB

shear layer vortices and the mean flow topology. To this end, a follow-up experimental campaign to that conducted in Chapter 5 is undertaken, utilizing the same wind tunnel facility, model, flow conditions, and forcing technique. Disturbance development in the region near the mean separation point is measured via hot-wire anemometry, while planar and tomographic PIV measurements are utilized to capture reliable statistics and the three-dimensional evolution of the shear layer vortices in the aft portion of the LSB, respectively.

6.2 Description of Experiments

The same wind tunnel facility, model, flow conditions and forcing techniques discussed in Section 5.2.2 were employed, with a schematic of the experimental setup provided in Fig. 6.1. Therefore, by maintaining the same free-stream velocity (5.75 m s^{-1}) and pressure distribution imposed by the displacement body, a separation bubble was formed on the top surface of the flat plate that extended from $\widetilde{x} = 0$ to $\widetilde{x} \approx 70$, matching the LSB studied in Chapter 5, as seen in Fig. 6.2. The previous Cartesian coordinate system is used, with the origin located such that $x = 0$ is located at the location of mean flow separation with no forcing (490.5 mm from the plate leading edge), while $y = 0$ and $z = 0$ are located at the top surface and midspan of the plate, respectively. Based on the displacement thickness at separation when the flow is not forced ($\delta_{1s} = 2$ mm), and a free-stream velocity of 5.75 m s^{-1}, the nominal Reynolds number for the experiments was once again $Re_{\delta_{1s}} = 750$.

The AC-DBD actuators described in Section 5.2.1 (Fig. 5.1) were employed to introduce controlled disturbances upstream of the LSB. A subset of the cases considered in Chapter 5 were selected, including: (i) the natural/unforced flow, (ii) two-dimensional forcing, and (iii) three-dimensional forcing with a spanwise wavelength of $\widetilde{\lambda}_z = 25$. Since a single set of actuators can provide either two-dimensional or spanwise modulated forcing, the set did not need to be changed between cases. The set of actuators was recessed into the plate so as not to perturb the flow and placed to locate the two-dimensional discharge area at $\widetilde{x} = -310$. The equipment and parameters for plasma actuation described in Section 5.2.1 were utilized ($V_{pp} = 6$ kV, $f_c = 5$ kHz, $f_m = 133$ Hz).

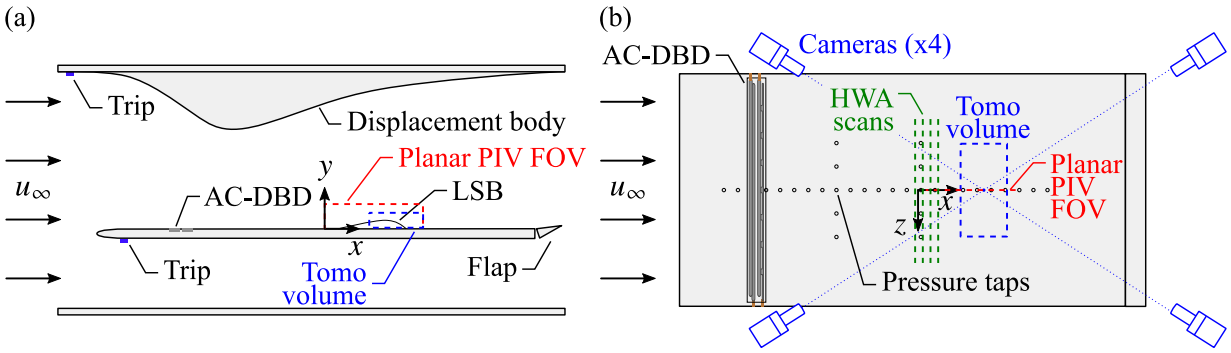

Figure 6.1: (a) Side and (b) top view of experimental setup. The setup from Fig. 5.3 is maintained, with additional equipment added for hot-wire anemometry (HWA) and tomographic PIV measurements. Tomographic camera arrangement shown in (b).

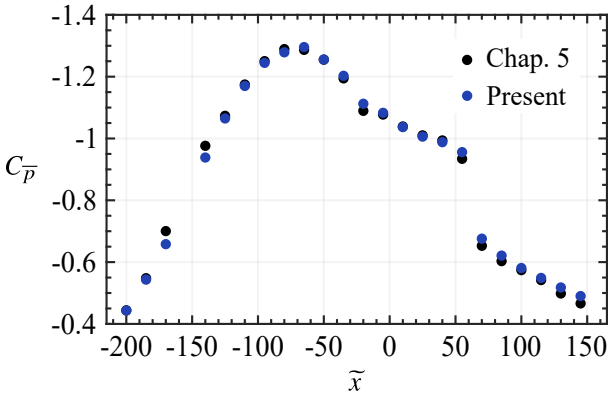

Figure 6.2: Mean streamwise static pressure distributions showing equivalence between the Chapter 5 and present experiments. Measurement uncertainty is given by the marker size.

Duty cycles of 25% and 23% were employed for the two-dimensional and $\widetilde{\lambda}_z = 25$ forcing cases, respectively, providing closely matching total momentum coefficients between the two forcing cases, $C_\mu = (12.2 \pm 2.4) \times 10^{-4}$ and $(12.0 \pm 2.4) \times 10^{-4}$, respectively, as determined in Section 5.3 (Table 5.2).

Disturbance development near the mean separation point was measured via hot-wire anemometry, with the approximate measurement locations shown in Fig. 6.1b. The measurements were performed in spanwise scans at wall-normal heights equal to the local displacement thickness (approx. $y = 2\,\text{mm}$) where the mean streamwise velocity is approximately equal to $0.65u_\infty$ ($3.75\,\text{m}\,\text{s}^{-1}$). These measurement locations were selected based on the anticipation of measurable disturbance amplitudes at a distance from the wall where errors due to rectification and near-wall conduction are expected to be low. A Dantec 55P15 boundary layer probe was used for all measurements, which was angled at approximately 10° to the plate surface, in accordance with the recommendations of Brendel & Mueller [24]. The hot-wire sensor was operated by a TSI IFA-300 constant temperature anemometer bridge, with the bridge outputs digitized using a 24-bit National Instruments 9234 data acquisition module. The sensor was held in place by a rigid sting aligned in the streamwise direction, which was mounted to a 3-axis Zaber DE51T3 traversing system located downstream of the test section exit. 300, 150, and 150 mm of maximum travel were available in the spanwise, streamwise, and wall-normal directions, respectively, with an estimated uncertainty in traverse movements of 15 µm. Position of the hot-wire sensor relative to the coordinate system was determined via a telescopic optical setup, with the uncertainty in its position in all coordinate directions estimated to be less than 0.06 mm. The presence of the sting and traversing system were confirmed via surface pressure measurements to have no measurable impact on the mean flow. Sampling was performed at 51.2 kHz for a total of 5 s, thus collecting 2.56×10^5 samples per measurement location. A wait period of 10 s was used between traverse movements to ensure any vibrations resulting from the movement had died out. To enable phase-averaging of the results, the plasma forcing signal was split prior to amplification and served as the start trigger for the measurements.

Calibration of the hot-wire sensor was performed *in-situ*, with the tunnel off and a TSI 1127 Velocity Calibrator placed inside the open test section. The reference velocity provided by the

Table 6.1: Parameters for PIV experiments.

Parameter	Planar	Tomographic	Unit
Laser	EverGreen 200 mJ/pulse Nd:YAG		–
Camera	PCO sCMOS 5.5MP (x2 planar, x4 tomo)		–
Lens focal length	105	200	mm
Lens $f_\#$	5.6	11	–
Sensor resolution	2560×733	2560×1800	px
Final area/volume	4767×733	$1499 \times 165 \times 2605$	px/vox
	130×20	$69 \times 7.6 \times 120$	mm
PIV mode	Double-frame		–
Acquisition mode	Indep. sampling & phase-locked		–
Sampling rate	15 (indep.), 14.77 (phase-locked)		Hz
Laser pulse sep.	70	100	µs
Max. particle disp.	20	17	px/vox
No. of samples	2400 (indep.), 300 (per phase)		–
Final window size	16×16	$20 \times 20 \times 20$	px/vox
Vector pitch	0.11	0.23	mm
Avg. uncertainty	1	2.9	% of u_∞

calibrator was estimated by measuring the pressure drop across its nozzle using a Honeywell HSC series pressure transducer with full range of ±160 Pa, resulting in an uncertainty of less than 2% on velocities greater than $0.3u_\infty$. Calibration was performed daily, using 17 calibration points spanning between $0 \leq u/u_\infty \leq 2$, with a fourth order polynomial fit to the voltage response of the hot-wire used. Based on the discussions provided in Appendix B.3, the uncertainty in the hot-wire measurements is estimated to be less than 3% of u_∞ within the measured velocity range ($0.6 \leq u/u_\infty \leq 0.78$).

Flow development in the separation bubble was measured using planar and tomographic PIV configurations (Fig. 6.1), with the salient parameters for each configuration summarized in Table 6.1. For both configurations, the flow was seeded with a glycol-water based fog with a mean particle diameter on the order of 1 µm. Illumination was provided by a Quantel EverGreen 200 mJ/pulse Nd:YAG laser, with synchronization between the cameras and laser handled through a LaVision timing unit. Data acquisition and processing was performed using LaVision's DaVis 10 software. Data were acquired in independent sampling and phase-locked acquisition modes, with the plasma forcing signal split prior to amplification and sent to the timing unit to serve as the phase-locking reference. For the phase-locked acquisitions, 300 samples per phase were collected for a total of 12 phases, while independent sampling was done at 15 Hz with a total of 2400 samples collected.

Measurements were performed in the x-y plane for the planar configuration, using two PCO sCMOS 5.5MP cameras arranged in streamwise succession. Each camera was fitted with a Nikon 105 mm focal length macro lens set to $f_\# = 5.6$. With the fields of view overlapped by 12%, a total FOV of 130×20 mm was achieved. The magnification factor for both cameras was 0.24,

yielding resolutions of 37 px/mm. Double-frame particle images were acquired using a frame separation time of 70 µs, keeping particle displacements under 20 px. Particle displacements were calculated using an iterative, multi-grid cross-correlation scheme with window deformation [212], starting and ending with window sizes of 64×64 px and 16×16 px, respectively, with 75% overlap between windows. The resulting vector pitch is 0.11 mm in both the x and y directions. The results were post-processed using the universal outlier detection method [247], with the resulting vector fields stitched together using a cosine weighted blending function in the overlap region. The random errors in the measurements were estimated using the correlation statistics method [251]. The average uncertainty within the fore portion of the LSB and the free-stream is estimated at 1% of u_∞, while higher levels ($\sim$3%) are present in the aft portion of the LSB.

For the tomographic configuration, four PCO sCMOS 5.5MP cameras were used. These were placed in rectangular arrangement above the flat plate at inclination angle of approximately 27° with respect to the y-axis. Each camera was fitted with a Nikon 200 mm focal length macro lens set to $f_\# = 11$, with a Scheimpflug adapter used to align the focal plane with the camera sensor. The laser beam was collimated using a set of spherical lenses, then expanded to illuminate the volume of interest using a cylindrical lens. Light attenuation effects at the volume boundaries was mitigated through the use of a knife edge filter. A physical calibration was performed by imaging a calibration target placed at three wall-normal planes within the volume. This calibration was then refined using volume self-calibration [250], which reduced the standard deviation in the volume calibration to less than ±0.1 px. Double-frame particle images were acquired using a frame separation time of 100 µs, keeping particles displacements under 17 px. Volume reconstruction from the acquired images was obtained through the Simultaneous Implementation of Multiplicative Algebraic Reconstruction Techniques (SMART) [12], yielding a total interrogation volume of $1499 \times 165 \times 2605$ voxel (vox). Vector calculation was performed iteratively using cubic windows and 75% overlap, with initial and final windows lengths of 96 and 20 vox, respectively. The final volume is $69 \times 7.6 \times 120$ mm containing $300 \times 33 \times 521$ vectors, resulting in a vector pitch of 0.23 mm in all three coordinate directions. The findings of Lynch & Scarano [129] can provide a rough estimate of the uncertainty on instantaneous velocity measurements, which is estimated to be 0.5 vox away from the wall, corresponding to 2.9% of the free-stream velocity, with higher uncertainties expected near the wall. However, this is not a rigorous determination of the uncertainty associated with the tomographic measurement, which is challenging for any investigator given the complexity of the technique. A full discussion of the contributing factors to uncertainty in tomographic PIV measurements is provided in Appendix B.2. In order to establish the reliability of the tomographic results, a detailed comparison with equivalent planar PIV measurements will be conducted, since a more robust estimate of uncertainty is available for the latter.

6.3 Time-Averaged Characteristics

Statistical quantities from the planar and tomographic measurements are first analyzed to establish the mean characteristics of the investigated LSB. From the planar PIV measurements, Fig. 6.3 presents mean streamwise velocity and rms quantities of the streamwise and wall-normal velocity

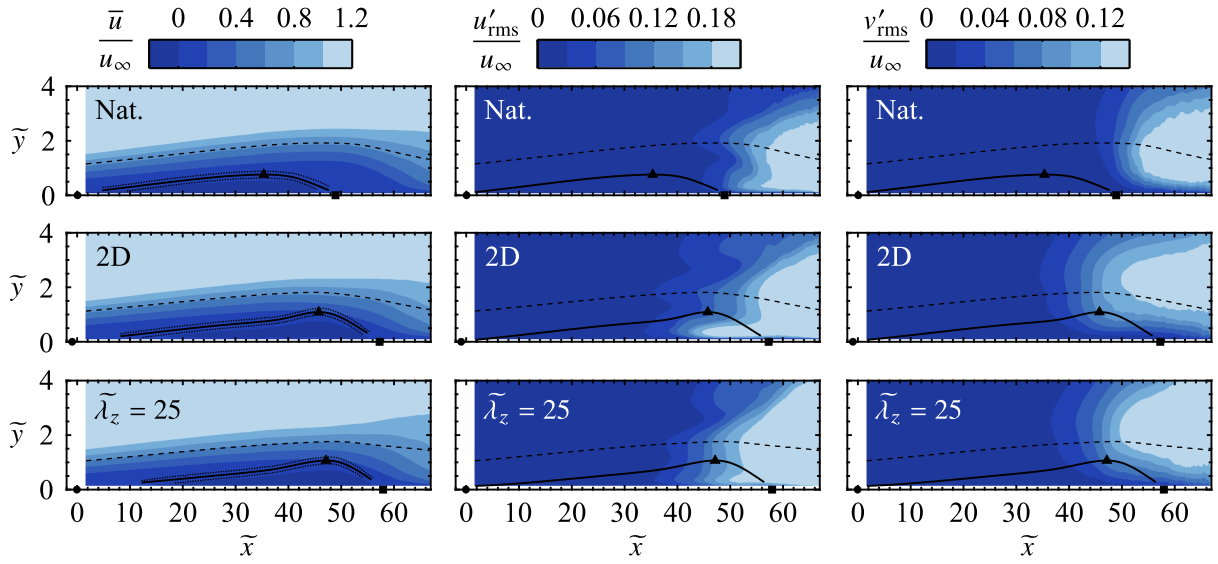

Figure 6.3: Planar PIV contours of mean streamwise velocity ($\overline{u}$), and rms of fluctuating streamwise (u'_{rms}) and wall-normal (v'_{rms}) velocity. Solid lines mark the dividing streamlines, whose uncertainty is indicated by the dotted lines. Circle, triangle, and square markers denote estimated mean separation, maximum bubble height, and reattachment points, respectively. Dashed lines indicate displacement thickness.

fluctuations at $\widetilde{z} = 0$. As the same experimental setup, flow conditions and forcing configurations of Chapter 5 were utilized, the LSB characteristics reported in Figs. 5.17 and 5.18 are expected here. Thus, the same methods in characterizing the mean LSB topology through identification of the mean dividing streamline are employed [58, 76, 172], with the results shown in Fig. 6.3, and a summary of values provided in Table 6.2. Estimation of the mean separation point is possible as a result of capturing the fore portion of the LSB in the current experiments, with a value of $\overline{\widetilde{x_s}} = 0.1 \pm 7.0$ estimated for the natural flow, which does not change, within the experimental uncertainty, on account of the two or three-dimensional forcing. The relatively high uncertainty in $\overline{\widetilde{x_s}}$ is a result of the relatively shallow angle of the mean dividing streamline in the fore portion of the LSB, which is sensitive to the uncertainty in determining the location of the wall.

A few conclusions can be drawn from the comparison of the Chapters 5 and 6 results presented in Table 6.2. First, the LSB characteristics for the two-dimensional and $\widetilde{\lambda}_z = 25$ forcing cases show good agreement between the two experimental campaigns, with nearly all values agreeing within the uncertainty bounds. Comparing the flow topologies reported in Figs. 5.17 and 5.18, and Fig. 6.3 for these two cases supports this assertion, as both the mean streamwise velocity and rms contours show similar patterns in the aft portion of the bubble ($\widetilde{x} \gtrsim 35$), while differences in the mean dividing streamlines result from resolving the fore portion of the LSB in the current experiments.

Second, and most importantly, poor agreement is seen between the results of the natural case, as the mean maximum bubble height and reattachment locations are significantly more downstream in the Chapter 5 results, as reported in Table 6.2 and seen through comparison of Figs. 5.17a and 6.3. This indicates that the LSB has changed in length, shifted upstream, or a combination of

Table 6.2: Comparison of LSB characteristics at $\widetilde{z} = 0$ from the planar PIV results of Chapters 5 and 6 (Figs. 5.17 and 6.3, respectively).

Case	Parameter	Chapter 5	Chapter 6
Nat.	$\widetilde{\overline{x}}_s$	–	0.1 ± 7.0
	$\widetilde{\overline{x}}_h$	44.6 ± 0.2	35.4 ± 2.8
	$\widetilde{\overline{x}}_r$	57.0 ± 1.0	50.0 ± 2.9
2D	$\widetilde{\overline{x}}_s$	–	-0.9 ± 7.1
	$\widetilde{\overline{x}}_h$	45.2 ± 0.2	45.8 ± 0.7
	$\widetilde{\overline{x}}_r$	55.3 ± 1.2	57.3 ± 2.6
$\widetilde{\lambda}_z = 25$	$\widetilde{\overline{x}}_s$	–	-0.1 ± 7.2
	$\widetilde{\overline{x}}_h$	45.6 ± 0.2	47.1 ± 0.9
	$\widetilde{\overline{x}}_r$	56.3 ± 1.0	57.9 ± 2.0

both in the current experiments. As flows involving separation bubbles are extremely sensitive to the experimental conditions [173, 174], the changes in the natural LSB characteristics could be the result of minor changes in external factors (*e.g.*, acoustic environment, slight difference in model positioning, climatic induced changes in facility operating conditions) that are beyond the control of the experimentalist. These factors would influence the natural LSB since it is the external disturbance environment that provides the input disturbances for the ensuing transition process, while providing deterministic input disturbances via forcing almost entirely eliminates this dependence. Evidence of these minor discrepancies are seen in the streamwise pressure plots of Fig. 6.2, where the results are in good general agreement but show some minor differences. Finally, it must be noted that the sampling time of the PIV measurements in Chapter 6 is an order of magnitude larger than that of Chapter 5 ($t^*_{\delta_{1s}} = 4.6 \times 10^5$ versus 1×10^4). Therefore, if changes in the natural LSB occur over a relatively long time scale, such as shear layer flapping [47, 266] and/or bursting [58, 205], then such phenomena would manifest in the time-averaged results of Chapter 6, while remaining statistically unresolved by the high-speed PIV of Chapter 5. A strong case for this will be made through the discussions that follow in this chapter.

Figure 6.4 presents a comparison between the planar and tomographic measurements at $\widetilde{z} = 0$ for the natural flow. Note that due to experimental limitations, no tomographic data are available below $\widetilde{y} = 0.35$. Overall, the agreement between the measurements is very good, with the mean streamwise velocity profiles in the aft portion of the bubble showing excellent agreement (Fig. 6.4a). Only slight discrepancies are seen in the mean wall-normal velocity profiles, which are attributed to the significantly lower magnitudes and relatively higher uncertainty levels for this velocity component. Good agreement is also found between the measured velocity fluctuations, as seen for u'_{rms} and v'_{rms} in Figs. 6.4c and 6.4d, respectively. Slight discrepancies are apparent at the most upstream and downstream stations, $\widetilde{x} = 32$ and 62, respectively, which are a result of the relatively low and high fluctuating amplitudes at these stations, respectively, in addition to the significant spatial filtering applied by the tomographic processing algorithm. However, the

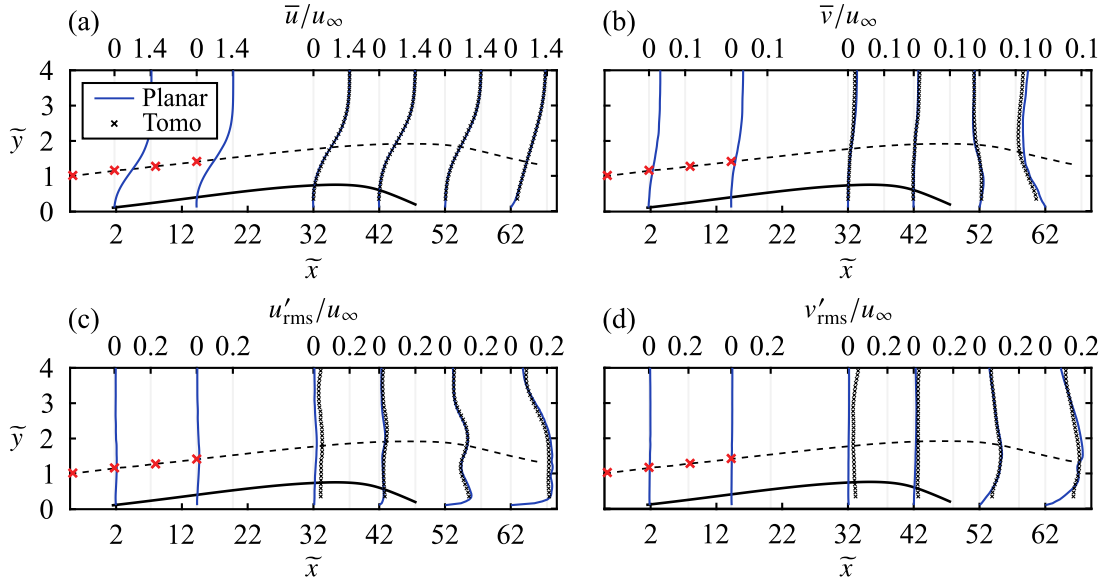

Figure 6.4: Comparison of statistical quantities between planar and tomographic PIV measurements at $\widetilde{z} = 0$ for the natural case. Solid and dashed black lines indicate the mean dividing streamline and displacement thickness, respectively, estimated from the planar PIV. Red × markers indicate locations of the spanwise scanning hot-wire measurements.

overall excellent agreement between the planar and tomographic measurements establishes that an accurate representation of the flow is expected from the tomographic measurements.

Insight into the three-dimensional topology of the LSB is gained through examination of mean streamwise velocity in the $\widetilde{y} = 0.46$ plane measured in the tomographic configuration. The results are presented in Fig. 6.5, with the spanwise trend in the mean streamwise maximum bubble height location also plotted, which is determined using the same approach illustrated in Fig. 6.3 for all x-y planes available in the tomographic volume. The results are smoothed across the span using a sliding kernel of width $\Delta\widetilde{z} = 3$, with the indicated uncertainty bounds determined based on random PIV error propagation and the variability of results within the smoothing kernel. Immediately apparent is a distinct spanwise non-uniformity present in the natural flow (Fig. 6.5a), which is characterized by a peak and valley structure with a spanwise wavelength of $\widetilde{\lambda}_z \approx 25$. Significant changes in the maximum bubble height location across the span are apparent (solid black line in Fig. 6.5a), with values varying by as much as ±7.5 in the $\widetilde{x}$-direction from the spanwise averaged value, $\overline{\widetilde{x}_{\mathrm{h}}} \approx 43$. Reliable estimates of the mean reattachment locations are not possible given the near-wall limitations of the tomographic configuration, however, the reverse flow region is captured in the measurements (darkest shade of blue in Fig. 6.5), which also shows the same distinct spanwise non-uniform trend.

While the LSB investigated in Chapter 4 showed strong spanwise uniformity (Figs. 4.18 and 4.19), other investigators have reported strong spanwise non-uniformities in LSBs [151, 153, 198]. Most notably, Rist & Augustin [198], in a DNS study, induced a peak and valley distribution in an LSB by introducing oblique disturbances in the upstream boundary layer. In an experimental investigation, Michelis *et al.* [153] noted strong spanwise non-uniformity in an LSB formed

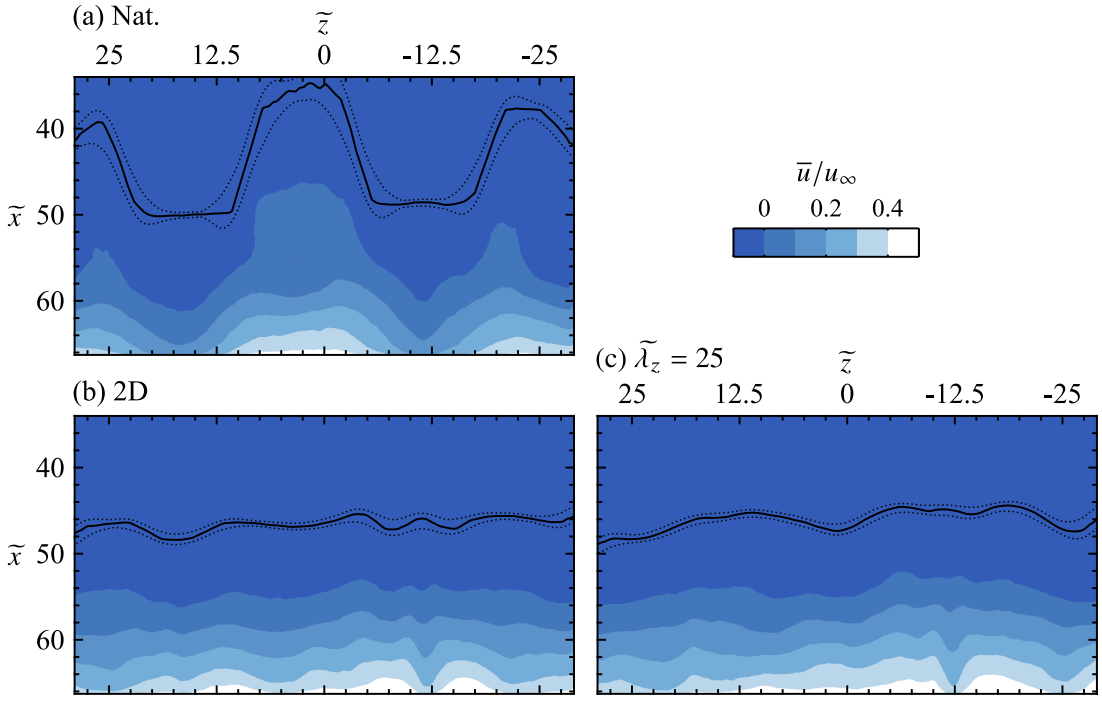

Figure 6.5: Mean streamwise velocity contours in the $\widetilde{y} = 0.46$ plane. Flow is from top-to-bottom. Solid lines indicate the spanwise trend in the streamwise location of mean maximum bubble height, estimated from x-y plane tomographic measurements using the same approach illustrated in Fig. 6.3. The $\overline{\widetilde{x}_h}$ results are smoothed using a sliding kernel of width $\Delta\widetilde{z} = 3$, with the uncertainty bounds (dotted lines) determined based on random PIV error propagation and the variability of results within the smoothing kernel.

over a flat plate, which was eliminated by promoting formation of spanwise uniform shear layer vortices through forcing. The same observation is reported here, as applying either the two or three-dimensional forcing significantly increases the two-dimensionality of the mean flow field. The spanwise non-uniformity seen in the natural flow and the subsequent effect of forcing reveals the cause for discrepancy between the results of Chapters 5 and 6. For the natural flow, where differences are significant, the spanwise non-uniformity leads to a high degree of variability in the LSB characteristics at $\widetilde{z} = 0$ (Table 6.2), which is where the planar PIV measurements were performed. Therefore, any minor change in the experimental facility, setup or procedure (*e.g.*, acoustic environment, model positioning, facility operating conditions, *etc.*) could result in significant changes in the measured statistical quantities of the natural LSB, particularly in the region of $\widetilde{z} = 0$. Furthermore, the fact that these differences are almost entirely eliminated when the flow is forced indicates that the source of the discrepancy stems from the external disturbance environment, which likely manifests in the flow as a low frequency modulation. It must be noted that the spanwise wavelength of the spanwise non-uniformity in the natural flow almost exactly matches that of the spanwise modulated forcing case, $\widetilde{\lambda}_z = 25$. This points to an inherent preference of the baseline flow for disturbance amplification at this spanwise wavelength. However, as noted in Figs. 6.5a and 6.5b, the outcomes are vastly different between the natural flow and spanwise

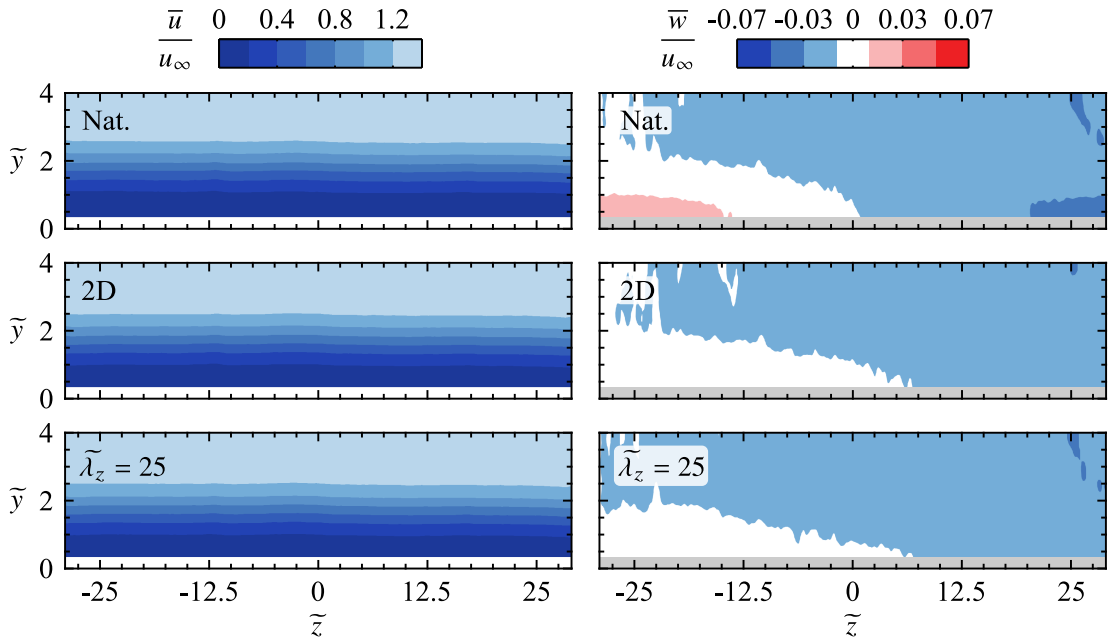

Figure 6.6: Mean streamwise and spanwise velocity contours in the $\widetilde{x} = 32$ plane.

modulated forcing case, which points to different mechanisms for disturbance amplification. These mechanisms are examined in detail and differentiated throughout the remainder of this chapter.

Figure 6.6 presents contours of mean streamwise and spanwise velocity in a cross-flow (y-z) plane at $\widetilde{x} = 32$, which is upstream of the mean streamwise locations of maximum bubble height (Fig. 6.5), thus locating the plane in the fore portion of the LSB for all cases (Fig. 6.3). Here, the mean streamwise velocity profile is spanwise uniform, with flow in the spanwise direction remaining below 2% of the free-stream in most locations, which is within the uncertainty of tomographic measurements. The result is particularly noteworthy for the natural case, since it indicates that the spanwise non-uniformity observed further downstream (Fig. 6.5a) is the result of some phenomenon whose effects become significant in the aft portion of the LSB, while the incoming flow is essentially two-dimensional. The conclusion, as will be demonstrated in Section 6.5, is that the shear layer vortices form and develop in a spanwise non-uniform manner, producing the signatures seen in Fig. 6.5.

6.4 Disturbance Development

The results in Figs. 6.3 and 6.4 demonstrate that disturbance amplitudes remain low in the fore portion of the LSB ($\widetilde{x} \lesssim 32$), and therefore fall within the uncertainty of both the planar and tomographic PIV measurements. As a result, more sensitive measurements are required to resolve disturbances in this region, which is the purpose of the hot-wire measurements. These were performed in spanwise scans at the streamwise locations marked by the red × markers in Fig. 6.4. The scan locations are $\widetilde{x} = -4.5$, 1.75, 8.0, and 14.25, with the y position equal to the local displacement thickness. In order to isolate the fundamental perturbation mode, the

measured streamwise velocity fluctuations are band-pass filtered about $St_{0\delta_{1s}} = 0.046 \pm 0.004$ ($f_0 = 133\,\text{Hz} \pm 10$) using a fourth order Butterworth filter, with a zero-phase delay achieved by filtering signals in the forward and then reverse directions. Since no phase information is available for the natural case, root-mean-square values are calculated for each measurement position from a total of 2.56×10^5 samples. For the forcing cases, the results are phase-averaged relative to the forcing cycle, whose frequency matches the fundamental frequency. A total of 72 phases bins with a width of $St_{\delta_{1s}} = 3.5 \times 10^{-3}$ ($f = 1$ Hz) is used, with a total of 2660 samples averaged per phase.

The results are presented in Fig. 6.7, where upstream of separation ($\widetilde{x} = -4.5$) disturbance amplitudes are low, while higher amplitude fluctuations may be present closer to the surface, as is traditionally seen in attached boundary layers [214, 216]. However, measurements could not be performed in this region due to significant errors related to wall effects on the convective heat transfer at the probe [50, 120] and rectification errors [30] that would result downstream of separation. Nevertheless, due to convective amplification, disturbance amplitudes increase at the downstream stations. Comparing the natural flow with the two-dimensional forcing case reveals that disturbance amplitudes are approximately doubled in the presence of the forcing at the most downstream location (*cf.* rms and peak-to-peak amplitudes at $\widetilde{x} = 14.25$ in Figs. 6.7a and 6.7b, respectively). Distinct peaks at $\widetilde{z} = -11$ and 17.5 are seen for the natural case (Fig. 6.7a), which are in alignment with the peak locations in the $\overline{u}$ field (Fig. 6.5a). Therefore, the spanwise non-uniformity observed in the time-averaged results of the natural flow may be the result of preferential disturbance amplification at certain spanwise locations. In contrast, when the flow is forced with two-dimensional disturbances, disturbance growth is relatively spanwise uniform (Fig. 6.7b), with any slight spanwise non-uniformities resulting from imperfect disturbance production (Fig. 5.8), and/or potentially the same root cause for preferred amplification seen in the natural flow.

In comparison to the two-dimensional forcing case, stark changes in the topology and development of disturbances are seen when the flow is forced at a spanwise wavelength of $\widetilde{\lambda}_z = 25$ (Fig. 6.7c). As noted by the difference in scale on the left-hand axis of Figs. 6.7b and 6.7c, disturbance amplitudes are notably higher for the $\widetilde{\lambda}_z = 25$ case, with a distinct spanwise modulation apparent at a wavelength that matches that of the forcing. The two depicted phases show that, through half of the forcing cycle, local maxima in the disturbance amplitudes alternate between locations downstream of the spanwise modulated actuator's active regions ($\widetilde{z} = -25$, 0, and 25 at $\theta = 0$) and the centre of the actuator gap regions ($\widetilde{z} = -12.5$ and 12.5 at $\theta = \pi$). Furthermore, the alternating pattern of peaks and valleys between successive streamwise stations at spanwise locations such as $\widetilde{z} = -12.5$ indicates that the spacing of the stations, $\Delta\widetilde{x} = 6.25$, is approximately equal to half the fundamental streamwise wavelength. Thus, the streamwise wavelength of the disturbances is approximately $\widetilde{\lambda}_x = 12.5$, which agrees well with the predominant streamwise wavelength of the shear layer vortices reported in Section 5.5.

As discussed in Section 2.2, it is well established that a Kelvin-Helmholtz type instability of the separated shear layer is responsible for disturbance amplification in the fore portion of LSBs [20, 46, 197, 243], leading to the transition process within LSBs being initially driven by the convective amplification of two-dimensional disturbances [118, 139, 141]. Such is the case when two-dimensional forcing is applied in the current experiments (Fig. 6.7a). However, the results from $\widetilde{\lambda}_z = 25$ point to the possibility of other instability mechanisms, leading to

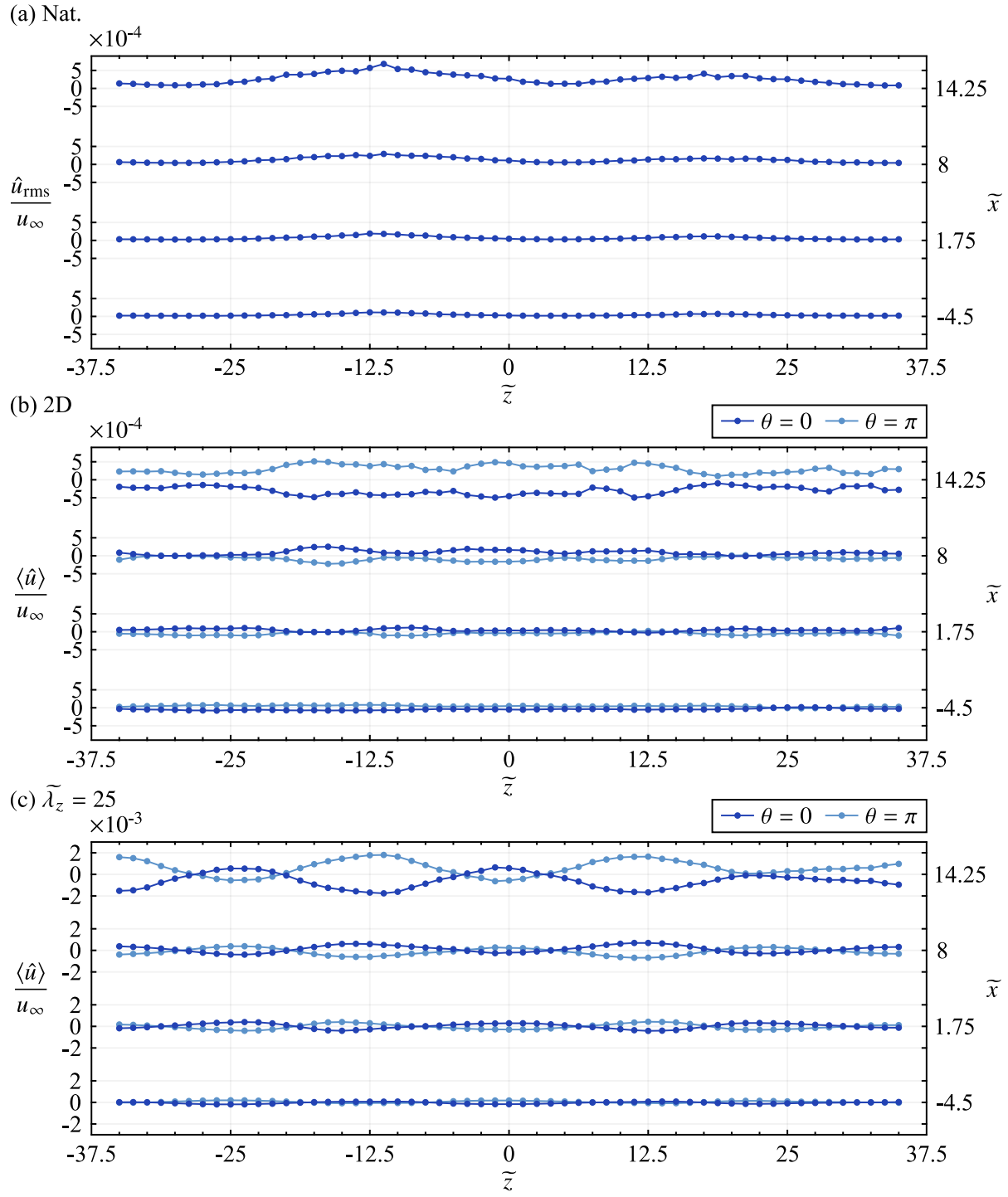

Figure 6.7: (a) Root-mean-square and (b)–(c) phase-averaged streamwise perturbations of the fundamental frequency measured via HWA at several streamwise stations, $y = \delta_1$, and across the span. Note the difference in scale between (a)–(b) and (c) on the left-hand axis.

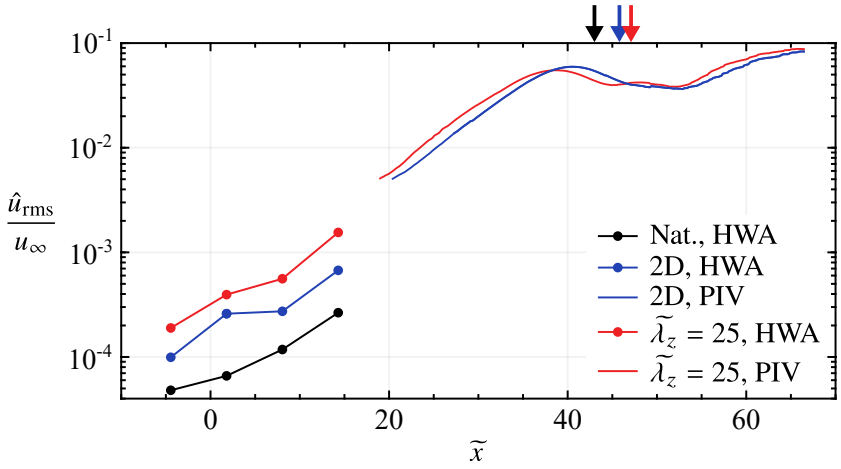

Figure 6.8: Streamwise growth of perturbation of the fundamental frequency at $\widetilde{z} = 0$, $y = \delta_1$, as measured by hot-wire and planar PIV. Minimum threshold of 0.5% of u_∞ applied to PIV results. Arrows (coloured according to legend) indicate $\overline{\widetilde{x}_{\mathrm{h}}}$.

the three-dimensional input disturbances outgrowing two-dimensional disturbances of the same initial amplitude, which is ensured though equal momentum coefficients between the two forcing configurations (Table 5.2).

The streamwise growth of disturbances of the fundamental frequency, quantified through the rms of phase-averaged streamwise velocity fluctuation, *i.e.*, $\hat{u}_{\mathrm{rms}}$, is examined in Fig. 6.8, where a composite of hot-wire and planar PIV results is presented. For the hot-wire measurements, $\hat{u}_{\mathrm{rms}}$ is calculated from the phase-averaged results at $\widetilde{z} = 0$, with the rms taken across the 72 available phases (Fig. 6.7). For the planar PIV, results from phase-locked acquisitions are used, and are therefore limited to the two forcing cases. Note that disturbance amplitudes at streamwise positions upstream of $\widetilde{x} \approx 24$ fall within the noise level of the PIV measurements, and therefore a minimum threshold of 0.5% of u_∞ is applied to the PIV results presented in Fig. 6.8. This cut-off value was determined based on the uncertainty in the PIV measurements (Table 6.1) and where the results deviated from the expected exponential trend [118, 135, 136].

Figure 6.8 shows the significant increase in disturbance amplitude in the fore portion of the LSB ($\widetilde{x} < 15$) on account of the forcing, with disturbance amplitudes for the two-dimensional and $\widetilde{\lambda}_z = 25$ cases at $\widetilde{x} = 14.25$ approximately 5 and 2.2 times higher than the amplitude of the natural disturbances. Thus, at this streamwise location the amplitude ratio between the $\widetilde{\lambda}_z = 25$ and two-dimensional forcing cases is approximately 2.2, which indicates the stability characteristics of the upstream laminar boundary layer favour amplification of the spanwise modulated disturbances. From the PIV data, the difference in amplitudes between the two forcing cases is significantly reduced, with the amplitude ratio reduced from 2.2 at $\widetilde{x} = 14.25$ to 1.3 by $\widetilde{x} = 30$. This indicates a change in stability characteristics from the upstream boundary, leading to the preferential amplification of purely two-dimensional disturbances in the LSB. That being said, the initially higher amplitude of the three-dimensional disturbances persists throughout the length of the LSB, until their growth begins to saturate at $\widetilde{x} \approx 38$, downstream of which saturation of the two-dimensional disturbances follows soon after.

The streamwise growth of disturbances depicted in Fig. 6.8 captures total amplitude, which consists of both normal and spanwise spatial modes in varying ratio based on the forcing case (Fig. 6.7). These constituent components of the disturbances are quantified through a spatial Fourier analysis on both the hot-wire and tomographic PIV data. As before, disturbances at the fundamental frequency are isolated through bandpass filtering and phase-averaging of the hot-wire and PIV data, respectively, with signals extracted at $y = \delta_1$. Exemplary signals are presented in Fig. 6.9, from which the depicted wavenumber spectra are calculated using the entire spanwise extent of the measurement domains. $\widetilde{\lambda}_z = 25$ is defined as the fundamental wavelength, $\widetilde{\lambda}_{z0}$, with the corresponding wavenumber, $\widetilde{k}_{z0} = 0.04$, used for non-dimensionalization. The fundamental streamwise wavenumber is $\widetilde{k}_{x0} = 0.08$ and is also used for non-dimensionalization, allowing for the notation $(k_x, k_z) = (m, \pm n)$ in specifying Fourier modes, where m and n are integer multiples of the fundamental wavenumbers. As is evident from the wavenumber spectra presented in Fig. 6.9, the resolution is relatively coarse about $(1, \pm 1)$ due the finite span of the HWA and PIV measurements domains, each containing only 57 and 521 points (padded to 64 and 1024, respectively) over extents of $\Delta\widetilde{z} = 70$ and 60, respectively. Nevertheless, the distinct $\widetilde{\lambda}_z = 25$ wavelength present in the sample velocity signals is captured in the spectra, with distinct peaks present at $(1, \pm 1)$ for both the HWA and PIV data. Thus, the method can quantify the relative modal contributions to the total disturbance amplitude, with particular attention paid to the fundamental normal (1,0) and first spanwise $(1, \pm 1)$ Fourier modes. Note that due to the convective nature of the disturbances, the amplitudes of the spatial Fourier modes change with phase at a given streamwise position. Therefore, the wavenumber spectra at each x position are averaged across all phases, allowing for the growth of the modes to be tracked with downstream development.

Figures 6.10 and 6.11 present the streamwise growth of the spatial Fourier modes as captured by the hot-wire and tomographic PIV measurements, respectively. When the flow is forced with two-dimensional perturbations, initial disturbance growth in the LSB is almost entirely confined to the normal mode, with all (1,0) amplitudes reported upstream of $\widetilde{x} = 12.45$ at least three orders of magnitude larger than any spanwise mode (Fig. 6.10a). This is consistent with the disturbance development depicted in Fig. 6.7b, where amplitude modulation in the phase-averaged disturbances is nearly spanwise uniform. Disturbance growth remains confined to the (1,0) mode up until the mean maximum bubble height location, as seen in Fig. 6.11a, downstream of which relatively long wavelength ($k_z < k_{z0}$) modes begin to appear. As will be discussed in the following section, the vortex formation process occurs upstream of $\overline{\widetilde{x}_h}$. Therefore, the results indicate that in the presence of two-dimensional forcing, disturbances remain two-dimensional in the fore portion of the LSB and through the vortex formation process, with spanwise modes only appearing further downstream as vortex breakup begins to occur.

For the $\widetilde{\lambda}_z = 25$ forcing case, peaks are observed at both (1,0) and $(1, \pm 1)$ in the hot-wire measurements (Fig. 6.10b), with both modes growing in amplitude as disturbances convect downstream. The amplitude ratio between the normal and first spanwise modes remains relatively constant at 30 : 1 over the three most downstream HWA stations, indicating that, while the normal mode dominates in terms of amplitude, both modes are subject to comparable amplification rates. This is supported by the findings of Michelis *et al.* [153] and Rist & Augustin [198], both of which found comparable amplification rates near mean separation between normal and spanwise

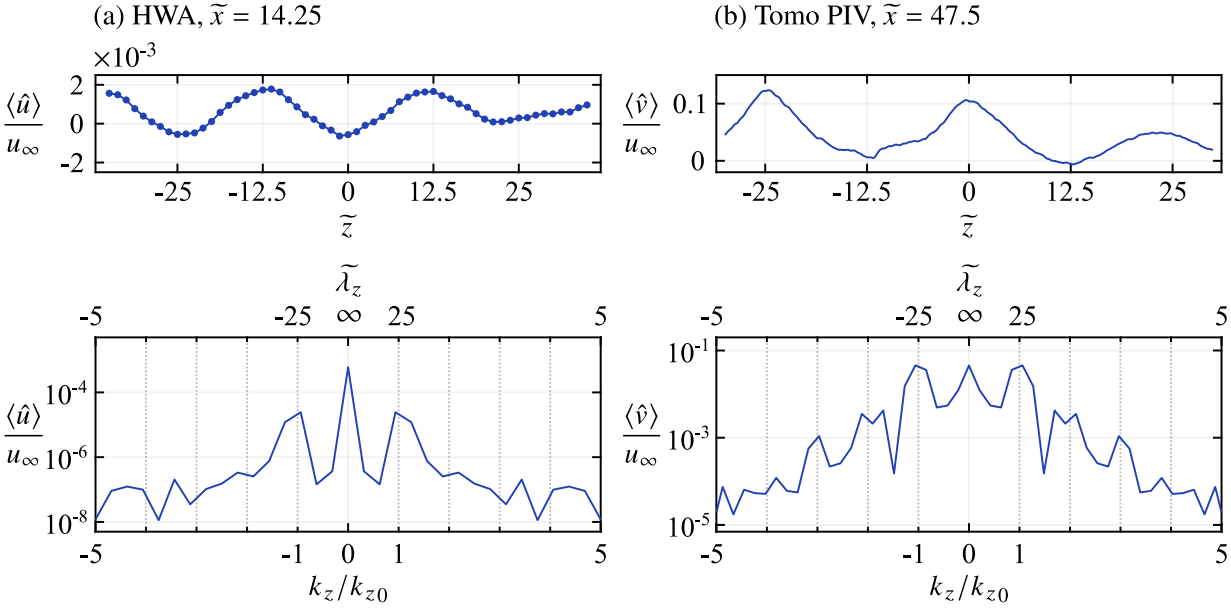

Figure 6.9: *Top row:* Phase-averaged fundamental perturbations modes at $y = \delta_1$ and exemplary streamwise stations for the $\widetilde{\lambda}_z = 25$ forcing case measured by (a) hot-wire and (b) tomographic PIV. *Bottom row:* Corresponding spanwise wavenumber/wavelength spectra.

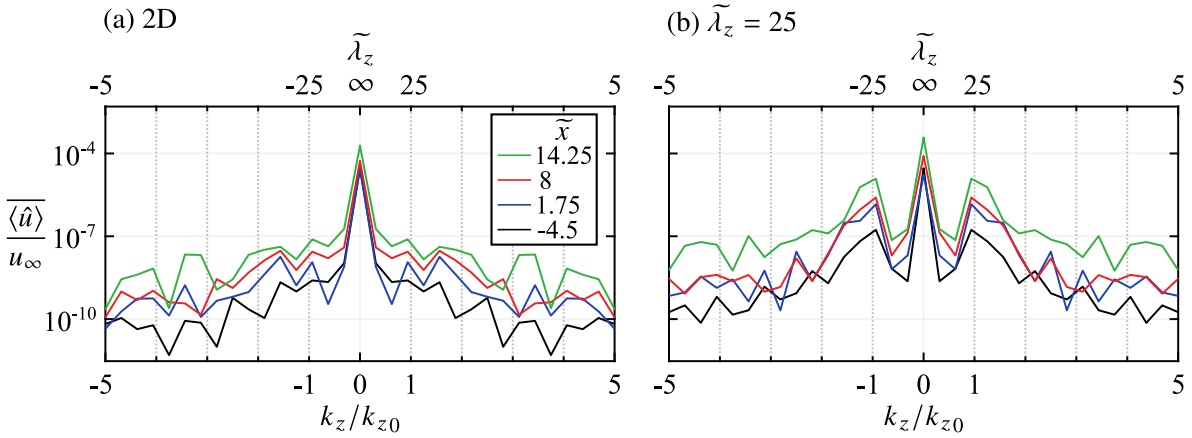

Figure 6.10: Streamwise growth of spatial Fourier modes of the fundamental frequency along $y = \delta_1$ as measured by hot-wire.

modes with oblique wave angles less than $\vartheta = 30°$. In the current experiment, the ratio of the fundamental streamwise to spanwise wavenumbers, k_{x0}/k_{z0}, is 2, yielding an oblique wave angle of $\vartheta = 26.5°$.

Farther into the LSB, the tomographic PIV measurements show strong growth in the (1,0) mode upstream of $\widetilde{x_h}$ for the $\widetilde{\lambda}_z = 25$ case (Fig. 6.11b), while activity at $(1, \pm 1)$ is not detected upstream of $\widetilde{x} \approx 44$. As this spatial mode was detected upstream by the HWA measurements, it is likely present, however it remains undetected in this region as a result low amplitude levels

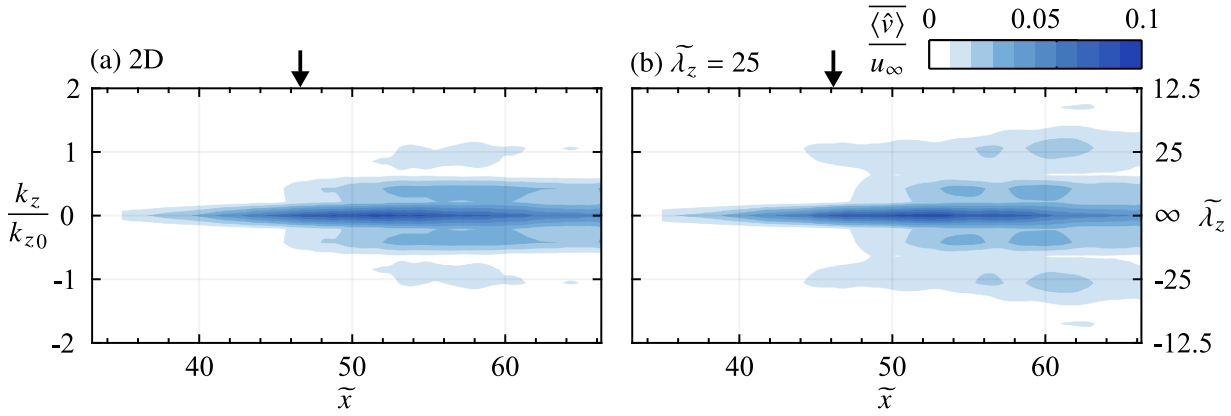

Figure 6.11: Streamwise growth of spatial Fourier modes of the fundamental frequency along $y = \delta_1$ as measured by tomographic PIV. Arrows marks spanwise-averaged $\overline{\widetilde{x_h}}$.

(relative to the tomographic PIV noise level) and averaging the spatial Fourier results across the phases. Nevertheless, the activity in the $(1, \pm 1)$ mode is first detected at $\widetilde{x} = 44$, which is just upstream of $\overline{\widetilde{x_h}}$ and where vortex formation occurs. The ramifications of the growth of this spatial mode on the ensuing development of the shear layer vortices in the LSB remains to be investigated in detail (Section 6.5). What has been made clear in this section is that the disturbance growth upstream of and in the LSB depends strongly on the spanwise wavelength of the input disturbance (Figs. 6.7 and 6.8). Under either of the two forcing configurations considered, the disturbance growth is primarily driven by the fundamental perturbation's normal spatial mode, while growth can also occur in the $(1, \pm 1)$ spatial mode (Figs. 6.10 and 6.11).

6.4.1 Linear Stability Predictions

Linear stability theory (LST) (Section 3.3.1) is well suited to provide insight into the stability characteristics in the fore portion of the LSB on account of the flow being largely two-dimensional (Fig. 6.6) and disturbance amplitudes remaining small (Fig. 6.7) in this region. The primary goal is to investigate the growth of the normal and spanwise modes seen in the measurements (Figs. 6.7, 6.10, and 6.11), particularly in the region downstream of the hot-wire measurements, where disturbance amplitudes remained too low to be resolved by PIV (Fig. 6.8). In the analysis, Eqn. 3.5 governs the growth of small, wave-like perturbations with angular frequency Ω, and streamwise and spanwise complex wavenumbers, $\alpha = \alpha_r + \alpha_i$ and $\beta = \beta_r + \beta_i$, respectively. This is the spatial formulation of the problem (*e.g.*, Schmid & Henningson [215]), where Ω and β_r are prescribed and the eigenvalue problem is solved for spatial growth rates. On account of the flow being nearly spanwise invariant in the LSB fore portion (Fig. 6.6), disturbance growth in the spanwise direction is assumed negligible ($\beta_i = 0$), and the problem is reduced to a solution for α. The stability of a particular disturbance is indicated by the sign of α_i, while the magnitude gives the growth/damping rate. In this context, more negative values of α_i correspond to higher growth rates, with this terminology employed throughout. Eqn. 3.5 is solved numerically using Chebyshev polynomial base functions and the companion matrix technique to treat eigenvalue non-linearity [25]. Further information regarding the solution method can be found in van Ingen

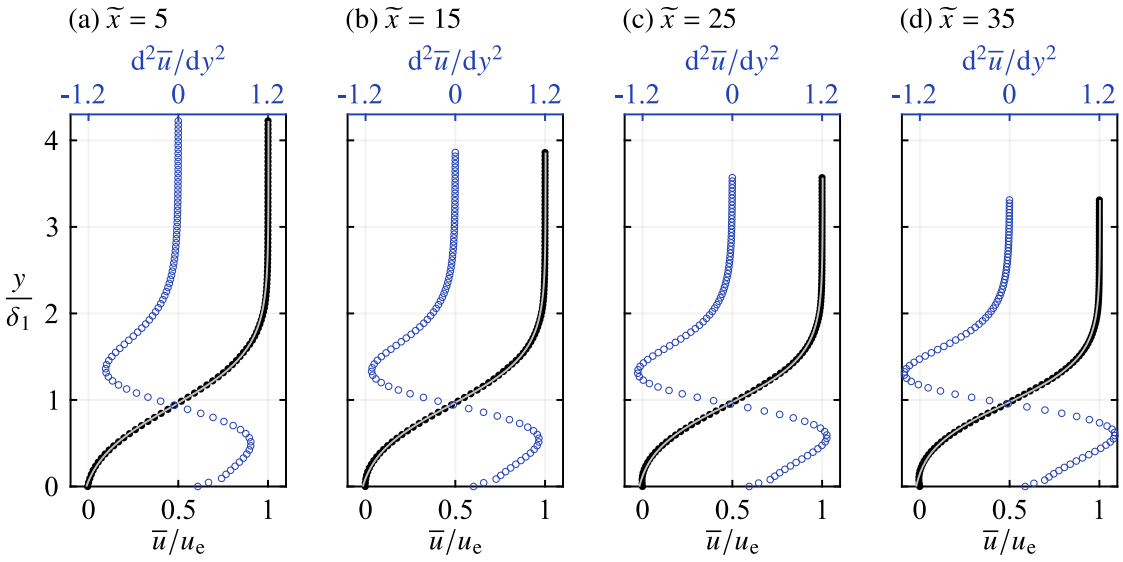

Figure 6.12: Mean velocity profiles measured via planar PIV at $\widetilde{z} = 0$ (black markers) in the natural flow and corresponding hyperbolic tangent fits (solid grey lines, Eqn. 5.3) used in LST calculations. Second derivatives in y (blue markers) are evaluated on the fitted curves at the spatial resolution of the measured data.

& Kotsonis [240].

Measured mean streamwise velocity profiles at discrete streamwise locations serve as an input to the LST calculations, therefore making the analysis local. Spatial gradients estimated from PIV measurements often have a relatively high noise level due to the finite spatial resolution of the measurement technique [248], to which stability predictions can be highly sensitive [23]. Therefore, stability analysis is performed using hyperbolic tangent fits (Eqn. 5.3) to the planar PIV data measured at $\widetilde{z} = 0$ (Fig. 6.3), with fits of this type shown to provide accurate stability predictions [20, 23, 45]. Exemplary velocity profiles and the corresponding fits for the natural flow are shown in Fig. 6.12, where the second derivative of the fitted curved in y has been evaluated at the spatial resolution of the measured data.

For validation purposes, LST predictions and experimental results are compared in Fig. 6.13. The experimental results come from the hot-wire measurements since these were performed in the region where disturbance amplitudes remain low (Fig. 6.4), in addition to providing an independent verification of results since the LST analysis uses planar PIV measurements as input. A measure of amplitude growth is quantified from the LST results through the computation of N factors (Eqn. 3.7), however, the critical location at which disturbances first become unstable, x_{cr}, lies upstream of the planar PIV field of view for all relevant frequencies and therefore cannot be determined directly. However, in the fore portion of the LSB, α_i may be approximated by a second-order polynomial, as demonstrated by Jones *et al.* [91] (see their Fig. 11). Based on this, x_{cr} is estimated by extrapolating the curve fit to $\alpha_i = 0$, which is found to be at $\widetilde{x}_{cr} = -16.5$ for $St_{0\delta_{1s}} = 0.046$ and $\beta_r = 0$ in the natural flow. A direct comparison of N factors with the measured disturbances is not possible since their initial disturbance amplitude, A_{cr}, is unknown and likely could not be measured even if attempted. Therefore, following other investigators [153,

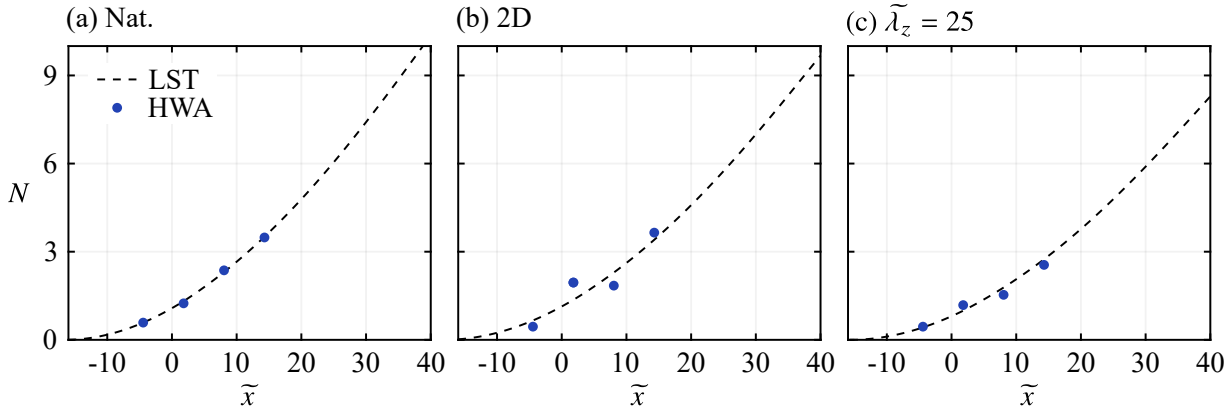

Figure 6.13: Comparison of N factors for $St_{0\delta_{1s}} = 0.046$ from LST results ($\beta_r = 0$) and hot-wire measurements at $\widetilde{z} = 0$. Experimental N factors are matched to LST predictions using a least-squares approach.

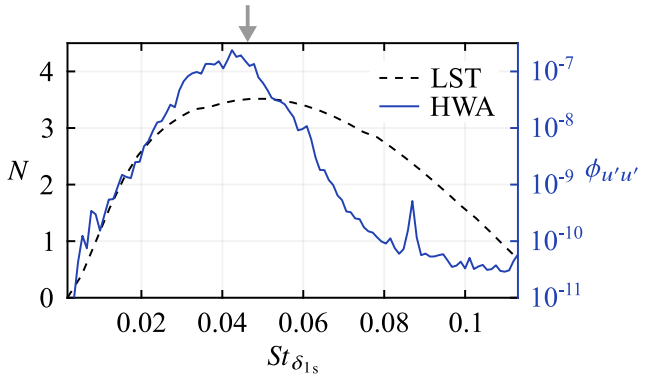

Figure 6.14: Comparison of spectra of LST N factors and measured streamwise velocity fluctuations for the natural case at $\widetilde{x} = 14.25$, $\widetilde{z} = 0$. Grey arrow indicates $St_{0\delta_{1s}}$.

215, 261], the amplification factors are matched across the four measurement locations using a least-squares approach, thus allowing for an estimate of A_{cr} for a given frequency using Eqn. 3.7. The agreement seen in Fig. 6.13 is excellent for all cases.

The validity of the LST predictions are further supported by a comparison of the frequency spectra of LST N factors and experimental streamwise velocity fluctuations at $\widetilde{x} = 14.5$ for the natural case. This is presented in Fig. 6.14, where both spectra show elevated energy content centred at the fundamental disturbance frequency, $St_{0\delta_{1s}} = 0.046$. Thus, based on the good agreement seen in disturbance amplification rates and unstable frequencies (Figs. 6.13 and 6.14, respectively), it is established that the employed LST analysis is suitable for determining stability characteristics in the fore portion of the LSB.

Stability diagrams showing the variation in streamwise growth rates with frequency and streamwise position for $\beta_r = 0$ are presented in Fig. 6.15 for the three investigated cases. The contour separating the white and lightest shade of blue sits at $\alpha_i = 0$ and therefore delineates the curve of neutral stability, with all disturbances of characteristics falling within the coloured region

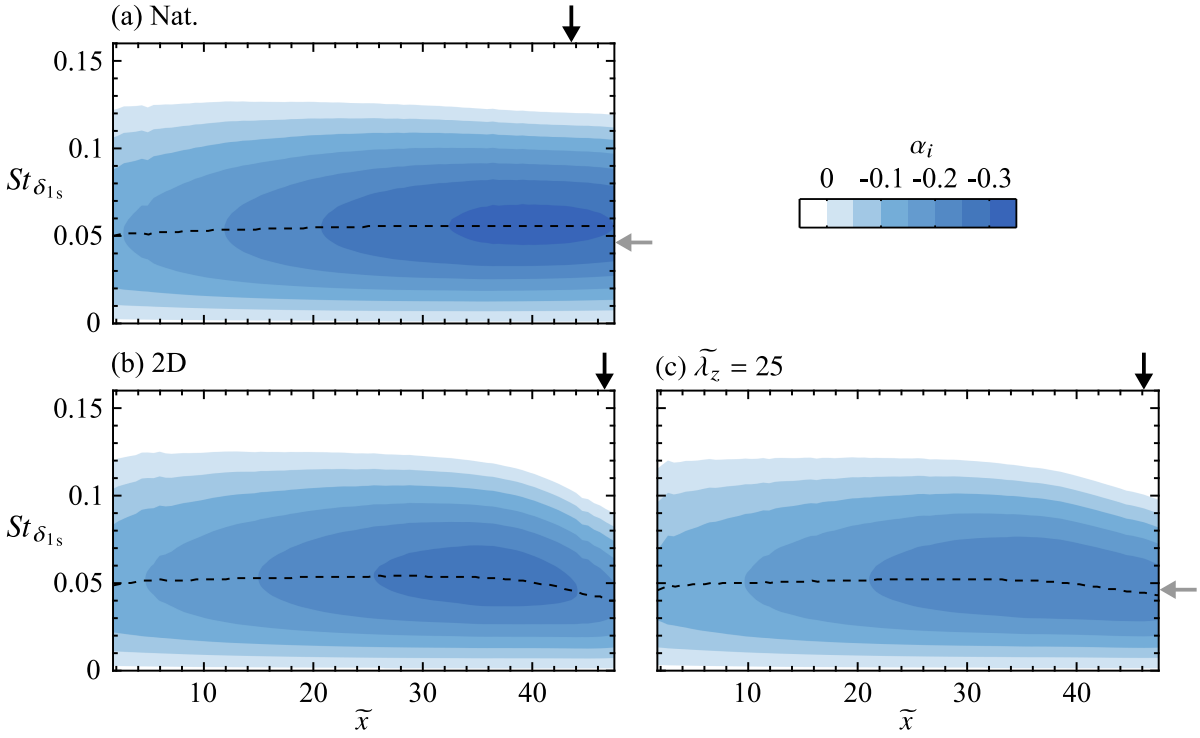

Figure 6.15: Contours of LST predicted streamwise growth rates for $\beta_r = 0$. Dashed lines indicate loci of most unstable frequencies. Black and grey arrows indicate spanwise-averaged $\overline{\widetilde{x_h}}$ and $St_{0_{\delta_{1s}}}$, respectively.

being convectively unstable ($\alpha_i < 0$). As previously mentioned, for the range of frequencies relevant to the LSB ($0.01 \lesssim St_{\delta_{1s}} \lesssim 0.1$), the curve of neutral stability extends upstream of the PIV field of view for all cases. The blacked dashed lines indicate the streamwise trend in the most unstable frequency, which for the natural case (Fig. 6.15a) remains relatively constant at $St_{\delta_{1s}} = 0.05$ throughout the streamwise domain, with LST calculations performed up to and just downstream of the spanwise-averaged mean maximum bubble height location. This is in good agreement with the experimentally determined fundamental frequency, $St_{0_{\delta_{1s}}} = 0.046$.

In the presence of forcing, both types (Figs. 6.15b and 6.15c) lead to significant reductions in growth rates at the fundamental frequency, *i.e.*, mode (1,0), as the maximum streamwise growth rate in the natural flow, $\alpha_i = -0.31$, decreases in magnitude by approximately 13% and 22% on account of the two-dimensional and $\widetilde{\lambda}_z = 25$ forcing, respectively, with reductions on this order extending throughout the fore portion of the LSB. Reduced growth rates on the account of applied forcing has been reported in previous works (Refs. [134, 135, 198, 261] and in Appendix A), and is attributed to the mean flow deformation mechanism proposed by Marxen & Rist [140]. Across the three cases, the $\widetilde{\lambda}_z = 25$ case is subject to the lowest disturbance growth rates, which is significant and is in alignment with the observations of the experimentally determined disturbance development (Fig. 6.8). There it was found that disturbance amplitudes were initially higher for the $\widetilde{\lambda}_z = 25$ near the separation point, while further downstream comparable amplitudes levels were found, indicating that growth rates for two-dimensional forcing cases must be higher in the

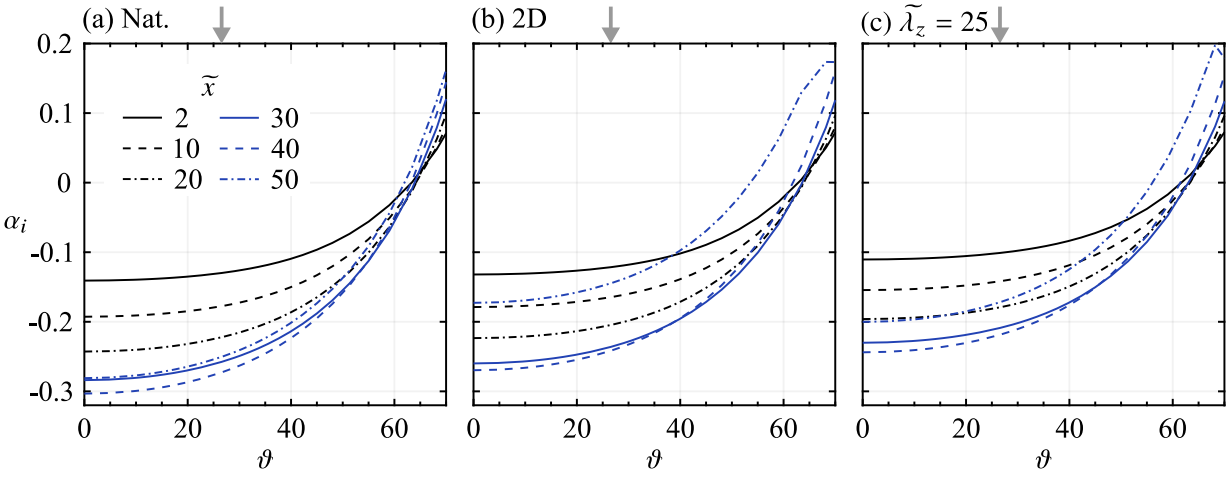

Figure 6.16: Streamwise growth rate as a function of wave angle at several streamwise stations and $St_{0\delta_{1s}}$. The arrows indicate the wave angle of the $(1, \pm 1)$ mode, $\vartheta = 26.5°$.

region $15 \lesssim \widetilde{x} \lesssim 20$, which is supported by the LST findings. Whether or not this is a direct outcome of growth in only the (1,0) mode remains to be determined through the examination of LST results for non-zero spanwise wavenumbers.

The stability of oblique disturbances in the fore portion of the LSB is assessed in Fig. 6.16, where streamwise growth rates are plotted as function of wave angle, $\vartheta = \arctan(\beta_r/\alpha_r)$, at several streamwise stations. The growth rates correspond to the fundamental frequency, and therefore wave angles of $\vartheta = 0°$ and $\pm 25.6°$ give the (1,0) and $(1, \pm 1)$ modes, respectively. Across the three studied cases, nearly all oblique disturbances with a wave angle of less than 60° are unstable, with the noted exception being at $\widetilde{x} = 50$, which is well within the region where disturbances amplitude have reached levels that likely incite non-linear interactions (Fig. 6.3). For all cases and streamwise positions, the highest growth rates are found for the (1,0) mode, with comparable levels of amplification seen for wave angles of $\vartheta \lesssim 30°$, agreeing with the previously discussed findings of Refs. [153, 198]. At the most upstream stations ($\widetilde{x} = 2$ and 10) the reduction in growth rate with increasing wave angle within $0 \leq \vartheta \leq 30$ is minimal, with the range of wave angles that experience comparable growth rates narrowing about 0° with increasing streamwise position. Thus, for all three flows investigated, as disturbances develop downstream of the separation point, the fundamental normal mode and oblique waves of $\vartheta \lesssim 30$ will initially grow at comparable rates. As the modes progress further downstream, oblique waves of higher wave angles (lower spanwise wavelengths) will continually 'fall off' due to growth rates that are reducing compared to the lower wave angle disturbances. Thus, given input disturbances that provide a full spectrum of spanwise wavelengths, the larger wavelength disturbances will be most amplified as they convect through the fore portion of the LSB. These findings supports the increased effectiveness of the $\widetilde{\lambda}_z = 25$ forcing case, in terms of effecting change in disturbance and flow development, in comparison to the two other forcing configurations considered in Chapter 5, since the disturbances produced by the latter two configurations were subject to decreasing growth rates on account of their higher wave angles ($\vartheta = 33.7°$ and 45° from $\widetilde{\lambda}_z = 18.75$ and 12.5, respectively).

In comparing Figs. 6.16b and 6.16c, it is clear that all amplification rates for the two-dimensional

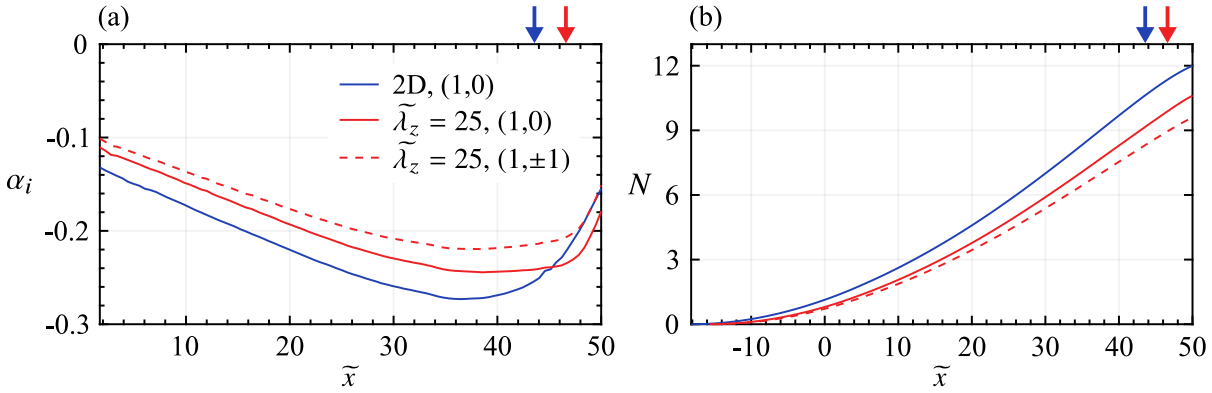

Figure 6.17: Comparison of streamwise amplification (a) rates and (b) factors for the fundamental normal and spanwise modes, (1,0) and $(1, \pm 1)$, respectively. Arrows (coloured according to legend) indicate spanwise-averaged $\overline{\widetilde{x}_h}$.

forcing case are higher than those of the $\widetilde{\lambda}_z = 25$ forcing case. A direct comparison of the modes pertinent to the 2D and $\widetilde{\lambda}_z = 25$ forcing cases is made in Fig. 6.17, where streamwise trends in amplification rates and factors are presented for the (1,0) and $(1, \pm 1)$ modes. The results show that all modes are unstable and experience comparable growths rates throughout the fore portion of the LSB. Therefore, according to the theory of transition onset at some critical disturbance amplitude [224, 239], an attempt to predict which of the two considered forcing scenarios would lead to earlier transition could be made, which could involve assuming linear superposition between the normal and spanwise modes. However, the experimental results have already established that comparable total disturbance amplitudes are found between the two forcing cases into the aft portion of the LSB (Fig. 6.8), leading to largely similar mean topologies (Fig. 6.3). Therefore, the defining distinction between the two forcing cases is not related to which scenario leads to an earlier onset of transition. Rather, the LST analysis firmly establishes the spanwise modes targeted by the $\widetilde{\lambda}_z = 25$ forcing as unstable, allowing for an evaluation of the effect that allocating input energy to unstable spanwise modes has on the development of the shear layer vortices and the ensuing vortex dynamics.

6.5 Three-Dimensional Flow Development

Thus far, mean features and disturbance development in the separation bubble have been characterized (Sections 6.3 and 6.4, respectively). The link between these two facets of the flow is now established, as the coherent structures that manifest from the disturbances are examined and their role in producing the observed mean flow field and its statistics is elucidated. Figure 6.18 presents instantaneous iso-surfaces of the Q-criterion [84] for the three investigated cases. Similar to the flow development seen in Chapter 5 (Fig. 5.13a), the snapshots of the natural flow (Fig. 6.18a) show coherent spanwise-oriented vortices with significant spanwise undulations, with the vortices forming in proximity to the mean maximum bubble height location. Across all the depicted snapshots, the spanwise locations at which the vortices surge forward in the streamwise direction

directly correspond with where the mean maximum height location is advanced downstream, with the trend consistent across the entire dataset. Thus, as has been reported previously [112, 134, 260], the shear layer vortices are the dominant factor in defining the mean topology of the aft portion of the LSB. Here, it is established that consistent spanwise deformations in the shear layer vortices result in a corresponding peak and valley structure of the aft portion of the LSB, as characterized by the maximum bubble height location. Furthermore, the same trend is expected in the mean reattachment location, since previous findings have established that changes in the maximum bubble height location coincide with commensurate changes in the mean reattachment location (Section A.3.1 and Refs. [134, 135, 260]).

Figures 6.18b and 6.18c present instantaneous snapshots showing shear layer vortex topology for the two-dimensional and $\widetilde{\lambda_z} = 25$ forcing cases, respectively. In comparison to the natural flow (Fig. 6.18a), both types of forcing result in the vortex formation process occurring further upstream, with the majority of snapshots presented in Figs. 6.18b and 6.18c showing structures near and upstream of $\widetilde{x} = 40$. Furthermore, these upstream structures show a much higher degree of spanwise uniformity compared to the natural flow, as was seen in the results of Chapter 5 (Figs. 5.13b and 5.13e). Across both forcing cases, the structures downstream of the mean maximum bubble height location show significant spanwise deformations compared to their upstream counterparts, with many of the downstream filaments deformed into a peak and valley arrangement. The observation of spanwise undulatory vortex filaments in the aft portion of LSBs has been observation across all results presented in this thesis (Chapters 4–6 and Appendix A), indicating that they are a fundamental aspect of the flow development.

Returning to the natural flow, with the link established between the spanwise trend in the mean maximum bubble height and the shear layer vortices, a statistical estimate of the predominant spanwise wavelength of naturally developing vortices can be made from the approximate peak-to-peak spanwise distance in $\widetilde{\overline{x_h}}$ since this result is time-averaged. From Fig. 6.5a, this is estimated at $\widetilde{\lambda_z} \approx 28$, which corresponds precisely with the most prevalent wavelength detected through the wavelet analysis employed in Chapter 5 (Fig. 5.15a). While results from the LST analysis (Fig. 6.16a) indicate that disturbances of this spanwise wavelength (corresponding to $\vartheta = 23.7°$) at the fundamental frequency would experience growth rates comparable to that of the most amplified spatial mode, the evidence suggests that this spanwise modulation of the natural flow is not associated with the fundamental frequency. First, the significant differences between the planar PIV results of Chapters 5 and 6 (Table 6.2) point to the presence of a low frequency modulation that is not fully captured by the high-speed measurements of Chapter 5. Second, if the modulation was associated with the fundamental frequency then one would expect forcing at this frequency to enhance the features seen in the natural flow. This is not the case, as forcing results in stark changes in the development of the shear layer vortices (Fig. 6.18) and subsequently the mean topology of the bubble (Fig. 6.5). Thus, it is more likely that the changes in stability induced by the forcing (Fig. 6.15) result in a significant reduction in the effects of the phenomenon causing the spanwise modulation of the natural flow. Finally, further evidence that associates this phenomenon with a frequency lower than the fundamental frequency is provided in Section 6.5.1.

The three-dimensional development of the shear layer vortices for the two forcing cases is examined in Fig. 6.19, where phase-averaged results are shown for four phases within the forcing cycle. Beginning with the two-dimensional forcing case, the most upstream structure in

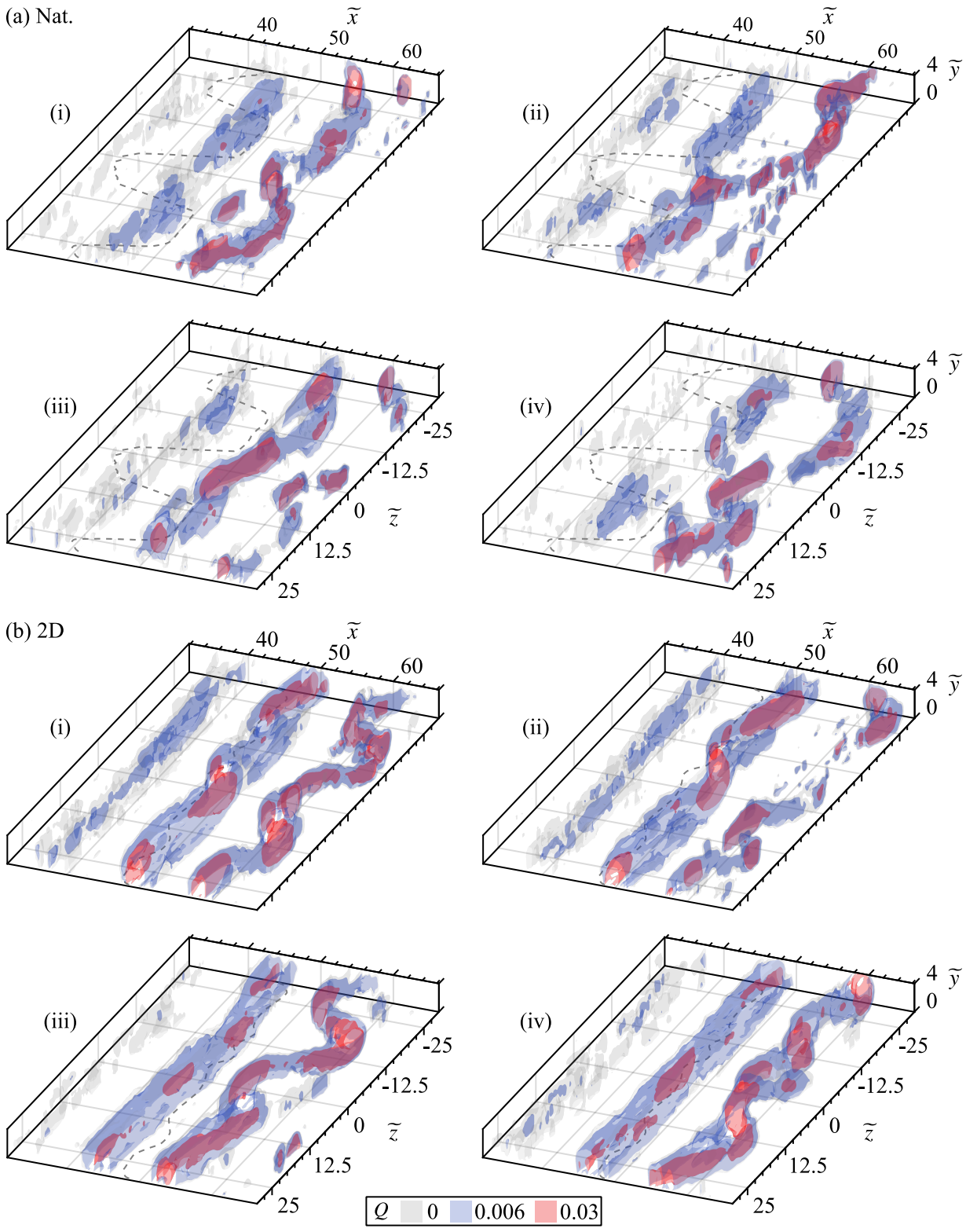

Figure 6.18: Instantaneous iso-surfaces of the Q-criterion [84]. Dashed lines indicate $\overline{\widetilde{x}_{\mathrm{h}}}$.

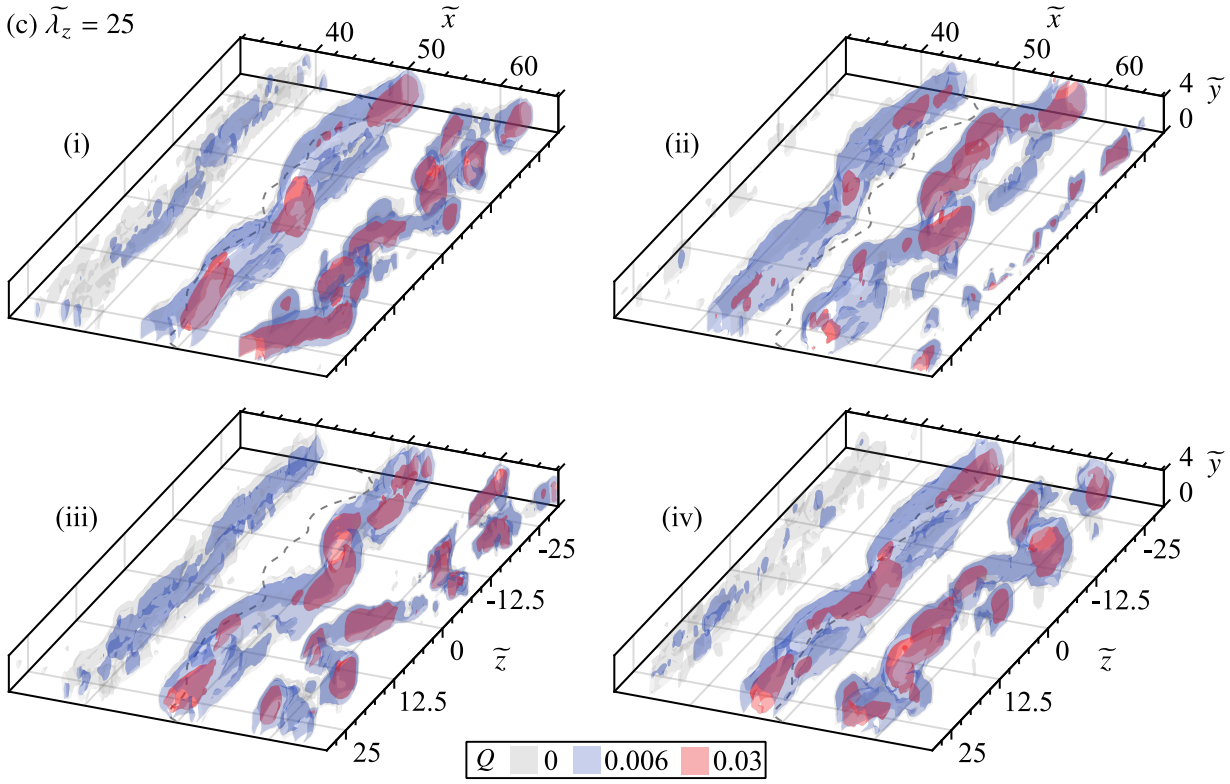

Figure 6.18 (cont.): Instantaneous iso-surfaces of the Q-criterion [84]. Dashed lines indicate $\overline{\widetilde{x_h}}$.

Fig. 6.19a-i, labelled I, is almost entirely two-dimensional, which is maintained as it convects downstream, reaching the mean maximum bubble height location in Fig. 6.19a-iv. At $\overline{\widetilde{x_h}}$, the spatial Fourier analysis showed the emergence of spanwise modes (Fig. 6.11a), which is consistent with the development seen in vortex II, as it is not until this structure is downstream of $\overline{\widetilde{x_h}}$ that vortex breakup begins to take place. Note that vortex II is the same structure as vortex I, only a full 2π later in the forcing cycle. Break-up of vortex II takes place between Figs. 6.19(a-i)–(a-iv), with multiple dislocations developing over the span of the filament, marked by the gaps in the $\langle Q \rangle = 0.012$ level, with the structure formed into a spanwise undulatory shape, which is most clearly seen in the top view provided in Fig. 6.20a.

Evaluating the flow development of the $\widetilde{\lambda}_z = 25$ case (Fig. 6.19b) reveals that, similar to the two-dimensional forcing case, the most upstream structure in Fig. 6.19b-i, labelled III, is largely two-dimensional, however a spanwise undulation in the vortex filament is discernible, with the wavelength matching that of the forcing. It is noted that detection of this wavelength in the spatial Fourier analysis (Fig. 6.11b) occurs much further downstream, which is an artifact of averaging the Fourier analysis results across all phases. As was reported in Chapter 5 (Figs. 5.13e and 5.16b), the locations at which the vortex bulges forward in the streamwise direction ($\widetilde{z} = -25$, 0, and 25) are downstream of the three-dimensional actuator's active region (Fig. 5.1c) and are aligned with the peaks seen in the spanwise hot-wire scans (Fig. 6.7c). Thus, the small amplitude disturbances tracked through the fore portion of the LSB (Section 6.4) are found to manifest in the shear layer vortices through the development of a spanwise undulations of a matching wavelength. Tracking

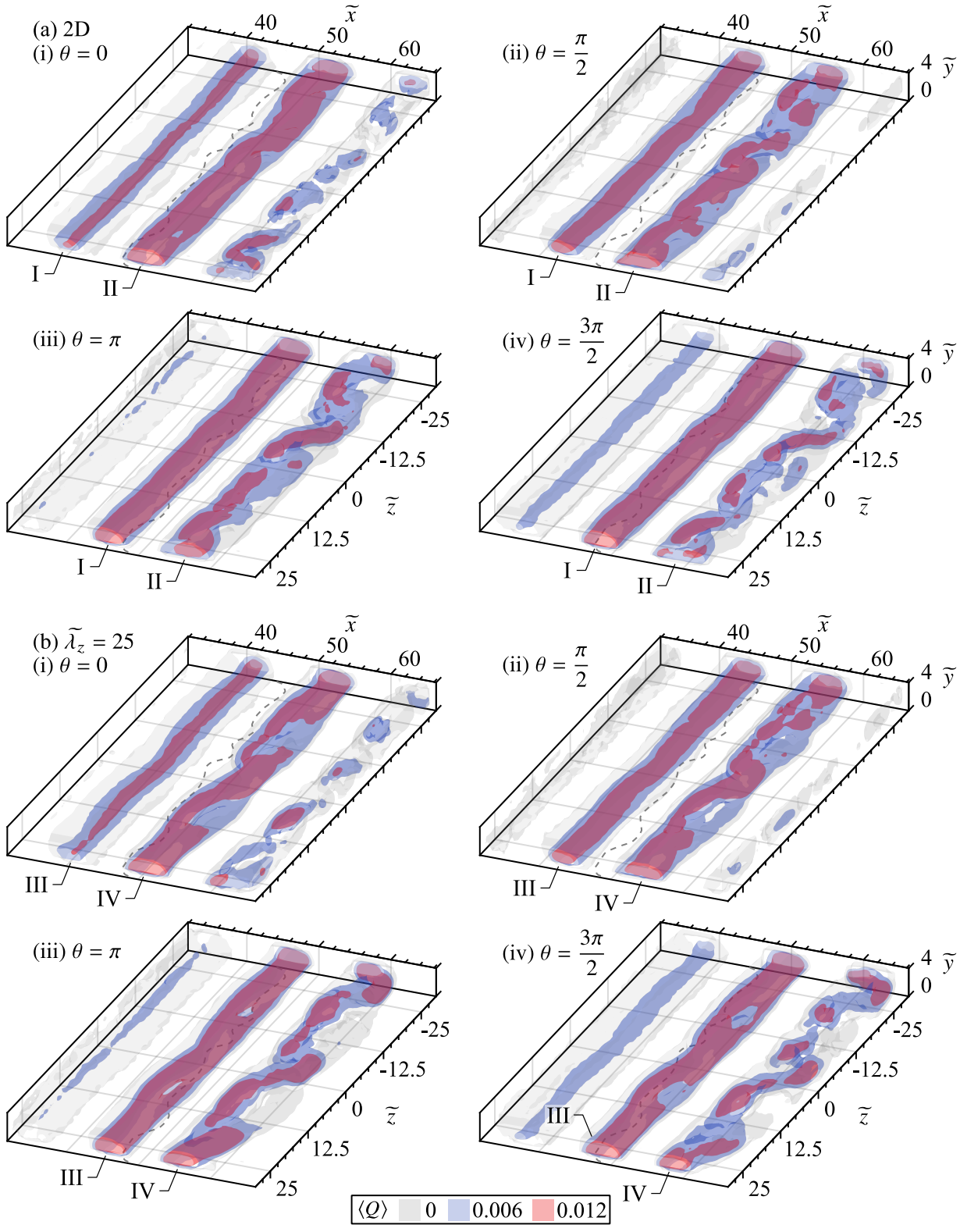

Figure 6.19: Sequences of phase-averaged Q-criterion [84]. Dashed lines indicate $\overline{\widetilde{x}_h}$.

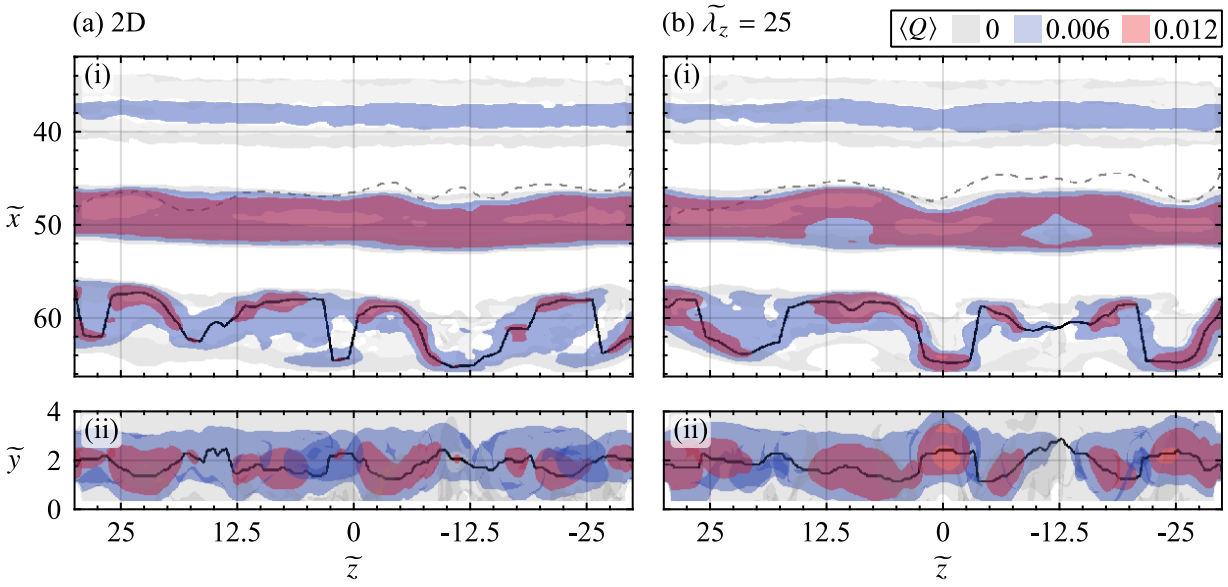

Figure 6.20: (i) Top and (ii) end views of phase-averaged Q-criterion [84] for $\theta = 3\pi/2$ phase. End views show values of $\langle Q \rangle$ downstream of $\widetilde{x} = 54$ only. Black solid lines estimate the core of the most downstream vortex. Grey dashed lines indicate $\widetilde{x_h}$.

structure III as it develops downstream reveals that this undulation intensifies, with a distinct undulatory shape seen in the vortex filament one full cycle later (structure IV in Fig. 6.19b-i). In contrast, in the presence of two-dimensional forcing, structures at the same streamwise position remained largely spanwise uniform (*e.g.*, vortex II in Fig. 6.19a-i). As structure IV develops downstream, the vortex filament becomes increasingly distorted with dislocations appearing at various locations across the span, however, the overall spanwise peak and valley arrangement of the filament is preserved, as seen in Figs. 6.19b-iv and 6.20b.

Figure 6.20 presents top (x-z) and end views (y-z) of the $\theta = 3\pi/2$ phases presented in Fig. 6.19, in which the core of the most downstream structure is estimated through local maxima detected in $\langle Q \rangle$, with the results spatially smoothed in the x-direction using a kernel of width $\Delta\widetilde{x} = 1$. Through identification of the vortex cores, it is evident that the streamwise forward sections of the filaments are also displaced farther from the wall, with the effect more pronounced for the $\widetilde{\lambda}_z = 25$ case (*e.g.*, consider the filament sections at $\widetilde{z} = 0$ in Figs. 6.20a and 6.20b). In Chapter 5, the same vortex topology was observed (Fig. 5.16), and a vortex filament model was developed (Section 5.5.1), showing a spanwise undulatory vortex filaments self-induces a net rotational motion, causing its streamwise forward sections to tilt away from the surface, thus leading to a continual intensification of vortex stretching in a shear flow. The constant observation of streamwise forward vortex segments that are tilted away from the surface in this chapter (Fig. 6.20) and the two previous (Figs. 4.26 and 5.16) indicates that these dynamics are intrinsic to the breakup process of the studied shear layer vortices.

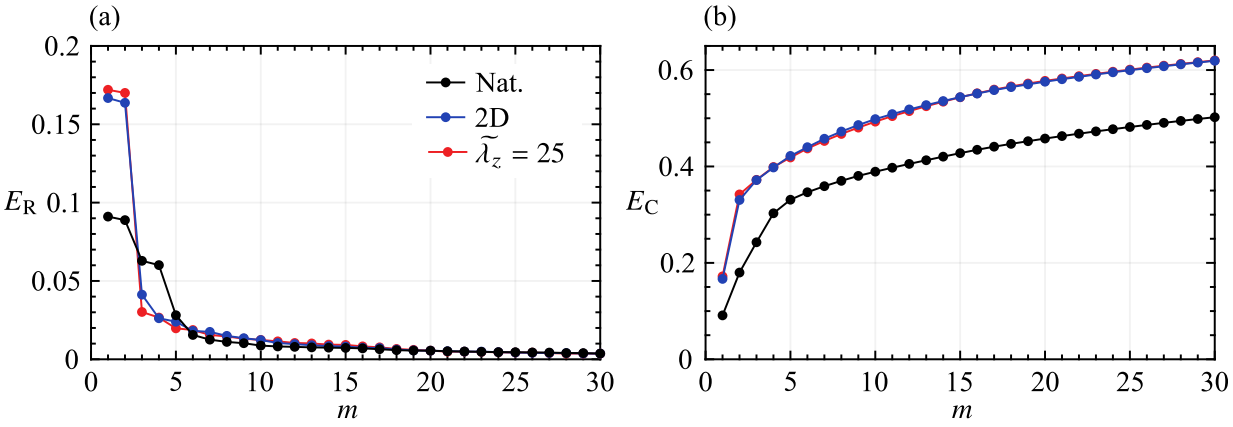

Figure 6.21: POD (a) relative and (b) cumulative modal energy distributions.

6.5.1 Proper Orthogonal Decomposition

To gain further insight into the characteristics of the coherent structures present in the studied LSB, proper orthogonal decomposition (Section 3.3.2) is performed on the tomographic data using the snapshot method of Sirovich [223]. For each case, a total of 2400 snapshots were used in the computation. The code used is provided in Appendix D.2, which required special consideration given that the size of each dataset (approx. 128 GB) exceeds the typical amount of memory available in a personal computer.

Figure 6.21 presents the relative and cumulative energy distributions across the first 30 modes. As is typically seen for flows involving large-scale propagating coherent structures [124, 241, 244, 260], a significant portion of the total turbulent kinetic energy is captured within a small number of modes, with these values at approximately 50% for the natural flow, and 62% for the two forcing cases (Fig. 6.21b). Additionally, the most energetic modes are grouped into pairs of similar energy levels (*i.e.*, modes 1 and 2 for all cases, and modes 3 and 4 for the natural cases in Fig. 6.21a). The paired nature of the modes was confirmed through inspection of their spatial distribution/eigenfunctions, which show a distinct streamwise phase offset of $\pi/2$. Therefore, every other spatial mode is plotted in Fig. 6.22 for brevity.

For the two forcing cases (Figs. 6.22b and 6.22c), the most energetic mode pair features a distinct spanwise uniform and streamwise periodic spatial structure that associates these modes with the LSB shear layer vortices (*cf.* Fig. 6.19). The signature is strongest in the wall-normal component of the spatial mode, $\gamma_v^{(1)}$, with similar features also identifiable in the streamwise component, $\gamma_u^{(1)}$. For the two-dimensional forcing case (Fig. 6.22a), the first mode shows a high level of spanwise uniformity that persists until the mean maximum bubble height location, downstream of which a random distribution of spanwise fluctuations is present, thus reducing the spanwise coherence of the mode's total velocity magnitude in this region. This is consistent with the flow development depicted in Fig. 6.19a, where the vortex filaments remained spanwise uniform until just downstream of $\widetilde{\overline{x_h}}$, after which the turbulent breakup process began. The first mode of the $\widetilde{\lambda}_z = 25$ case shows similar features (Fig. 6.22b), with one important distinction, as the spanwise wavelength imparted by the forcing is evident, most notably in $\gamma_v^{(1)}$. For this mode,

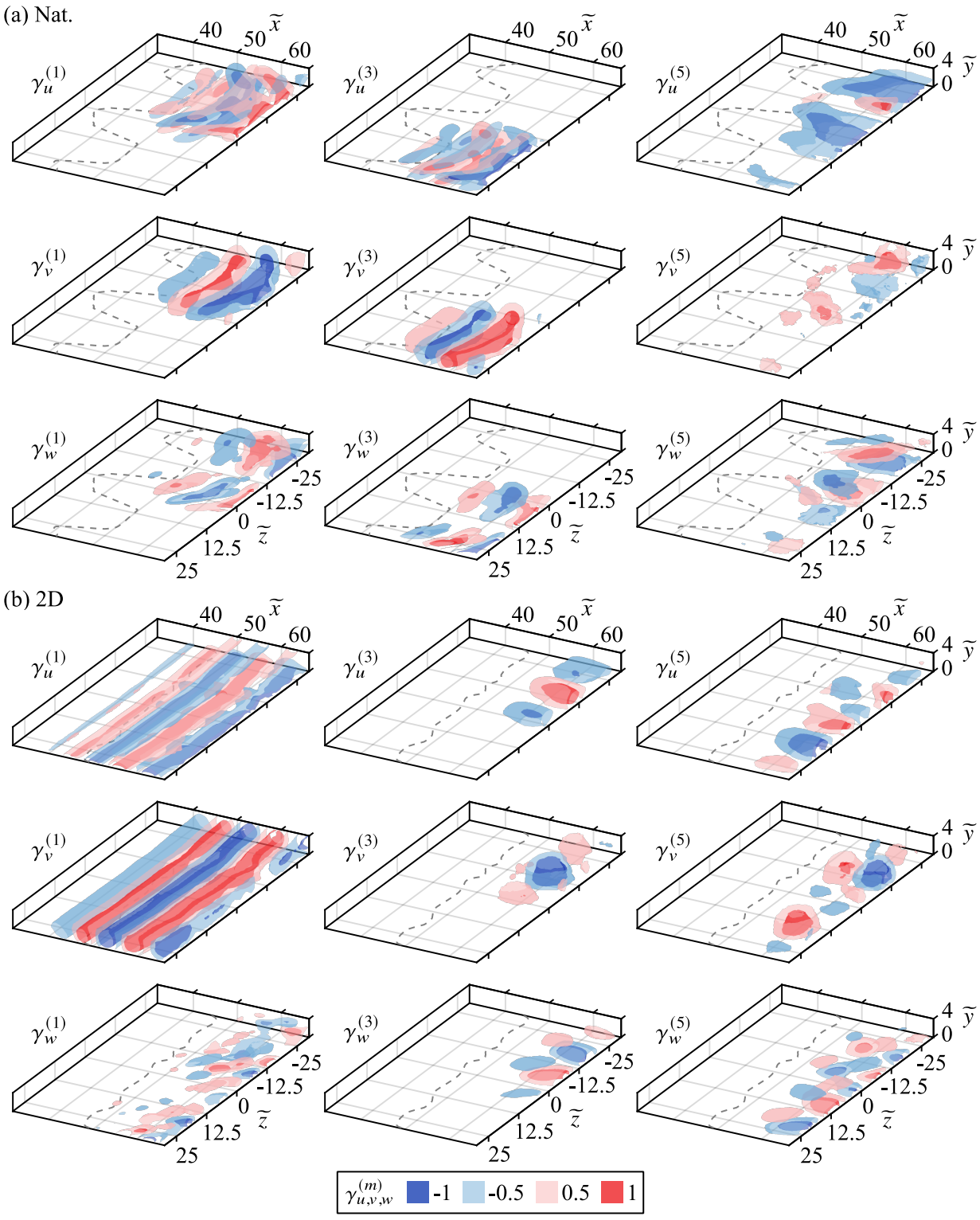

Figure 6.22: Normalized POD spatial modes. Dashed lines indicate $\overline{\widetilde{x}_\mathrm{h}}$.

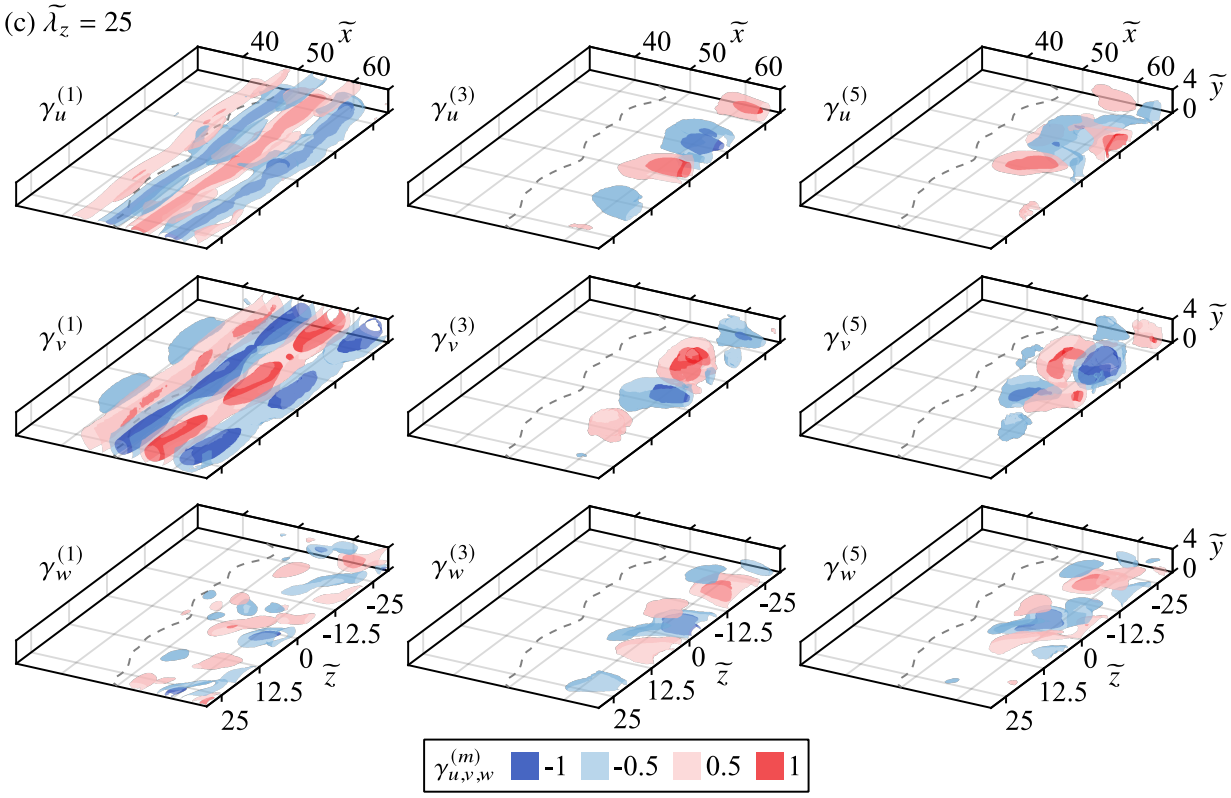

Figure 6.22 (cont.): Normalized POD spatial modes. Dashed lines indicate $\overline{\widetilde{x}_\mathrm{h}}$.

the highest intensity fluctuations are found at $\widetilde{z} = -25$, 0, and 25, which are aligned with the spanwise modulated actuator's active regions and where the vortex filament surges forward in the streamwise direction (Fig. 6.19b).

From Figs. 6.22b and 6.22c, modes 3 and 5 for both the two-dimensional and $\widetilde{\lambda}_z = 25$ cases show spatially periodic structures in the spanwise direction for all three velocity components. These structures are located downstream of $\overline{\widetilde{x}_\mathrm{h}}$, where deformation and break up of the shear layer vortices take place (Fig. 6.19), and so these POD modes indicate that there is a spatial periodicity associated with these processes. Indeed, the spanwise wavelength of the $\gamma^{(3)}$ mode for the $\widetilde{\lambda}_z = 25$ case matches the forcing, indicating that, in addition to the spanwise wavelength already present in the shear layer vortices ($\gamma_v^{(1)}$), further deformations develop at the forcing wavelength as part of the vortex breakdown process. This could be associated with the production of strong wall-normal and spanwise velocity fluctuations through the re-orientation of the filament's spanwise vortices, as discussed in Section 4.3.3 (Fig. 4.26). Structures of the same wavelength, albeit localized to only a portion of the spanwise domain, are observed in mode 3 of the two-dimensional forcing case, indicating that same phenomenon likely influences the vortex breakdown process. For both cases, mode 5 shows a more spatially random distribution of structures of varied spanwise wavelengths, indicating that this mode is associated with turbulent breakup and/or higher harmonics of the coherent motions.

In contrast to the two forcing cases, the most energetic mode for the natural flow does not show

spanwise uniformity across the measurement domain (Fig. 6.22a). Rather, both the streamwise and wall-normal components depict structures associated with vortex shedding localized to within $-30 \lesssim \widetilde{z} \lesssim 0$, while the same is seen in the third mode, except localized to $0 \lesssim \widetilde{z} \lesssim 30$. These two zones align with the peak and valley structure of $\widetilde{\overline{x_h}}$ and the mean velocity field (Fig. 6.5a), providing further confirmation that the statistical characteristics of the flow are dictated by the development of the shear layer vortices. In the instantaneous snapshots provided in Fig. 6.18a, the shear layer vortices are consistently distorted at $\widetilde{z} = 0$, which alongside the POD results, point to 'cellular' vortex shedding processes localized to these zones, as opposed to the spanwise uniform process observed when the flow is forced. Further evidence that this activity is the result of a low frequency modulation of the natural flow is provided through an assessment of the POD temporal coefficients, $b^{(m)}$. These are presented in cross-plots for selected mode pairs in Fig. 6.23.

As outlined by van Oudheusden *et al.* [241], the temporal coefficients for mode pairs related to the same coherent motions, although statistically uncorrelated, are expected to be dependent, and therefore are predicted to form an ellipse:

$$\frac{b^{(m)}}{2e^{(m)}} + \frac{b^{(m+1)}}{2e^{(m+1)}} = 1, \tag{6.1}$$

where $e^{(m)}$ is the eigenvalue associated with mode m. The relationship is expected to hold true for modes 1 and 2 for all the investigated cases, in addition to modes 3 and 4 for the natural flow, and so these modes are cross-plotted in Fig. 6.23. The expected result is found for the two forcing cases in Figs. 6.23c and 6.23d, as the strong periodicity induced in the shear layer vortices by the forcing leads to all realizations falling on the unit circle. The minimal scatter about the circle indicates that amplitude variation from cycle-to-cycle is relatively low. In contrast, both mode pairs for the natural flow, while forming a circular pattern, show significant scatter about the unit circle and therefore significant cycle-to-cycle amplitude modulations are present in the vortex shedding process. These amplitude modulations are most likely to occur on a time scale greater than that of the vortex shedding process since it is the slowest motions in a flow that generally contain most of the turbulent kinetic energy.

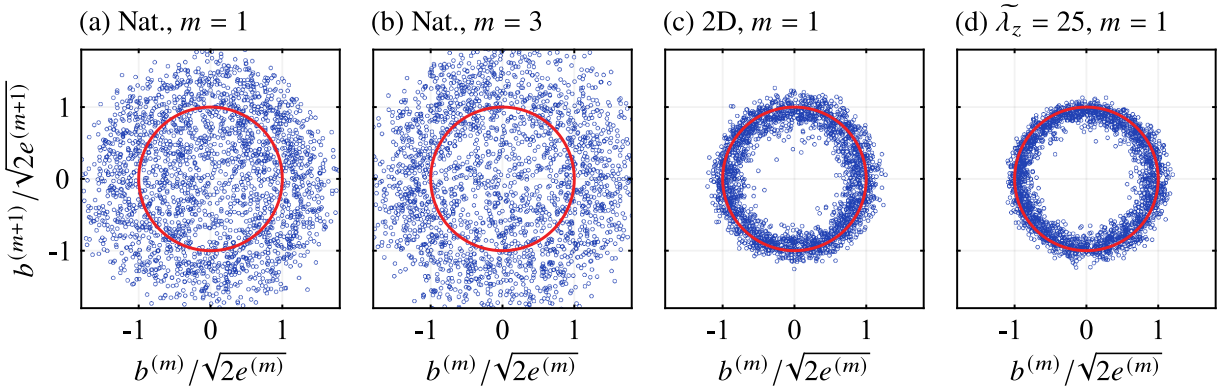

Figure 6.23: Cross-plot of POD temporal coefficients for select mode pairs. Unit circle in red.

6.6 Concluding Remarks

In this chapter, the growth of spanwise disturbance modes in a laminar separation bubble was investigated, with special consideration paid to the stability characteristics that dictate the growth of such modes and the ensuing effect of their development on the dynamics of the LSB shear layer vortices. Disturbance modes were targeted using the forcing technique developed and validated in Chapter 5, allowing for the introduction of two-dimensional or spanwise modulated perturbations of equivalent amplitude. A spanwise wavelength of $\widetilde{\lambda}_z = 25$ was selected for investigation, corresponding to two times the fundamental streamwise wavelength of disturbances in the LSB. In total, three cases were considered: (i) the naturally developing flow, and forcing with spanwise wavelengths of (ii) infinite (two-dimensional), and (iii) $\widetilde{\lambda}_z = 25$. The same wind tunnel facility, model, and flow conditions of the Chapter 5 experiments were employed, and thus a similar LSB, characterized by a nominal Reynolds number of $Re_{\delta_{1_s}} = 750$, was studied. Measurements were performed using hot-wire anemometry and tomographic PIV, with the former employed in the fore portion of the bubble where disturbance amplitudes are relatively low. Furthermore, planar PIV measurements were performed on a single plane within the tomographic volume, thus providing a means for validating the tomographic measurements, in addition to providing reliable input data for stability calculations.

In assessing the time-averaged characteristics of the flow field, comparison of the planar and tomographic measurements showed excellent agreement on all statistical quantities, thus establishing the tomographic measurements as reliable. For all cases, the flow in the fore portion of the LSB was found to be essentially spanwise uniform, with mean flow velocities in the spanwise direction reported at less than 2% of the free-stream velocity. Downstream, in the region where the shear layer vortices formed, the spanwise uniformity of the two forcing cases and natural flow were in stark contrast, as the former was spanwise uniform, while the latter featured a peak and valley arrangement in the mean streamwise velocity field and subsequently the spanwise trend in the mean maximum bubble height location. These features were shown to be directly related to the development of the shear layer vortices, as in the presence of forcing the vortices were two-dimensional at formation and featured strong spanwise coherence. In contrast, in the natural flow the vortices were found to shed in localized regions across the span, with strong distortions in the filaments between these shedding 'cells'. Confirmation relating this phenomenon to a low frequency modulation of the natural LSB was provided through consideration of three factors. These included differences reported in the flow field statistics based on sampling time, an assessment of the stability changes invoked by the forcing, and the temporal characteristics of the natural flow elucidated through POD analysis. Nevertheless, the spanwise wavelength of the modulated natural flow matched that of the 2 : 1 three-dimensional forcing case, indicating that this low frequency modulation may be the underlying source for preferential amplification of disturbances of this spanwise wavelength. Therefore, the growth of spanwise modes at this 2 : 1 wavelength ratio may be entirely particular to the considered LSB, and therefore may not apply universally.

Through the hot-wire measurements, small amplitude disturbances of a frequency matching that of the LSB's primary Kelvin-Helmholtz instability were identified, which underwent convective amplification downstream of the mean separation point. When forced at this fundamental frequency

in a two-dimensional manner, disturbance growth was found to be largely two-dimensional. When spanwise modulated forcing was applied, significant changes in the topology and development of the disturbances were noted, as a distinct spanwise modulation matching the forcing wavelength was noted in the disturbance profile. Furthermore, for the same streamwise station, disturbance amplitudes for this case were found to be significantly higher than those of the two-dimensional forcing case, indicating a preferential amplification of spanwise modes in the upstream boundary layer.

Tracking disturbance development further downstream revealed that disturbance amplitudes between the two forcing cases reached comparable levels in the region just upstream of the mean maximum bubble height location, despite the higher amplitudes of the spanwise forced disturbances near separation. This indicated a change in the stability characteristics from the upstream boundary layer, leading to higher amplification rates in the two-dimensionally forced flow. This was supported through linear stability analysis, which showed that, as a result the forcing induced mean flow deformation [140], amplification rates in the fore portion of the LSB reduced compared to the natural flow, with the most significant reductions found for the spanwise modulated forcing cases.

The LST analysis also provided a means for quantifying the amplification rates of disturbance modes of varied spanwise wavelength, finding that, regardless of the forcing scenario, the normal mode was subject to the highest growth rates throughout the length of the LSB, while disturbance modes of an oblique wave angle of less than 30° were subject to reduced, yet comparable growth rates. The ratio of the spanwise to streamwise wavelength of the employed forcing was 2, corresponding to a wave angle of 26.5°, thus confirming the unstable nature of the LSB toward the employed forcing. Furthermore, these LST findings support the increased effectiveness of this forcing configuration in comparison to the other two investigated in Chapter 5, as their corresponding wave angles were 33.7° and 45°. The unstable nature of the spanwise modes was experimentally verified through a spatial Fourier analysis of the hot-wire and tomographic PIV data, both of which confirmed their presence and streamwise amplification.

The effect of the growth of the unstable spanwise modes on the development of the shear layer vortices and the ensuing vortex dynamics was assessed. The small amplitude disturbances tracked through the fore portion of the LSB were found to manifest in the shear layer vortices, imparting a spanwise wavelength, if present, in the vortex filaments. Thus, in the case of the two-dimensional forcing, the shear layer vortices remained largely two-dimensional until their breakdown to turbulence, while for the $\widetilde{\lambda}_z = 25$ significant undulations at a spanwise wavelength matching that of the forcing developed in the filaments. The streamwise forward sections of the filaments were displaced further from the wall, with the same vortex topology reported in Chapter 5. There it was argued that spanwise undulatory vortex filaments self-induce a net rotational motion, causing its streamwise forward sections to lift away from the surface, thus leading to a continual intensification of vortex stretching in a shear flow. The consistent observation of these vortex motions in this chapter, and the two previous, indicates that these dynamics are intrinsic to the breakup process of shear layer vortices in laminar separation bubbles.

Chapter 7

Conclusions and Recommendations

The main findings of this work are summarized and recommendations for future work are given.

7.1 Conclusions

In this thesis, laminar separation bubbles were studied via experimental means in the pursuit of several objectives, which were laid out in Section 1.1 and are repeated here:

- Establish if vortex merging in LSBs can be influenced through subharmonic forcing. If so, assess the effects on the mean flow topology.
- Characterize the three-dimensional evolution of shear layer vortices in a laminar separation bubble. Elucidate the role, if any, played by the development of spanwise undulations.
- Develop a forcing technique capable of producing disturbances of a desired spanwise wavelength that holds all other parameters constant (amplitude, frequency, *etc.*).
- Establish if disturbance growth in an LSB is spanwise wavelength dependent. Evaluate the presence of any instability mechanism that may lead to preferential modal growth.
- Link spanwise disturbance growth to changes in the ensuing vortex dynamics, and hence changes in the mean flow topology.

The main findings, as they relate to these objectives, are summarized as follows.

7.1.1 Natural Flow Development and Vortex Merging

The first two objectives were addressed in Chapter 4, where an LSB formed over a NACA 0018 airfoil at a chord Reynolds number of 125 000, an angle of attack of 4°, and a free-stream turbulence intensity of 0.07% was studied. The experimental findings came from PIV measurements collected in a variety of configurations, allowing for two-dimensional, time-resolved evaluations of the flow, in addition to conditional volumetric reconstructions of the flow field using phase-locked, scanning PIV measurements. In addition to leaving the flow to develop naturally, acoustic forcing was applied at the LSB's fundamental and subharmonic frequencies, with a relatively low excitation level selected to avoid substantial mean flow modifications.

The time-averaged topology of the LSB was found to be strongly two-dimensional across the airfoil span, while the flow development was characterized by the periodic roll-up of the separated shear layer, forming vortices upstream of the mean maximum height location. The vortices were strongly two-dimensional at formation, but quickly developed spanwise deformations with downstream convection, leading to their breakdown to smaller scales near the mean reattachment location. The deformations took the form of spanwise undulations in the vortex filaments, that developed over a relatively fixed range of values, $1.5 \lesssim \lambda_z/\lambda_z \lesssim 7$. These undulations continually intensified with downstream convection as a result of the streamwise forward sections of the vortex filament lifting away from the surface. This motion re-oriented the structure's spanwise vorticity into the streamwise and wall-normal directions, forming hairpin-like structures that were tilted forward and extended above the vortex core region.

With respect to vortex merging, the phenomenon was found to occur naturally in the LSB, while forcing at the subharmonic and fundamental frequencies promoted and inhibited merging respectively. Through a vortex merging detection scheme, it was found that 18% of primary structures at the midspan plane merged in the natural LSB. This value increased to 64% in the presence of subharmonic forcing, and decreased to 8% when forcing was applied at the fundamental frequency. Despite subharmonic forcing having a significant effect on the prevalence of vortex merging, the mean topology of the LSB remained relatively unchanged compared to the natural flow. As it is generally accepted that reattachment is facilitated by the shear layer vortices, this implied that the increase in strength of individual structures as a result of merging was balanced by the reduction in their frequency, resulting in largely unchanged mean LSB topology. Furthermore, the vortex merging process was found to occur in a spanwise non-uniform manner, as localized merging events occurred away from sections where forward and rearward bulges developed in the vortex filaments.

7.1.2 Three-Dimensional Forcing Technique

The third objective was addressed in Chapter 5, where a novel forcing technique capable of producing deterministic, three-dimensional disturbances modulated to a desired spanwise wavelength was developed and characterized. Alternating current, dielectric barrier discharge plasma actuators were used, with two dimensional forcing achieved through operating of a single spanwise uniform actuator. For three-dimensional disturbance production, two actuators were arranged in streamwise succession and operated simultaneously. The upstream actuator produced a spanwise uniform disturbance, which was then spanwise modulated by the output of the downstream actuator, with a relative phase delay used to superimpose the two outputs.

A detailed characterization of the actuators was carried out in quiescent and in-flow conditions to determine the spanwise and streamwise disturbance topology, net momentum injection, and phase delay needed for disturbance superposition. The quiescent characterization involved flow visualizations and planar PIV measurements, and showed that all actuators provide a spanwise uniform injection of streamwise momentum through the production of relatively weak, wall-parallel streamwise jets in the regions where the actuator's high voltage and ground electrodes overlap. Thus, two-dimensional output was achieved from an actuator with spanwise continuous electrode overlap, while three-dimensional disturbances at a desired spanwise wavelength were achieved by introducing gaps in the electrode overlap, as no streamwise velocity was generated in the gap regions.

The generated thrust and associated momentum coefficients were estimated for all actuators using a control volume analysis applied to PIV measurements. The results highlighted higher sectional thrust generated by the two-dimensional actuator due to end effects that decrease momentum output at the edges of the overlap regions. This, coupled with different total lengths of the thrust producing regions, lead to different total thrust production for all actuators considered. The assumed superposition of momentum output for actuators arranged in streamwise succession was shown to be valid. This, alongside the linear trend between thrust output and forcing duty cycle, allowed for the identification of operating duty cycles that gave equal amounts of total momentum output for a given actuator configuration, while holding all other forcing parameters constant.

The in-flow characterization was used to determine the phase delay needed for disturbance superposition, which was found to be invariant to spanwise wavelength. With the correct phase delay, disturbances were successfully superimposed within the LSB, as the streamwise wavelength of the superimposed disturbances matched that of the two-dimensional disturbances. Thus, across the developed forcing configurations, the spanwise wavelength of the produced disturbances was varied, while the total momentum input, and disturbance frequency and streamwise wavelength were held constant.

7.1.3 Growth of Spanwise Disturbances

The final two objectives were addressed in Chapters 5 and 6, where flow development in an LSB was studied and the effects of targeting disturbance modes using the forcing technique developed in Chapter 5 were examined. The LSB was formed over a flat plate with an imposed adverse pressure gradient at a nominal Reynolds number of $Re_{\delta_{1_s}} = 750$. Measurements were spread across two experimental campaigns, and were performed through hot-wire anemometry, and planar and tomographic particle image velocimetry. Results from three cases were examined in detail: (i) the natural (unforced) flow, (ii) two-dimensional forcing, and (iii) three-dimensional forcing with a spanwise-to-streamwise wavelength length ratio of 2 : 1, while a subset of results were considered for smaller wavelength ratios (1.5 : 1 and 1 : 1).

In assessing the time-averaged characteristics of the flow field, flow in the fore portion of the LSB was found to be essentially spanwise uniform, with mean velocities in the spanwise direction being less than 2% of the free-stream velocity. Downstream, in the region where the shear layer vortices formed, the spanwise uniformity of the forcing cases and the natural flow were in stark contrast, as the former was spanwise uniform, while the latter featured a peak and valley arrangement in the mean streamwise velocity field and subsequently the spanwise trend in the mean maximum bubble height location. These features were directly linked to the shear layer vortices, as in the presence of forcing the vortices were two-dimensional at formation and featured strong spanwise coherence. In contrast, in the natural flow, the vortices shed in localized regions across the span, with strong distortions in the filaments between these shedding ‘cells’. Confirmation relating this phenomenon to a low frequency modulation of the natural LSB was provided through the consideration of three factors. These included differences reported in the flow field statistics based on sampling time, an assessment of the changes in stability incurred by the forcing, and temporal characteristics of the natural flow elucidated through proper orthogonal decomposition analysis. Nevertheless, the spanwise wavelength of the modulated natural flow matched that of the 2 : 1 three-dimensional forcing case, indicating that this low frequency modulation may be the underlying source for preferential amplification of disturbances of this spanwise wavelength. Therefore, the growth of spanwise modes at this 2 : 1 wavelength ratio may be particular to the considered LSB.

By tracking disturbance development throughout the length of the LSB, small amplitude disturbances of a frequency matching the primary Kelvin-Helmholtz instability were identified, which underwent convective amplification downstream of the mean separation point. When forced at this fundamental frequency in a two-dimensional manner, disturbance growth was two-dimensional. When the 2 : 1 spanwise modulated forcing was applied, a distinct spanwise

modulation matching the forcing wavelength was noted in the disturbance profile. Furthermore, for the same streamwise station, disturbance amplitudes for this case were found to be significantly higher than those of the two-dimensional forcing, indicating a preferential amplification of spanwise modes in the upstream boundary layer. Further downstream, disturbance amplitudes between these two cases reached comparable levels in the region just upstream of the mean maximum bubble height location. This indicated a change in the stability characteristics from the upstream boundary layer, leading to higher amplification rates in the two-dimensional forced flow. Linear stability analysis supported this, showing that, as a result of the induced mean flow deformation, amplification rates in the fore portion of the LSB reduced compared to the natural flow, with the most significant reductions occurring for the spanwise modulated forcing case.

The amplification rates of disturbances of varied spanwise wavelength were also quantified through LST analysis, finding that, regardless of the forcing scenario, the normal (two-dimensional) mode was subject to the highest growth rates throughout the length of the LSB. Disturbance modes of an oblique wave angle of less than 30°, while unstable, were subject to comparable, yet reduced, growth rates. Thus, disturbance growth in the LSB is confirmed to be spanwise wavelength dependent, with the employed $2:1$ spanwise-to-streamwise wavelength ratio corresponding to a wave angle of 26.5°. Furthermore, this confirmed why this particular forcing configurations produced more substantial changes in the flow development than the other two investigated in Chapter 5 ($1.5:1$ and $1:1$), as their corresponding wave angles are 33.7° and 45°, respectively. The unstable nature of the spanwise modes predicted through LST was experimentally verified through a spatial Fourier analysis of the hot-wire and tomographic data, both of which confirmed their presence and streamwise amplification.

The effect of unstable spanwise modal growth on the development of the shear vortices and the ensuing vortex dynamics was assessed. The small amplitude perturbations tracked through the fore portion of the LSB manifested in the shear layer vortices, imparting a spanwise wavelength, if present, in the vortex filaments. Thus, in the case of two-dimensional forcing, the shear layer vortices remained largely two-dimensional until their breakdown, while for the three-dimensional forcing case, significant spanwise undulations developed at the $2:1$ ratio prescribed by the forcing. The vortex filaments surged forward in the streamwise direction downstream of the three-dimensional actuator's active region, while lagging behind at spanwise locations downstream of the actuator gaps. These filament motions, coupled with the strong mean shear, led to a continual intensification of vortex stretching, leading to rapid filament deformations. These observations were supported through a simple model that considered the development of a vortex filament subject to Biot-Savart induction and mean flow convection. The results of the model confirmed that as a result of the filament's spanwise undulatory shape, a net rotational motion is imparted on the filament through Biot-Savart self-induction, causing the streamwise forward and rearward sections of the filament to tilt away and toward the surface, respectively. This, coupled with the wall-normal velocity gradient, causes the filament to stretch in the streamwise direction. These vortex motions were consistently observed throughout all the studied LSBs (Chapters 4–6), and apply more broadly to all LSBs, since regardless of how spanwise undulations are initially produced in a vortex filament, if present, the filament will tend to develop in the way shown in any near-wall shear flow. Thus, these dynamics are found to be intrinsic to the breakup process of shear layer vortices in laminar separation bubbles.

7.2 Recommendations

The mean spanwise non-uniformity observed in the natural LSB studied in Chapters 5 and 6 (Fig. 6.5a) should be investigated in detail. All of the available evidence in this study points toward a low frequency modulation of the flow, the exact source of which is unknown. In other experiments, high levels of free-stream turbulence have led to highly irregular and spanwise non-uniform vortex shedding in LSBs, however, this is not consistent with the suspected low frequency nature of the observed phenomenon and the turbulence intensity of the TU Delft A-Tunnel, which is verified at less than 0.09%. Therefore, other possible sources should be investigated, including low frequency activities stemming from operation of the tunnel (aeroacoustic or mechanical vibrations), imperfections in the flat plate model and displacement body (potentially matching a spatial wavelength of approx. 50 mm), and acoustic signatures developed in the test section (*e.g.*, standing waves established in the spanwise and/or wall-normal directions).

The results in Chapter 6 revealed a preferential amplification of spanwise modes in the boundary layer upstream of the LSB. This should be investigated. Measurements of this nature were attempted as part of this work, however, they were ultimately unsuccessful due to the extremely low disturbance amplitudes, even when the flow was forced and measurements were performed using hot-wire anemometry. While more sensitive measurements can be attempted, an order of magnitude increase in sensitivity is likely required, which is beyond the capabilities of most measurement techniques. Higher forcing amplitudes could be used to render the disturbances measurable, however this will likely incur significant mean flow deformations, thus changing the very flow being studied. Therefore, it is the author's opinion that a combined numerical/experimental approach would be the most effective, with disturbance development studied in a simulation subject to initial/boundary conditions based on experimental measurements.

The developed forcing technique should be applied to study the growth of spanwise modes in other LSBs. In particular, the preferred amplification of disturbance with a spanwise-to-streamwise wavelength ratio of 2 : 1 may stem from the low frequency modulation of the base flow studied in Chapters 5 and 6. Thus, these unstable disturbance characteristics may be unique to only the studied LSB. Indeed, other investigators have reported a range of predominant spanwise wavelengths in LSBs, $1 \lesssim \lambda_z/\lambda_x \lesssim 7$. Thus, other LSB configuration (airfoil and flat plate) should be studied to establish if there is any commonality among the most unstable spanwise wavelengths. Furthermore, the effects of larger spanwise wavelengths should be examined, as the stability analysis done as part of this work predicts increasing amplification rates with increasing spanwise wavelength. Spanwise wavelengths in the range of $2.5 \leq \lambda_z/\lambda_x \leq 7$ would be good candidates. Another aspect that should be investigated is the amplitude ratio of the normal and spanwise modes for a given spanwise modulated forcing case. This parameter was not varied in the current work, with the ratio between the two kept constant in order to maintain equal total momentum with the two-dimensional forcing case. Varying this parameter may give additional insight into the effects of spanwise modal growth on vortex development and the mean topology of LSBs.

Throughout this thesis, conclusions regarding any potentially active secondary instabilities in the LSB were avoided on the basis that the employed analysis techniques were not well suited for their identification. In particular, these types of instabilities are usually identified through techniques such as secondary/global/Floquet stability analysis, with are better suited for numerical

investigations. Applications of these techniques to experimental data should be pursued. In particular, PIV measurements may be suitable in providing the required base flow.

While the airfoil (Chapter 4) and flat plate (Chapters 5 and 6) LSBs studied in this thesis exhibit many similarities, their differences were not cross-examined. As many investigations (including this one) rely on the flat plate LSB as a suitable analog for those found in practice, *i.e.*, those formed over airfoils, a detailed study cross-examining these two configurations should be conducted. This work established the significant influence of the incoming disturbances, and therefore certain aspects unique to an airfoil LSB, such as fluctuations of the leading edge separation point due shedding in the wake and surface curvature, are expected to have considerable influence.

The forcing technique developed as part of this thesis presents itself as a useful diagnostic tool for the study of laminar–turbulent transition, as it can be easily adapted and used in the study of other canonical flows. Good candidates could be boundary layers (without separation) and free shear layers, as both have noted dependencies on three-dimensional disturbance development. Furthermore, due to the flexibility afforded by plasma actuators, further novel forcing configurations can be developed to target specific modes and/or instabilities. For example, a pure oblique wave could be generated by arranging individual actuator elements across the span, which are then operated with an increasing phase delay. This work established that superposition of plasma actuator outputs is possible, and therefore two oblique waves of opposite angles could be generated and superimposed with a two-dimensional mode, thus producing a experimental version of the triadic resonance mechanism reported in attached boundary layers.

Finally, with regards to advancing the state-of-the-art in the study of LSBs, it is the author's opinion that configurations that are more representative of real-world application must be pursued. The majority of studies to-date (including this one) have relied on two-dimensional laboratory configurations, namely the airfoil and flat plate configurations. Across the current body of work, many aspects of LSBs are considered well established for these two-dimensional configurations, including the time-averaged topology, basics of the transition process, and the characteristics of the formed coherent structures. Furthermore, in relation to these aspects, the effects of applying flow control and/or varying certain basic parameters, such as the Reynolds number and angle of attack, and are also relatively well established. Thus, extensive reference material is available for relatively 'simple' flow configurations, from which investigations examining more complex configurations can branch off. Based on relevant applications, some research avenues to consider include LSBs formed on real wings (finite wings, wings with sweep, at junctions, surfaces with imperfections), LSBs in dynamic systems (turbine blades in motions, flapping wings, pitching and/or heaving airfoils), and the effects of free-stream turbulence on LSBs.

References

[1] Adrian, R. J. & Westerweel, J. 2011 *Particle Image Velocimetry*. Cambridge University Press. ISBN. ↩

[2] Alam, M. & Sandham, N. D. 2000 Direct numerical simulation of 'short' laminar separation bubbles with turbulent reattachment. *J. Fluid Mech.* **403**, 223–250. DOI. ↩

[3] Amiet, R. K. 1976 Noise due to turbulent flow past a trailing edge. *J. Sound Vib.* **47** (3), 387–393. DOI. ↩

[4] Amitay, M. & Glezer, A. 2002 Role of Actuation Frequency in Controlled Flow Reattachment over a Stalled Airfoil. *AIAA J.* **40** (2), 209–216. DOI. ↩

[5] Amitay, M., Smith, D. R., Kibens, V., Parekh, D., & Glezer, A. 2001 Aerodynamic Flow Control over an Unconventional Airfoil Using Synthetic Jet Actuators. *AIAA J.* **39** (3), 361–370. DOI. ↩

[6] Andersson, P., Berggren, M., & Henningson, D. S. 1999 Optimal disturbances and bypass transition in boundary layers. *Phys. Fluids* **11** (1), 134–150. DOI. ↩

[7] Arbey, H. & Bataille, J. 1983 Noise generated by airfoil profiles placed in a uniform laminar flow. *J. Fluid Mech.* **134**, 33–47. DOI. ↩

[8] Arcondoulis, E. J. G., Doolan, C. J., Zander, A. C., & Brooks, L. A. 2010 A review of trailing edge noise generated by airfoils at low to moderate Reynolds number. *Acoust. Aust.* **38** (3), 129–133. URL. ↩

[9] Arnal, D., Julien, J. C., & Michel, R. 1977 Analyse experimentale et calcul de l'apparition et du developpement de la transition de la couche limit. In *AGARD Conf. Proc. 224*, 13–1 to 13–7. ↩

[10] Ashpis, D. E. & Reshotko, E. 1990 The vibrating ribbon problem revisited. *J. Fluid Mech.* **213**, 531–547. DOI. ↩

[11] Atassi, H. 1984 Feedback in separated flows over symmetric airfoils. In *9th AIAA Aeroacoustics Conf.* Williamsburg, VA, Oct 15–17. DOI. ↩

[12] Atkinson, C. & Soria, J. 2009 An efficient simultaneous reconstruction technique for tomographic particle image velocimetry. *Exp. Fluids* **47**, 553–568. DOI. ↩

[13] Balzer, W. & Fasel, H. F. 2016 Numerical investigation of the role of free-stream turbulence in boundary-layer separation. *J. Fluid Mech.* **801**, 289–321. DOI. ↩

[14] Berkooz, G., Holmes, P., & Lumley, J. L. 1993 The Proper Orthogonal Decomposition in the Analysis of Turbulent Flows. *Annu. Rev. Fluid Mech.* **25**, 539–575. DOI. ↩

[15] Bernal, L. P. & Roshko, A. 1986 Streamwise vortex structure in plane mixing layers. *J. Fluid Mech.* **170**, 499–525. DOI. ↩

[16] Bernardini, C., Benton, S. I., Chen, J.-P., & Bons, J. P. 2014 Pulsed Jets Laminar Separation Control Using Instability Exploitation. *AIAA J.* **52** (1), 104–115. DOI. ↩

[17] Bertolotti, F. P., Herbert, T., & Spalart, P. R. 1992 Linear and nonlinear stability of the Blasius boundary layer. *J. Fluid Mech.* **242**, 441–474. DOI. ↩

[18] Blasius, H. 1908 Grenzschichten in Flüssigkeiten mit kleiner Reibung. *Zeitschrift für Math. und Phys.* **56**, 1–37. URL. ↩

[19] Boiko, A. V., Grek, G. R., Dovgal, A. V., & Kozlov, V. V. 2002 *The Origin of Turbulence in Near-Wall Flows*. Springer. ISBN. ↩

[20] Boutilier, M. S. H. & Yarusevych, S. 2012 Separated shear layer transition over an airfoil at a low Reynolds number. *Phys. Fluids* **24** (8), 084105. DOI. ↩

[21] Boutilier, M. S. H. & Yarusevych, S. 2012 Effects of End Plates and Blockage on Low-Reynolds-Number Flows Over Airfoils. *AIAA J.* **50** (7), 1547–1559. DOI. ↩

[22] Boutilier, M. S. H. & Yarusevych, S. 2012 Parametric study of separation and transition characteristics over an airfoil at low Reynolds numbers. *Exp. Fluids* **52** (6), 1491–1506. DOI. ↩

[23] Boutilier, M. S. H. & Yarusevych, S. 2013 Sensitivity of linear stability analysis of measured separated shear layers. *Eur. J. Mech. - B/Fluids* **37**, 129–142. DOI. ↩

[24] Brendel, M. & Mueller, T. J. 1988 Boundary-layer measurements on an airfoil at low Reynolds numbers. *J. Aircr.* **25** (7), 612–617. DOI. ↩

[25] Bridges, T. J. & Morris, P. J. 1984 Differential eigenvalue problems in which the parameter appears nonlinearly. *J. Comput. Phys.* **55** (3), 437–460. DOI. ↩

[26] Brinkerhoff, J. R. & Yaras, M. I. 2011 Interaction of viscous and inviscid instability modes in separation bubble transition. *Phys. Fluids* **23** (12), 124102. DOI. ↩

[27] Broeren, A. P. & Bragg, M. B. 2001 Spanwise Variation in the Unsteady Stalling Flowfields of Two-Dimensional Airfoil Models. *AIAA J.* **39** (9), 1641–1651. DOI. ↩

[28] Brooks, T. F. & Hodgson, T. H. 1981 Trailing edge noise prediction from measured surface pressures. *J. Sound Vib.* **78** (1), 69–117. DOI. ↩

[29] Brooks, T. F., Pope, D. S., & Marcolini, M. A. 1989 Airfoil Self-Noise and Prediction. *Tech. rep.*, NASA Ref. Pub. 1218. URL. ↩

[30] Bruun, H. H. 1995 *Hot-Wire Anemometry: Principles and Signal Analysis*. Oxford University Press. ISBN. ↩

[31] Burgmann, S., Brücker, C., & Schröder, W. 2006 Scanning PIV measurements of a laminar separation bubble. *Exp. Fluids* **41** (2), 319–326. DOI. ↩

[32] Burgmann, S., Dannemann, J., & Schröder, W. 2008 Time-resolved and volumetric PIV measurements of a transitional separation bubble on an SD7003 airfoil. *Exp. Fluids* **44** (4), 609–622. DOI. ↩

[33] Burgmann, S. & Schröder, W. 2008 Investigation of the vortex induced unsteadiness of a separation bubble via time-resolved and scanning PIV measurements. *Exp. Fluids* **45** (4), 675–691. DOI. ↩

[34] Carmichael, B. H. 1981 Low Reynolds Number Airfoil Survey. *Tech. rep.*, NASA Contract Report No. 165803. URL. ↩

[35] Cerretelli, C. & Williamson, C. 2003 The physical mechanism for vortex merging. *J. Fluid Mech.* **475**, 41–77. DOI. ↩

[36] Chang, R. C., Hsiao, F.-B., & Shyu, R.-N. 1992 Forcing level effects of internal acoustic excitation on the improvement of airfoil performance. *J. Aircr.* **29** (5), 823–829. DOI. ↩

[37] Chue, S. 1975 Pressure probes for fluid measurement. *Prog. Aerosp. Sci.* **16** (2), 147–223. DOI. ↩

[38] Clercx, H. J. H., Maassen, S. R., & van Heijst, G. J. F. 1999 Decaying two-dimensional turbulence in square containers with no-slip or stress-free boundaries. *Phys. Fluids* **11** (7), 1963–1963. DOI. ↩

[39] Collins, F. G. & Zelenevitz, J. 1975 Influence of Sound upon Separated Flow over Wings. *AIAA J.* **13** (3), 408–410. DOI. ↩

[40] Corke, T. C., Enloe, C. L., & Wilkinson, S. P. 2010 Dielectric Barrier Discharge Plasma Actuators for Flow Control. *Annu. Rev. Fluid Mech.* **42**, 505–529. DOI. ↩

[41] Craik, A. D. D. 1971 Non-linear resonant instability in boundary layers. *J. Fluid Mech.* **50** (02), 393–413. DOI. ↩

[42] Currie, I. G. 2012 *Fundamental Mechanics of Fluids*. 4th ed. Taylor and Francis. ISBN. ↩

[43] Daubechies, I. 1992 *Ten Lectures on Wavelets*. Society for Industrial and Applied Mathematics. DOI. ↩

[44] Desquesnes, G., Terracol, M., & Sagaut, P. 2007 Numerical investigation of the tone noise mechanism over laminar airfoils. *J. Fluid Mech.* **591**, 155–182. DOI. ↩

[45] Dini, P., Selig, M. S., & Maughmer, M. D. 1992 Simplified linear stability transition prediction method for separated boundary layers. *AIAA J.* **30** (8), 1953–1961. DOI. ↩

[46] Diwan, S. S. & Ramesh, O. N. 2009 On the origin of the inflectional instability of a laminar separation bubble. *J. Fluid Mech.* **629**, 263–298. DOI. ↩

[47] Dovgal, A. V., Kozlov, V. V., & Michalke, A. 1994 Laminar boundary layer separation: instability and associated phenomena. *Prog. Aerosp. Sci.* **30**, 61–94. ↩

[48] Drazin, P. G. & Reid, W. H. 1981 *Hydrodynamic Stability*. Batchelor, G. K. & Miles, J. W., editors. 2nd ed. Cambridge University Press. ISBN. ↩

[49] Durscher, R. & Roy, S. 2012 Evaluation of thrust measurement techniques for dielectric barrier discharge actuators. *Exp. Fluids* **53** (4), 1165–1176. DOI. ↩

[50] Durst, F. & Zanoun, E. 2002 Experimental investigation of near-wall effects on hot-wire measurements. *Exp. Fluids* **33**, 210–218. DOI. ↩

[51] Elsinga, G. E., Scarano, F., Wieneke, B., & van Oudheusden, B. W. 2006 Tomographic particle image velocimetry. *Exp. Fluids* **41** (6), 933–947. DOI. ↩

[52] Embacher, M. & Fasel, H. F. 2014 Direct numerical simulations of laminar separation bubbles: investigation of absolute instability and active flow control of transition to turbulence. *J. Fluid Mech.* **747**, 141–185. DOI. ↩

[53] Farge, M. 1992 Wavelet Transforms and their Applications to Turbulence. *Annu. Rev. Fluid Mech.* **24**, 395–458. arXiv: 1508.05650. DOI. ↩

[54] Feero, M. A., Goodfellow, S. D., Lavoie, P., & Sullivan, P. E. 2015 Flow Reattachment Using Synthetic Jet Actuation on a Low-Reynolds-Number Airfoil. *AIAA J.* **53** (7), 2005–2014. DOI. ↩

[55] Fitzgerald, E. J. & Mueller, T. J. 1990 Measurements in a separation bubble on an airfoil using laser velocimetry. *AIAA J.* **28** (4), 584–592. DOI. ↩

[56] Fridman, A. 2008 *Plasma Chemisty*. Cambridge University Press. ISBN. ↩

[57] Gad-el-Hak, M. 1989 Flow Control. *Appl. Mech. Rev.* **42** (10), 261–292. DOI. ↩

[58] Gaster, M. 1967 The Structure and Behaviour of Laminar Separation Bubbles. *Aeronaut. Res. Counc.* **RM 3595**. URL. ↩

[59] Gaster, M. 1968 Growth of Disturbances in Both Space and Time. *Phys. Fluids* **11** (4), 723–727. DOI. ↩

[60] Gerakopulos, R. & Yarusevych, S. 2012 Novel Time-Resolved Pressure Measurements on an Airfoil at a Low Reynolds Number. *AIAA J.* **50** (5), 1189–1200. DOI. ↩

[61] Gerakopulos, R. J. 2011 *Investigating Flow over an Airfoil at Low Reynolds Numbers Using Novel Time-Resolved Surface Pressure Measurements*. MASc. Thesis, University of Waterloo. URL. ↩

[62] Giguere, P. & Selig, M. S. 1997 Low Reynolds Number Airfoils for Small Horizontal Axis Wind Turbines. *Wind Eng.* **21** (6), 367–380. URL. ↩

[63] Glezer, A. 2011 Some aspects of aerodynamic flow control using synthetic-jet actuation. *Philos. Trans. R. Soc. A Math. Phys. Eng. Sci.* **369**, 1476–1494. DOI. ↩

[64] Glezer, A. & Amitay, M. 2002 Synthetic Jets. *Annu. Rev. Fluid Mech.* **34** (1), 503–529. DOI. ↩

[65] Grant, S. I. & Phillips, W. R. 2008 *Electromagnetism*. 2nd ed. Wiley. ↩

[66] Green, J. E. 1966 Two-dimensional turbulent reattachment as a boundary-layer problem. *Tech. rep.* ↩

[67] Greenblatt, D. & Wygnanski, I. J. 2000 The control of flow separation by periodic excitation. *Prog. Aerosp. Sci.* **36** (7), 487–545. DOI. ↩

[68] Häggmark, C. P., Hildings, C., & Henningson, D. S. 2001 A numerical and experimental study of a transitional separation bubble. *Aerosp. Sci. Technol.* **5** (5), 317–328. DOI. ↩

[69] Hain, R., Kähler, C. J., & Radespiel, R. 2009 Dynamics of laminar separation bubbles at low-Reynolds-number aerofoils. *J. Fluid Mech.* **630**, 129–153. DOI. ↩

[70] Helmholtz, H. 1867 LXIII. On Integrals of the Hydrodynamical Equations, which express Vortex-motion. *Philos. Mag. Ser. 4* **33** (226), 485–512. DOI. ↩

[71] Herbert, T. 1988 Secondary Instability Of Boundary Layers. *Annu. Rev. Fluid Mech.* **20**, 487–526. DOI. ↩

[72] Ho, C.-M. & Huang, L.-S. 1982 Subharmonics and vortex merging in mixing layers. *J. Fluid Mech.* **119**, 443–473. DOI. ↩

[73] Ho, C.-M. & Huerre, P. 1984 Perturbed Free Shear Layers. *Annu. Rev. Fluid Mech.* **16** (1), 365–424. DOI. ↩

[74] Hodson, H. P. & Howell, R. J. 2005 Bladerow Interactions, Transition, and High-Lift Aerofoils in Low-Pressure Turbines. *Annu. Rev. Fluid Mech.* **37**, 71–98. DOI. ↩

[75] Hodson, H. P. & Howell, R. J. 2005 The role of transition in high-lift low-pressure turbines for aeroengines. *Prog. Aerosp. Sci.* **41** (6), 419–454. DOI. ↩

[76] Horton, H. P. 1968 *Laminar separation bubbles in two and three dimensional incompressible flow*. PhD thesis, Queen Mary College, University of London. URL. ↩

[77] Hosseinverdi, S. & Fasel, H. F. 2019 Numerical investigation of laminar–turbulent transition in laminar separation bubbles: the effect of free-stream turbulence. *J. Fluid Mech.* **858**, 714–759. DOI. ↩

[78] Howe, M. S. 1998 *Acoustics of Fluid–Structure Interactions*. Batchelor, G. K., Freund, L. B., Leibovich, S., & Tvergaard, V., editors. Cambridge University Press. DOI. ↩

[79] Hsiao, F.-B., Jih, J.-J., & Shyu, R.-N. 1997 The effect of acoustics on flow passing a high-AOA airfoil. *J. Sound Vib.* **199** (2), 177–188. DOI. ↩

[80] Huang, L. S., Maestrello, L., & Bryant, T. D. 1987 Separation control over an airfoil at high angles of attack by sound emanating from the surface. In *19th AIAA Fluid Dyn. Plasma Dyn. Lasers Conf.* Honolulu, HI, USA. DOI. ↩

[81] Huerre, P. 2000 Open Shear Flow Instabilities. In Batchelor, G. K., Moffatt, H. K., & Worster, M. G., editors, *Perspect. Fluid Dyn. A Collect. Introd. to Curr. Res.* Pp. 159–229. Cambridge University Press. ISBN. ↩

[82] Huerre, P. & Monkewitz, P. A. 1990 Local and Global Instabilities in Spatially Developing Flows. *Annu. Rev. Fluid Mech.* **22** (1), 473–537. DOI. ↩

[83] Huerre, P. & Rossi, M. 1998 Hydrodynamic instabilities in open flows. In Godreche, C. & Manneville, P., editors, *Hydrodyn. Nonlinear Instab.* Cambridge University Press. ↩

[84] Hunt, J. C. R., Wray, A. A., & Moin, P. 1988 Eddies, streams, and convergence zones in turbulent flows. *Cent. Turbul. Res. Rep. CTR-S88* 193–208. ↩

[85] Istvan, M. S., Kurelek, J. W., & Yarusevych, S. 2018 Turbulence Intensity Effects on Laminar Separation Bubbles Formed over an Airfoil. *AIAA J.* **56** (4), 1335–1347. DOI. ↩

[86] Istvan, M. S. & Yarusevych, S. 2018 Effects of free-stream turbulence intensity on transition in a laminar separation bubble formed over an airfoil. *Exp. Fluids* **59** (3), 52. DOI. ↩

[87] Jayaraman, B., Thakur, S., & Shyy, W. 2007 Modeling of Fluid Dynamics and Heat Transfer Induced by Dielectric Barrier Plasma Actuator. *J. Heat Transfer* **129** (4), 517. DOI. ↩

[88] Jeong, J. & Hussain, F. 1995 On the identification of a vortex. *J. Fluid Mech.* **285**, 69–94. DOI. ↩

[89] Jimenez, J. 1983 A spanwise structure in the plane shear layer. *J. Fluid Mech.* **132**, 319–336. DOI. ↩

[90] Jiménez, J., Moffatt, H. K., & Vasco, C. 1996 The structure of the vortices in freely decaying two-dimensional turbulence. *J. Fluid Mech.* **313**, 209–222. DOI. ↩

[91] Jones, L. E., Sandberg, R. D., & Sandham, N. D. 2010 Stability and Receptivity Characteristics of a Laminar Separation Bubble on an Aerofoil. *J. Fluid Mech.* **648**, 257–296. DOI. ↩

[92] Jones, L. E., Sandberg, R., & Sandham, N. D. 2008 Direct numerical simulations of forced and unforced separation bubbles on an airfoil at incidence. *J. Fluid Mech.* **602**, 175–207. DOI. ↩

[93] Jones, L. E. & Sandberg, R. D. 2011 Numerical analysis of tonal airfoil self-noise and acoustic feedback-loops. *J. Sound Vib.* **330** (25), 6137–6152. DOI. ↩

[94] Joslin, R. D., Streett, C. L., & Chang, C.-L. 1993 Spatial direct numerical simulation of boundary-layer transition mechanisms: Validation of PSE theory. *Theor. Comput. Fluid Dyn.* **4** (6), 271–288. DOI. ↩

[95] Kachanov, Y. S., Kozlov, V. V., & Levchenko, V. Y. 1982 Origin of turbulence in boundary layers. In number see Boiko et al. 2002. Nauka. ↩

[96] Kachanov, Y. S. Y. 1994 Physical Mechanisms of Laminar-Boundary-Layer Transition. *Annu. Rev. Fluid Mech.* **26** (1), 411–482. DOI. ↩

[97] Kachanov, Y. S. & Levchenko, V. Y. 1984 The resonant interaction of disturbances at laminar-turbulent transition in a boundary layer. *J. Fluid Mech.* **138**, 209–247. DOI. ↩

[98] Kähler, C., Sammler, B., & Kompenhans, J. 2002 Generation and control of tracer particles for optical flow investigations in air. *Exp. Fluids* **33**, 736–742. DOI. ↩

[99] Karamcheti, K. 1980 *Principles of Ideal-Fluid Aerodynamics*. 2nd ed. Krieger. ↩

[100] Kawall, J. G., Shokr, M., & Keffer, J. F. 1983 A digital technique for the simultaneous measurement of streamwise and lateral velocities in turbulent flows. *J. Fluid Mech.* **133**, 83–112. DOI. ↩

[101] Keane, R. D. & Adrian, R. J. 1992 Theory of cross-correlation analysis of PIV images. *Appl. Sci. Res.* **49** (3), 191–215. DOI. ↩

[102] Kelly, R. E. 1967 On the stability of an inviscid shear layer which is periodic in space and time. *J. Fluid Mech.* **27** (04), 657–689. DOI. ↩

[103] Kelvin, L. 1869 On Vortex Motion. *Proc. R. Soc. Edinburgh* ↩

[104] Kerswell, R. R. 2002 Elliptical Instability. *Annu. Rev. Fluid Mech.* **34** (1), 83–113. DOI. ↩

[105] Kibens, V. 1980 Discrete Noise Spectrum Generated by Acoustically Excited Jet. *AIAA J.* **18** (4), 434–441. DOI. ↩

[106] Kirk, T. M. & Yarusevych, S. 2017 Vortex shedding within laminar separation bubbles forming over an airfoil. *Exp. Fluids* **58** (5), 43. DOI. ↩

[107] Klebanoff, P. S., Tidstrom, K. D., & Sargent, L. M. 1962 The three-dimensional nature of boundary-layer instability. *J. Fluid Mech.* **12** (01), 1–34. DOI. ↩

[108] Kotsonis, M. & Ghaemi, S. 2011 Forcing mechanisms of dielectric barrier discharge plasma actuators at carrier frequency of 625 Hz. *J. Appl. Phys.* **110** (11), 113301. DOI. ↩

[109] Kotsonis, M., Ghaemi, S., Veldhuis, L., & Scarano, F. 2011 Measurement of the body force field of plasma actuators. *J. Phys. D. Appl. Phys.* **44** (4), 045204. DOI. ↩

[110] Kotsonis, M. 2015 Diagnostics for characterisation of plasma actuators. *Meas. Sci. Technol.* **26** (9), 092001. DOI. ↩

[111] Kurelek, J. W. 2016 *Transition in a Laminar Separation Bubble and the Effect of Acoustic Excitation*. MASc. Thesis, University of Waterloo. ↩

[112] Kurelek, J. W., Kotsonis, M., & Yarusevych, S. 2018 Transition in a separation bubble under tonal and broadband acoustic excitation. *J. Fluid Mech.* **853**, 1–36. DOI. ↩

[113] Kurelek, J. W., Lambert, A. R., & Yarusevych, S. 2016 Coherent Structures in the Transition Process of a Laminar Separation Bubble. *AIAA J.* **54** (8), 2295–2309. DOI. ↩

[114] Laitone, E. V. 1997 Wind tunnel tests of wings at Reynolds numbers below 70 000. *Exp. Fluids* **23** (5), 405–409. DOI. ↩

[115] Lambert, A. R. & Yarusevych, S. 2017 Characterization of Vortex Dynamics in a Laminar Separation Bubble. *AIAA J.* **55** (8), 2664–2675. DOI. ↩

[116] Lambert, A. R. & Yarusevych, S. 2019 Effect of angle of attack on vortex dynamics in laminar separation bubbles. *Phys. Fluids* **31** (6), 064105. DOI. ↩

[117] Landau, L. D. & Lifschitz, E. M. 1987 Fluid Mechanics. Vol. 6. In *Course Theorectical Phys.* 2nd ed. Pergamon Press. ↩

[118] Lang, M., Rist, U., & Wagner, S. 2004 Investigations on controlled transition development in a laminar separation bubble by means of LDA and PIV. *Exp. Fluids* **36** (1), 43–52. DOI. ↩

[119] Lang, W., Gardner, A. D., Mariappan, S., Klein, C., & Raffel, M. 2015 Boundary-layer transition on a rotor blade measured by temperature-sensitive paint, thermal imaging and image derotation. *Exp. Fluids* **56** (6), 1–14. DOI. ↩

[120] Lange, C. F., Durst, F., & Breuer, M. 1999 Wall effects on heat losses from hot-wires. *Int. J. Heat Fluid Flow* **20**, 34–47. DOI. ↩

[121] Laurien, E. & Kleiser, L. 1989 Numerical simulation of boundary-layer transition and transition control. *J. Fluid Mech.* **199**, 403–440. DOI. ↩

[122] LeBlanc, P., Blackwelder, R., & Liebeck, R. 1989 A Comparison Between Boundary Layer Measurements in a Laminar Separation Bubble Flow and Linear Stability Theory Calculations. In Mueller, T. J., editor, *Low Reynolds Number Aerodyn.* Pp. 189–205. Spinger Berlin Heidelberg. DOI. ↩

[123] Lengani, D. & Simoni, D. 2015 Recognition of coherent structures in the boundary layer of a low-pressure-turbine blade for different free-stream turbulence intensity levels. *Int. J. Heat Fluid Flow* **54**, 1–13. DOI. ↩

[124] Lengani, D., Simoni, D., Ubaldi, M., & Zunino, P. 2014 POD analysis of the unsteady behavior of a laminar separation bubble. *Exp. Therm. Fluid Sci.* **58**, 70–79. DOI. ↩

[125] Lengani, D., Simoni, D., Ubaldi, M., Zunino, P., & Bertini, F. 2017 Analysis of the Reynolds stress component production in a laminar separation bubble. *Int. J. Heat Fluid Flow* **64**, 112–119. DOI. ↩

[126] Lin, N., Reed, H. L., & Saric, W. S. 1992 Effect of Leading-Edge Geometry on Boundary-Layer Receptivity to Freestream Sound. In *Instab. Transition, Turbul.* Pp. 421–440. Springer New York. DOI. ↩

[127] Lissaman, P. B. S. 1983 Low-Reynolds-Number Airfoils. *Annu. Rev. Fluid Mech.* **15** (1), 223–239. DOI. ↩

[128] Lumley, J. L. 1967 The structure of inhomogeneous turbulence. In Yaglom, A. M. & Tatarski, V. I., editors, *Atmos. Turbul. Wave Propag.* Pp. 166–178. Nauka. ↩

[129] Lynch, K. P. & Scarano, F. 2014 Experimental determination of tomographic PIV accuracy by a 12-camera system. *Meas. Sci. Technol.* **25** (8), 084003. DOI. ↩

[130] Ma, X., Karamanos, G.-S., & Karniadakis, G. E. 2000 Dynamics and low-dimensionality of a turbulent near wake. *J. Fluid Mech.* **410**, 29–65. DOI. ↩

[131] Mack, L. M. 1984 Boundary-Layer Linear Stability Theory. In *Spec. Course Stab. Transit. Laminar Flow*. AGARD Report No. 709. URL. ↩

[132] Malkiel, E. & Mayle, R. E. 1996 Transition in a Separation Bubble. *J. Turbomach.* **118** (4), 752. DOI. ↩

[133] Marchman, J. F. 1987 Aerodynamic testing at low Reynolds numbers. *J. Aircr.* **24** (2), 107–114. DOI. ↩

[134] Marxen, O. & Henningson, D. S. 2011 The effect of small-amplitude convective disturbances on the size and bursting of a laminar separation bubble. *J. Fluid Mech.* **671**, 1–33. DOI. ↩

[135] Marxen, O., Kotapati, R. B., Mittal, R., & Zaki, T. 2015 Stability analysis of separated flows subject to control by zero-net-mass-flux jet. *Phys. Fluids* **27** (2), 024107. DOI. ↩

[136] Marxen, O., Lang, M., & Rist, U. 2012 Discrete linear local eigenmodes in a separating laminar boundary layer. *J. Fluid Mech.* **711**, 1–26. DOI. ↩

[137] Marxen, O., Lang, M., & Rist, U. 2013 Vortex Formation and Vortex Breakup in a Laminar Separation Bubble. *J. Fluid Mech.* **728**, 58–90. DOI. ↩

[138] Marxen, O., Lang, M., Rist, U., Levin, O., & Henningson, D. S. 2009 Mechanisms for spatial steady three-dimensional disturbance growth in a non-parallel and separating boundary layer. *J. Fluid Mech.* **634**, 165–189. DOI. ↩

[139] Marxen, O., Lang, M., Rist, U., & Wagner, S. 2003 A Combined Experimental/Numerical Study of Unsteady Phenomena in a Laminar Separation Bubble. *Flow, Turbul. Combust.* **71** (1-4), 133–146. DOI. ↩

[140] Marxen, O. & Rist, U. 2010 Mean flow deformation in a laminar separation bubble: separation and stability characteristics. *J. Fluid Mech.* **660**, 37–54. DOI. ↩

[141] Marxen, O., Rist, U., & Wagner, S. 2004 Effect of Spanwise-Modulated Disturbances on Transition in a Separated Boundary Layer. *AIAA J.* **42** (5), 937–944. DOI. ↩

[142] Maucher, U., Rist, U., & Wagner, S. 2000 Refined Interaction Method for Direct Numerical Simulation of Transition in Separation Bubbles. *AIAA J.* **38** (8), 1385–1393. DOI. ↩

[143] McAuliffe, B. R. & Yaras, M. I. 2005 Separation-Bubble-Transition Measurements on a Low-Re Airfoil Using Particle Image Velocimetry. In *Vol. 3 Turbo Expo 2005, Parts A B*, pp. 1029–1038, Reno, NV, USA. ASME. DOI. ↩

[144] McAuliffe, B. R. & Yaras, M. I. 2010 Transition Mechanisms in Separation Bubbles Under Low- and Elevated-Freestream Turbulence. *J. Turbomach.* **132** (1), 011004. DOI. ↩

[145] McWilliams, J. C. 1990 The vortices of two-dimensional turbulence. *J. Fluid Mech.* **219**, 361–385. DOI. ↩

[146] Melling, A. 1997 Tracer particles and seeding for particle image velocimetry. *Meas. Sci. Technol.* **8** (12), 1406–1416. DOI. ↩

[147] Merino-Martínez, R., Rubio Carpio, A., Lima Pereira, L. T., van Herk, S., Avallone, F., Ragni, D., & Kotsonis, M. 2020 Aeroacoustic design and characterization of the 3D-printed, open-jet, anechoic wind tunnel of Delft University of Technology. *Appl. Acoust.* **170**, 107504. DOI. ↩

[148] Meunier, P., Le Dizès, S., & Leweke, T. 2005 Physics of vortex merging. *Comptes Rendus Phys.* **6** (4-5), 431–450. DOI. ↩

[149] Michalke, A. 1969 A note on spatially growing three-dimensional disturbances in a free shear layer. *J. Fluid Mech.* **38** (04), 765–767. DOI. ↩

[150] Michelis, T. 2017 *Boundary Layer Separation: Diagnostics and Control*. PhD Thesis, Delft University of Technology. DOI. ↩

[151] Michelis, T., Kotsonis, M., & Yarusevych, S. 2018 Spanwise flow development within a laminar separation bubble under natural and forced transition. *Exp. Therm. Fluid Sci.* **96** (January), 169–179. DOI. ↩

[152] Michelis, T., Yarusevych, S., & Kotsonis, M. 2017 Response of a laminar separation bubble to impulsive forcing. *J. Fluid Mech.* **820**, 633–666. DOI. ↩

[153] Michelis, T., Yarusevych, S., & Kotsonis, M. 2018 On the origin of spanwise vortex deformations in laminar separation bubbles. *J. Fluid Mech.* **841**, 81–108. DOI. ↩

[154] Miksad, R. W. 1972 Experiments on the nonlinear stages of free-shear-layer transition. *J. Fluid Mech.* **56** (04), 695–719. DOI. ↩

[155] Miksad, R. W. 1973 Experiments on nonlinear interactions in the transition of a free shear layer. *J. Fluid Mech.* **59** (01), 1–21. DOI. ↩

[156] Miozzi, M., Capone, A., Costantini, M., Fratto, L., Klein, C., & Di Felice, F. 2019 Skin friction and coherent structures within a laminar separation bubble. *Exp. Fluids* **60** (1), 13. DOI. ↩

[157] Moffat, R. J. 1982 Contributions to the Theory of Single-Sample Uncertainty Analysis. *J. Fluids Eng.* **104** (2), 250–258. DOI. ↩

[158] Moffat, R. J. 1988 Describing the uncertainties in experimental results. *Exp. Therm. Fluid Sci.* **1** (1), 3–17. DOI. ↩

[159] Moin, P. & Mahesh, K. 1998 Direct Numerical Simulation: A Tool in Turbulence Research. *Annu. Rev. Fluid Mech.* **30** (1), 539–578. DOI. ↩

[160] Monkewitz, P. A. & Huerre, P. 1982 Influence of the velocity ratio on the spatial instability of mixing layers. *Phys. Fluids* **25** (7), 1137. DOI. ↩

[161] Montelpare, S. & Ricci, R. 2004 A thermographic method to evaluate the local boundary layer separation phenomena on aerodynamic bodies operating at low Reynolds number. *Int. J. Therm. Sci.* **43** (3), 315–329. DOI. ↩

[162] Moreau, E. 2007 Airflow control by non-thermal plasma actuators. *J. Phys. D. Appl. Phys.* **40**, 605–636. DOI. ↩

[163] Morkovin, M. V., Reshotko, E., & Herbert, T. 1994 Transition in open flow systems - a reassessment. *Bull. Am. Phys. Soc.* **39**, 1882. ↩

[164] Morkovin, M. V. 1969 On the Many Faces of Transition. In Wells, C. S., editor, *Viscous Drag Reduct.* Pp. 1–31. Springer US. DOI. ↩

[165] Morton, B. R. 1984 The generation and decay of vorticity. *Geophys. Astrophys. Fluid Dyn.* **28** (3-4), 277–308. DOI. ↩

[166] Mueller, T. J. & DeLaurier, J. D. 2003 Aerodynamics of Small Vehicles. *Annu. Rev. Fluid Mech.* **35** (1), 89–111. DOI. ↩

[167] Mueller, T. J., Pohlen, L. J., Conigliaro, P. E., & Jansen, B. J. 1983 The influence of free-stream disturbances on low Reynolds number airfoil experiments. *Exp. Fluids* **1** (1), 3–14. DOI. ↩

[168] Mueller, T. J. 1985 Low Reynolds Number Vehicles. *Tech. rep.*, AGARDograph No. 288. ISBN. ↩

[169] Nash, E. C., Lowson, M. V., & McAlpine, A. 1999 Boundary-layer instability noise on aerofoils. *J. Fluid Mech.* **382**, 22–61. DOI. ↩

[170] Nati, A., de Kat, R., Scarano, F., & van Oudheusden, B. W. 2015 Dynamic pitching effect on a laminar separation bubble. *Exp. Fluids* **56** (9), 172. DOI. ↩

[171] Nishioka, M., Asai, M., & Yoshida, S. 1990 Control of flow separation by acoustic excitation. *AIAA J.* **28** (11), 1909–1915. DOI. ↩

[172] O'Meara, M. & Mueller, T. J. 1987 Laminar separation bubble characteristics on an airfoil at low Reynolds numbers. *AIAA J.* **25** (8), 1033–1041. DOI. ↩

[173] Ol, M. V., McCauliffe, B. R., Hanff, E. S., Scholz, U., & Kähler, C. 2005 Comparison of Laminar Separation Bubble Measurements on a Low Reynolds Number Airfoil in Three Facilities. In *35th AIAA Fluid Dyn. Conf. Exhib.* Toronto, ON, Canada. DOI. ↩

[174] Olson, D. A., Katz, A. W., Naguib, A. M., Koochesfahani, M. M., Rizzetta, D. P., & Visbal, M. R. 2013 On the challenges in experimental characterization of flow separation over airfoils at low Reynolds number. *Exp. Fluids* **54** (2), 1470. DOI. ↩

[175] Orr, W. M. 1907 The Stability or Instability of the Steady Motions of a Perfect Liquid and of a Viscous Liquid. *Proc. R. Irish Acad. Sect. A Math. Phys. Sci.* **27**, 9–138. URL. ↩

[176] Orszag, S. A. & Kells, L. C. 1980 Transition to turbulence in plane Poiseuille and plane Couette flow. *J. Fluid Mech.* **96** (01), 159–205. DOI. ↩

[177] Orszag, S. A. & Patera, A. T. 1983 Secondary instability of wall-bounded shear flows. *J. Fluid Mech.* **128**, 347–385. DOI. ↩

[178] Owen, P. R. & Klanfer, L. 1953 On the Laminar Boundary Layer Separation from the Leading Edge of a Thin Aerofoil. *Tech. rep.*, R.A.E. Report No. Aero 2508. URL. ↩

[179] Parker, R. 1966 Resonance effects in wake shedding from parallel plates: Some experimental observations. *J. Sound Vib.* **4** (1), 62–72. DOI. ↩

[180] Parker, R. 1967 Resonance effects in wake shedding from parallel plates: Calculation of resonant frequencies. *J. Sound Vib.* **5** (2), 330–343. DOI. ↩

[181] Paterson, R. W., Vogt, P. G., Fink, M. R., & Munch, C. L. 1973 Vortex Noise of Isolated Airfoils. *J. Aircr.* **10** (5), 296–302. DOI. ↩

[182] Pauley, L. L. 1994 Response of Two-Dimensional Separation to Three-Dimensional Disturbances. *J. Fluids Eng.* **116** (3), 433. DOI. ↩

[183] Pelletier, A. & Mueller, T. J. 2000 Low Reynolds Number Aerodynamics of Low-Aspect-Ratio, Thin/Flat/Cambered-Plate Wings. *J. Aircr.* **37** (5), 825–832. DOI. ↩

[184] Pereira, R., Ragni, D., & Kotsonis, M. 2014 Effect of external flow velocity on momentum transfer of dielectric barrier discharge plasma actuators. *J. Appl. Phys.* **116** (10), 103301. DOI. ↩

[185] Plogmann, B., Herrig, A., & Würz, W. 2013 Experimental investigations of a trailing edge noise feedback mechanism on a NACA 0012 airfoil. *Exp. Fluids* **54** (5), 1480. DOI. ↩

[186] Prandtl, L. 1904 Über Flüssigkeitsbewegung bei sehr kleiner Reibung. In *Verh. III Int. Math-Kongr.* Heidelberg, Germany. ↩

[187] Prandtl, L. & Tietjens, O. G. 1934 *Fundamentals of Hydro- and Aeromechanics*. ISBN. ↩

[188] Pröbsting, S., Scarano, F., & Morris, S. C. 2015 Regimes of tonal noise on an airfoil at moderate Reynolds number. *J. Fluid Mech.* **780**, 407–438. DOI. ↩

[189] Pröbsting, S., Serpieri, J., & Scarano, F. 2014 Experimental investigation of aerofoil tonal noise generation. *J. Fluid Mech.* **747**, 656–687. DOI. ↩

[190] Pröbsting, S. & Yarusevych, S. 2015 Laminar separation bubble development on an airfoil emitting tonal noise. *J. Fluid Mech.* **780**, 167–191. DOI. ↩

[191] Raffel, M., Willert, C., Wereley, S., & Kompenhans, J. 2007 *Particle Image Velocimetry: A Practical Guide*. 2nd ed. Springer. DOI. ↩

[192] Rai, M. M. & Moin, P. 1993 Direct Numerical Simulation of Transition and Turbulence in a Spatially Evolving Boundary Layer. *J. Comput. Phys.* **109** (2), 169–192. DOI. ↩

[193] Reshotko, E. 2001 Transient growth: A factor in bypass transition. *Phys. Fluids* **13** (5), 1067–1075. DOI. ↩

[194] Rinoie, K. & Takemura, N. 2004 Oscillating behaviour of laminar separation bubble formed on an aerofoil near stall. *Aeronaut. J.* **108** (1081), 153–163. DOI. ↩

[195] Rist, U. & Fasel, H. 1995 Direct numerical simulation of controlled transition in a flat-plate boundary layer. *J. Fluid Mech.* **298**, 211. DOI. ↩

[196] Rist, U. & Maucher, U. 2002 Investigations of time-growing instabilities in laminar separation bubbles. *Eur. J. Mech. - B/Fluids* **21** (5), 495–509. DOI. ↩

[197] Rist, U., Maucher, U., & Wagner, S. 1996 Direct numerical simulation of some fundamental problems related to transition in laminar separation bubbles. In Désidér, J.-A., Hirsch, C., La Tallec, P., Pandolfi, M., & Périaux, J., editors, *Comput. Fluid Dyn. 96*, pp. 319–325. Wiley. ↩

[198] Rist, U. & Augustin, K. 2006 Control of Laminar Separation Bubbles Using Instability Waves. *AIAA J.* **44** (10), 2217–2223. DOI. ↩

[199] Rizzetta, D. P. & Visbal, M. R. 2011 Numerical Investigation of Plasma-Based Control for Low-Reynolds-Number Airfoil Flows. *AIAA J.* **49** (2), 411–425. DOI. ↩

[200] Rodríguez, D. & Gennaro, E. M. 2018 Enhancement of disturbance wave amplification due to the intrinsic three-dimensionalisation of laminar separation bubbles. *Aeronaut. J.* (April), 1–16. DOI. ↩

[201] Rodríguez, D., Gennaro, E. M., & Juniper, M. P. 2013 The two classes of primary modal instability in laminar separation bubbles. *J. Fluid Mech.* **734**, R4. DOI. ↩

[202] Rodríguez, D. & Theofilis, V. 2010 Structural changes of laminar separation bubbles induced by global linear instability. *J. Fluid Mech.* **655**, 280–305. DOI. ↩

[203] Rogers, M. M. & Moser, R. D. 1992 The three-dimensional evolution of a plane mixing layer: the Kelvin–Helmholtz rollup. *J. Fluid Mech.* **243**, 183–226. DOI. ↩

[204] Ross, J. A., Barnes, F. H., Burns, J. G., & Ross, M. A. S. 1970 The flat plate boundary layer. Part 3. Comparison of theory with experiment. *J. Fluid Mech.* **43** (04), 819–832. DOI. ↩

[205] Sandham, N. D. 2008 Transitional separation bubbles and unsteady aspects of aerofoil stall. *Aeronaut. J.* **112** (1133), 395–404. DOI. ↩

[206] Saric, W. S., Reed, H. L., & Kerschen, E. J. 2002 Boundary-Layer Receptivity to Freestream Disturbances. *Annu. Rev. Fluid Mech.* **34** (1), 291–319. DOI. ↩

[207] Saric, W. S. 1990 Low-Speed Experiments: Requirements for Stability Measurements. In Hussaini, M. Y. & Voigt, R. G., editors, *Instab. Transition; Proc. Work. Hampton, VA, USA, 1989*, pp. 162–174. Springer. DOI. ↩

[208] Saric, W. S., Reed, H. L., & White, E. B. 2003 Stability and Transition of Three-Dimensional Boundary Layers. *Annu. Rev. Fluid Mech.* **35** (1), 413–440. DOI. ↩

[209] Saric, W. S. & Thomas, A. S. W. 1984 Experiments on the subharmonic route to turbulence in boundary layers. In Tatsumi, T., editor, *Turbul. choatic Phenom. fluids; Proc. Int. Symp. Kyoto, Japan, 1983*, pp. 117–122. Elsevier. URL. ↩

[210] Sato, M., Nonomura, T., Okada, K., Asada, K., Aono, H., Yakeno, A., Abe, Y., & Fujii, K. 2015 Mechanisms for laminar separated-flow control using dielectric-barrier-discharge plasma actuator at low Reynolds number. *Phys. Fluids* **27** (11), 117101. DOI. ↩

[211] Scarano, F. 2013 Tomographic PIV: principles and practice. *Meas. Sci. Technol.* **24**, 012001. DOI. ↩

[212] Scarano, F. & Riethmuller, M. L. 2000 Advances in iterative multigrid PIV image processing. *Exp. Fluids* **29** (7), S051–S060. DOI. ↩

[213] Schlichting, H. 1933 Zur Entstehung der Turbulenz bei der Plattenströmung. *Nachrichten von der Gesellschaft der Wissenschaften zu Göttingen, Math. Klasse* 182–208. URL. ↩

[214] Schlichting, H. & Gersten, K. 2000 *Boundary-Layer Theory*. 8th ed. Springer-Verlag. ISBN. ↩

[215] Schmid, P. J. & Henningson, D. S. 2001 Stability and Transition in Shear Flows. In Marsden, J. E. & Sirovich, L., editors, *Appl. Math. Sci. Vol. 142*. Springer. ↩

[216] Schubauer, G. & Skramstad, H. 1947 Laminar boundary-layer oscillations and transition on a flat plate. *J. Res. Natl. Bur. Stand. (1934).* **38** (2), 251. DOI. ↩

[217] Sciacchitano, A., Neal, D. R., Smith, B. L., Warner, S., Vlachos, P. P., Wieneke, B., & Scarano, F. 2015 Collaborative framework for PIV uncertainty quantification: comparative assessment of methods. *Meas. Sci. Technol.* **26** (7), 074004. DOI. ↩

[218] Sciacchitano, A., Wieneke, B., & Scarano, F. 2013 PIV uncertainty quantification by image matching. *Meas. Sci. Technol.* **24** (4), 045302. DOI. ↩

[219] Serna, J. & Lázaro, B. J. 2014 The final stages of transition and the reattachment region in transitional separation bubbles. *Exp. Fluids* **55** (4), 1695. DOI. ↩

[220] Serna, J. & Lázaro, B. J. 2015 On the bursting condition for transitional separation bubbles. *Aerosp. Sci. Technol.* **44**, 43–50. DOI. ↩

[221] Serpieri, J., Yadala Venkata, S., & Kotsonis, M. 2017 Conditioning of cross-flow instability modes using dielectric barrier discharge plasma actuators. *J. Fluid Mech.* **833**, 164–205. DOI. ↩

[222] Simoni, D., Lengani, D., Ubaldi, M., Zunino, P., & Dellacasagrande, M. 2017 Inspection of the dynamic properties of laminar separation bubbles: free-stream turbulence intensity effects for different Reynolds numbers. *Exp. Fluids* **58** (6), 66. DOI. ↩

[223] Sirovich, L. 1987 Turbulence and the Dynamics of Coherent Structures. *Q. Appl. Math.* **XLV** (3), 561–590. URL. ↩

[224] Smith, A. M. O. & Gamberoni, N. 1956 Transition, Pressure Gradient and Stability Theory. *Tech. rep.*, Douglas Aircraft Company, Inc. ↩

[225] Sommerfeld, A. 1908 Ein Beitrag zur hydrodynamischen Erklärung der turbulenten Flüssigkeitsbewegung. In *Proc. 4th Int. Congr. Math. III*, pp. 116–124, Rome, Italy. ↩

[226] Sørensen, J. N. 2011 Aerodynamic Aspects of Wind Energy Conversion. *Annu. Rev. Fluid Mech.* **43**, 427–448. DOI. ↩

[227] Spalart, P. R. & Strelets, M. K. 2000 Mechanisms of transition and heat transfer in a separation bubble. *J. Fluid Mech.* **403**, 329–349. DOI. ↩

[228] Spalart, P. R. & Yang, K.-S. 1987 Numerical study of ribbon-induced transition in Blasius flow. *J. Fluid Mech.* **178**, 345–365. DOI. ↩

[229] Strazisar, A. J., Reshotko, E., & Prahl, J. M. 1977 Experimental study of the stability of heated laminar boundary layers in water. *J. Fluid Mech.* **83** (02), 225–247. DOI. ↩

[230] Strunz, M. & Speth, J. F. 1987 A new laminar water tunnel to study the transition process in a Blasius boundary layer and in a separation bubble and a new tool for industrial aerodynamics and hydrodynamic research. *Tech. rep.*, AGARD CP 413. ↩

[231] Stuart, J. T. 1962 Non-linear effects in hydrodynamic stability. In Rolla, F. & Koiter, W. T., editors, *Proc. 10th Int. Congr. Appl. Mech.* Pp. 63–97, Stresa, Italy. Elsevier. ↩

[232] Tani, I. 1964 Low-speed flows involving bubble separations. *Prog. Aerosp. Sci.* **5**, 70–103. DOI. ↩

[233] Theofilis, V. 2011 Global Linear Instability. *Annu. Rev. Fluid Mech.* **43**, 319–352. DOI. ↩

[234] Thomas, F. O., Corke, T. C., Duong, A., Midya, S., & Yates, K. 2019 Turbulent drag reduction using pulsed-DC plasma actuation. *J. Phys. D. Appl. Phys.* **52**, 434001. DOI. ↩

[235] Thomas, F. O., Kozlov, A., & Corke, T. C. 2008 Plasma Actuators for Cylinder Flow Control and Noise Reduction. *AIAA J.* **46** (8), 1921–1931. DOI. ↩

[236] Tollmien, W. 1930 Über die Entstehung der Turbulenz. In *Vor. aus dem Gebiete der Aerodyn. und verwandter Gebiete*, pp. 18–21. Springer Berlin Heidelberg. DOI. ↩

[237] Tropea, C., Yarin, A., & Foss, J. F., eds. 2007 *Springer Handbook of Experimental Fluid Mechanics*. Springer-Verlag. ISBN. ↩

[238] Van Ingen, J. L. & Boermans, M. M. 1986 Aerodynamics at low Reynolds numbers: a review of theoretical and experimental research at Delft University of Technology. In *Proc. Aerodyn. Low Reynolds Numbers Int. Conf.* London, UK. The Royal Aeronautical Society. ↩

[239] Van Ingen, J. 1956 A suggested semi-empirical method for the calculation of the boundary layer transition region. *Tech. rep.*, Delft University of Technology, Report VTH-74. URL. ↩

[240] Van Ingen, J. & Kotsonis, M. 2011 A two-parameter method for e^N transition prediction. In *6th AIAA Theor. Fluid Mech. Conf.* Honolulu, HI, USA. DOI. ↩

[241] Van Oudheusden, B. W., Scarano, F., van Hinsberg, N. P., & Watt, D. W. 2005 Phase-resolved characterization of vortex shedding in the near wake of a square-section cylinder at incidence. *Exp. Fluids* **39** (1), 86–98. DOI. ↩

[242] Vincent, A. & Meneguzzi, M. 1991 The satial structure and statistical properties of homogeneous turbulence. *J. Fluid Mech.* **225**, 1–20. DOI. ↩

[243] Watmuff, J. H. 1999 Evolution of a wave packet into vortex loops in a laminar separation bubble. *J. Fluid Mech.* **397**, 119–169. DOI. ↩

[244] Wee, D., Yi, T., Annaswamy, A., & Ghoniem, A. F. 2004 Self-sustained oscillations and vortex shedding in backward-facing step flows: Simulation and linear instability analysis. *Phys. Fluids* **16** (9), 3361–3373. DOI. ↩

[245] Welch, P. 1967 The use of fast Fourier transform for the estimation of power spectra: A method based on time averaging over short, modified periodograms. *IEEE Trans. Audio Electroacoust.* **15** (2), 70–73. DOI. ↩

[246] Westerweel, J. 1997 Fundamentals of digital particle image velocimetry. *Meas. Sci. Technol.* **8** (12), 1379–1392. DOI. ↩

[247] Westerweel, J. & Scarano, F. 2005 Universal outlier detection for PIV data. *Exp. Fluids* **39** (6), 1096–1100. DOI. ↩

[248] Westerweel, J., Elsinga, G. E., & Adrian, R. J. 2013 Particle Image Velocimetry for Complex and Turbulent Flows. *Annu. Rev. Fluid Mech.* **45** (1), 409–436. DOI. ↩

[249] White, F. M. 2006 *Viscous Fluid Flow*. 3rd ed. McGraw Hill. ISBN. ↩

[250] Wieneke, B. 2008 Volume self-calibration for 3D particle image velocimetry. *Exp. Fluids* **45**, 549–556. DOI. ↩

[251] Wieneke, B. 2015 PIV uncertainty quantification from correlation statistics. *Meas. Sci. Technol.* **26** (7), 074002. DOI. ↩

[252] Willert, C. & Gharib, M. 1991 Digital particle image velocimetry. *Exp. Fluids* **10** (4), 181–193. arXiv: K26HX2P53NR16411. DOI. ↩

[253] Williamson, C. H. K. 1992 The natural and forced formation of spot-like 'vortex dislocations' in the transition of a wake. *J. Fluid Mech.* **243**, 393–441. DOI. ↩

[254] Williamson, C. H. K. 1996 Vortex Dynamics in the Cylinder Wake. *Annu. Rev. Fluid Mech.* **28**, 477–539. DOI. ↩

[255] Wolf, E., Kähler, C. J., Troolin, D. R., Kykal, C., & Lai, W. 2011 Time-resolved volumetric particle tracking velocimetry of large-scale vortex structures from the reattachment region of a laminar separation bubble to the wake. *Exp. Fluids* **50** (4), 977–988. DOI. ↩

[256] Wray, A. & Hussaini, M. Y. 1984 Numerical Experiments in Boundary-Layer Stability. *Proc. R. Soc. London, Ser. A* **392** (1803), 373–389. URL. ↩

[257] Wynnychuk, D. W. & Yarusevych, S. 2020 Characterization of Laminar Separation Bubbles Using Infrared Thermography. *AIAA J.* **58** (7), 2831–2843. DOI. ↩

[258] Yarusevych, S., Kawall, J. G., & Sullivan, P. E. 2006 Airfoil Performance at Low Reynolds Numbers in the Presence of Periodic Disturbances. *J. Fluids Eng.* **128** (3), 587. DOI. ↩

[259] Yarusevych, S., Kawall, J. G., & Sullivan, P. E. 2008 Separated-Shear-Layer Development on an Airfoil at Low Reynolds Numbers. *AIAA J.* **46** (12), 3060–3069. DOI. ↩

[260] Yarusevych, S. & Kotsonis, M. 2017 Effect of Local DBD Plasma Actuation on Transition in a Laminar Separation Bubble. *Flow, Turbul. Combust.* **98** (1), 195–216. DOI. ↩

[261] Yarusevych, S. & Kotsonis, M. 2017 Steady and transient response of a laminar separation bubble to controlled disturbances. *J. Fluid Mech.* **813**, 955–990. DOI. ↩

[262] Yarusevych, S., Sullivan, P. E., & Kawall, J. G. 2009 On vortex shedding from an airfoil in low-Reynolds-number flows. *J. Fluid Mech.* **632**, 245–271. DOI. ↩

[263] Zaman, K. B. M. Q. 1992 Effect of acoustic excitation on stalled flows over an airfoil. *AIAA J.* **30** (6), 1492–1499. DOI. ↩

[264] Zaman, K. B. M. Q., Bar-Sever, A., & Mangalam, S. M. 1987 Effect of acoustic excitation on the flow over a low- Re airfoil. *J. Fluid Mech.* **182**, 127–148. DOI. ↩

[265] Zaman, K. B. M. Q. & McKinzie, D. J. 1991 Control of laminar separation over airfoils by acoustic excitation. *AIAA J.* **29** (7), 1075–1083. DOI. ↩

[266] Zaman, K. B. M. Q., Mckinzie, D. J., & Rumsey, C. L. 1989 A natural low-frequency oscillation of the flow over an airfoil near stalling conditions. *J. Fluid Mech.* **202**, 403–442. DOI. ↩

[267] Zelman, M. B. & Maslennikova, I. I. 1993 Tollmien-Schlichting-wave resonant mechanism for subharmonic-type transition. *J. Fluid Mech.* **252**, 449. DOI. ↩

[268] Zhang, W., Hain, R., & Kähler, C. J. 2008 Scanning PIV investigation of the laminar separation bubble on a SD7003 airfoil. *Exp. Fluids* **45** (4), 725–743. DOI. ↩

Appendices

Appendix A

Effect of Tonal and Broadband Acoustic Excitation on LSB Transition

Transition in an LSB formed over an airfoil is studied experimentally, and the effects of tonal and broadband acoustic excitation are considered. For equal input energy levels, these two types of excitation produce equivalent changes in the mean LSB topology. A cross-examination of LST predictions and measured disturbance characteristics show non-linear interactions play a crucial role in the transition process, leading to significantly different disturbance development for the tonal and broadband excited flows.

Parts of this appendix have been adapted from

Kurelek, J. W., Kotsonis, M. & Yarusevych, S. 2018 Transition in a separation bubble under tonal and broadband acoustic excitation. *J. Fluid Mech.* **853**, 1–36. DOI.

A.1 Introduction

One of the prevailing themes throughout Sections 2.1.4 and 2.2 is the importance of a transitioning flow's sensitivity to environmental disturbances. Of particular practical relevance to separation bubbles is airfoil self-noise production, where tonal or broadband noise is generated at the trailing edge of an airfoil [29]. Strong acoustic tones are commonly observed on airfoils operating in the low Reynolds number domain [169, 181, 189]. This occurs when laminar boundary layer separation or LSB formation occurs close to the trailing edge, and the strongly coherent perturbations amplified in the separated shear layer produce tones when scattered at the airfoil trailing edge [7, 44, 188]. In contrast, when the LSB is located closer to the leading edge and a turbulent boundary layer forms over the aft portion of the airfoil, broadband noise emissions are produced at the trailing edge [3, 28]. The occurrence of such noise emissions can have notable effect on the flow development. In aeroacoustic investigations, the upstream propagation of tonal noise has been shown to establish an acoustic feedback loop [7, 11, 93, 185], thus affecting the development of shear layer perturbations responsible for the noise emissions. Pröbsting & Yarusevych [190] demonstrate that such a feedback loop, dictated by either suction or pressure side LSBs, can alter LSB characteristics.

As a result of these phenomena being coupled by a feedback loop, it is difficult to assess the effect of airfoil-self noise emissions on LSB development. Furthermore, a cross-examination between the effects of tonal and broadband noise emissions on LSB dynamics has yet to be done in a controlled environment. Such an investigation has merit since the transition process within a laminar separation bubbles is broadband in nature [19], *i.e.*, the flow is unstable to disturbances over a range of frequencies. Thus, the non-linear mechanisms by which amplified perturbations interact in separation bubble flows are hypothesized to have significant impacts on flow development, since such mechanisms play key roles in the later stages of the transition processes in other canonical flows. In the case of the laminar boundary layer, Boiko *et al.* [19] note that the continued growth of two Tollmien-Schlichting waves with close but distinct frequencies incites the growth of fluctuations at not only their own frequencies and harmonics, but also at the sum and difference frequencies and their harmonics. All of these waves grow, interact, and generate further harmonics, thus quickly realizing a broadband spectra of fluctuations. Similar observations have been made in the investigation of free shear layers excited at multiple frequencies [154, 155]. By exciting two distinct frequencies acoustically, Miksad [155] found the same generation of fluctuations at sum and difference frequencies, in addition to harmonics and subharmonics. Moreover, non-linear mode competition between disturbances was found to be important, as the two excited modes suppressed each others' growth, with a tendency for fluctuating energy to become distributed among a broad range of frequencies. Thus, it was necessary to employ a disturbance growth model that took non-linear effects into account to accurately describe the transition process.

The present investigation is carried out to determine the effects of tonal and broadband acoustic excitation on flow development and transition in a laminar separation bubble. Disturbances are introduced in a controlled manner from an external source, so as to decouple the interdependence of flow development and acoustic emissions due to airfoil-self noise production. In addition to the unperturbed case, where broadband disturbances present in the environment serve as input to the unstable flow, two excitation cases are considered: (i) tonal excitation at the frequency of

the most amplified disturbances in the natural flow, and (ii) broadband excitation: white noise band-pass filtered to the unstable frequency range of the natural flow. The aim is then to cross-examine these cases and elucidate any underlying physical differences in the transition processes and the associated changes in flow development. The flow field is assessed via time-resolved, two-component Particle Image Velocimetry (PIV). Two separate experimental configurations are employed to characterize streamwise and spanwise aspects of the flow development. The time-resolved nature of the measurements allows for characterization of the temporal evolution across the entire range of relevant time scales. The experimental results are complemented by LST analysis, and the elucidated differences in the evolution of perturbations are related to changes in vortex dynamics and mean topological features of the bubble.

A.2 Description of Experiments

Experiments were conducted in the closed-loop wind tunnel located at the University of Waterloo's Fluid Mechanics Research Laboratory (Section 3.1.1). The tunnel test section is 0.61×0.61 m in cross-section, 2.44 m long, and has a nominal free-stream turbulence intensity less than 0.1%. Furthermore, the free-stream was verified to have no significant spectral content within the frequency range of interest to this investigation, $100 \leq f \leq 2000$ Hz ($2 \leq St_c \leq 42$). The test section free-stream uniformity was verified to be within ±0.5%. The free-stream velocity was set based on the measured pressure drop across the contraction calibrated against a Pitot-static tube in the empty test section, with the associated uncertainty in the free-stream velocity estimated to be less than 2%.

Tests were performed using the NACA 0018 airfoil model described in Section 3.1.3. A surface-attached coordinate system is employed, where x, y, and z are defined as the wall-tangent, wall-normal, and spanwise coordinates, respectively, with the origin set to the airfoil model's leading edge and mid-span point. The model is equipped with twenty-five Panasonic WM-62C back electret condenser microphones installed under 0.8 mm diameter ports, twenty-two of which are distributed along the chord in a staggered row. Each microphone was calibrated in the airfoil model relative to a reference 4189 Brüel and Kjær microphone. All microphones have a flat response (±1 dB) in the range $100 \leq f \leq 2000$ Hz ($2 \leq St_c \leq 42$). For all acoustic measurements, up to eight microphones were sampled simultaneously at 40 kHz for a total of 2^{22} samples using a National Instruments PCI-4472 data acquisition card, which applies a hardware low-pass filter at the Nyquist limit to all sampled signals.

All tests were performed at an angle of attack of 4° and a free-stream velocity of $u_\infty = 9.6\,\mathrm{m\,s^{-1}}$, corresponding to a chord-based Reynolds number of $Re_c = 125\,000$. The solid blockage ratio at the investigated angle of attack is 6.1%, and no blockage corrections were applied to the measured surface pressure distributions [21]. The angle of attack was set using a digital protractor with a resolution of 0.1°. For the given flow conditions, separation bubbles form on both the suction and pressure surfaces, with the latter forming close to the trailing edge. To avoid the establishment of a feedback loop between the suction side transition process and tonal noise emissions due to the pressure side LSB [190], the pressure side boundary layer was tripped at $x/c = 0.4$ by a 10 mm wide strip of randomly distributed three-dimensional roughness elements.

Time-resolved, two-component PIV was employed in two separate planes to characterize spatio-temporal flow development in the separation bubble and the effect of acoustic excitation. The tests were performed in the two configurations depicted in Fig. A.1. The flow was seeded using a glycol-water based fog with a mean particle diameter of 4 µm and illuminated by a laser sheet produced by a Photonics DM20-527 high-repetition rate Nd:YLF pulsed laser. The laser beam was introduced through the side wall of the test section and conditioned into a sheet approximately 1 mm thick. For the side-view configuration, Fig. A.1a, the sheet was oriented parallel to the airfoil cross-section and passed through the mid-span plane. For the top-view, Fig. A.1b, the sheet was oriented parallel to the airfoil surface within the investigated field of view (FOV). For both configurations, images were captured by two Photron SA4 high-speed cameras synchronized with the laser via a LaVision timing unit controlled through LaVision's DaVis 8 software.

Table A.1 provides an overview of the parameters for the PIV experiments. For the side view configuration (Fig. A.1a), the high-speed cameras were fitted with Nikon 200 mm fixed focal length macro lenses set to an aperture number ($f_\#$) of 4. The cameras' sensors were cropped to 1024×512 px and the fields of view were adjusted to maximize the spatial resolution in the aft portion of the separation bubble, while maintaining equal magnification factors of 0.67 for both cameras. The fields of view were overlapped by 10% and images were acquired in double-frame mode at a sampling rate of 3.8 kHz. For the top-view PIV measurements (Fig. A.1b), the cameras were fitted with Nikon 105 mm fixed focal length macro lenses set to $f_\# = 3.8$. The streamwise extent of the FOV was set to match that of the combined FOV for the side-view configuration. The second camera was employed to extend the FOV in the spanwise direction, while maintaining an overlap of 10%. For both cameras, the full sensor resolution of 1024×1024 px and equal magnification factors of 0.33 were used. Images were acquired in double-frame mode at a rate of 1.95 kHz. In this configuration, one camera was set normal to the field of view and the second camera had to be tilted (Fig. A.1b). Thus, to maintain the entire field of view in focus, the second camera was equipped with a Scheimpflug adapter.

For both PIV configurations, the focus was adjusted to produce particle images approximately 2 to 3 px in diameter. An iterative multi-grid cross-correlation scheme with window deformation [212] was used to compute velocity fields. A final interrogation window size of 16×16 px with 75% overlap was selected, with each window containing, on average, 14 particles. As a result, the vector pitches in the PIV data are 0.12 mm and 0.24 mm for the side and top view configurations, respectively. The results were post-processed using the universal outlier detection algorithm [247]. Once the respective vector fields were calculated, the mean velocity fields for each camera were cross-correlated in the overlap region to align the FOVs. The vector fields were then interpolated onto the surface-attached coordinate system with a cosine weighted blending function employed in the overlap region. The random errors in the PIV measurements were evaluated using the particle image disparity method [217, 218], with the associated average uncertainties in the velocity fields estimated to be less than 6% and 6.5% within 95% confidence for the side and top view configurations, respectively. Comparable uncertainties for the two configurations were achieved by minimizing the out-of-plane loss of particles for the top-view by selecting a frame separation time that kept particle displacements less than or equal to 9 px, in comparison to 17 px for the side-view.

Sound excitation was provided by a Pyramid WH88 sub-woofer placed within the test section

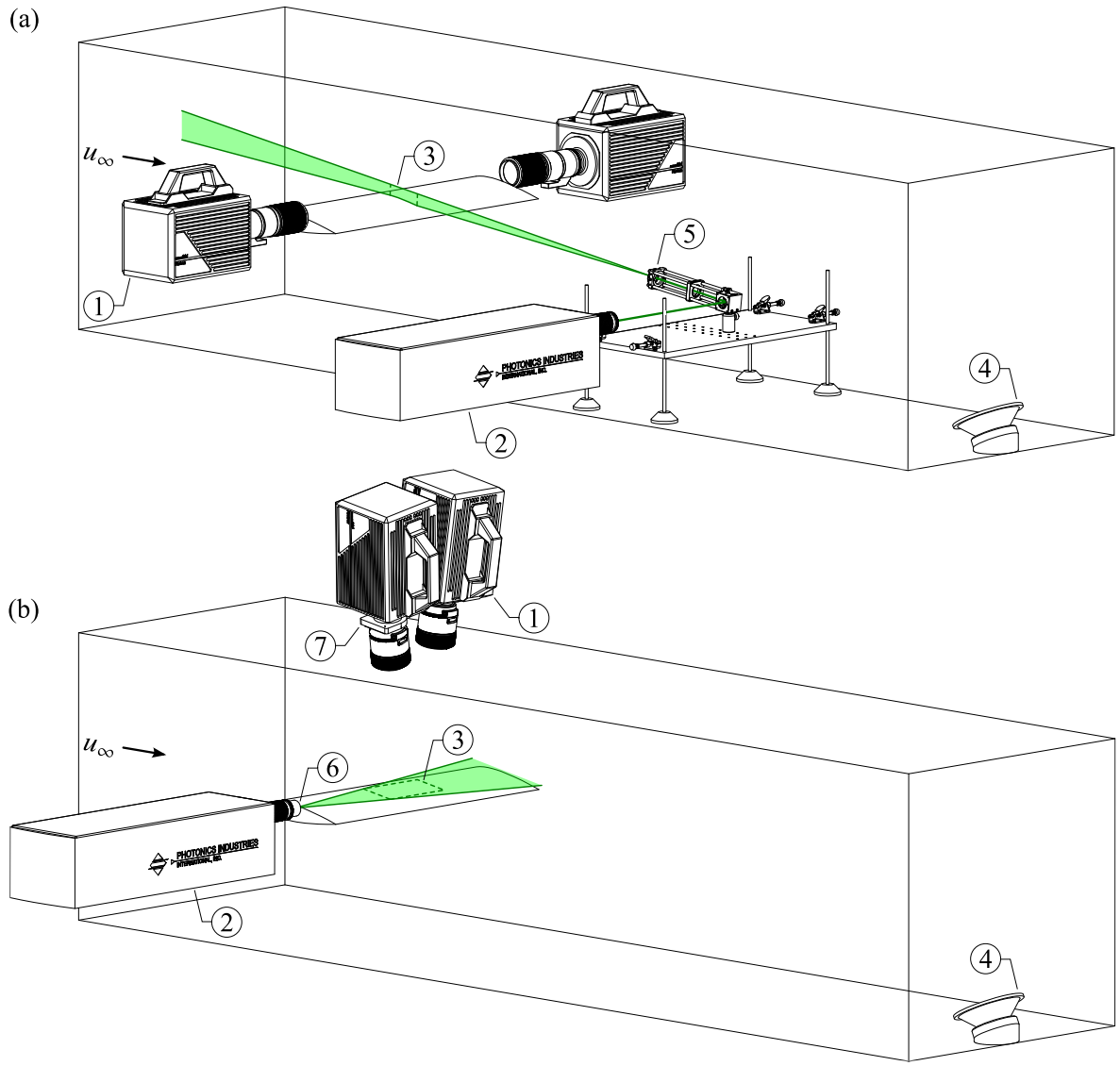

Figure A.1: (a) Side view and (b) top view experimental configurations for PIV measurements. ① High-speed cameras; ② laser with focusing optics; ③ field of view; ④ speaker; ⑤ side view sheet optics located $3c$ downstream of airfoil trailing edge; ⑥ top view sheet optics; ⑦ Scheimpflug adapter.

on an vibration isolating pad, $6c$ downstream of the airfoil trailing edge. The presence of the speaker and the PIV sheet forming optics within the test section (Fig. A.1a) were confirmed via pressure measurements to have no measurable influence on mean LSB characteristics. The speaker was driven by an amplifier, with the excitation signal supplied by a National Instruments USB-6259 data acquisition unit. A 4189 Brüel and Kjær microphone was used to quantify the background noise level in the test section at $Re_c = 125\,000$, as well as sound excitation at the airfoil suction surface in quiescent conditions. Based on the instrument's accuracy for a frequency range of 40 to 1000 Hz, the uncertainty in the measured sound pressure levels (SPLs) is estimated

Table A.1: Parameters for PIV experiments.

Parameter	Side-view	Top-view	Unit
Laser	Photonics DM20-527		
Cameras	Photron SA4		
Lens focal length	200	105	mm
Lens $f_\#$	4	2.8	
Magnification factor	0.67	0.33	
Sensor resolution	1024×512	1024×1024	px
Total field of view	54×12.5	54×102	mm
PIV mode	Double-frame		
Sampling rate	3.8	1.95	kHz
Frame separation time	40	60	µs
Outer-flow displacement	17	9	px
Number of samples	5456	2728	
Window size	16×16		px
Vector pitch	0.12	0.24	mm

to be ±0.2 dB. In addition, the amplitude of the sound excitation was verified to be uniform over the chordwise and spanwise extents of the investigated areas, as SPLs varied within ±0.6 dB.

In addition to the naturally developing flow, two types of excitation are investigated: (i) tonal excitation at the frequency of the most amplified disturbances in the unperturbed flow, *i.e.* the fundamental frequency, $St_{0_c} = 15.6$, and (ii) broadband: white noise band-pass filtered to the unstable frequency band of the unperturbed flow, $10.4 \leq St_c \leq 20.8$. Spectra of fluctuating surface pressure near the natural separation point for all the investigated cases are presented in Fig. A.2. For the natural case, a broad elevated energy content is seen around the fundamental frequency ($St_{0_c} = 15.6$) in the spectrum and is attributed to natural transition occurring in the separated shear layer downstream of the measurement location. As expected for unforced transition in a low disturbance environment, the natural spectrum is devoid of any significant peaks near the fundamental frequency, therefore ensuring no narrow-band environmental emissions are affecting the shear layer transition process. Figures A.2a and A.2b show the spectra for the tonal and broadband excitation cases, respectively. The results demonstrate that any given excitation is composed of only its intended frequencies and do not excite any resonant modes in the test facility. In order to facilitate proper comparison between tonal and broadband excitation cases, care was taken to ensure equivalent acoustic energy levels within the unstable frequency band of the natural flow, $10.4 \leq St_c \leq 20.8$. A measure of such energy is the SPL for a given case computed within the unstable frequency band. For both excitation types considered, the same excitation amplitudes, in terms of SPL, were investigated: 89.5, 90.4, 97.2, and 94.9 dB. The cases studied and their characteristic SPLs are summarized in Table A.2.

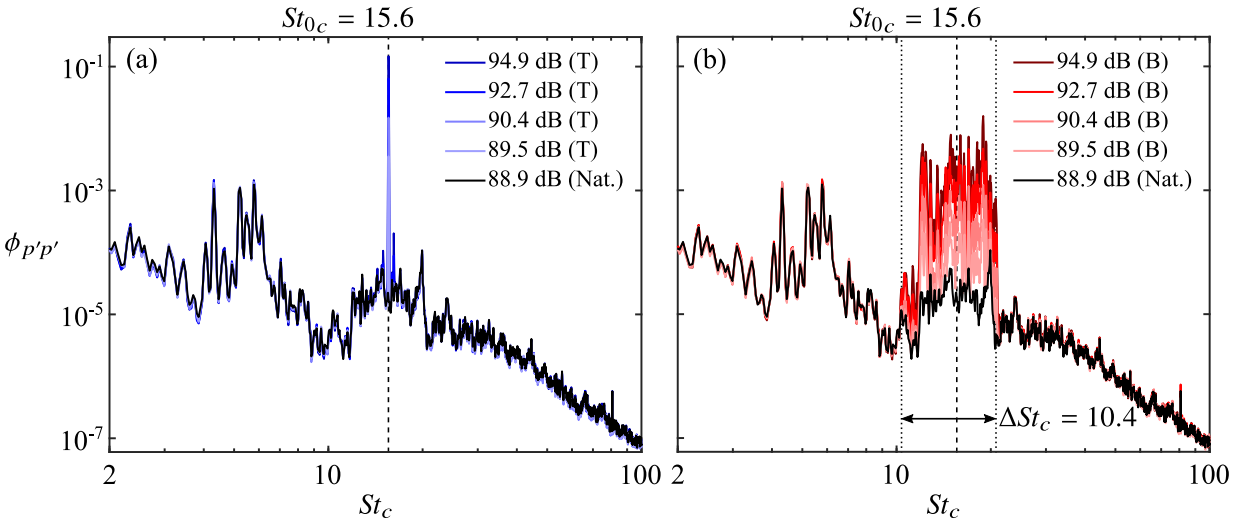

Figure A.2: Spectra of fluctuating surface pressure measured near the natural separation point for (a) tonal and (b) broadband excitation.

Table A.2: Investigated sound pressure levels. All SPLs calculated within $10.4 \leq St_c \leq 20.8$.

Case	SPL [dB]				
Natural	88.9	–	–	–	–
Tone (T)	–	89.5	90.4	92.7	94.9
Broadband (B)	–	89.5	90.4	92.7	94.9

A.3 Results

The results presented herein pertain to experiments performed at an angle of attack of 4 degrees and a chord Reynolds number of 125 000. For these conditions, the effects of tonal and broadband acoustic excitation on the transition process within a separation bubble are considered.

A.3.1 Time-Averaged Flow Field

Figure A.3 depicts the effect of excitation of the time-averaged velocity field characteristics of the separation bubble. The mean outline of the separation bubble is identified using the locus of zero streamwise velocity points [55], and is used to estimate the separation (x_s) and reattachment (x_r) points, in addition to the maximum bubble height (y_h) and its streamwise location (x_h). The uncertainties in determining x_s, y_h, x_h, and x_r from the $\overline{u} = 0$ streamline are indicated by the dotted lines in Fig. A.3, which are determined by propagating the PIV random error estimates and the uncertainty in locating the airfoil surface through the determination of these locations [158].

The mean streamwise velocity contours in Fig. A.3 show the presence of a separation bubble that extends from $x_s/c = 0.352 \pm 0.027$ to $x_r/c = 0.565 \pm 0.009$ and reaches its maximum height at $x_h/c = 0.514 \pm 0.005$ for the natural case. Reverse flow is present near the airfoil surface within

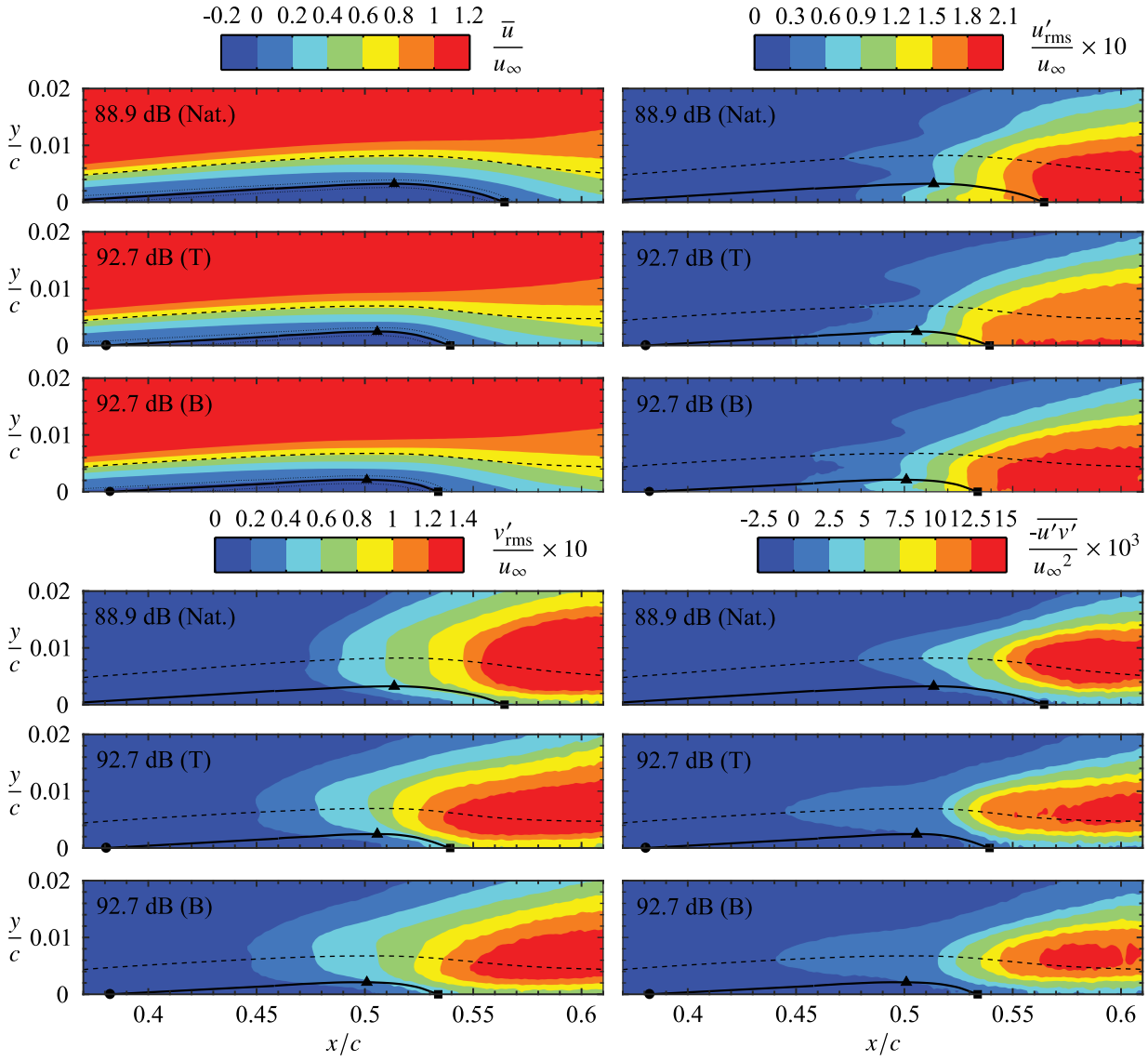

Figure A.3: Mean ($\overline{u}$) and rms (u'_{rms}, v'_{rms}) fluctuating velocity contours, and Reynolds shear stress ($\overline{u'v'}$) contours. Solid lines mark the $\overline{u} = 0$ streamlines, whose uncertainty limits are indicated by the dotted lines. Circle, triangle, and square markers denoted mean separation, maximum bubble height and reattachment points, respectively. Dashed lines indicate displacement thickness.

the separation bubble, and the maximum reverse flow velocity across all cases examined is 4% of u_∞, thus indicating the flow is only convectively unstable [2, 196, 201, 202]. In the presence of forcing, both tonal and broadband excitation cause the streamwise extent and height of the bubble to decrease. In particular, boundary layer separation is delayed, the maximum bubble height reduces, and the mean reattachment point advances upstream, as has been reported for separation bubbles subjected to locally introduced periodic excitation [135, 260, 261].

A comparison of integral shear layer parameters is presented in Fig. A.4 for all excitation cases. Regardless of the excitation type, increasing in excitation amplitude causes reductions in

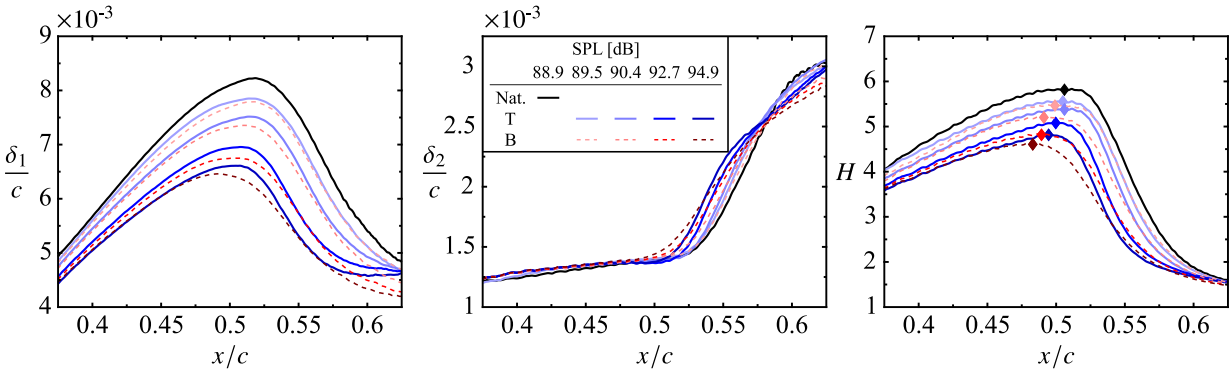

Figure A.4: Effect of excitation on integral shear layer parameters. *From left-to-right*: displacement thickness, momentum thickness, and shape factor. Diamond markers denote shape factor maxima.

the displacement thickness (δ_1). The momentum thickness (δ_2) does not change appreciably in the fore portion of the bubble, $x/c \lesssim 0.5$, where flow in the near wall region is nearly stagnant. The onset of the rapid increase in the momentum thickness is advanced upstream when the excitation is applied at higher amplitudes. The observed increase in δ_2 is due to the later stages of flow transition in the aft portion of the bubble, and it takes place where the growth in displacement thickness begins to saturate and, thus, the shape factor (H) peaks. Shape factor maxima are indicated by the diamond markers in Fig. A.4, whose streamwise location is denoted as x_H. Good agreement is found between x_H and the streamwise locations of maximum bubble height (Fig. A.3). The observed trends are in agreement with previous reports of experimentally measured integral shear layer parameters in separation bubbles [24, 260].

The root-mean-square (rms) contour plots in Fig. A.3 show the spatial amplification of velocity fluctuations in the separation bubble. In particular, the streamwise rms velocity field (u'_{rms}) shows distinct triple peak in wall-normal profiles, which are consistent with those reported in previous investigations [20, 118, 243, 260]. Upstream of mean reattachment, significant amplification follows the two near-wall peaks, indicating the growth of disturbances within the reverse flow region and the separated shear layer, with the latter following the displacement thickness. The strong amplification of wall-normal velocity fluctuations (v'_{rms}) is also observed within the separated shear layer, with maximum values attained at the wall-normal location of the displacement thickness. As expected, the streamwise development of the Reynolds shear stress ($\overline{u'v'}$) is similar to that of the velocity fluctuations, with the locus of $\overline{u'v'}$ minima following the separated shear layer closely. In the presence of excitation, the rms contours reveal shear layer disturbances reach higher amplitudes at earlier streamwise locations; more clearly seen in the v'_{rms} fields. Of particular interest is the amplitude of fluctuations reached at the bubble maximum height location. For the exemplary cases shown in Fig. A.3, and all other excitation amplitudes investigated, a relatively constant value of $u'_{\text{rms}} = v'_{\text{rms}} \approx 0.06u_\infty$ is found at the maximum height location, regardless of excitation type or amplitude. The observation is noteworthy since this location is where the momentum thickness and wall shear stress begin to increase rapidly, and the H factor reaches maximum values, indicating that the time-averaged transition takes place when velocity fluctuations in the shear layer reach a fixed critical amplitude.

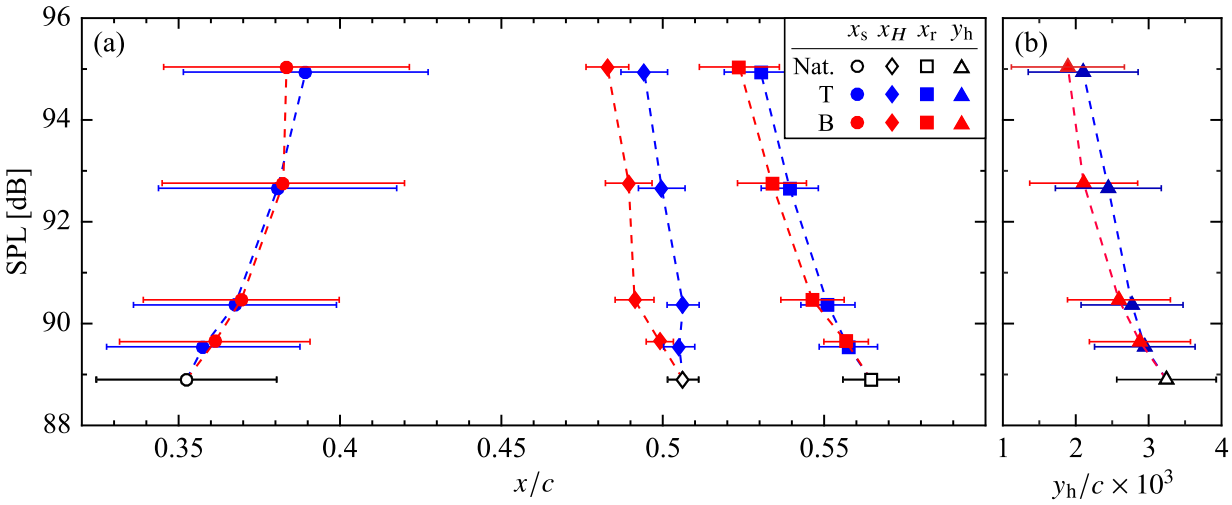

Figure A.5: Effect of excitation on (a) mean streamwise locations of separation, maximum shape factor, and reattachment, and (b) maximum bubble height. Points of equal SPL are offset slightly in the vertical direction for clarity.

The effects of excitation type and amplitude on the mean separation bubble characteristics are summarized in Fig. A.5. Regardless of the type of excitation, increasing excitation amplitude leads to a continuous reduction in the streamwise and wall-normal extents of the separation bubble. Upstream of x_H, *i.e.*, in the fore portion of the bubble, disturbance amplitudes are relatively low (Fig. A.3), and therefore their growth is expected to be well modelled by LST [20, 68, 135]. It can be conjectured that the upstream movement of the maximum shape factor is due to excitation providing higher initial disturbance amplitudes to which the LSB transition process is receptive. This assertion is examined in Section A.3.2, where linear stability analysis is performed on the experimental data, in conjunction with an assessment of the effects of non-linear interactions among disturbances. Such analysis sheds light on the differences between tonal and broadband excitation, as the results in Fig. A.5 give a preliminary indication that broadband excitation can be as effective at accelerating transition in the separation bubble as tonal excitation.

Excitation also reduces the size of the aft portion of the bubble, *i.e.* the region between x_H and x_r. However, for all cases examined, the extent of the aft portion relative to the total bubble length, $(x_r - x_H)/(x_r - x_s)$, is nearly constant at approximately 25%. Therefore, both types of acoustic excitation are effective in proportionally decreasing both the fore and aft portion of the bubble. It is in the aft portion where shear layer roll-up occurs and the role of coherent structures is important [113, 134, 261]. How these phenomena are affected by the forcing is examined in detail in Section A.3.3.

A.3.2 Growth and Interaction of Disturbances

To study the convective streamwise amplification of forced disturbances, LST is employed, which provides a model for the amplification of small amplitude disturbances in a parallel laminar flow, as discussed in Section 3.3.1. The Orr-Sommerfeld equation (Eqn. 3.6) is employed in a spatial

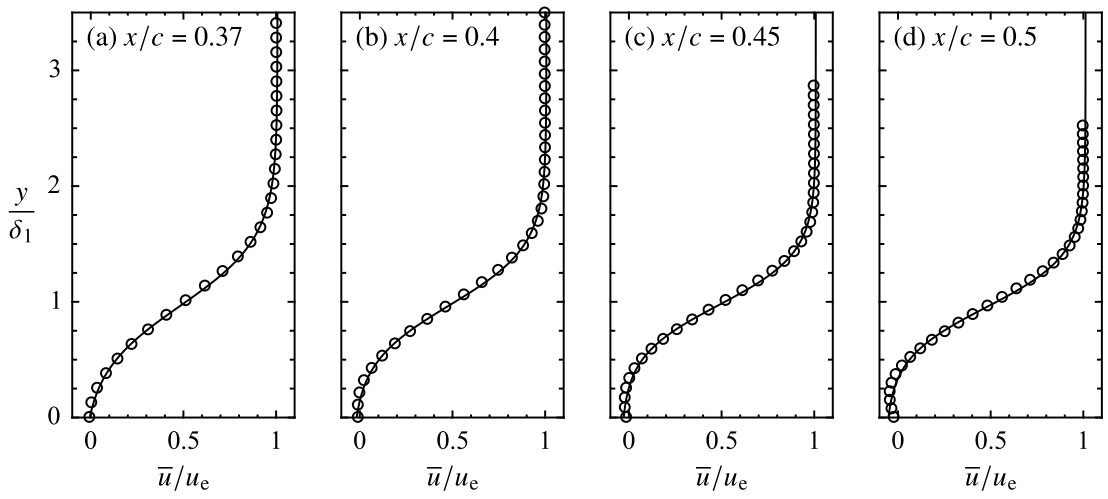

Figure A.6: Measured velocity profiles (markers) in the natural flow and corresponding hyperbolic tangent fits (solid lines, Eqn. 5.3) used in LST calculations.

formulation (*e.g.*, Ref. [215]), where Ω is prescribed and the eigenvalue problem is solved for α, thus modelling the convective amplification of single frequency disturbances. Equation 3.6 is solved numerically using Chebyshev polynomial base functions, with the companion matrix technique used to treat eigenvalue non-linearity [25]. Additional information regarding the solution method can be found in van Ingen & Kotsonis [240].

Measured mean streamwise velocity profiles at given streamwise locations serve as input to the LST calculations, therefore making the analysis local. Spatial gradients estimated from PIV measurements often have a relatively high noise level due to the finite spatial resolution of the measurement technique [248], to which LST predictions can be highly sensitive [23]. Therefore, stability analysis is performed using hyperbolic tangent fits (Eqn. 5.3) to the experimental data, which have been shown to provide reasonable stability predictions [20, 45] that are relatively insensitive to scatter in the data [23]. Exemplary velocity profiles and their corresponding fits for the natural flow conditions are shown in Fig. A.6.

For validation purposes, results from the LST predictions and the experimental data are compared for the natural case in Fig. A.7. A measure of amplitude growth is quantified from the LST results by integrating the spatial growth rates (α_i) according to Eqn. 3.7 to recover N factors. To do so, the streamwise location where the disturbance first becomes unstable (x_{cr}) must be known, which falls upstream of the PIV field of view and therefore cannot be determined directly. However, in the fore portion of the LSB, α_i may be approximated by a second-order polynomial (*e.g.*, see figure 11 from Jones *et al.* [91]). Based on this, x_{cr} can be estimated by extrapolating the curve fit to $\alpha_i = 0$. In Fig. A.7a, the experimental spectrum of wall-normal velocity fluctuations shows an amplified band of disturbances within $10 \lesssim St_c \lesssim 20$, with the highest energy content found approximately at $St_c = 15.6$, *i.e.*, the fundamental frequency. The overlaid plot of N factors shows good agreement between the LST predicted and experimental measured unstable frequency ranges, with the most unstable frequency predictions differing by approximately 17%. Such a discrepancy has been reported in similar studies [20, 259] and does not significantly impact the present investigation since here the interest lies in the relative changes in stability characteristics

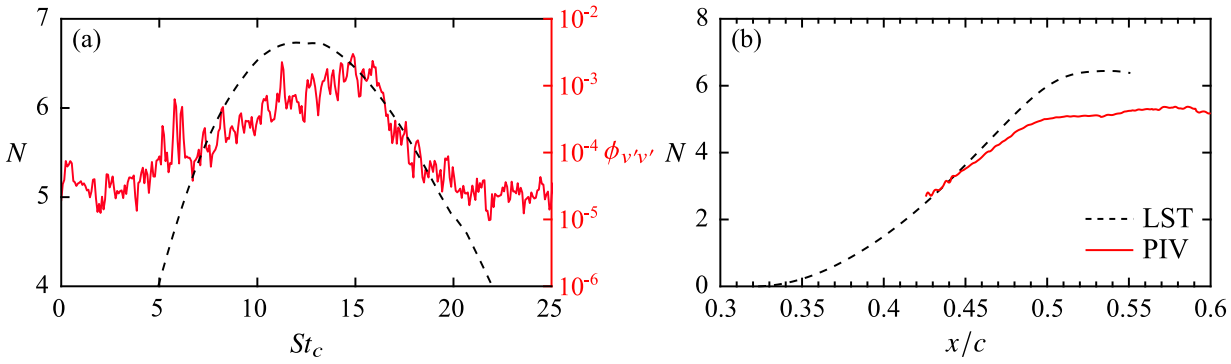

Figure A.7: Validation of LST results for the natural flow. (a) LST N factors and experimental spectrum of v' at the streamwise location of maximum bubble height. (b) LST and experimental N factors for $St_c = 15.6$.

when the flow is excited.

Figure A.7b shows a comparison of LST and experimental N factors for $St_c = 15.6$, where the measured wall-normal velocity fluctuations have been bandpass filtered to within $St_c = 15.6 \pm 0.2$ in order to compute amplification factors associated with this frequency. A direct comparison of N factors is not possible since disturbances in the experiment can only be detected well downstream of x_{cr}, where they reach measurable amplitudes. Therefore, following Schmid & Henningson [215], the amplification factors are matched at a reference location where the measured disturbance amplitude reaches $A = 0.005u_\infty$ ($x/c = 0.44$ in Fig. A.7b), thus allowing for an estimate of A_0 for a given frequency, according to Eqn. 3.7. Comparing the LST and experimental N factors reveals that the linear growth of disturbances is accurately captured within $0.42 < x/c < 0.46$ in the experiment, downstream of which disturbance growth begins to saturate and the agreement with LST deteriorates due to non-linear effects becoming significant. Similar results are also obtained for both the tonal and broadband excited cases, confirming that LST reliably predicts stability characteristics in the fore portion of the studied separation bubbles.

The changes in stability characteristics with excitation are depicted in Fig. A.8, where contours of the LST predicted spatial growth rates are presented. As per the spatial formulation employed, negative values of α_i correspond to convectively amplified disturbances. For the natural case, downstream of separation the frequency of the maximal growth rates increases to a value of approximately $St_c = 13.6$ reached at $x/c = 0.45$, after which the frequency decreases toward the maximum bubble height location. It is in this region where amplification of disturbances is detected in the experiments and agrees well with the LST predictions (Fig. A.7b). For both types of excitation considered, their application results in significant decrease in the magnitude of growth rates, as the maximum growth in the natural flow, $-\alpha_i c \approx 52$, decreases by approximately 30% for both excitation cases shown (Figs. A.8b and A.8c). A less significant effect is seen on the frequency of maximum growth rates, as both tonal and broadband excitation reduce this frequency to approximately $St_c = 13.1$ at $x/c = 0.42$, *i.e.*, a reduction of approximately 4%. The more significant effect of excitation on maximum growth rate than the corresponding frequency is also reported in Refs. [134, 135, 261], and is attributed to the mean flow deformation (Fig. A.3). As excitation reduces the size of the separation bubble, the region of disturbance growth (*i.e.*, the

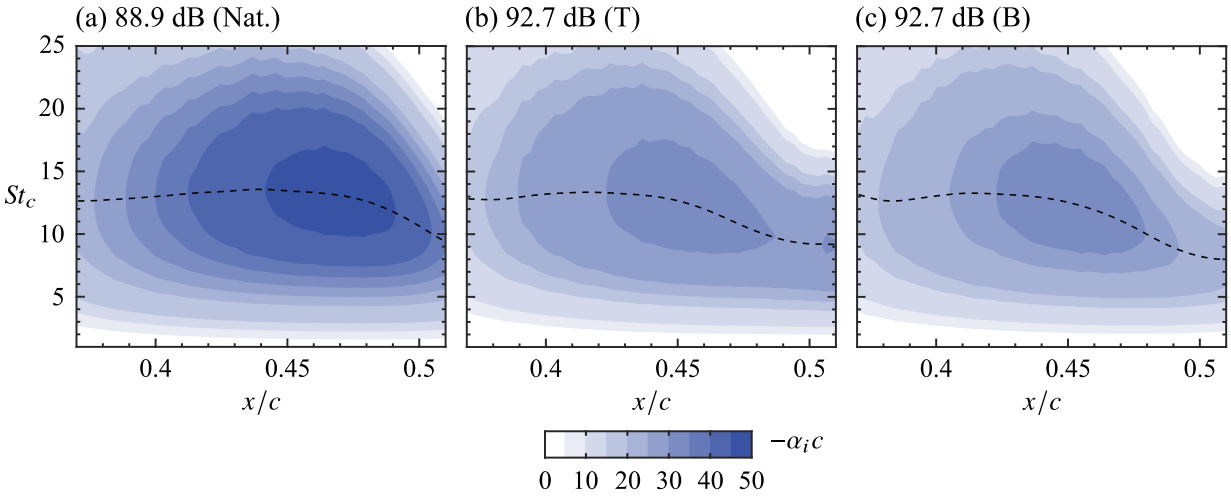

Figure A.8: Contours of LST predicted spatial growth rates. Dashed lines indicate loci of growth rate maxima.

separated shear layer) is brought closer to the wall, which has a damping effect [47].

As established throughout Section A.3.1, tonal and broadband excitation at equivalent SPLs (*i.e.*, equivalent input energy levels) produce comparable changes in the mean flow fields (*e.g.*, Figs. A.3 and A.5), despite tonal excitation providing a higher initial disturbance amplitude at or close to the frequency at which the LSB is most unstable (Fig. A.8). One hypothesis for this result is that, as seen in Fig. A.8, excitation modifies the frequency of most unstable disturbances, albeit minimally, and so the tonal excitation becomes less effective, while the broadband case is able to excite this new most unstable frequency. This hypothesis is examined in Fig. A.9, where LST predicted N factors and disturbance amplitudes are compared for equivalent tonal and broadband excitation cases.

Consistent with the closely matching spatial growth rates for the considered excitation cases (Figs. A.8b and A.8c), the amplification curves in Fig. A.9a show nearly equivalent N factors for frequencies near and below the tonal excitation frequency, $St_{0_c} = 15.6$. Using these LST N factors, the streamwise growth in disturbance amplitude is determined using Eqn. 3.7 and initial disturbance amplitudes, which are estimated by matching LST and experimental N factors (as outlined by the discussion of Fig. A.7b). The resulting LST predicted disturbance amplitudes (Fig. A.9b) show, as expected, the highest initial disturbance amplitude for tonal excitation (*cf.* Fig. A.2), which, coupled with its N factor curve, results in the tonally excited disturbance outgrowing all disturbances in the broadband case. Thus, according to LST and the theory of transition onset at some critical disturbance amplitude [224, 239], tonal excitation should lead to earlier transition, which is clearly not the case in the experimental data (Figs. A.3–A.5).

It is evident that the assumptions inherent to LST render the technique unable to accurately model the entire transition process. To assess the degree to which disturbance interaction and competition impacts the studied transition processes, spatial growth rates are estimated from the experimental measurements. Such estimates are made by extracting the fluctuating wall-normal velocity signals along $y = \delta_1$, and then band-pass filtering the time signals via integration of their

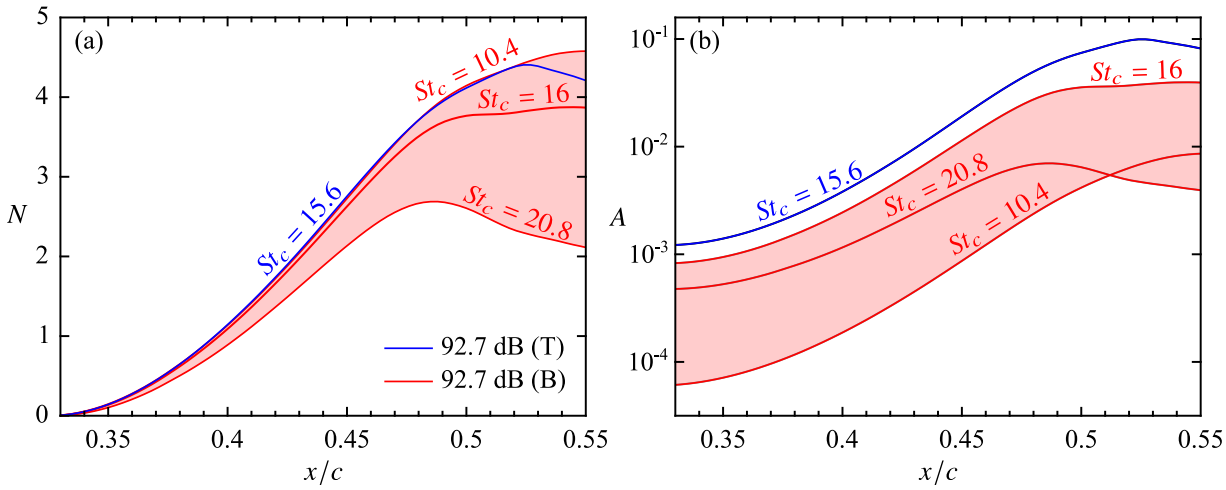

Figure A.9: Comparison of LST predicted (a) N factors and (b) disturbance amplitudes for frequencies within the excitation bands. Initial disturbance amplitudes are estimated through matching LST and experimental N factors (Fig. A.7b). Curves for all broadband excited frequencies fall within the red shaded regions.

frequency spectra using a band of width $St_c = \pm 0.2$ centred at the desired frequency. The resulting spatial curves are then smoothed using a sliding kernel with width $0.03c$, and the local spatial growth rates are determined from the local curve slopes. The results are presented in Fig. A.10 for the natural, tonal and broadband cases, where overall growth rate magnitudes compare favourably with the LST predictions (Fig. A.8). For the natural case (Fig. A.10a), amplification of disturbances is first detected at approximately $x/c = 0.41$ and at the fundamental frequency, followed by disturbances within the unstable frequency band, $10 \lesssim St_c \lesssim 20$, amplifying farther downstream. Near the streamwise location of maximum shape factor, there is rapid growth at all measurable frequencies, which is indicative of the onset of transition. A similar progression is seen for the broadband case (Fig. A.10c), except that earlier amplification of disturbances is detected due to the excitation. Most notably, the rapid emergence of growth at all frequencies shifts upstream to approximately $x/c = 0.49$, consistent with the location of shape factor maximum. For the case of tonal excitation (Fig. A.10b), a drastic change in the growth of disturbances is observed, as excitation at $St_{0c} = 15.6$ effectively confines growth to only that frequency from the beginning of the measured domain to $x/c \approx 0.47$. Growth of disturbances over a wide band of frequencies only begins to occur at $x/c = 0.5$, which is where the process takes place for the natural case, despite the drastically different energy input levels (Fig. A.2).

It can be concluded from Fig. A.10b that the strong amplification of the tonally excited disturbance damps growth of all other disturbances, thus affecting the transition process. This is examined further in Fig. A.11, where experimentally determined perturbation modes for frequencies within the naturally unstable frequency band are presented and compared to LST predicted growth rates. For the natural case (Fig. A.11a), good agreement is found for frequencies $St_c \leq 15.6$ where disturbance amplification is first detected, $0.43 \lesssim x/c \lesssim 0.46$. Thus, the growth of these disturbances is independent and is not affected by non-linear interactions until downstream of $x/c \approx 0.46$. The same can be said for the broadband excited flow (Fig. A.11c), except here

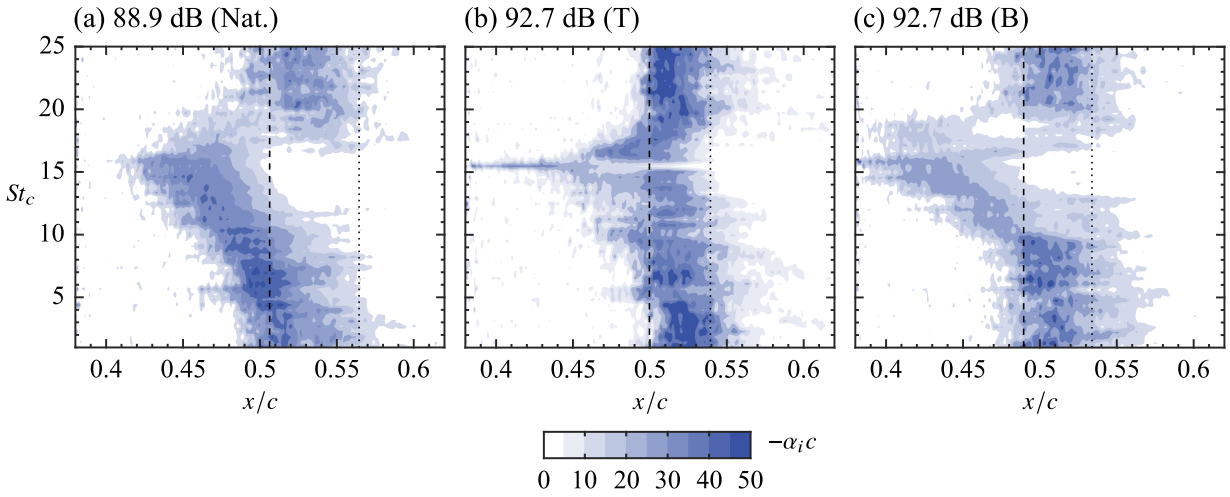

Figure A.10: Contours of experimentally measured spatial growth rates of frequency filtered wall-normal disturbances in the separated shear layer ($y = \delta_1$). Dashed and dotted lines denote x_H/c and x_r/c, respectively.

agreement with LST is found across all frequencies within the excitation band. The agreement with LST at the higher frequencies, $St_c > 15.6$, is attributed to the broadband excitation providing disturbances of significant amplitude at these frequencies for amplification. When the flow is excited tonally (Fig. A.11b), the damping effect on the growth of disturbance all frequencies other than that of the excitation becomes immediately apparent, as only the excited frequency grows according to its LST predictions, while the growth at all other frequencies is delayed. Moreover, the agreement between LST predictions and experimental measurements for the tonal excitation frequency persist further downstream, where non-linear interactions resulted in decreased growth for the natural and broadband excitation cases.

The observed differences in the development of disturbances can be explained through the weakly non-linear disturbance growth model proposed by Landau & Lifschitz [117] and further developed by Stuart [231]:

$$\frac{\mathrm{d}\,|A_1|^2}{\mathrm{d}x} = 2\,|A_1|^2\left(-\alpha_i + \sum_{j=1}^{n} \ell_j\,|A_j|^2\right), \tag{A.1}$$

which describes the spatial amplification of a disturbance of amplitude A_1 as a result of its initial linear growth rate, α_i, and the non-linear effects imposed by self-interaction ($j = 1$) and interaction with disturbances of all other frequencies ($j \neq 1$). The Landau coefficients (ℓ_j) describe the nature of the interactions, with $\ell_j > 0$ and $\ell_j < 0$ corresponding to non-linear effects resulting in additional amplification or damping, respectively, while linear theory is recovered when $\ell_j = 0$. Drazin & Reid [48] note that, for external flows over bodies, the Landau coefficients are generally negative and thus non-linear effects serve to damp disturbance growth. This is corroborated by the present results, as all instances of good agreement between LST and experimental measurement are followed by a damping of the experimentally measured disturbance, leading to growth saturation

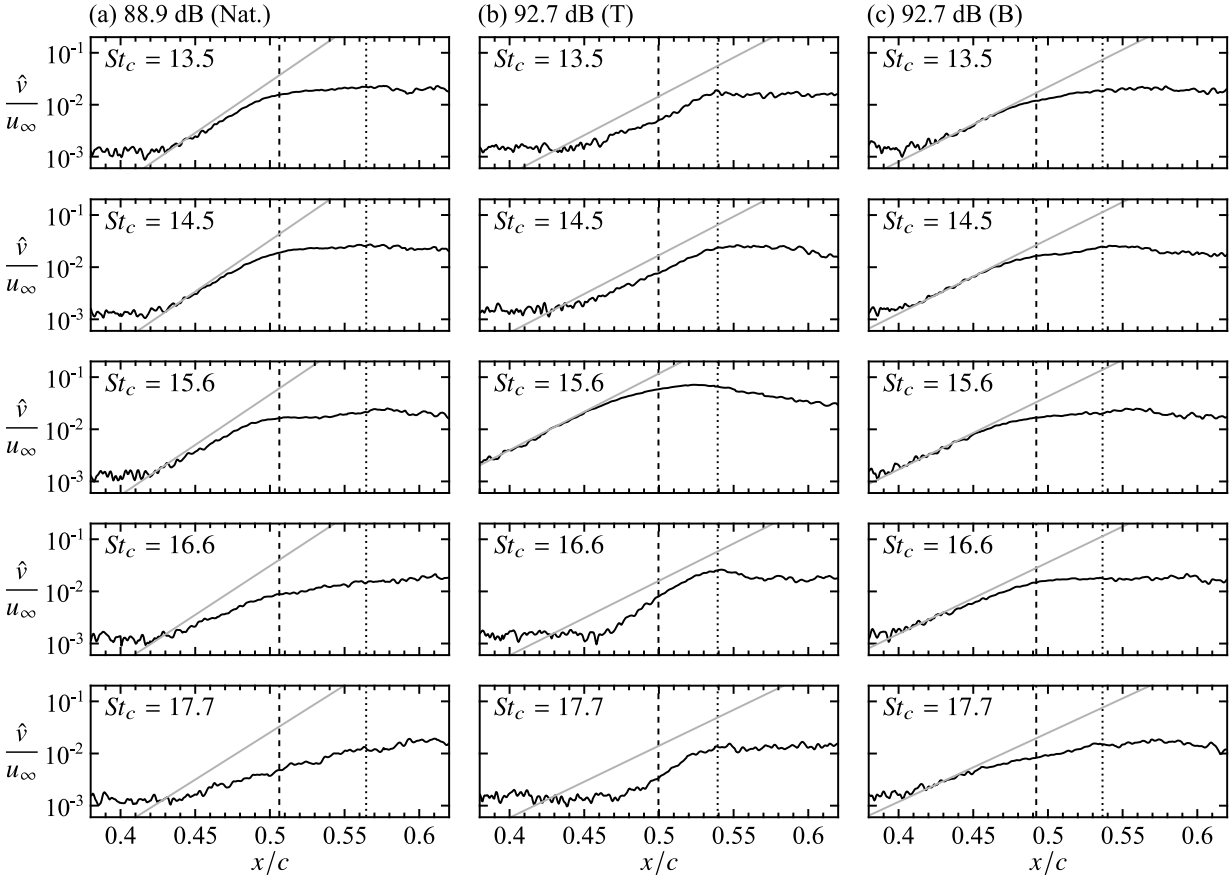

Figure A.11: Growth of frequency filtered wall-normal disturbances within the separated shear layer ($y = \delta_1$). Grey lines indicate LST predicted growth rates at $x/c = 0.43$. Dashed and dotted lines denote x_H/c and x_r/c, respectively.

soon after (*e.g.*, Figs. A.7b and A.11). Furthermore, in addition to the Landau coefficients, Eqn. A.1 highlights that the degree to which disturbances are damped depends on the amplitude of the disturbance with which the interaction is taking place. Therefore the presence of a relatively high amplitude disturbance is expected to damp disturbance growth at all other frequencies. Such is the case observed in Figs. A.10b and A.11b for the tonal excitation case, while for the broadband case (Figs. A.10c and A.11c) perturbation amplitudes are more moderate, and so all unstable disturbances grow initially at their LST predicted rates, followed by non-linear damping taking place farther downstream.

The non-linear interactions and their impact on transition reported here are, to the authors' knowledge, have not been previously reported for separation bubbles. However, similar observations have been reported for boundary layers [95] and free shear layers [154, 155]. Specifically, Miksad [155] notes that when exciting free shear layers using two strong acoustic tones, the competing growth of the two instabilities leads to reduced growth rates in comparison to the single excitation cases. Furthermore, excitation at multiple frequencies was found to promote the redistribution of fluctuating energy to all possible frequencies, which Miksad linked to a faster increase in the shear layer momentum thickness, and hence an accelerated transition of the shear layer. Similar

reports are made by Kachanov *et al.* [95], who excited multiple TS modes in a laminar boundary layer. In the present investigation, tonal and broadband excitation lead to strikingly different transition processes but can lead to very similar mean effects on the flow field (Figs. A.3 and A.5). Further, transition in a laminar separation bubble can be either dominated by a large amplitude disturbance of a single frequency which damps the growth of all other disturbances (Figs. A.10b and A.11b), or by a band of disturbances of moderate and equal amplitudes, that all initially grow in accordance with linear theory (Fig. A.11c). For both cases, a rapid redistribution of spectral energy to all frequencies follows (Figs. A.10b and A.10c), with this phenomena occurring earlier for the broadband case, despite equal energy inputs. The 'broadband transition route' is also representative of the natural transition case (Figs. A.10a and A.11a).

Important ramifications regarding the comparison of LST predictions with experimental and numerical results are made clear from the findings of this investigations. Numerous authors have noted this agreement to be surprisingly good (*e.g.*, Refs. [135, 136, 261]), with the valid region extending until very close to where disturbance growth saturates [118], despite the relatively large amplitudes of the instability waves in this region. Furthermore, and perhaps counter-intuitively, it has been reported that the agreement improves with increasing disturbance input levels [260]. In general, these assertions are supported by the findings presented here (Fig. A.11), with the crucial caveat being that the degree to which LST and experimental/numerical results agree is entirely dictated by the relative importance of non-linear effects for the particular disturbance mode being considered. For example, when all unstable disturbance amplitudes are small, and thus non-linear effects are not important, excellent agreement is found with LST until disturbance amplitudes become more moderate (*i.e.*, the broadband excitation case, Fig. A.11c). On the other hand, if one disturbance mode is preferentially excited, then its development dominates all others via non-linear damping, while experiencing strong linear growth of its own (Fig. A.11b). Thus, it can be conjectured that if only one dominant disturbance mode is present in the flow, then the non-linear effects imposed by the other, relatively weak, disturbances are not significant and so the dominant mode grows in strong accordance with LST predictions.

A.3.3 Coherent Structures

Thus far, mean features and disturbance development in the separation bubble have been characterized (Sections A.3.1 and A.3.2, respectively). The link between these two facets of the flow is established in this section, as the coherent structures that manifest from the disturbances are examined and their role in producing the observed mean flow field and its statistics is elucidated.

Flow development in the aft portion of the separation bubble for the natural, tonal, and broadband cases is depicted in Fig. A.12 using instantaneous contours of spanwise vorticity (ω_z). Contours of the λ_2-criterion [88] are added to aid in identifying coherent structures, in addition to dashed lines to assist in tracking individual structures between frames. The spacing and slope of these lines give an indication of the streamwise wavelength (λ_x) and convective velocity of the structures, respectively. For all cases, the flow development is characterized by the roll-up of the separated shear layer into vortices upstream of the maximum shape factor location ($x_H/c = 0.51$ for the natural case). These shear layer vortices then convect downstream and undergo deformations within the vicinity of mean reattachment ($x_r/c = 0.56$ for the natural case),

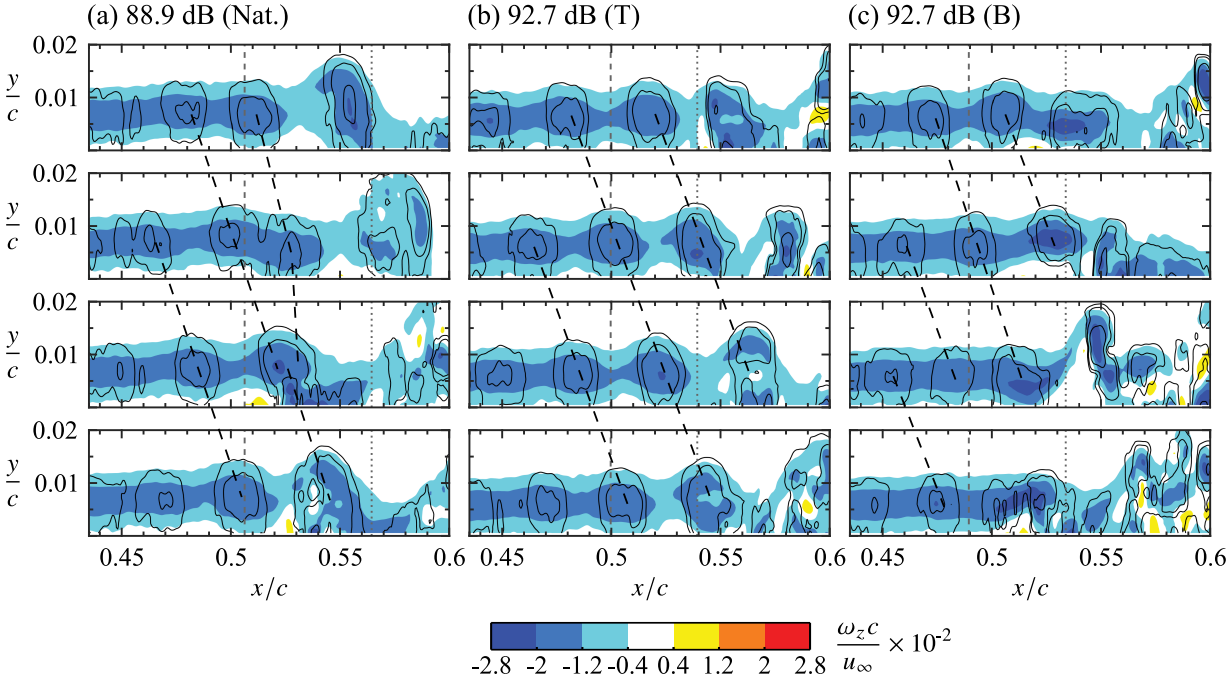

Figure A.12: Sequences of instantaneous contours of spanwise vorticity. Consecutive frames are separated by $t_c^* = 3.8 \times 10^{-2}$. Black lines indicate λ_2-contours [88]. Black dashed lines trace the same vortices in a sequence. Grey dashed and dotted lines denote x_H/c and x_r/c, respectively.

leading to their breakdown to smaller scales. Both the natural and broadband excited flows are quasi-periodic (Figs. A.10a and A.10c), and so significant temporal variability is expected in the flow development. An example of such an occurrence is shown for the natural case (Fig. A.12a), where two vortices develop with sufficiently different convective velocities that they coalesce to form a merged structure. The process may also occur for the broadband excited flow, however, identification of clearly merged structure is difficult due to the earlier onset of breakdown. Vortex merging in naturally developing separation bubbles has also been observed by Kurelek *et al.* [113] and Lambert & Yarusevych [115].

From Fig. A.12, it is clear that excitation significantly affects flow development, as both tonal and broadband excitation cause vortex formation at earlier streamwise positions, consistent with the upstream shift in x_H and earlier detectable disturbance amplification (Fig. A.10). However, the mean convective velocity and streamwise wavelength of the shear layer vortices in the excited flows (Figs. A.12b and A.12b) remain largely unchanged compared to those of the natural case (Fig. A.12a), which is attributed to the close matching of the excitation frequency and the naturally unstable frequencies. Estimating the average streamwise wavelength of the structures from the spacing of the black dashed lines in Fig. A.12 gives a value of $\lambda_x/c \approx 0.04$. By promoting the development of a single harmonic disturbance (Fig. A.11b), it is clear that tonal excitation locks the vortex formation process to the excitation frequency, thus resulting in significantly reduced temporal variability in both the convective velocity and streamwise wavelength of the shed structures. As such, vortex merging is not observed throughout the entire recorded sequence for the presented tonal excitation case. Similar observations have been made for free shear layers forced

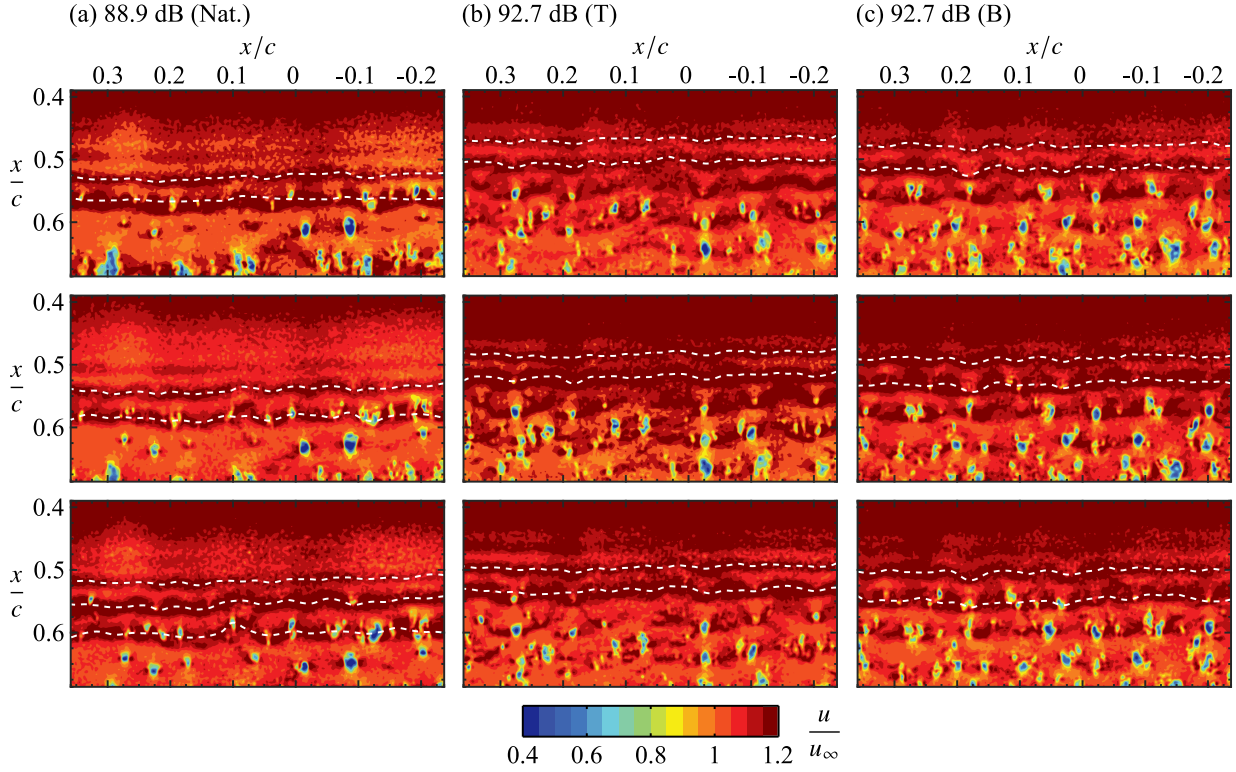

Figure A.13: Sequnces of instantaneous contours of streamwise velocity. Flow is from top-to-bottom. Consecutive frames are separated by $t_c^* = 2.5 \times 10^{-2}$. White dashed lines indicate smoothed spline fits to the centre of selected structures.

at their 'fundamental' vortex shedding frequency [73, 81]. The coherence of the tonally excited structures also appears to be increased in comparison to the broadband case, as the structures in Fig. A.12b tend to persist further downstream than those seen in Fig. A.12c. This assertion will be examined in detail through the analysis that follows in this section.

PIV measurements completed in the top-view configuration (Fig. A.1b) allow for quantitative assessment of both the streamwise and spanwise development of the shear layer vortices. The measurement plane was positioned such that it passed through the top-halves of the spanwise rollers, thus allowing for their identification as periodic spanwise bands of high streamwise velocity in the planar fields, as seen in Fig. A.13.

Flow is from top-to-bottom in Fig. A.13 and smoothed spline fits are added to the centre of selected vortices to aid in tracking their development. Spanwise coherent structures are first identifiable near the maximum shape factor location ($x_H/c = 0.51$ for the natural case), consistent with where roll-up is observed in the side-view measurements (Fig. A.12). Shortly downstream of roll-up, the structures develop spanwise deformations within the vicinity of the mean reattachment point ($x_r/c = 0.56$ for the natural case). These deformations intensify as the structures continue to convect downstream, which eventually leads to the emergence of localized vortex breakup, *i.e.*, the regions of low velocity fluid that appear over the span of the vortex filaments at $x/c \gtrsim 0.55$ throughout Fig. A.13. The formation of spanwise uniform shear layer vortices is consistent with

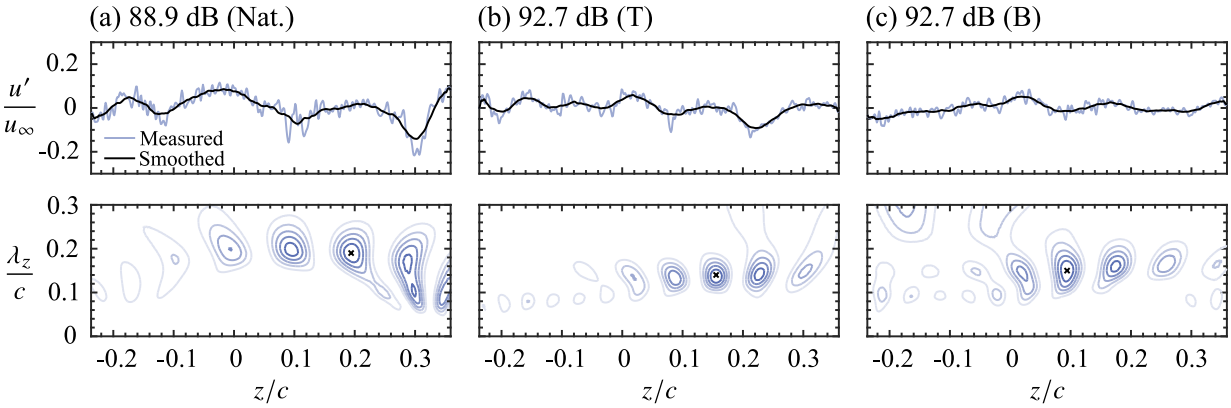

Figure A.14: *First row:* Exemplary fluctuating streamwise velocity sampled across the span at x_H. *Second row:* Corresponding wavelet coefficients. Maximum wavelet coefficient denoted by $\times$ marker.

the observations of Refs. [92, 137, 170], which according to Michelis *et al.* [153] is an indication of the relative dominance of normal over oblique modes. Furthermore, the development of spanwise deformations leading to localized regions of vortex breakup is consistent with the vortex breakup mechanism for an LSB proposed by Kurelek *et al.* [113].

While general trends in spanwise flow development are similar between the natural and excitation cases, the upstream shift in the roll-up location due to excitation, identified previously in the side-view measurements (Fig. A.12), is also clearly seen in Fig. A.13. Furthermore, both types of excitation appear to modify the predominant spanwise deformation wavelength(s) of the vortex filaments, as a visual comparison between the cases presented in Fig. A.13 suggests that spanwise deformations of shorter wavelengths tend to initially develop when the flow is excited. To affirm this observation, spanwise wavelength characteristics are quantified through wavelet analysis (Section 3.3.3), which is preferred over spatial Fourier analysis due to the limited spanwise extent of the field of view. From the top-view PIV measurements, streamwise fluctuating velocity signals are extracted at several streamwise locations, smoothed using a spatial kernel of width $0.02c$, and wavelet coefficients are calculated using the Morlet wavelet [43]. Exemplary instantaneous spanwise distributions of velocity fluctuations and their corresponding wavelet coefficients are presented in Fig. A.14. For a given time instant, the predominant spanwise wavelength is estimated from the maximum wavelet coefficient, with the process repeated for all time realizations and statistical samples obtained as a result. The data is presented using histograms in Fig. A.15 at three reference streamwise locations. For the natural case (Fig. A.15a) at x_H/c, the distribution of λ_z is nearly symmetric about a mean value of $\overline{\lambda_z}/c = 0.19$, with predominant wavelengths concentrated within $0.08 \lesssim \lambda_z/c \lesssim 3.2$, which is in good agreement with the visualized structures in Fig. A.13. Furthermore, comparing the predominant spanwise and streamwise wavelengths of the structures gives a range of $2 \lesssim \lambda_z/\lambda_x \lesssim 7$, which is consistent with the results of previous investigations [113, 137, 153].

From Fig. A.15a, the mean spanwise deformation wavelength shifts to lower values as the vortices convect from the maximum shape factor location to the mean reattachment point and beyond it, reaching a value of $\overline{\lambda_z}/c = 0.11$ at the furthest downstream station. This shift is

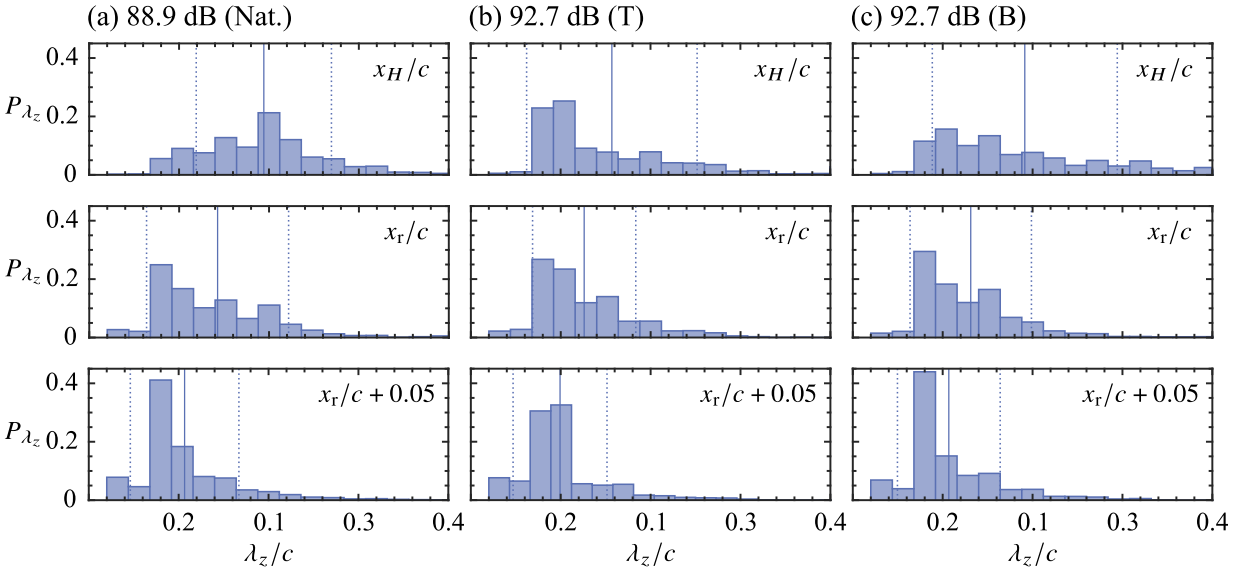

Figure A.15: Spanwise wavelength probability distributions determined from spatial wavelet analysis (Fig. A.14). Dotted lines indicate standard deviation from the mean (solid line).

associated with the aforementioned localized vortex breakup regions seen in Fig. A.13a, with the low velocity zones being separated by a spanwise spacing of about $0.1c$. In Section A.3.2, it was established that disturbances in the broadband excited flow grow in an accelerated, yet similar manner to the natural case, which is also reflected in the development of the spanwise deformations, as Fig. A.13c shows that initial deformations occur over a relatively broad range of wavelengths centred at $\lambda_z/c \approx 0.2$, which shifts to $\lambda_z/c \approx 0.1$ as the vortices convect downstream and begin to break down. In contrast, when the flow is subjected to tonal excitation (Fig. A.13b), at x_H/c there is a more pronounced mean tendency in the distribution toward $\lambda_z/c = 0.1$, indicating that tonal excitation promotes deformations of this wavelength. Thus, tonal excitation is shown to organize shear layer vortex development, not only by locking the shedding frequency and streamwise wavelength (Fig. A.12b), but also by reducing variability in spanwise deformations, promoting a spanwise wavelength equal to approximately two times the streamwise wavelength of the structures.

To further analyze the effect of excitation on coherent structure characteristics, POD analysis is performed on the top-view (x–z plane) measurements using the snapshot method [223]. Figure A.16 presents the first four most energetic spatial modes coloured by the streamwise component ($\gamma_u^{(n)}$). From Fig. A.16 it is clear that all modes are paired, *i.e.*, modes 1 and 2, and modes 3 and 4. A distinct streamwise phase offset of $\pi/2$ can be seen for each mode pair, which is typical for a number of different flows involving propagating coherent structures [124, 241, 244, 260]. For all cases, the two most energetic modes are associated with the spanwise shear layer vortices, as these mode shares several key features with previous results, namely, a consistent streamwise wavelength (cf. Fig. A.12), and spanwise uniform structures that form further upstream when excited (cf. Fig. A.13). The associated temporal coefficients, not shown for brevity, also feature dominant periodicity at the shedding frequency of the rollers. It is instructive to compare the

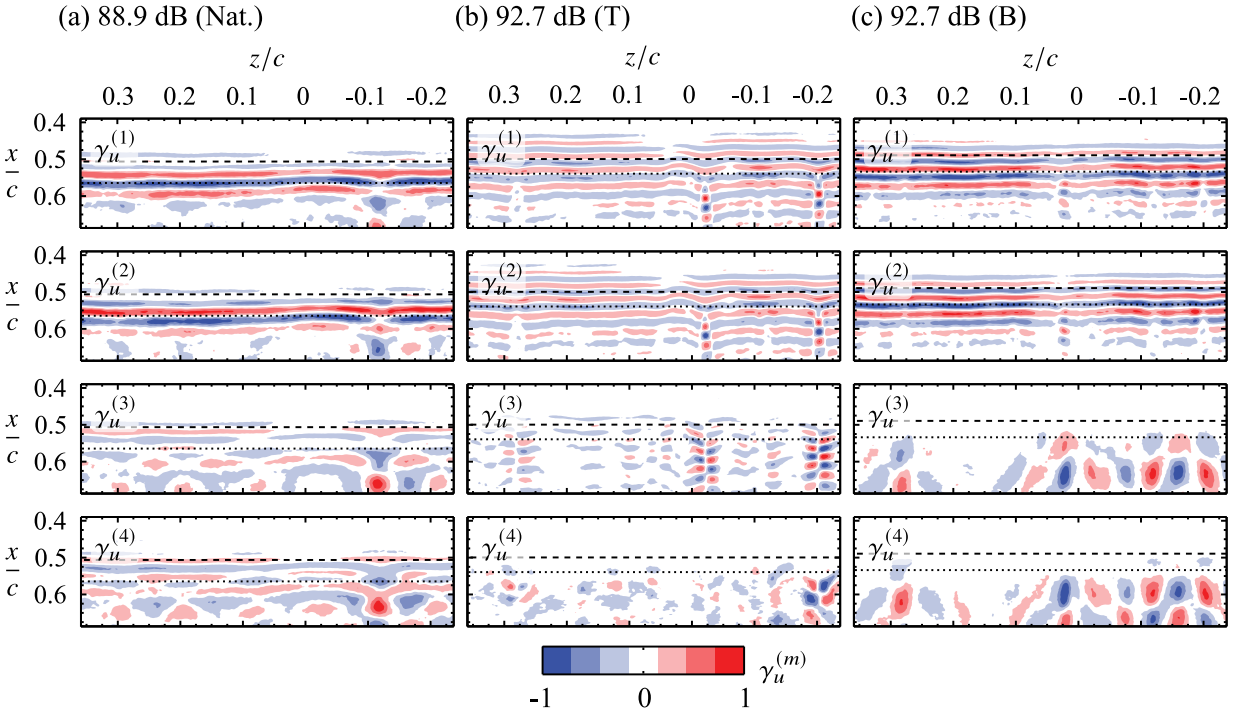

Figure A.16: Streamwise component of the normalized POD spatial modes. Dashed and dotted lines denote x_H/c and xr/c, respectively.

$\gamma_u^{(1)}$ and $\gamma_u^{(2)}$ modes for the tonal and broadband cases in Figs. A.16b and A.16c, respectively. Such a comparison reveals that while the structures form at similar streamwise locations, they persist further downstream in the presence of tonal excitation, presumably since tonal excitation specifically targets this mode while the broadband excitation does not. This is further supported through the examination of the relative (E_R) and cumulative (E_C) modal energy distributions, presented in Fig. A.17. Consistent with its excitation input spectrum (Fig. A.2b), broadband excitation leads to a small increase in the relative energy of the first two modes (Fig. A.17a), and a comparable cumulative distribution over the first twenty modes to the natural case (Fig. A.17b). In contrast, tonal excitation leads to an increase of approximately 125% in the most energetic mode pair, which is to be expected given that tonal excitation specifically targets these modes.

Analysis of the top-view measurements revealed that spanwise deformations with a wavelength of $\lambda_z/c \approx 0.1$ tend to develop in the vortex filaments in the aft portion of the bubble and downstream of mean reattachment for all cases (Figs. A.13 and A.15). Added insight into these deformations is provided by the POD results, as structures with a corresponding spanwise wavelength are evident in the POD spatial modes (*e.g.*, modes 3 and 4 in Fig. A.16). The capture of these structures by the POD analysis indicates that these deformations tend to occur repeatedly with prevalence at some spanwise locations. A similar observation is made in the experiments of Michelis *et al.* [152] (see their Fig. 3b), who studied a separation bubble formed on a flat plate. In theirs and this experiment, careful attention was paid to the model and facility to prevent triggering any spanwise modulation of disturbances, however, whether the occurrence of these spanwise deformations at these preferred spanwise locations is a result of the underlying physics or is due to some minute imperfection

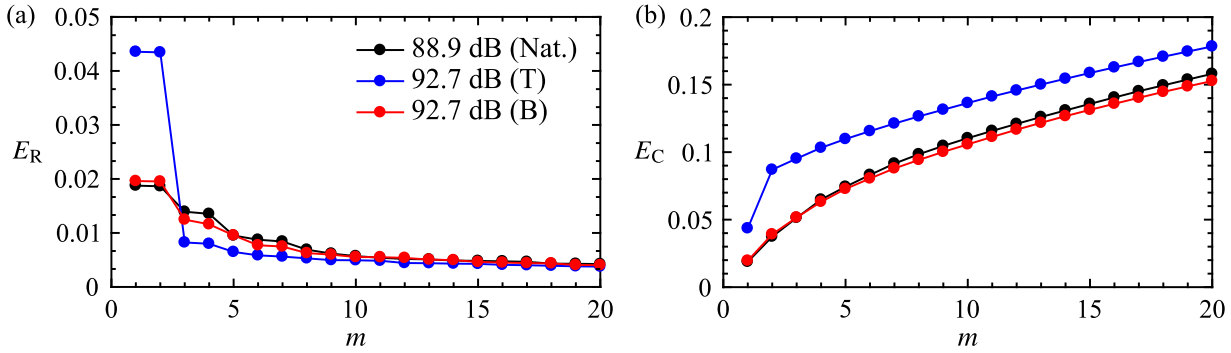

Figure A.17: Effect of excitation on POD (a) relative and (b) cumulative modal energy distributions.

in the experimental setup is unclear. Nevertheless, it is apparent that such repeated spanwise deformations associated with some preferential wavelength are inherent to the development and breakup of the main shear layers rollers.

A.4 Concluding Remarks

The present investigation examined the effects of tonal and broadband acoustic excitation on flow development and transition in a laminar separation bubble. The bubble was formed on the suction side of a NACA 0018 airfoil in a closed-loop wind tunnel facility at a Reynolds number of 125 000 and an angle of attack of 4°. Disturbances were introduced in a controlled manner from an external source to decouple the interdependence of flow development and acoustic emissions inherent to airfoil self-noise production. The flow field was assessed via time-resolved, two-component PIV. Two separate configurations were employed to evaluate streamwise and spanwise aspects of the flow development. The results show that, for equivalent energy input levels within the naturally unstable frequency band, tonal and broadband excitation produce similar changes in the mean separation bubble topology. In particular, both result in delayed boundary layer separation, a reduction in the maximum bubble height, and upstream advancement in the shape factor maximum and mean reattachment locations.

Local linear stability analysis is shown to accurately model incipient disturbance growth for all cases examined. Consistent with previous investigations [134, 135, 261], the LST results show that excitation significantly reduces disturbance growth rates, while only slightly modifying the frequency of the most amplified disturbances. Despite this modification, according to the LST predictions, the most amplified mode in the presence of tonal excitation should outgrow all broadband excited individual modes and thus lead to earlier transition for the former case, which is in contradiction with the experimental observations. This is shown to be the result of non-linear effects. Specifically, in the case of tonal excitation, transition is dominated by the amplification of a single excited wave, which grows in strong accordance with linear theory and significantly damps the growth of all other disturbances as a result of its relatively high amplitude. In contrast, disturbance amplitudes across the entire unstable frequency range are more moderate for the natural and broadband excited flows, and so all unstable disturbances initially grow in accordance

with linear theory. For all cases, a rapid redistribution of perturbation energy to a broad range of frequencies follows, with the phenomenon occurring earliest for the broadband case and at more or less equivalent streamwise locations for the tonal and natural cases, despite drastically different input energy levels.

The significance of non-linear disturbance interactions reported herein have important ramifications regarding the comparison of LST predictions with experimental and numerical results. Several authors have noted this agreement to be surprisingly good [118, 135, 136, 261] even in flow regions where instability waves attain relatively large amplitudes. In general, these assertions are supported, with the crucial caveat being that agreement is entirely predicated on the relative importance of non-linear effects for the particular disturbance mode being considered. For example, when all unstable disturbance amplitudes are small and thus non-linear effects not important, excellent agreement is found with LST until disturbance amplitudes become relatively large, as is observed for the broadband and natural cases. On the other hand, if one disturbance mode is preferentially excited, then its development dominates all others via non-linear damping. As a consequence, the non-linear effects imposed on the dominant mode are weak, and so the dominant mode grows in strong accordance with LST.

Examination of the time-resolved flow development reveals that the unstable flow disturbances produce quasi-periodic shear layer vortices, that form through the roll-up of the separated shear layer just upstream of the maximum shape factor location. For all cases, these structures are strongly two-dimensional and oriented in the spanwise direction at formation, before undergoing significant spanwise deformations, ultimately leading to their breakdown. The spanwise deformations of the shear layer rollers are shown to fall within a range of wavelengths that covers two to seven times their streamwise wavelength. Tonal excitation is shown to have the most distinct effect on the development of the shear layer vortices. Specifically, it leads to earlier formation, a fixed shedding frequency and streamwise wavelength, increased spanwise coherence, and enhances the organization of spanwise deformations at a wavelength equal to two times the streamwise wavelength.

Appendix B

Uncertainty Estimation

Details are provided regarding the estimation of uncertainty for all critical results presented in this thesis.

The uncertainty analysis framework was established in Section 3.4. Here, detailed information is provided on the steps followed to produce the uncertainty estimates presented throughout the main chapters.

B.1 Experimental Conditions

B.1.1 UW Experiments

The chord-based Reynolds number for the experiments of Chapter 4 and Appendix A was $Re_c = 125\,000 \pm 2.90\%$. The uncertainty estimate is based on uncertainties in three measured quantities: the free-stream velocity, u_∞, airfoil chord length, c, and fluid kinematic viscosity, ν. The airfoil chord length is known to a high degree of precision and therefore does not contribute significantly to the uncertainty. The kinematic viscosity was determine indirectly through measurement of the ambient temperature and pressure. Temperature was measured by means of a K-type thermocouple installed in the wind tunnel, with measurements taken after a minimum 30 minute run time to allow for tunnel conditions to reach steady state. Ambient pressure was measured outside the tunnel using a mercury barometer. The uncertainty in the ambient temperature and pressure are estimated at ±0.1% and ±0.01%, respectively, which combine to give an estimate of $U_\nu = \pm 0.1\%$ on the kinematic viscosity. The free-stream velocity was determined by measuring the pressure drop across the tunnel contraction, relating this to the free-stream dynamic pressure through a calibration relationship, and then calculating u_∞ using Bernoulli's principle. The contraction pressure drop was measured using a Setra Model 239 differential pressure transducer with full range of 500 Pa, resulting in an uncertainty of ±0.3%, which takes into account the innate accuracy of the device and temporal fluctuations in the measurement. This uncertainty in the contraction pressure drop is then converted to one of the free-stream dynamic pressure using Eqn. 3.10 and the calibration relationship, resulting in an uncertainty on p_{dyn} of ±5.76%, with the major contributing factor being the quality of the calibration fit. Then, this uncertainty is converted to one on u_∞ according to Bernoulli's principle, which is root-sum-squared with the fluid density uncertainty (±0.1%) to give a final estimate of the free-stream velocity uncertainty, $U_{u_\infty} = \pm 2.89\%$. The uncertainty in the Reynolds number is then calculated using Eqn. 3.10, resulting in $U_{Re_c} = \pm 2.90\%$.

The airfoil's angle of attack was 4° ± 0.16, and was set using a digital protractor with an angular resolution of 0.1°. The main contributor to the uncertainty in the angle of attack is a possible bias error introduced through the determination of the aerodynamic zero angle of attack. This angle was determined by measuring lift coefficients over a range of negative and positive angles within which the lift slope is expected to be linear. By fitting a linear trend to these data and finding the angle that gives zero lift via interpolation, the uncertainty in the aerodynamic zero angle of attack is estimated, and found to be ±0.15°. Thus, the combined uncertainty is $U_{\text{AOA}} = \pm 0.16°$, or approximately 4% of the investigated value.

The sound pressure level (SPL) in the test section with and without acoustic excitation was measured to be 88.9 dB ± 0.1 and 89.5 dB ± 0.1, respectively. These were measured using a Brüel and Kjær 4192 condenser microphone, with a manufacturer reported accuracy of ±0.1 dB

within the frequency range of 40 to 1000 Hz, which spans the range of frequencies relevant to the investigation. For all cases, SPLs were verified to be uniform, within the uncertainty of the device, over the spanwise of the model. Therefore, the uncertainty in the reported SPLs is estimated to be ±0.1 dB.

B.1.2 TU Delft Experiments

The Reynolds number for the experiments of Chapters 5 and 6 was $Re_{\delta_{1_s}} = 750 \pm 15.2$, with a similar approach to that outlined in Section B.1.1 followed to obtain the uncertainty estimate. The length scale, the displacement thickness at the natural separation point, $\delta_{1_s} = 2.0\,\text{mm} \pm 0.25$, was determined from planar PIV measurements, with the process followed in determining its uncertainty described in Section B.2. The kinematic viscosity was again determined indirectly through measurement of the ambient temperature and pressure, with both measured within the anechoic plenum that serves as the open test section of the TU Delft A-Tunnel (Fig. 3.2). Ambient temperature was measured using an Omega PT100-1/3 DIN accuracy class RTD probe, while ambient pressure was measured using an Amphenol NPA-201 barometric pressure sensor, resulting in accuracies of 0.5% and 0.01%, respectively. Therefore, the uncertainty on the kinematic viscosity is $U_\nu = \pm 0.5\%$. The free-stream velocity was measured via a pitot-static tube installed in the test section, with the dynamic pressure measured via a Honeywell HSC series differential pressure transducer with a full range of ±160 Pa and an accuracy of ±0.8 Pa. Taking into account both this, the uncertainty associated with temporal fluctuations in the measured mean dynamic pressure, and the uncertainty in the fluid density (±0.11%), the uncertainty in the free-stream velocity is ±2.0% ($u_\infty = 5.75\,\text{m}\,\text{s}^{-1} \pm 0.11$). Thus, taking into account the uncertainty on the free-stream velocity, kinematic viscosity, and employed length scale, the uncertainty in the Reynolds number is ±2.1%.

B.2 PIV Measurements

Uncertainty estimates for PIV measurements are challenging, as the complexity of the measurement system lends to a multitude of errors, some of which cannot be quantified [191]. The research community has put forward a number of methods for PIV uncertainty quantification [217], with the correlation statistics method of Wieneke [251] selected for use in this thesis due to its implementation in the commercial DaVis software package. That being said, this method does not provide an all encompassing estimate of the uncertainty. Sources of uncertainty in PIV measurements are generally divided into two categories: (i) bias errors arising due to the calibration procedure, and (ii) randoms errors present in the particle images. The latter are propagated by the correlation analysis, which can introduce random errors of its own, into the velocity field result.

The uncertainties that arises due to the calibration procedure can be quantified. For both planar and tomographic configurations, a calibration relationship is determined by a imaging a target consisting of marks at known locations. The targets used throughout this work were CNC machined and as such the mark spacing is known to a high degree of precision (less than

±0.01 mm), and therefore this aspect does not contribute to the calibration uncertainty. For planar PIV configurations, a pinhole camera calibration relationship was used to relate the image and physical spaces, with fits matching the calibration images to a typical standard deviations of ±0.1 px, with some at higher values (±0.2–0.33 px). This is expressed as a percentage of the measurement based on the average particle displacement for a given planar configuration, which ranged between 10 and 20 px, therefore equating to uncertainties between 1.0% and 1.65%.

For the tomographic configuration, a pinhole calibration model was also used for the initial volume calibration, with a standard deviations between ±0.36–0.46 px across the four cameras. Volume self-calibration [250] was used to refine the accuracy of the calibration. A limited number of particles was introduced into the volume and imaged. Optical triangulation is used to estimate the particle positions, which is then compared across the cameras and the residual triangulation error (disparity) is used to correct each camera's calibration function. In doing so the standard deviation of the volume calibration was reduced to approximately ±0.1 px, which corresponds to approx. ±0.6% of the tomographic particle displacements. This calibration result is highly sensitive to camera positioning, with even slight changes introducing significant errors if they go undetected (*e.g.*, due to bumping a camera or vibrations from the operating the wind tunnel). Therefore, the volume self-calibration process was repeated before every test run, thus guaranteeing an uncertainty level related to calibration of less than ±0.6% for all datasets.

The random errors that occur in PIV measurements are more difficult to quantify, as they stem from many sources. Some examples that can significantly undermine a measured include: (i) changes in particle intensity between the first and second exposures, (ii) fluctuating background intensity, (iii) inherent camera noise, (iv) high velocity gradients, and (v) improper selection of cross-correlation parameters. Some studies have examined how these and other sources contribute to uncertainty in PIV through Monte-Carlo type simulations [101, 191, 246], finding that all these sources combine to give a general uncertainty level within ±0.04–0.1 px. However, this approach does not account for local variations in uncertainty (*e.g.*, in regions of high shear or low velocity magnitudes) and the benefits gained by advanced cross-correlation methods, such as iterative window deformations and weighting. A more comprehensive estimate of uncertainty due to random error sources is provided by the correlation statistics method [251], which incorporates the effects particle disparity, camera noise, and particle out-of-plane motions into a single estimate. The uncertainty is estimated by identifying residual intensity differences between the two interrogation windows that are correlated. Specifically, regardless of the overlap, the two interrogation windows never match perfectly and therefore the correlation peak is asymmetric. The contribution of each pixel in the cross-correlation to this asymmetry is quantified, producing a standard deviation that corresponds to a local uncertainty. Thus, the correlation statistics method gives an estimate of uncertainty for all interrogation window pairs, yielding an uncertainty field of the same size of the velocity field for each time instant.

A few examples are provided here to demonstrate how the uncertainty estimates from the correlation statistics method are handled. The first is presented in Fig. B.1, where the uncertainty fields for the time-resolved, side view PIV measurements of Chapter 4 (Table 4.1) are time-averaged and plotted in Fig. B.1a. This result in itself is useful, as it can be root-sum-squared with the uncertainty associated with calibration to give a 'total' uncertainty estimate for a PIV configuration, with these values reported throughout Chapters 4–6 and Appendix A (*e.g.*, Tables 4.1, 5.1, 6.1,

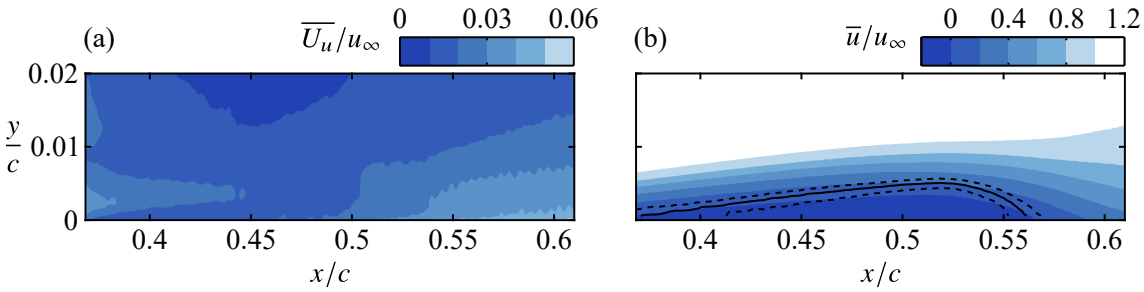

Figure B.1: (a) Exemplary time-averaged uncertainty field from the correlation statistics method [251], and (b) result of uncertainty propagation (dashed line) on the estimate of the mean dividing streamline (solid line).

and A.1). Furthermore, this uncertainty can be propagated through any analysis applied to the mean velocity field. For example, in Fig. B.1b the mean dividing stream (solid line) is determined from the time-averaged streamwise velocity field. Adding and subtracting the uncertainty field from the time-averaged one ($\overline{u} \pm \overline{U_u}$) provides upper and lower limits, on which the streamline is recomputed, giving the dashed lines in Fig. B.1b. This can be carried forward into further analysis, for example, in the determination of LSB characteristics, such as the mean separation, maximum height and reattachment locations. This gives the random error contributions to the uncertainty in these quantities, which is then root-sum-squared with other contributions, such as those related to calibration. This is the general approach followed in the analysis of time-averaged PIV velocity fields.

The approached is revised for the evaluation of uncertainty on instantaneous PIV velocity fields. Figure B.1a represents a map of the random error magnitude that may be present during at any particular instant during the measurement. Therefore, a random error/uncertainty field can be generated according to this map, with the result shown in Fig. B.2a where the errors are assumed to be normally distributed about zero with a standard deviation of the local value in $\overline{U_u}$. Then, this uncertainty can be propagated into an instantaneous velocity field, which is demonstrated with Figs. B.2b and B.2c. In doing this, any analysis method can be applied to these two fields, and the difference in the end results on account of the added noise can be quantified. For example, all instantaneous fields in a dataset can have this random noise added and then used as inputs for proper orthogonal decomposition (Section 3.3.2), giving a measure of the impact of the uncertainty on modal energy values and spatial topology. Or a time signal can be extracted, *e.g.*, Fig. B.2d, and the error contributions to PSD frequencies and amplitudes can be quantified. In all these approaches, in order to establish the uncertainty bounds to a statistical certainty, the process is repeated for a large numbers of randomly generated error fields (*e.g.*, 10^4 iterations), and the standard deviation in the change of the result is taken as the uncertainty bound.

Quantifying random error contributions to uncertainty in tomographic PIV measurements is less straightforward, as a robust uncertainty framework like the correlation statistics method has yet to be developed for the technique. Therefore, one must rely on empirical data to get an estimate of the uncertainty for a given configuration. Furthermore, all of the aforementioned random error sources present in planar measurements also apply to tomographic measurements, in addition to others that stem from the increased complexity of the technique. Most notably,

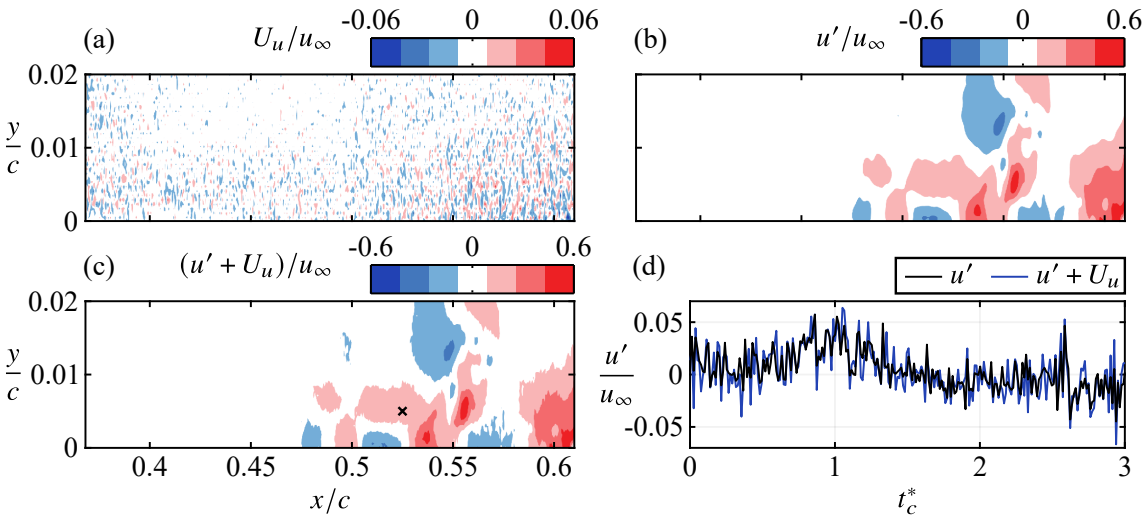

Figure B.2: (a) Exemplary randomly generated instantaneous uncertainty field. (b) Exemplary instantaneous fluctuating streamwise velocity field and (c) the same field with uncertainty added. (d) Time signal extracted at × marker in (c) with and without uncertainty added.

the tomographic reconstruction process introduces ghost particles, which are particles rendered into the reconstructed volume at points where there were no physical particles present. This is unavoidable due to ambiguities in the triangulation operation, however the introduction of ghost particles can be minimized through careful consideration of several factors, which Scarano [211] outlines as the proper selection of number of cameras, seeding density, light sheet thickness, volume calibration procedure, image pre-processing steps, and reconstruction algorithm settings.

First, a four camera setup was used, which offers a significant increase in reconstruction accuracy over two and three camera setups, while returns diminish as more cameras are added [129]. Second, with the respect to calibration, it was already established that the standard deviation of the initial physical volume calibration (±0.36–0.46 px) was refined down to ±0.1 px using the volume self-calibration technique, with the process repeated for each dataset to ensure any minor changes in the setup that may have occurred did not effect the accuracy of the calibration. With respect to the other factors, Scarano [211] recommends an *a posteriori* assessment through evaluation of the light intensity in the reconstructed volume. This is presented in Fig. B.3 for an exemplary volume. Figures B.3a and B.3b show the reconstructed light intensity distribution projected onto x-z and y-z planes, respectively, while the average intensity profiles in the z-direction are plotted in Fig. B.3c for the two laser pulses (the first pulse is shown in Figs. B.3a and B.3b).

Figures B.3a–c show appropriately sized reconstructed particles (approx. 2–3 vox in diameter) at a seeding density level that maximizes the number of particles without resorting to excessive particle overlap. Furthermore, the intensity is relatively uniform throughout the volume, with the peak at $z = 0.75$ mm corresponding to the actual position of the wall, where particles stuck to the surface contribute to a higher intensity. There is some uneven illumination between the two laser pulses, however, this is usually inherent to a particular laser and cannot be remedied without sending the laser to the manufacturer for tuning. Most importantly, there is a sharp roll-off in intensity between the illuminated and non-illuminated regions, which is attributed to careful

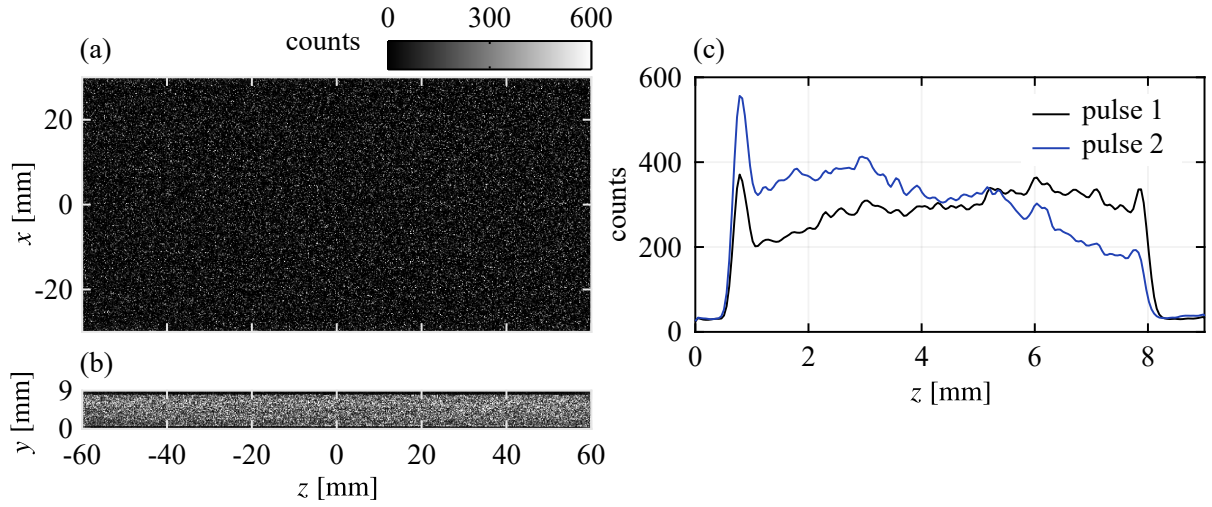

Figure B.3: (a) x-z and (b) y-z projections of an exemplary reconstructed tomographic volume. (c) Average intensity profiles in the z-direction.

tunning of the laser sheet and cameras. Since ghost particles are introduced everywhere and not just within the illuminated region, the intensity levels at $z < 0.75$ mm and $z > 8$ mm give a measure of the intensity of the ghost particles, which is approximately 30 counts. Comparing this to intensity of the particles in the illuminated region (approx. 300 counts) produces an estimated signal-to-noise ratio of 10, which is well above the minimum recommended ratio of 2 [211]. Therefore, ghost particles are not expected to have any significant impact on the correlation procedure, and thus on the final velocity field, as their intensity an order of magnitude lower than the real particles and, as outlined by Scarano [211], the probability of ghost particles forming a pair in the two interrogation windows being correlated is low for flows that exhibit a wide range of length scales, such as the LSB considered.

Lynch & Scarano [129] estimated the error in instantaneous tomographic velocity fields by comparing measurements from configurations that utilized 12, 6, 4, and 3 cameras, finding an error level of approximately ±0.5 vox for a carefully calibrated and well-tuned 4 camera setup. While the flow configuration under consideration (wake of a circular cylinder) is vastly different from the LSB considered in Chapter 6, the current investigation has followed all recommended guidelines for maximizing accuracy of tomographic PIV measurements, and therefore it is expected that the error level reported by Lynch & Scarano can serve as a rough estimate for this investigation. However, this is a rough estimate only, and the reliability of the tomographic measurements must be validated by other means. This is achieved in Chapter 6 by comparing equivalent results from the tomographic and planar PIV configurations (Fig. 6.4), as a robust estimate of uncertainty is available for the latter.

B.3 Hot-Wire Measurements

The accuracy of hot-wire measurements depends on many factors, including probe geometry, the calibration method, flow incidence angle, turbulence intensity, flow velocity, and proximity to solid surfaces [30]. Errors caused by obstructing the flow due to the presence of the probe and incidence angle have been limited by using a boundary layer type normal probe (Dantec 55P15) angled at 10° to the wall, as recommended by Brendel & Mueller [24] for HWA measurements in LSBs. A rigorous calibration procedure (details below) was followed that ensured the associated uncertainty was kept below 2% within the measured velocity range ($3.5 \leq u \leq 4.8\,\mathrm{m\,s^{-1}}$). Near wall effects, such as rectification errors, high uncertainty due to low velocities, and conduction to the surface, also do not contribute significantly since all measurements were performed at a minimum distance of 2 mm from the wall [30, 50, 120]. The work of Kawall *et al.* [100] established the uncertainties in HWA measurements related to turbulent fluctuations, with a broad range of cases covered (see their Tables 1 and 2). For generally representative conditions (flow velocities on the order of $2\,\mathrm{m\,s^{-1}}$ and free-stream fluctuations less than or equal to 5%), Kawall predicts an uncertainty due to turbulent fluctuations of 1.7%. Combining this through a root-sum-square with the calibration uncertainty gives the total estimate of uncertainty for the HWA measurements of this thesis, which is found to be 2.6% of u_∞ ($\pm 0.07\,\mathrm{m\,s^{-1}}$). It must be noted that this uncertainty can be reduced significantly through time and/or phase-averaging, since uncertainty reduces in proportion to the square root of the number of samples taken. This is one of the major benefits of HWA measurements, as a large number of samples can be taken at a high sampling rate, thus allowing for low amplitude disturbances to be detected at relevant frequencies in a time or phase-averaged sense (*e.g.*, Section 6.4).

Calibration of the hot-wire sensor was performed *in-situ* in order to eliminate additional uncertainties related to changing the mounting and orientation of the probe between calibration and measurements. The reference velocity was provided by a TSI 1127 Velocity Calibrator installed in the test section with the tunnel off, which was used in lieu of the tunnel's free-stream velocity due to a much higher accuracy at low flow velocities. The reference velocity was established by measuring the pressure drop across the calibrator's nozzle using a Honeywell HSC series pressure transducer with a full range of ±160 Pa and a 0.26% full-scale accuracy. Thus, the uncertainty on reference velocities greater than $1.75\,\mathrm{m\,s^{-1}}$ is 2%. HWA calibration relationships are sensitive to the ambient temperature [30], and therefore calibration was performed daily, using 17 calibration points that spanned $0 \leq u \leq 11.5\,\mathrm{m\,s^{-1}}$. A fourth order polynomial relating the voltage response of the probe to flow velocity was used.

B.4 Pressure Measurements

At the University of Waterloo, the mean surface pressure distributions of the airfoil (Fig. 4.17) were measured using Setra Model 239 high accuracy differential pressure transducers with a full range of ±500 Pa and a total accucracy of 0.14% of full-scale (±0.7 Pa). Each transducer was individually calibrated, using 10 references pressure that spanned their operaring range provided by a Druck DPI 610 low pressure calibrator. The uncertainty, as quantified by the root-mean-squared error

of the linear fits, is ±0.12 Pa. Strain gauge based pressure transducers, such as those employed, are sensitive to temperature [237]. Therefore, prior to each set of measurements, the drift due to temperature from the original calibration relationship was corrected for by measuring and applying a zero-pressure voltage offset. This kept uncertainty due to ambient temperature changes under ±0.2 Pa. Finally, the geometry of the pressure tap contributes to the measurement uncertainty. According to the results of Chue [37], the estimated uncertainty due to the geometry of the employed taps is ±0.14 Pa. Combining all these uncertainty estimates using Eqn. 3.9 produces a total uncertainty of ±0.75 Pa, which is equivalent to ±0.8% of the free-stream dynamic pressure.

At TU Delft, the flat plate's imposed pressure distribution (Figs. 5.4 and 6.2) was measured using Honeywell Honeywell HSC series pressure transducer with a full range of ±160 Pa and a total accuracy of 0.26% of full-scale (±0.8 Pa). This uncertainty estimate covers the contributions due to calibration, hysteresis, non-linearity and non-repeatability effects. Sensitivity to ambient temperature changes was again addressed by correcting the original calibration by applying a zero-pressure voltage offset that was determined prior to each data collection period. This kept the uncertainty associated with temperature drift less than ±0.2 Pa. The pressure tap geometry for the flat plate is identical to the airfoil (both are 0.4 mm diameter holes), and therefore the uncertainty due to tap geometry is once again ±0.14 Pa according to Chue [37]. Thus, combining all these uncertainty estimates gives a total uncertainty of ±0.84 Pa, which is equivalent to ±4.6% of the free-stream dynamic pressure.

Appendix C

Supplementary Results

Additional results are provided that support the findings presented in Chapters 4 through 6.

C.1 Chapter 4 Supplementary Results

C.1.1 Three-Dimensional Features

In Section 4.3.3, it was found that the energy content of the POD modes that captured the shear layer vortices (modes numbers $m = 1$ and 2) did not increase when forcing was applied at the fundamental frequency (F forcing case), despite this forcing specifically targeting the vortices. This is seen in the results of Fig. 4.24, and is the result of two compounding factors. First, the forcing amplitude of the F case is relatively weak (only 0.6 dB above the SPL of the natural flow) and therefore a significant increase in the energy levels is not expected. This is confirmed through POD analysis at the plane presented in Figs. 4.24 and 4.25 ($y/c = 3 \times 10^{-3}$) at others in Fig. C.1, where the energy levels of the first two modes of the Nat. and F cases are always within 1% of each other, which falls within the uncertainty on E_R. Second, the $y/c = 3 \times 10^{-3}$ plane presented in Figs. 4.24 and 4.25 is close to the surface, which appears to have a significant effect on the energy levels recovered in the POD analysis. This is also confirmed in Fig. C.1, where results from a higher amplitude forcing case, F + 3.2 dB, are included. Even at the higher excitation amplitude, an increase in the energy of the first modes at the near wall plane is not seen ($y/c = 3 \times 10^{-3}$), while the expected result is seen at planes further from the wall ($y/c = 6 \times 10^{-3}$ and 16×10^{-3}). While the result is interesting and may merit future investigation, it does not impact the results presented in Section 4.3.3, as the purpose of the presented POD analysis was to establish the presence of near-wall spanwise velocity fluctuations in the natural flow, which was successfully demonstrated (Fig. 4.25).

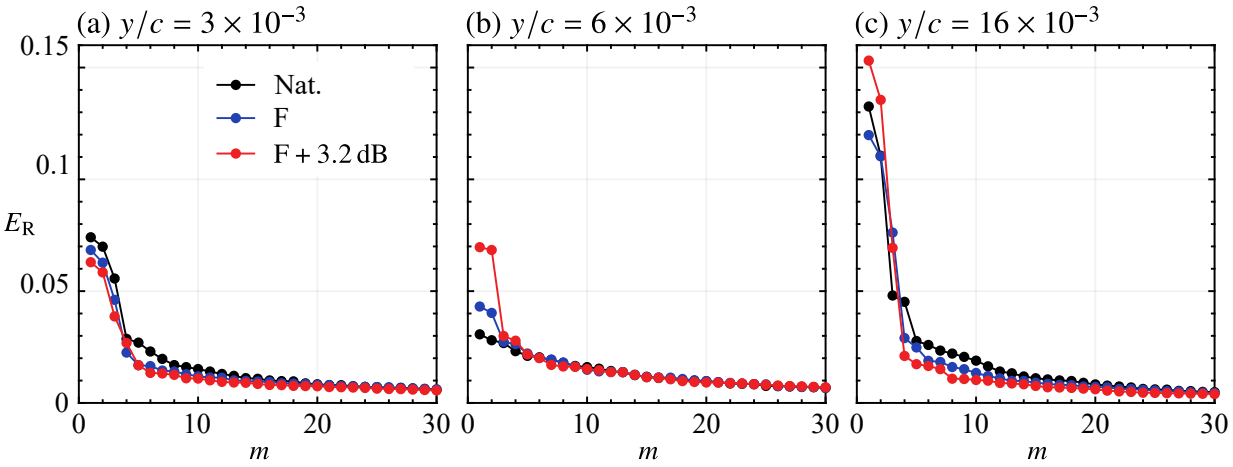

Figure C.1: POD relative modal energy distributions for (u, w) modes at several y-planes and the same domain as Figs. 4.24 and 4.25. F + 3.2 dB is the same forcing as the F case from Chapter 4, with a 3.2 dB higher forcing amplitude.

C.2 Chapter 5 Supplementary Results

C.2.1 Quiescent Characterization

In Section 5.3 flow visualizations results were presented for only the two-dimensional and $\widetilde{\lambda}_z = 25$ cases (Fig. 5.5). This was due to completing the flow visualization component of the quiescent characterization campaign prior to having established all forcing cases that would be carried forward into future experiments. Therefore, flow visualizations are not available for the $\widetilde{\lambda}_z = 12.5$ and 18.75 cases. Other spanwise wavelengths were tested, namely $\widetilde{\lambda}_z = 8$ and 16, which ultimately were not selected for future investigations, however the results do provide some interesting observation. These are presented alongside the two-dimensional and $\widetilde{\lambda}_z = 25$ cases in Figs. C.2 and C.3, which show the induced flow during the start-up and steady state phases of the actuation, respectively.

As was noted in Section 5.3, the flow visualizations in Figs. C.2 and C.3 show that actuation produce a streamwise jet that is spanwise uniform across continuous regions of electrode overlap during both the start-up and steady state phases. Therefore, the induced flow by the two-dimensional actuator is spanwise uniform across the entire actuator length. For the spanwise modulated actuators, the streamwise jets are only produced with the regions of the electrode overlap, with the flow remaining essentially stagnant in between. This is most evident for the $\widetilde{\lambda}_z = 16$ and 25 cases (Figs. C.2c–d and C.3c–d), whereas jet interaction effects may be present for the $\widetilde{\lambda}_z = 8$ case as both Figs. C.2b and C.3b show jets that are noticeably wider than those of the larger wavelength cases. It is for this reason that the $\widetilde{\lambda}_z = 8$ case was not selected for further investigation, as spanwise modulated actuators that produced the same total amount of momentum per active region were desired, which was achieved with the $\widetilde{\lambda}_z = 12.5$, 18.75 and 25 actuators.

C.2.2 In-Flow Characterization

Prior to the in-flow characterization and subsequent preliminary LSB study of Chapter 5, the fundamental disturbances characteristics of the natural LSB needed to be determined so that the appropriate forcing parameters could be selected. This was accomplished by performing high speed, planar PIV measurements for the natural LSB (*i.e.*, the same dataset presented in Figs. 5.17a and 5.18a), which were then analyzed to identify the frequency and streamwise wavelength of the fundamental disturbances. These results are presented here, which begins with POD analysis of the PIV velocity dataset. Figure C.4 presents the relative and cumulative modal energy distributions, which show that the two most energetic modes are of approximately the same energy level and combine to account for 35% of the flow's total turbulent kinetic energy. Thus, as has been seen through this thesis, this highly energetic mode pair captures shedding and propagation of the shear layer vortices in the LSB. This is made clear through visual inspection of the POD spatial eigenfunctions for these modes, presented in Fig. C.5. The mean dividing streamline for the natural case, determined in Chapter 5 (Fig. 5.17a), is also plotted.

Figure C.5 shows strong, spatially coherent streamwise and wall-normal velocity fluctuations that reach measurable amplitudes in the fore portion of the LSB ($\widetilde{x} \lesssim 45$) and undergo convective

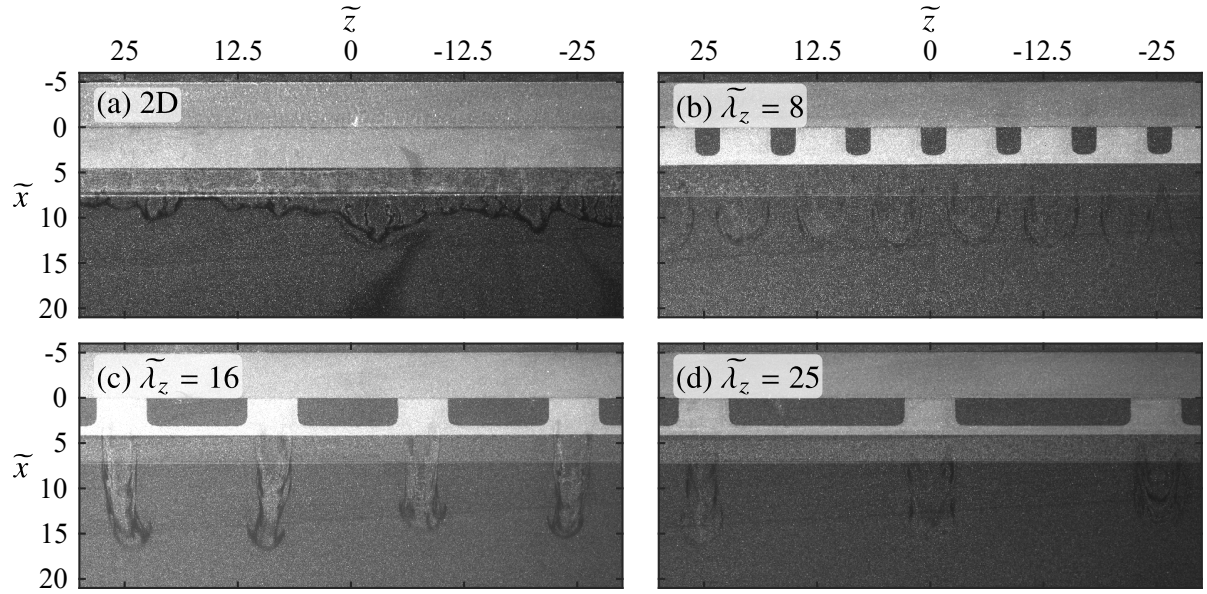

Figure C.2: Visualization of flow induced for various plasma actuators during the start-up phase ($V_{pp} = 6\,\text{kV}$, $f_c = 5\,\text{kHz}$, 100% duty cycle). Flow is from top-to-bottom.

amplification. The streamwise wavelength of these disturbances is determined by identifying local extrema in the wall-normal spatial modes, $\gamma_v^{(1)}$ and $\gamma_v^{(2)}$, which are denoted by the × markers in Fig. C.5. The streamwise distance between these marks, averaged across the two modes, is $\Delta\widetilde{x} = 6.30$ which is a measure of half the disturbance streamwise wavelength, and thus $\widetilde{\lambda}_x$ for the natural case is estimated at $\widetilde{\lambda}_x = 12.6$. This value is of significance as it allows for spanwise-to-streamwise wavelength ratio of the considered forcing cases to be determined. The spanwise wavelengths of the cases are $\widetilde{\lambda}_z = 12.5$, 18.75, and 25, and thus the ratios are $\lambda_z/\lambda_x = 1$, 1.5, and 2, respectively. These are the values carried forward into Chapters 5 and 6.

The fundamental disturbance frequency also needed to be determined so that the plasma forcing could be modulated to this frequency, and thus the fundamental K-H instability targeted. This was determined through spectral analysis of the wall-normal velocity fluctuations in the aft portion of the LSB (sampled at $\widetilde{x} = 46.5$, $\widetilde{y} = 2$) and the POD temporal coefficients of the two most energetic modes, $b^{(1)}$ and $b^{(2)}$. These results are presented in Fig. C.6, where the spectrum of $b^{(2)}$ is not plotted as it is nearly identical to that of $b^{(1)}$. For the both the wall-normal velocity fluctuations and the POD temporal coefficients, the spectra show the highest energy levels within a band centred at 133 Hz, thus this frequency is taken as the fundamental disturbance frequency, f_0/St_0, and is to be used in modulating the output of plasma forcing (alongside an appropriate duty cycle) in order to target the LSB's primary K-H instability.

To summarize, through analysis of the natural flow, the streamwise wavelength and frequency of the fundamental disturbances present in the LSB have been identified as $\widetilde{\lambda}_z = 12.6$ and $f_0 = 133\,\text{Hz}$. These values are used throughout Chapters 5 and 6, both for selection of appropriate forcing parameters and in the analysis of the experimental results that follows.

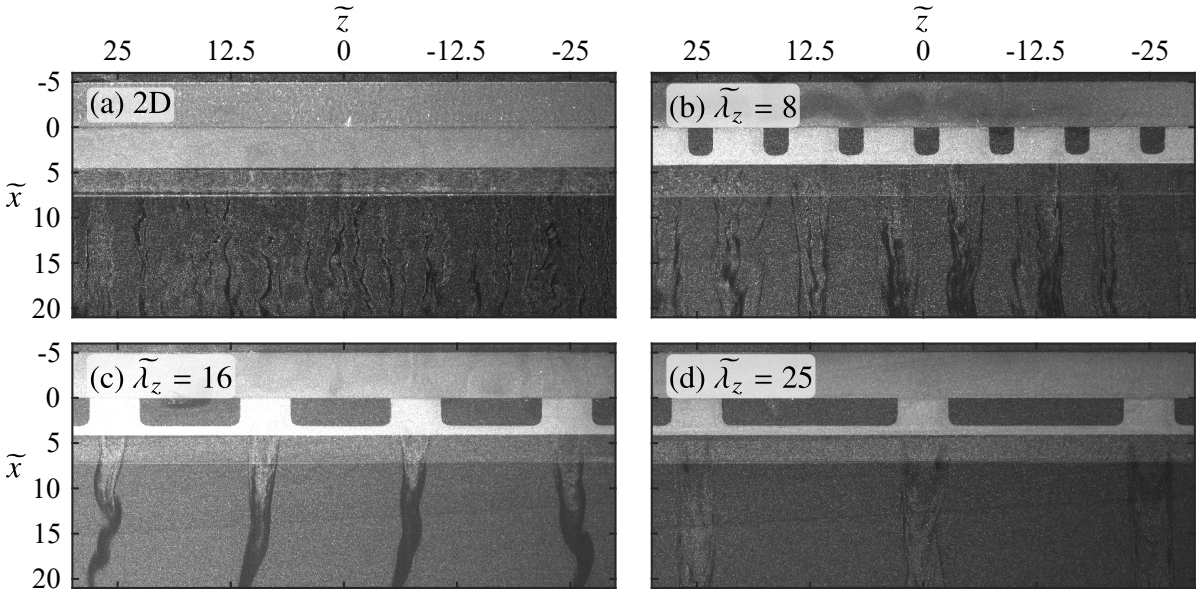

Figure C.3: Visualization of flow induced for various plasma actuators during the steady state phase ($V_{pp} = 6\,\text{kV}$, $f_c = 5\,\text{kHz}$, 100% duty cycle). Flow is from top-to-bottom.

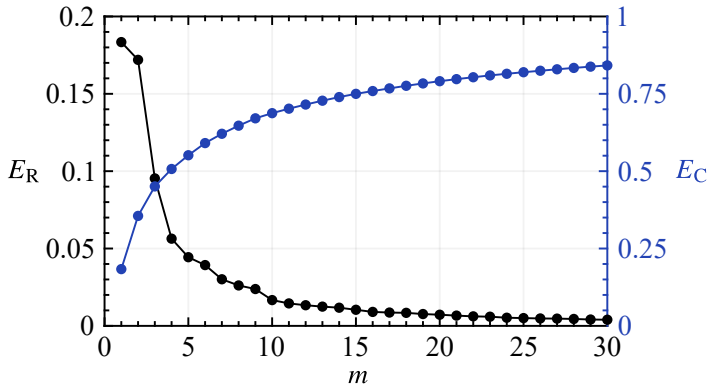

Figure C.4: POD relative and cumulative modal energy distributions for the Chapter 5 natural case (side view PIV measurements).

C.2.3 Effect on LSB Flow Development: Preliminary Study

In Section 5.5 analysis at different x-y planes for the $\widetilde{\lambda}_z = 25$ forcing case revealed significantly different disturbance development depending on the plane's location relative to the undulations that the developed in the vortex filaments. Specifically at $\widetilde{z} = 0$, where the vortex filaments surged forward in the streamwise direction and tilted away from the surface (Fig. 5.16b)), disturbance development, in terms of the v'_{rms} contours, was largely similar to the two-dimensional case (Fig. 5.18). However, at $\widetilde{z} = 12.5$, where the filaments lagged behind in the streamwise direction and tilted toward the wall (again Fig. 5.16b), the regions of high velocity fluctuations were found to be closer to the surface, and did not increase monotonically with increasing streamwise position

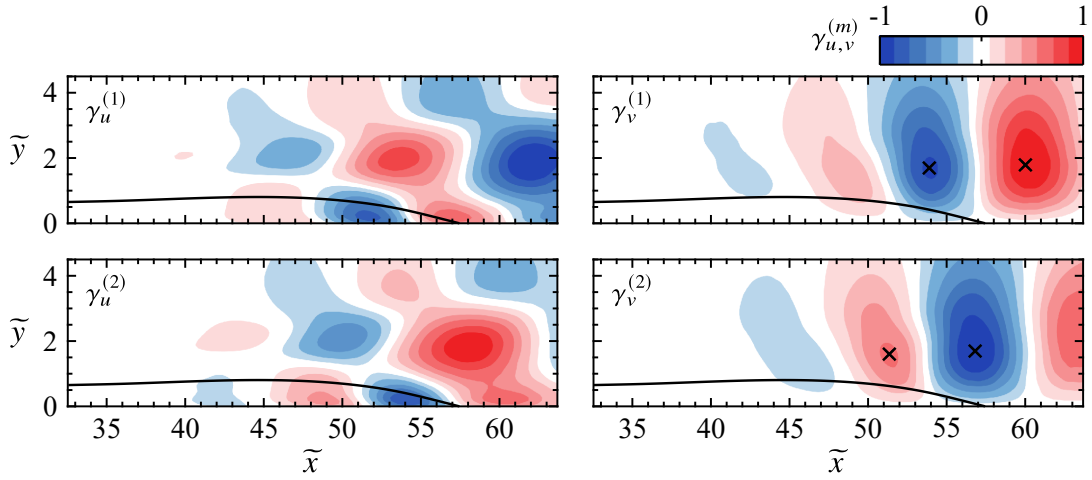

Figure C.5: Streamwise and wall-normal components of normalized POD spatial modes for the natural case. × markers denote selected local extrema. Solid lines mark the dividing streamline.

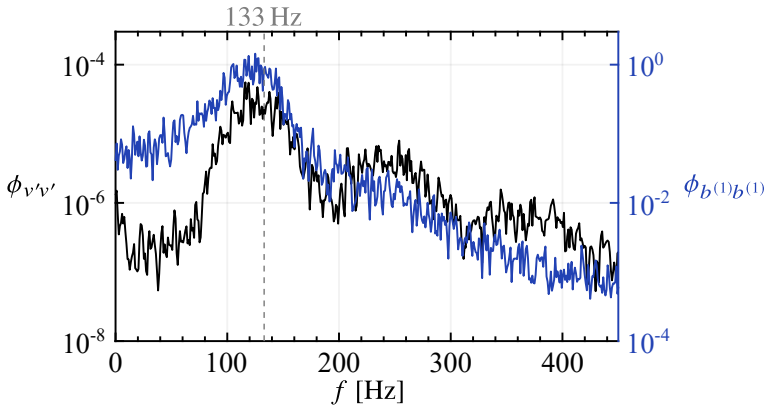

Figure C.6: Frequency spectra of wall-normal velocity fluctuations sampled at $\widetilde{x} = 46.5$, $\widetilde{y} = 2$, and POD temporal coefficients for the most energetic mode, $b^{(1)}$.

in the aft portion of the bubble (Fig. 5.18c). In particular, disturbance amplitudes in terms of v'_{rms} did not continually increase in the region $50 \leq \widetilde{x}58$, and it was speculated that the wall-normal velocity fluctuations were re-distributed into other directions by the vortex dynamics. Figure C.7 presents rms contours of the streamwise velocity fluctuations for the same cases and at the same planes as Fig. 5.18. For the $\widetilde{\lambda}_z = 25$ case at the $\widetilde{z} = 12.5$ plane, streamwise disturbance amplitudes do rise continuously and quite rapidly within $50 \leq \widetilde{x} \leq 58$, both at the wall ($\widetilde{y} \approx 0.25$) and at the second peak from the wall ($\widetilde{y} \approx 2$). Thus the assertion that the wall-normal velocity fluctuations are redistributed is supported. However, given that this PIV configuration only measured u and v, it is impossible to say if the fluctuations were also redistributed into the spanwise direction. This was part of the motivation behind pursuing tomographic PIV measurements in Chapter 6 (also Tomo PIV is cool and I got to go back to Delft).

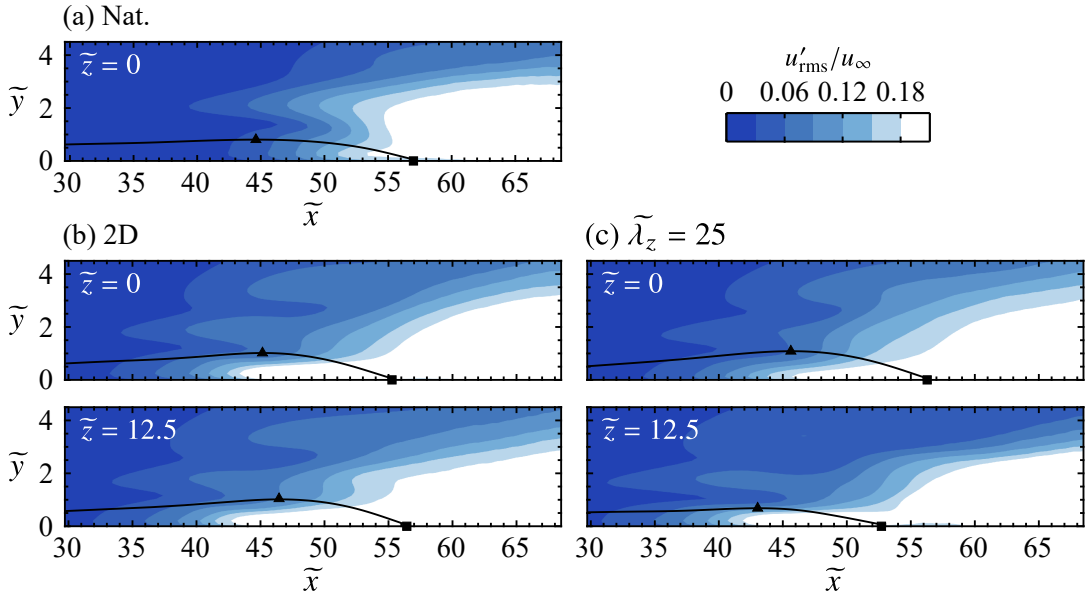

Figure C.7: Rms of fluctuating streamwise velocity contours at same spanwise locations as Figs. 5.17 and 5.18. Solid lines mark the dividing streamlines. Triangle and square markers denote estimated mean maximum bubble height and reattachment points, respectively.

Appendix D

Code Repository

A few of the MATLAB codes developed as part of this thesis are provided and briefly described.

D.1 Vortex Filament Model

The implementation of the vortex filament model presented in Section 5.5.1 is provided in Section D.1.1, alongside several of its subroutines (Sections D.1.2–D.1.5). The main routine is straightforward, as it serves to initialize the conditions for the simulations (filament in terms of its parametric equations and other parameters, external flow parameters, time step duration and number of steps), after which the simulation subroutine is called (Section D.1.3), which does all the heavy lifting. Of note in the main routine, is the modelling of the external flow velocity profile using Eqn. 5.3, which is the profile proposed by Dini *et al.* [45] and is evaluated by calling the Dini subroutine (Section D.1.2).

The variables passed into the simulation subroutine include the initial location of the filaments (defined by a set of parametric equations that give discrete points in space when evaluated), the circulation of each filament, Γ, flags indicating if each filament forms a closed loop, the parametric equations defining the external flow, and time stepping parameters. First, some housekeeping is done (lines 46–65 in Section D.1.3), with the simulation beginning on line 68. For each time step and for each filament, first the velocity that the filament self-induces is calculated on line 72 where the Biot-Savart self-induction subroutine (Section D.1.4) is called. The result is stored in a variable for the velocity of the filament at each of its points, which is then updated based on the velocity induced by all other filaments (lines 76–81), which is determined by calling the Biot-Savart induction subroutine (Section D.1.5). The final contribution to the filament's velocity is that of the free-stream (lines 85–88), after which the filament's position at the next time step is predicted based on all velocity contributions and the prescribed time step (lines 91–93). This process is then repeated for the prescribed number of time steps, thus completing the simulation. Some final housekeeping is performed to prepare the output (lines 98–105), which includes filament locations and velocities at all time steps.

Two of the critical operations in the simulation subroutine are the calculation of the velocity components that a filament self-induces (Section D.1.4), and are induced by other filaments (Section D.1.5). For the former, a filament (in terms of its spatial location), its circulation, a solid core radius, and a flag indicating if the filament forms a closed loop are passed in. The essential steps to calculating the self-induced velocity include discretizing the filament and determining each segment's length (lines 48–49), and then calculating the direction of the vorticity vector for each segment (lines 52–58). This is why a closed loop indicator is required, as a central differences can be used for all segments if the filament is a closed loop, while forward and backward differences need to be used for the end points in the case the filament is not closed. This may seem like a minor detail, however, significant numerical errors were created in earlier implementations of this subroutine by not treating the end points, which would then propagate across throughout the domain. In the current implementation, the numerical errors present at the end points (since no real vortex filament can have a abrupt start and end point) are at least confined to the start and end regions, while a central region where the effects of the errors are insignificant can be identified. With the filament segments and corresponding vorticity vector directions determined, the velocity at each filament point is then evaluated by summing all other point's contribution according to the Biot-Savart law (Eqn. 2.6). This is done over (lines 64–73), where the 'solid core radius' comes into effect, where the contribution of points within that distance are neglected entirely (line 68),

thus avoiding the singularity for $|\vec{r}| \to 0$.

The Biot-Savart induction subroutine in Section D.1.5 is very similar to the self-induction subroutine (Section D.1.4) and could likely have been combined into one elegant implementation if the author wasn't a sub-par coder and (somewhat) lazy. But, hey, this is a thesis based in fluid mechanics, not computer science, so it will do just fine. In essence the function discretizes the passed in filament (lines 50–51), determines the direction of its vorticity vectors (lines 54–55), with no treatment of end points or the solid core region needed since the points being evaluated do not lie on the filament itself. The probed points are evaluated (lines 61–68) and the output is returned.

D.1.1 Main Routine

```
1  %-------------------------------------------------------------------------
2  % Setup
3  %-------------------------------------------------------------------------
4  clear; clc
5
6  % Filament parametric equation
7  a = 1.25; % amplitude
8  l = 25; % wavelength
9  t = (0:(pi/36):32*pi-(pi/36))';
10 xf = @(t) a*sin(2*pi/l*t)+31;
11 yf = @(t) t;
12 zf = @(t) t*0+2;
13 f = {xf,yf,zf,t};
14 % Filament circulation
15 Gamma = -19.5;
16 % Filament solid core radius
17 r = 0.99*pi/18;
18 % Does filament form a closed loop?
19 closed = 0; % 0 => No, 1=> Yes
20
21 % Mirrored filament
22 zfm = @(t) t*0-2;
23 xfm = @(t) a*sin(2*pi/l*t)+31;
24 fm = {xfm,yf,zfm,t};
25
26 % Mean velocity field
27 u = @(x,y,z) diniMod(0.01114,5.553e+04,2.021,4.791e+04,3125,z);
28 v = @(x,y,z) x*0;
29 w = @(x,y,z) x*0;
30 V = {u,v,w};
31
32 % Mirrored velocity field
33 um = @(x,y,z) diniMod(0.01114,5.553e+04,2.021,4.791e+04,3125,-1*z);
34 Vm = {um,v,w};
35
36 % Package
37 f_p = {f,fm};
```

```
G_p = {Gamma,-1*Gamma};
r_p = {r,r};
closed_p = {closed,closed};
V_p = {V Vm};

%-------------------------------------------------------------------------
% Simulate
%-------------------------------------------------------------------------
dt = 1/30000; % Time step
n = 500; % Number of steps

[fS,vS] = biotSavartSim(f_p,G_p,r_p,closed_p,V_p,dt,n);
```

D.1.2 Dini *et al.* [45] Subroutine

```
%-------------------------------------------------------------------------
% Evaluates the function
% U/U_edge = (1-c1)/2 + (1+c1)/2 * tanh(c2(y-c3)/c4))
%-------------------------------------------------------------------------
% INPUTS
% c1 = c1
% c2 = c2
% c3 = c3
% c4 = c4
% c5 = U_edge
% y = wall-normal points at which to evaluate solution
%-------------------------------------------------------------------------
% OUTPUT
% u = streamwise velocity
%-------------------------------------------------------------------------
function u = diniMod(c1,c2,c3,c4,c5,y)
u = c5.*((1-c1)/2+(1+c1)/2.*tanh(c2.*(y-c3)./c4));
```

D.1.3 Simulation Subroutine

```
%-------------------------------------------------------------------------
% Simulates the motion of a vortex filament due to Biot-Savart
% self-induction, Biot-Savart induction from other vortex filaments,
% and a mean flow field.
%-------------------------------------------------------------------------
% INPUTS
% f = cell of cells, each containing parametric equations defining the
% filaments.
%   f{1}{1} = x1(t)  f{2}{1} = x2(t)
%   f{1}{2} = y1(t)  f{2}{2} = y2(t)
%   f{1}{3} = z1(t)  f{2}{3} = z2(t)
%   f{1}{4} = t1     f{2}{4} = t2,       etc..
%
% Gamma = cell of filament circulation [L^2/T]
```

```
%
% r = cell of filament solid core radii [L], within which Biot-Savart
% self induction does not apply
%
% closed = cell of logicals. Are the filaments closed loops?
%   0 = No
%   1 = Yes
%
% V = cell of cells, each containing parametric equations defining mean
% flow fields.
%   V{1}{1} = u1(x,y,z)  V{2}{1} = u1(x,y,z)
%   V{1}{2} = v1(x,y,z)  V{2}{2} = v2(x,y,z)
%   V{1}{3} = w1(x,y,z)  V{2}{3} = w2(x,y,z)    etc...
%
% dt = time step for simulation [T]
%
% n = number of steps for simulation
%-------------------------------------------------------------------------
% OUTPUTS
% f = cell of filament points, within each cell dim 3 is time
%   f{1}(:,1,:) = x1    f{2}(:,1,:) = x2
%   f{1}(:,2,:) = y1    f{2}(:,2,:) = y2
%   f{1}(:,3,:) = z1    f{2}(:,3,:) = z2    etc...
%
% vf = cell of velocity at filament points, within each cell dim 3 is time
%   vf{1}(:,1,:) = u1   vf{2}(:,1,:) = u2
%   vf{1}(:,2,:) = v1   vf{2}(:,2,:) = v2
%   vf{1}(:,3,:) = w1   vf{2}(:,3,:) = w2   etc...
%-------------------------------------------------------------------------
function [f,vf] = biotSavartSim(f,Gamma,r,closed,V,dt,n)
% Unpackage
for i = 1:length(f)
    temp = f{i};
    % Parameter
    t = temp{4};

    % Filament
    if i == 1
        ft = [temp{1}(t) temp{2}(t) temp{3}(t)];
    elseif i == 2
        ft = cat(3,ft,[temp{1}(t) temp{2}(t) temp{3}(t)]);
    end
end
f = ft;
clearvars temp ft

% Initialize
temp = zeros(size(f,1),size(f,2),size(f,3),n);
vf = temp;
temp(:,:,:,1) = f;
f = temp;

```

```
% Loop time
for i = 1:size(f,4)
    % Loop filaments
    for j = 1:size(f,3)
        % Self-induced velocity
        [uBSS,vBSS,wBSS] = biotSavartSelf(f(:,:,j,i),Gamma{j},r{j},closed{j
            });
        vf(:,:,j,i) = [uBSS vBSS wBSS];

        % Induced velocity
        for k = 1:size(f,3)
            if k ~= j
                [uBS,vBS,wBS] = biotSavart(f(:,:,k,i),Gamma{k},f(:,:,j,i),0);
                vf(:,:,j,i) = vf(:,:,j,i) + [uBS vBS wBS];
            end
        end

        % Free-stream velocity
        Vt = V{j};
        u = Vt{1}(f(:,1,j,i),f(:,2,j,i),f(:,3,j,i));
        v = Vt{2}(f(:,1,j,i),f(:,2,j,i),f(:,3,j,i));
        w = Vt{3}(f(:,1,j,i),f(:,2,j,i),f(:,3,j,i));
        vf(:,:,j,i) = vf(:,:,j,i) + [u v w];

        % Update position
        f(:,1,j,i+1) = f(:,1,j,i) + vf(:,1,j,i)*dt;
        f(:,2,j,i+1) = f(:,2,j,i) + vf(:,2,j,i)*dt;
        f(:,3,j,i+1) = f(:,3,j,i) + vf(:,3,j,i)*dt;
    end
end

% Package for output
tempf = cell(1,size(f,3));
tempv = tempf;
for i = 1:length(tempf)
    tempf{i} = permute(f(:,:,i,:),[1 2 4 3]);
    tempv{i} = permute(vf(:,:,i,:),[1 2 4 3]);
end
f = tempf;
vf = tempv;

close(h);
```

D.1.4 Biot-Savart Self-Induction Subroutine

```
%-------------------------------------------------------------------------
% Computes self-induced velocity on a vortex filament as a result of
% Biot-Savart induction.
%-------------------------------------------------------------------------
% INPUTS
% f = parametric equations defining filament
```

```
%   f{1} = x(t)
%   f{2} = y(t)
%   f{3} = z(t)
%   f{4} = t
% OR
% f = filament points
%   f(:,1) = x
%   f(:,2) = y
%   f(:,3) = z
%
% Gamma = filament circulation [L^2/T]
%
% r = radius of filament solid core [L]
%   filament radius within which Biot-Savart does not apply
%
% closed = Does filament form a closed loop?
%   0 = No
%   1 = Yes
%-------------------------------------------------------------------------
% OUTPUT
% u, v, w = induced velocity components at probed points [L/T]
%-------------------------------------------------------------------------
function [u,v,w] = biotSavartSelf(f,Gamma,r,closed)
% Parametric or points
if iscell(f) % Parametric
    % t
    t = f{4};
    if size(t,2) > size(t,1)
        t = t';
    end

    % Filament
    f = [f{1}(t) f{2}(t) f{3}(t)];
else % Points
    % Check for correct probed points format
    if size(f,2) ~= 3
        error('Filaments points formatted incorrectly. Exiting');
    end
end

% Filament segment lengths
dl = [diff(f(1:2,:)); diff(f(:,:))]/2 + [diff(f(:,:)); diff(f(end-1:end,:))
    ]/2;
dl = sqrt(dl(:,1).^2+dl(:,2).^2+dl(:,3).^2);

% Filament vorticity vectors
if closed
    F = [gradient([f(end,1); f(:,1); f(1,1)]) gradient([f(end,2); f(:,2); f
        (1,2)]) gradient([f(end,3); f(:,3); f(1,3)])];
    F = F(2:end-1,:);
else
    F = [gradient(f(:,1)) gradient(f(:,2)) gradient(f(:,3))];
```

```
end
F = F./repmat(vecnorm(F,2,2),1,size(F,2)); % Normalize

% Intialize
V = zeros(size(f));

% Loop probed points
for i = 1:size(f,1)
    % Sum contributions of filament
    for j = 1:size(f,1)
        R = f(i,:) - f(j,:);
        if norm(R) > r
            V(i,:) = V(i,:) + cross(F(j,:),R)/(norm(R)^3)*dl(j);
        end
    end
end
V = Gamma/(4*pi).*V;

% Output
u = V(:,1);
v = V(:,2);
w = V(:,3);
```

D.1.5 Biot-Savart Induction Subroutine

```
%-------------------------------------------------------------------------
% Computes induced velocity at probed points as a result of Biot-Savart
% induction from vortex filament of circulation Gamma.
%-------------------------------------------------------------------------
% INPUTS
% f = parametric equations defining filament
%   f{1} = x(t)
%   f{2} = y(t)
%   f{3} = z(t)
%   f{4} = t
% OR
% f = filament points
%   f(:,1) = x
%   f(:,2) = y
%   f(:,3) = z
%
% Gamma = filament circulation [L^2/T]
%
% probe = probed points
%   probe(:,1) = x
%   probe(:,2) = y
%   probe(:,3) = z
%-------------------------------------------------------------------------
% OUTPUT
% u, v, w = induced velocity components at probed points [L/T]
%-------------------------------------------------------------------------
```

```
function [u,v,w] = biotSavart(f,Gamma,probe)
% Parametric or points
if iscell(f) % Parametric
    % t
    t = f{4};
    if size(t,2) > size(t,1)
        t = t';
    end
    % Filament
    f = [f{1}(t) f{2}(t) f{3}(t)];
else % Points
    % Check for correct filament points format
    if size(f,2) ~= 3
        error('Filaments points formatted incorrectly. Exiting');
    end
end

% Check for correct probed points format
if size(probe,2) ~= 3
    error('Probed points formatted incorrectly. Exiting');
end

% Filament segment lenths
dl = [diff(f(1:2,:)); diff(f(:,:))]/2 + [diff(f(:,:)); diff(f(end-1:end,:))
    ]/2;
dl = sqrt(dl(:,1).^2+dl(:,2).^2+dl(:,3).^2);

% Filament vorticity vectors
F = [gradient(f(:,1)) gradient(f(:,2)) gradient(f(:,3))];
F = F./repmat(vecnorm(F,2,2),1,size(F,2)); % Normalize

% Intialize
V = zeros(size(probe));

% Loop probed points
for i = 1:size(probe,1) % Normalize
    % Sum contributions of filament
    for j = 1:size(f,1)
        r = probe(i,:) - f(j,:);
        V(i,:) = V(i,:) + cross(F(j,:),r)/(norm(r)^3)*dl(j);
    end
end
V = V*Gamma/(4*pi); % Normalize

% Output
u = V(:,1);
v = V(:,2);
w = V(:,3);
```

D.1.6 Dini *et al.* Subroutine [45]

```
%-------------------------------------------------------------------------
% Evaluates the function
% U/U_edge = (1-c1)/2 + (1+c1)/2 * tanh(c2(y-c3)/c4))
%-------------------------------------------------------------------------
% INPUTS
% c1 = c1
% c2 = c2
% c3 = c3
% c4 = c4
% c5 = U_edge
% y = wall-normal points at which to evaluate solution
%-------------------------------------------------------------------------
% OUTPUT
% u = streamwise velocity
%-------------------------------------------------------------------------
function u = diniMod(c1,c2,c3,c4,c5,y)
u = c5.*((1-c1)/2+(1+c1)/2.*tanh(c2.*(y-c3)./c4));
```

D.2 POD of Large Datasets

As outlined in Section 3.3.2, the snapshot implementation of proper orthogonal decomposition requires the construction of a matrix that contains all the snapshots (Eqn. 3.8). This can lead to significant memory requirements, as the entire dataset must be loaded into memory, on top of which more memory is required in order to perform the needed operations. This can be prohibitive for even POD analysis on planar PIV data, as for example, a single dataset collected in Chapter 5 consists of 5000 snapshots (each consisting of two 1 megapixel images) that is approximately 4 GB in total size, and thus the computation will likely fail on any personal computer with 8 GB of RAM or less. Modern workstation PC are often equipped with much more RAM and so the computation can be performed, however, the tomographic PIV datasets collected in Chapter 6 are each approximately 128 GB in size and therefore either a PC with 256–512 GB of RAM or a modified approach to the computation was needed. The latter was opted for since the former is relatively expensive compared to the time it would take a graduate student to develop the new code.

A solution to performing POD on datasets too large to fit into memory was developed using the tall array functionality built into MATLAB. The implementation is provided in Section D.2.1. In essence, MATLAB tall arrays are arrays that exist on a local disk, rather than in memory, for which MATLAB has extended a number of its operation to be able to work with tall arrays, meaning a computation can be performed on the array without having to load it entirely into memory. Luckily, MATLAB's SVD function, which is used to perform POD, has been updated to included tall array support. Working with tall arrays requires some special considerations, which is why the dedicated function provided in Section D.2.1 was developed.

Here, a brief summary on the operation of the code is provided. First, the function is directed to the directory that contains all the snapshots, and its total size is analyzed to determine what portion of the data will fit into memory, and therefore the corresponding number of cycles it will take the read the data in (line 131). If data can be read in a single cycle then the user is warned

that the 'traditional' computational approach should be taken (line 137). Next the tall array source must be created (referred to in MATLAB terminology as a 'datastore'), with the raw snapshot files proving unsuitable since a specific form is expected for the tall array, which depends on the operations that will be performed. For the SVD operation, the tall array must be arranged with the realizations/measurements in the first dimension and the snapshots in the second dimension. Therefore, as the data is looped through (lines 167–225), each snapshot is read in (line 186) and trimmed down to only a portion of its realizations (line 189), with the snapshots concatenated in the second dimension and written to the datastore (line 210). As a result, the operation is relatively time inefficient since the most time consuming operation, which is reading in the snapshots, must be performed n times, where n is the number of cycles.

Once the datastore is in place, the rest is rather straightforward, as the source of the tall array is set to the datastore (lines 255–258) and the built-in SVD function is evaluated (line 275) to give the POD spatial eigenfunctions, eigenvalues, and temporal coefficients. Since the latter two require small memory footprints, their result can brought into memory immediately (line 281), in operation referred to as 'gathering' in MATLAB terminology, and then written to disk as final outputs (lines 283–284). The eigenfunctions/spatial modes cannot be gathered all at once, and so are written to disk in manageably sized groups (lines 258–334).

D.2.1 Big POD Routine

```
1  %--------------------------------------------------------------------------
2  % Computes the proper orthogonal decomposition of a data set too large to
3  % fit into memory
4  %--------------------------------------------------------------------------
5  % REQUIRED INPUTS
6  % dirs = Cell of directories.
7  %   dirs{1} = Input directory containing ONLY snapshots (no other
8  %   files in this folder). Each snapshot must be a mat file containting
9  %   a separate varaible per vector component. Each component can be
10 %   n-dimensional (1, 2 and 3 component data is supported).
11 %
12 %   dirs{2} = Output directory where POD result will be written.
13 %
14 %   dirs{3} = Path to mean mat file. Must be the same format as
15 %   the snapshots. Variable type of mean file is important (e.g., single,
16 %   double) since this sets the variable type for the POD result and has
17 %   significant impact on memory allocation.
18 %
19 %   dirs{4} (optional) = Directory where temporary files will go. If not
20 %   provided a tmp folder will be created in the output directory.
21 %
22 % NAME/VALUE PAIR OPTIONAL INPUTS
23 % MemUsage = Decimal value between 0 and 1 (exclusive).
24 % Default = 0.5
25 % Percentage of memory to use. Higher values will result in faster
26 %   processing times (fewer cycles) but may result in out of memory
27 %   or conversion errors (char to cell).
```

```
%
% ModesExport = 'all' or integer range (see examples)
% Default = 'all'
% Number of modes to export (written to disk).
% Numeric range examples: 1:10 (first ten modes)
%                         1:2:200 (every other mode up to mode 200)
%
% TmpExists = true or false.
% Default = false.
% Set to true if the temporary files already exsist (previously created
% by this function).
%
% KeepTmp = true or false.
% Default = false;
% Set to true to keep temporary files after processing.
%
% Suppress = true or false.
% Default = false.
% Set to true for reckless abandon (suppress warnings and the
% verification of temp files).
%
% NOTES
% - Modes are exported into individual mat files (M001.mat, etc.).
%   Each contains a cell array (phi) whose indices correspond to the
%   variables in the snapshot files. i.e., snapshot var1 <=> phi{1},
%   snapshot var 2 <=> phi{2}, etc..
% - Temporal coefficients and modal energy are exported as A.mat and
%   E.mat, respectively.
% - All values of E and A are exported, regardless of ModesExport.
%--------------------------------------------------------------------------
function bigPOD(dirs,varargin)
%% Prep work
clc;

% Check MATLAB version
if verLessThan('matlab','9.6')
    error('MATLAB R2019a or newer required');
end

% Input handling
p = inputParser;
addRequired(p,'dirs',@iscell);
addOptional(p,'MemUsage',0.5,@(x) isnumeric(x) && (x>0) && (x<1));
addOptional(p,'TmpExists',false,@islogical);
addOptional(p,'KeepTmp',false,@islogical);
addOptional(p,'Suppress',false,@islogical);
addOptional(p,'ModesExport','all');
parse(p,dirs,varargin{:});

% Check dir for trailing /
for i = 1:length(dirs)
    if ~strcmp(dirs{i}(end),'\') && i ~= 3
```

```
80          dirs{i} = [dirs{i} '\'];
81      end
82  end
83
84  % Directory handling
85  inDir = dirs{1};
86  outDir = dirs{2};
87  meanFile = dirs{3};
88  if length(dirs) < 4 % No tmp dir provided
89      tmpDir = [outDir 'tmp\'];
90      % Check if it exists and if not create it
91      if exist(tmpDir,'dir') ~= 7
92          mkdir(tmpDir);
93      end
94  else
95      tmpDir = dirs{4};
96  end
97
98  % Snapshots
99  snapshots = dir([inDir '*.mat']); % name of snapshots
100 n = length(snapshots); % number of snapshots
101 filesize = sum([snapshots.bytes]); % total file size of snapshots [bytes]
102
103 % Issue warning
104 if ~p.Results.Suppress && ~p.Results.TmpExists
105     clc;
106     disp(['WARNING: This operation will create ' num2str(round(filesize
            /(1024^3))) ' GB of temporary files in ' tmpDir]);
107     disp('Ensure you have sufficient space (and patience).');
108     disp('Press any key in the command window to continue');
109     pause; clc;
110 end
111
112 % Mean data
113 Uavg = struct2cell(load(meanFile))';
114 dims = size(Uavg{1}); % spatial dimensions
115 l = prod(dims)*3; % 1D size
116 Uavg = cell2mat(cellfun(@(x) reshape(x,numel(x),1),Uavg','UniformOutput',
        false));
117 varType = class(Uavg); % variable type to use throughout
118
119 % Memory available
120 mem = memory;
121 mem = p.Results.MemUsage*(mem.MemAvailableAllArrays - mem.MemUsedMATLAB);
122
123 % Variable type
124 if strcmp(varType,'single') %#ok<STISA>
125     bytesP = 4; % bytes per element for single
126 else
127     bytesP = 8; % bytes per element for double
128 end
129
```

```
% Number of cycles
cycles = ceil(l/(mem/(n*bytesP + 100)));

% Number of rows per 30 MB (~26 MB w compression) temp file
nRows = ceil(30E6/n/bytesP);

% 1 cycle warning
if cycles == 1 && ~p.Results.Suppress && ~p.Results.TmpExists
    disp('WARNING: You can likely fit all your data into memory.');
    disp('Consider using the ''traditional'' POD calculation method, which
       will be MUCH faster.');
    disp('Press any key in the command window to continue');
    pause; clc;
end

%% Temporary files
if ~p.Results.TmpExists
    % Delete any existing mat files in tmpDir
    toDelete = dir([tmpDir '*.mat']);
    for i = 1:length(toDelete)
        delete([tmpDir toDelete(i).name]);
    end

    % Determine ranges for cycles
    step = ceil(l/cycles);
    if rem(l,cycles) == 0
        range = [1:step:l; step:step:l];
    else
        range = [1:step:l; step:step:l l];
    end

    % Determine number of temp files per cycle
    nFiles = ceil(step/nRows);

    % Print spec
    printFormat = ['%0' num2str(ceil(log10(nFiles*cycles))) 'd.mat'];

    % Loop cycles
    for i = 1:cycles
        tic; % Start timer

        % Initialize
        U = zeros(range(2,i)-range(1,i)+1,n,varType);

        % Loop snapshots
        for j = 1:n
            % Show progress
            if i == 1
                fprintf(['Step 1 of 3: Temporary Files \n',...
                         'Cycle: ' num2str(i) '/' num2str(cycles) ', Loading
                            Snapshots: ' num2str(j) '/' num2str(n) '\n']);
            else
```

```
180                 fprintf(['Step 1 of 3: Temporary Files \n',...
181                         'Time to complete previous cycle: ' formatSecs(ct)
                                ' \n',...
182                         'Cycle: ' num2str(i) '/' num2str(cycles) ', Loading
                                Snapshots: ' num2str(j) '/' num2str(n) '\n']);
183             end
184
185             % Load
186             temp = struct2cell(load([inDir snapshots(j).name]));
187
188             % Re-arrange and subtract mean
189             temp = cell2mat(cellfun(@(x) reshape(x,numel(x),1),temp,'
                    UniformOutput',false));
190             U(:,j) = temp(range(1,i):range(2,i)) - Uavg(range(1,i):range(2,i
                    ));
191             clc;
192         end
193
194         % Write files
195         for j = 1:nFiles
196             % Show progress
197             if i == 1
198                 fprintf(['Step 1 of 3: Temporary Files \n',...
199                         'Cycle: ' num2str(i) '/' num2str(cycles) ', Writing
                                temp file: ' num2str((i-1)*nFiles+j) '/'
                               num2str(nFiles*cycles) '\n']);
200             else
201                 fprintf(['Step 1 of 3: Temporary Files \n',...
202                         'Time to complete previous cycle: ' formatSecs(ct)
                                ' \n',...
203                         'Cycle: ' num2str(i) '/' num2str(cycles) ', Writing
                                temp file: ' num2str((i-1)*nFiles+j) '/'
                               num2str(nFiles*cycles) '\n']);
204             end
205             if j == nFiles
206                 data = U((j-1)*nRows+1:end,:);
207             else
208                 data = U((j-1)*nRows+1:j*nRows,:);
209             end
210             save([tmpDir sprintf(printFormat,(i-1)*nFiles+j)],'data');
211             clc;
212         end
213
214         % Cycle time
215         ct = toc;
216
217         % Clean up
218         clearvars data U temp
219     end
220 else
221     clc;
222     fprintf(['Step 1 of 3: Temporary File \n',...
```

```
            'Temporary files are in place. Skipping creation.']);
    pause(2);
end

% Clean up
clearvars Uavg

%% POD
clc;
fprintf(['Step 2 of 3: POD \n',...
         'Deleting existing POD exports \n']);

% Delete any existing mat files in outDir
toDelete = dir([outDir '*.mat']);
for i = 1:length(toDelete)
    delete([outDir toDelete(i).name]);
end

% Modes
if strcmp(p.Results.ModesExport,'all')
    modes = (1:n);
else
    modes= p.Results.ModesExport;
end
nModes = n/(cycles*2); % Modes per cycles
cycles = ceil(length(modes)/nModes); % Number of cycles needed
groups = reshape([modes(:); NaN(mod(-numel(modes),cycles),1)],[],cycles);

% Create data store
clc;
disp('Step 2 of 3: POD');
ds = fileDatastore([tmpDir '*.mat'],'ReadFcn',@(fname) getfield(load(fname),
    'data'),...
                                    'UniformRead', true);

% Create velocity fluctuations tall array
Uf = tall(ds);

% Verify
if ~p.Results.Suppress
    clc;
    fprintf(['Step 2 of 3: POD \n',...
             'Verifying temp files \n']);
    tall_size = gather(size(Uf));
    if tall_size(1) ~= l || tall_size(2) ~= n
        error('Unexpected array size returned. Recreate your temporary files
            .');
    else
        disp('Expected array size returned. Continuing.');
        pause(2);
    end
end
```

```
273
274 % POD
275 [phi_tall,E,A] = svd(Uf,'econ');
276
277 % Energy and time coefficients
278 clc;
279 fprintf(['Step 2 of 3: POD \n',...
280          'Exporting temporal coefficients and modal energy.\n']);
281 [E,A] = gather(E,A);
282 E = diag(E).^2;
283 save([outDir 'A.mat'],'A');
284 save([outDir 'E.mat'],'E');
285
286 % Modes
287 printFormat = ['M%0' num2str(ceil(log10(n))) 'd.mat'];
288 c = 1;
289 for i = 1:size(groups,2)
290     tic; % start timer
291
292     % Show progress
293     clc;
294     if i == 1
295         fprintf(['Step 2 of 3: POD \n',...
296                  'Cycle: ' num2str(i) '/' num2str(size(groups,2)) ',
                        Gathering Modes.\n']);
297     else
298         fprintf(['Step 2 of 3: POD \n',...
299                  'Time to complete previous cycle: ' formatSecs(ct) ' \n',...
300                  'Cycle: ' num2str(i) '/' num2str(size(groups,2)) ',
                        Gathering Modes.\n']);
301     end
302
303     % Create group
304     group = groups(:,i);
305     group = group(~isnan(group));
306     phiGather = gather(phi_tall(:,group));
307
308     % Reshape and export
309     for j = 1:length(group)
310         clc;
311         if i == 1
312             fprintf(['Step 2 of 3: POD \n',...
313                      'Cycle: ' num2str(i) '/' num2str(size(groups,2)) ',
                            Exporting Mode: ' num2str(c) '/' num2str(numel(modes
                            )) '\n']);
314         else
315             fprintf(['Step 2 of 3: POD \n',...
316                      'Time to complete previous cycle: ' formatSecs(ct) ' \n
                            ',...
317                      'Cycle: ' num2str(i) '/' num2str(size(groups,2)) ',
                            Exporting Mode: ' num2str(c) '/' num2str(numel(modes
                            )) '\n']);
```

```
318         end
319 
320         % Reshape
321         phi = cell(1,length(dims));
322         for k = 1:length(phi)
323             phi{k} = reshape(phiGather((k-1)*prod(dims)+1:k*prod(dims),j),
                dims);
324         end
325 
326         % Export
327         save([outDir sprintf(printFormat,group(j))],'phi');
328         c = c + 1;
329     end
330     clc;
331 
332     % Cycle time
333     ct = toc;
334 end
335 
336 %% Clean up
337 clc;
338 disp('Step 3 of 3: Clean Up');
339 
340 % Shutdown parrellel pool
341 pool = gcp;
342 delete(pool);
343 
344 % Temp files
345 if ~p.Results.KeepTmp
346     toDelete = dir([tmpDir '*.mat']);
347     for i = 1:length(toDelete)
348         delete([tmpDir toDelete(i).name]);
349     end
350     disp('Temporary files deleted.');
351 else
352     disp('Temporary files left in place.');
353 end
354 disp('Operation completed.');
355 disp(['All files output to ' outDir]);
356 end
357 
358 % Format seconds into display friendly time
359 function [timeString] = formatSecs(s)
360     if s < 60
361         timeString = [num2str(round(s)) ' s'];
362     elseif s < 3600
363         timeString = [num2str(rem(floor(s/60),60)) ' m, ' num2str(rem(round(
            s),60)) ' s'];
364     else
365         timeString = [num2str(floor(s/3600)) ' h, ' num2str(rem(floor(s/60)
            ,60)) ' m, ' num2str(rem(round(s),60)) ' s'];
366     end
```

```
367 end
```

Scientific Contributions

Articles in Refereed Journals

[7] Toppings, C. E., **Kurelek, J. W.** & Yarusevych, S. 2020. Laminar Separation Bubble Development on a Finite Wing. *AIAA J*. **[In Review]**

[6] **Kurelek, J. W.**, Tuna, B. A., Yarusevych, S. & Kotsonis, M. 2020. Three-Dimensional Development of Coherent Structures in a Two-Dimensional Laminar Separation Bubble. *AIAA J*. Article in Advance.

[5] Tuna, B. A., **Kurelek, J. W.** & Yarusevych, S. 2019. Surface-Pressure-Based Estimation of the Velocity Field in a Separation Bubble. *AIAA J.*, **57** (9), 3825–3837

[4] **Kurelek, J. W.**, Yarusevych, S. & Kotsonis, M. 2019. Vortex merging in a laminar separation bubble under natural and forced conditions. *Phys. Rev. Fluids*, **4** (6), 063903

[3] **Kurelek, J. W.**, Kotsonis, M. & Yarusevych, S. 2018. Transition in a separation bubble under tonal and broadband acoustic excitation. *J. Fluid Mech.*, **853**, 1–36

[2] Istvan, M., **Kurelek, J. W.**, & Yarusevych, S. 2018. Turbulence Intensity Effects on Laminar Separation Bubbles Formed over an Airfoil. *AIAA J.*, **56** (4), 1335–1347

[1] **Kurelek, J. W.**, Lambert, A. R., & Yarusevych, S. 2016. Coherent Structures in the Transition Process of a Laminar Separation Bubble. *AIAA J.*, **54** (8), 2295–2309

Articles in Refereed Conference Proceedings

[7] **Kurelek, J. W.**, Yarusevych, S. & Kotsonis, M. 2019. The effect of three-dimensional forcing on flow development within a laminar separation bubble. In *11th Int. Symp. Turb. Shear Flow Phenom.*, Southampton, UK, July 30–Aug 2

[6] **Kurelek, J. W.**, Yarusevych, S. & Kotsonis, M. 2018. An Assessment of Flow Development in a Separation Bubble Subjected to Spanwise Modulated Disturbances using Particle Image Velocimetry. In *48th AIAA Fluid Dyn. Conf.*, Atlanta, GA, June 25–29

[5] **Kurelek, J. W.** & Yarusevych, S. 2017. Merging of coherent structures in a separation bubble. In *10th Int. Symp. Turb. Shear Flow Phenom.*, Chicago, IL, July 6–9

[4] **Kurelek, J. W.**, Tuna, B. A. & Yarusevych, S. 2017. Three-Dimensional Vortex Development in a Laminar Separation Bubble formed over an Airfoil. In *47th AIAA Fluid Dyn. Conf.*, Denver, CO, June 5–9

[3] **Kurelek, J. W.** & Yarusevych, S. 2016. The effect of acoustic excitation on the later stages of transition in a laminar separation bubble. In *46th AIAA Fluid Dyn. Conf.*, Washington, DC, July 13–17

[2] Istvan, M., **Kurelek, J. W.** & Yarusevych, S. 2016. The effect of free-stream turbulence on the structure of laminar separation bubbles. In *46th AIAA Fluid Dyn. Conf.*, Washington, DC, July 13–17

[1] **Kurelek, J. W.**, Lambert, A. & Yarusevych, S. 2015. Development of coherent structures within the laminar separation bubble of a NACA0018 airfoil. In *45th AIAA Fluid Dyn. Conf.*, Dallas, TX, June 22–26

Invited Talks

[1] **Kurelek, J. W.**, Kotsonis, M. & Yarusevych, S. 2020. Laminar Separation Bubble Bursting and Low Frequency Modulations: Prior Work and Recent Developments. In *AIAA SciTech Forum Expo.*, Orlando, FL, Jan 6–10

Conference Presentations

[9] **Kurelek, J. W.**, Kotsonis, M. & Yarusevych, S. 2019. Vortex Development in a Laminar Separation Bubble measured via Tomographic Particle Image Velocimetry. In *72nd Annu. Meet. APS Div. Fluid Dyn.*, Seattle, WA, Nov 23–26

[8] **Kurelek, J. W.**, Kotsonis, M. & Yarusevych, S. 2019. Three-Dimensional Disturbance Production using AC-DBD Plasma Actuation and the Effect on Transition in a Separation Bubble. In *1000 Isl. Fluid Mech. Meet.*, Gananoque, ON, Apr 26–28

[7] **Kurelek, J. W.**, Yarusevych, S. & Kotsonis, M. 2018. The effect of spanwise modulated DBD plasma forcing on flow development in a laminar separation bubble. In *71st Annu. Meet. APS Div. Fluid Dyn.*, Atlanta, GA, Nov 18–20

[6] **Kurelek, J. W.**, Yarusevych, S. & Kotsonis, M. 2017. The effect of tonal and broadband acoustic excitation on the transition process within a laminar separation bubble. In *70th Annu. Meet. APS Div. Fluid Dyn.*, Denver, CO, Nov 19–21

[5] **Kurelek, J. W.**, Tuna, B. A. & Yarusevych, S. 2017. A volumetric reconstruction of separation bubble flow over a NACA 0018 airfoil. In *1000 Isl. Fluid Mech. Meet.*, Gananoque, ON, Apr 21–23

[4] Tuna, B. A., **Kurelek, J. W.** & Yarusevych, S. 2017. Sensor-based estimation of the velocity field in a separation bubble. In *1000 Isl. Fluid Mech. Meet.*, Gananoque, ON, Apr 21–23

[3] **Kurelek, J. W.** & Yarusevych, S. 2016. Transition in a Laminar Separation Bubble and the Effect of Controlled Acoustic Disturbances. In *1000 Isl. Fluid Mech. Meet.*, Gananoque, ON, Apr 22–24

[2] **Kurelek, J. W.** & Yarusevych, S. 2015. An investigation of natural and forced transition in a laminar separation bubble via time-resolved Particle Image Velocimetry. In *68th Annu. Meet. APS Div. Fluid Dyn.*, Boston, MA, Nov 22–24

[1] **Kurelek, J. W.**, Lambert, A. R. & Yarusevych, S. 2015. Investigation of Roll-Up Vortices within the Laminar Separation Bubble of NACA 0018 Airfoil. In *1000 Isl. Fluid Mech. Meet*., Gananoque, ON, May 1–3